Operando study of CO_2 hydrogenation over Cu-Zn nanoparticle-based catalysts

Dissertation

zur Erlangung des Doktorgrades

an der Fakultät für Mathematik, Informatik und Naturwissenschaften

Fachbereich Physik

der Universität Hamburg

vorgelegt von

Esko Erik Beck

Hamburg

2024

Gutachter/innen der Disseration:	Prof. Dr. Andreas Stierle
	Prof. Dr. Bernhard Klötzer
Zusammensetzung der Prüfungskommission:	Prof. Dr. Andreas Stierle
	Prof. Dr. Bernhard Klötzer
	Prof. Dr. Daniela Pfannkuche
	Dr. Vedran Vonk
	Dr. Dieter Lott
Vorsitzende/r der Prüfungskommission:	Prof. Dr. Daniela Pfannkuche
Datum der Disputation:	31.01.2025
Vorsitzender des Fach-Promotionsausschusses PHYSIK:	Prof. Dr. Markus Drescher
Leiter des Fachbereichs PHYSIK:	Prof. Dr. Wolfgang J. Parak
Dekan der Fakultät MIN:	Prof. Dr.-Ing. Norbert Ritter

Eidesstattliche Versicherung

Hiermit versichere ich an Eides statt, die vorliegende Dissertationsschrift selbst verfasst und keine anderen als die angegebenen Hilfsmittel und Quellen benutzt zu haben.

Sofern im Zuge der Erstellung der vorliegenden Dissertationsschrift generative Künstliche Intelligenz (gKI) basierte elektronische Hilfsmittel verwendet wurden, versichere ich, dass meine eigene Leistung im Vordergrund stand und dass eine vollständige Dokumentation aller verwendeten Hilfsmittel gemäß der Guten wissenschaftlichen Praxis vorliegt. Ich trage die Verantwortung für eventuell durch die gKI generierte fehlerhafte oder verzerrte Inhalte, fehlerhafte Referenzen, Verstöße gegen das Datenschutz- und Urheberrecht oder Plagiate.

04.11.24 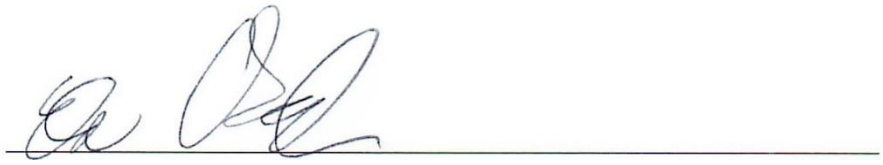

Datum Unterschrift der Doktorandin / des Doktoranden

„Your failures also permit you to see the flaws of your ideas, which are only revealed in the execution of them “

– Robert Greene

Summary

Methanol is one of the most widely produced chemicals globally, valued for its importance as both a chemical feedstock and a potential fuel in the transition toward a carbon-neutral economy. The industrial synthesis of methanol from syngas mixtures of CO, CO_2, and H_2 is facilitated by the use of the Cu-ZnO-Al_2O_3 (CZA) catalyst. Despite decades of research, the exact reaction mechanism of the CZA catalyst is still debated. Various theories have been proposed regarding the active sites of the catalyst, including copper-zinc alloys, copper decorated with zinc atoms, or a ZnO_x overlayer with oxygen vacancies at the Cu-ZnO interface.

Possibly the most important challenge to be overcome in order to advance the understanding of this catalytic system is the so-called pressure gap. This gap refers to the discrepancy between the ultra-high vacuum to ambient pressure conditions under which surface science techniques typically operate, and the high-pressure conditions (50 bar and above) encountered in real-world industrial processes. This thesis focuses on bridging the pressure gap by employing surface-sensitive X-ray diffraction (XRD) at both ambient and high pressures to gain structural insights into the CZA catalyst system. The primary goal was to investigate the dynamic behaviour of copper and zinc during methanol synthesis under various reaction gas mixtures and high pressures that simulate industrial conditions. For this purpose, two model systems of the catalyst were prepared using molecular beam epitaxy (MBE) under ultra-high vacuum (UHV) conditions: (1) a simplified model system comprising epitaxial Cu nanoparticles supported on single-crystal Al_2O_3 substrates, and (2) a ZnO-supported model system in which metallic Zn was first deposited onto the Al_2O_3 support, oxidized under UHV conditions, and then followed by the deposition of Cu. A custom MBE chamber was designed and commissioned for the precise deposition of metallic Zn, allowing precise control over the amount of Zn incorporated into the samples.

Structural analysis of the catalyst under operando conditions was enabled by the development and improvement of a special high-pressure surface XRD (SXRD) setup. This advanced system was utilized to gather novel structural information about the Cu and Cu_2O phases of the catalyst under various reaction gas mixtures, operating at a system pressure of 30 bar.

One of the major questions addressed in this thesis was whether a CuO_x-type structure or partially oxidized copper phase forms under reaction conditions. No evidence of such a phase above 575 K was found, either at ambient pressure or operando pressure. Instead, copper remained in its metallic state during exposure to various reaction gas mixtures, including CO, CO_2, and H_2. For both model systems, oxidation was observed only under pure Ar gas flow containing trace amounts of oxygen and water (around 1 ppm). The sample preparation yielded epitaxial (111)-oriented Cu nanoparticles, which were found to retain their crystal orientation with respect to the sapphire substrate under various reaction gas mixtures at ambient pressure, with a particle size ranging between 8-10 nm. Upon exposure to air at room temperature, these Cu nanoparticles formed core-shell Cu-Cu_2O structures, where the Cu_2O shell maintained the same crystal orientation as the Cu core. Even under high pressure reducing conditions, the Cu_2O shell remained stable below 575 K, with full reduction of the Cu occurring only at higher temperatures. Additionally, the formation of (110)-oriented Cu particles was observed if the sample temperature was increased stepwise to 575 K. These (110)-oriented particles displayed faster oxidation and reduction dynamics compared to (111)-oriented particles, despite comparable particle size.

A central focus of this work was the highly debated issue of Cu-Zn alloy formation during catalytic reactions. The study revealed the presence of two distinct Cu-Zn alloy phases: $Cu_{0.2}Zn_{0.8}$ and $Cu_{0.64}Zn_{0.36}$. The data suggest a dynamic interplay between these two alloy phases, dependent on the amount of hydrogen in the reaction gas mixture. Partial oxidation of the $Cu_{0.2}Zn_{0.8}$ phase occurred in reaction gases with little to no hydrogen, resulting in a transition to the more Cu-rich $Cu_{0.64}Zn_{0.36}$ phase. This transition was accompanied by the diffusion of zinc into the metallic copper particles and the potential formation of ZnO_x overlayers. These observations challenge the conventional understanding that the formation of ZnO/ZnO_x and Cu-Zn alloys phases is solely governed by the oxidizing or reducing nature of the gas environment. Instead, this work suggests that the amount of hydrogen in the gas mixture plays a crucial role in determining the formation and oxidation states of the Cu-Zn alloy phases.

Finally, the Al_2O_3 substrate was observed to remain stable across all investigated reaction gas mixtures and at both ambient and operando pressures. This confirms its stabilizing

role in the catalytic system, without any indication of active participation in the catalytic process itself.

Zusammmenfassung

Methanol ist eine der weltweit an den häufigsten produzierten Chemikalien, mit einer enormen Bedeutung sowohl als Ausgangsmaterial für die Herstellung diverser Derivate als auch als potenzieller Kraftstoff im Übergang zu einer CO_2-neutralen Wirtschaft. Die industrielle Synthese von Methanol aus Synthesegas, einer Mischung aus CO, CO_2 und H_2, wird durch den Einsatz des Cu-ZnO-Al_2O_3 (CZA)-Katalysators ermöglicht. Trotz jahrzehntelanger Forschung ist der genaue Reaktionsmechanismus des CZA-Katalysators nach wie vor umstritten. Verschiedene Theorien wurden bezüglich der aktiven Zentren des Katalysators aufgestellt, darunter Kupfer-Zink-Legierungen, mit Zinkatomen dekoriertes Kupfer oder eine dünne ZnOx-Schicht mit Sauerstoffleerstellen an der Cu-ZnO-Grenzfläche.

Eine der wichtigsten Herausforderungen der Forschung in diesem Beriech ist sogenannte Drucklücke. Diese Lücke bezieht sich auf die Diskrepanz zwischen den etablierten Techniken der Oberflächenanalyse auf der einen Seite, welche typischerweise im Druckbereich zwischen Ultrahochvakuum und Umgebungsdruck anwendbar sind, und auf der anderen Seite den Hochdruckbedingungen von 50 bar und mehr, die in realen industriellen Prozessen auftreten. In diesem Kontext, konzentriert sich diese Dissertation darauf, diese Drucklücke zu überbrücken, indem oberflächenempfindliche Röntgenbeugung (XRD) sowohl bei Umgebungs- als auch bei Hochdruckbedingungen eingesetzt wird, um strukturelle Einblicke in das CZA-Katalysatorsystem zu gewinnen. Das Hauptziel bestand darin, das dynamische Verhalten von Kupfer und Zink während der Methanolsynthese unter verschiedenen Reaktionsgasmischungen und hohem Druck, sogenannten *operando*-Bedingungen, die denen in der industriellen Anwendung nahekommen, zu untersuchen.

Zu diesem Zweck wurden zwei Modellsysteme des Katalysators unter Verwendung der Molekularstrahlepitaxie (MBE) unter Ultra-Hochvakuumbedingungen (UHV) hergestellt: (1) ein vereinfachtes Modellsystem, bestehend aus epitaktischen Cu-Nanopartikeln auf einkristallinen Al_2O_3-Substraten, und (2) ein ZnO-unterstütztes Modellsystem, bei dem metallisches Zink zuerst auf das Al_2O_3-Substrat aufgedampft und unter UHV-Bedingungen oxidiert wurde, bevor anschließend Cu aufgedampft wurde. Eine speziell angefertigte MBE-Kammer wurde entwickelt und in Betrieb genommen, um eine präzise Evaporation

von metallischem Zink zu ermöglichen und eine genaue Kontrolle über die Menge des aufgedampften Zinks zu gewährleisten.

Die strukturelle Analyse des Katalysators unter *operando* Bedingungen wurde durch die Entwicklung und Verbesserung eines speziellen Hochdruck-SXRD-Aufbaus (Surface X-Ray Diffraction) ermöglicht. Dieser fortschrittliche Aufbau wurde genutzt, um neue strukturelle Informationen über die Cu- und Cu_2O-Phasen des Katalysators unter verschiedenen Reaktionsgasmischungen bei einem Systemdruck von 30 bar zu gewinnen.

Eine der wichtigsten Fragestellungen dieser Arbeit war, ob sich unter Reaktionsbedingungen eine CuO_x-Struktur bzw. eine teilweise oxidierte Kupferphase bildet. Es wurde kein Nachweis für eine solche Phase bei Temperaturen über 575 K gefunden, weder bei Umgebungs- noch bei Operando-Druckbedingungen. Stattdessen blieb Kupfer unter allen genutzten Reaktionsgasmischungen, einschließlich CO, CO_2 und H_2, in seinem metallischen Zustand. Für beide Modellsysteme wurde eine Oxidation nur unter reinem Argon-Gasfluss beobachtet, der Spuren von Sauerstoff und Wasser (ca. 1 ppm) enthielt. Die Proben zeigten epitaktisch orientierte (111)-Cu-Nanopartikel, die ihre Kristallorientierung in Bezug auf das Saphirsubstrat unter verschiedenen Reaktionsgasmischungen bei Umgebungsdruck beibehielten und eine Partikelgröße von 8-10 nm aufwiesen. Bei Kontakt der Proben mit Luft bei Raumtemperatur bildeten diese Nanopartikel Cu-Cu_2O-Kern-Hülle-Strukturen, wobei die Cu_2O-Hülle die gleiche Kristallorientierung wie der Cu-Kern beibehielt. Selbst unter reduzierenden Bedingungen und höhen Drücken blieb die Cu_2O-Hülle unterhalb von 575 K stabil, wobei eine vollständige Reduktion des Cu erst bei höheren Temperaturen auftrat. Darüber hinaus wurde die Bildung von (110)-orientierten Cu-Partikeln beobachtet, wenn die Probentemperatur schrittweise auf 575 K erhöht wurde. Diese (110)-orientierten Partikel zeigten schnellere Oxidations- und Reduktionsdynamiken im Vergleich zu (111)-orientierten Partikeln, obwohl sie eine vergleichbare Partikelgröße aufwiesen.

Ein zentraler Schwerpunkt dieser Arbeit war die umstrittene Frage der Cu-Zn-Legierungsbildung während der katalytischen Reaktion. Die Untersuchungen zeigten die Präsenz von zwei verschiedenen Cu-Zn-Legierungsphasen: $Cu_{0.2}Zn_{0.8}$ und $Cu_{0.64}Zn_{0.36}$. Die Daten deuten auf ein dynamisches Wechselspiel zwischen diesen beiden Legierungsphasen hin, abhängig von der Menge an Wasserstoff in der

Reaktionsgasmischung. Eine teilweise Oxidation der $Cu_{0.2}Zn_{0.8}$-Phase trat in Reaktionsgasen mit wenig oder keinem Wasserstoff auf, was zu Transition in die kupferreichere $Cu_{0.64}Zn_{0.36}$-Phase führte. Dieser Übergang ging mit der Diffusion von Zink in die metallischen Cu-Partikel und möglicherweise der Bildung von ZnO_x-Schichten einher. Diese Beobachtungen stellen den aktuellen wissenschaftlichen Konsens zu diesem Thema in Frage, laut dem die Bildung von ZnO/ZnO_x-Phasen und Cu-Zn-Legierungen ausschließlich von der oxidierenden oder reduzierenden Wirkung des Reaktionsgases abhängig ist. Stattdessen legt diese Arbeit nahe, dass die Menge an Wasserstoff in der Gasmischung eine entscheidende Rolle bei der Bildung und dem Oxidationszustand der Cu-Zn-Legierungsphasen spielt.

Schließlich wurde festgestellt, dass das Al_2O_3-Substrat unter allen untersuchten Reaktionsgasmischungen sowie bei Umgebungs- und Operando-Druckbedingungen stabil blieb. Dies bestätigt seine stabilisierende Rolle im katalytischen System, ohne Hinweise auf eine aktive Teilnahme am Katalyseprozess selbst zu geben.

Table of Contents

1. Introduction

In 2023, the market size of the chemical industry worldwide amounted to $5.1 trillion, making it one of the largest business sectors globally [1]. The common fundamental challenge in this industry is to turn a certain combination of educts into a desired product, while keeping the process as efficient as possible regarding both energy consumption as well as high selectivity regarding the target chemical over unwanted by-products. This challenge is tackled by the utilisation of catalysts. These substances are present during the chemical reaction but are not consumed and ideally not changed by it, while decreasing the energy consumption of the process and or improving its turn-over frequency or product selectivity [2]. The effectiveness of catalysts is evident by their utilisation in the production of about 90% of all the chemicals manufactured globally [3]. Improving the effectiveness of catalysts through scientific research can therefore be an interesting route to reduce the energy consumption and environmental impact of the chemical industry [4]. Research in catalysis can potentially aid in tackling the global challenge of climate change in a more direct way as well. Advancements in the effectiveness of catalysts can not only improve the efficiency of well-established industrial processes, but they can also turn a hitherto unprofitable process into an economically viable one. Enhanced catalysts could for example, make carbon capture processes more feasible, allowing for the capture of CO and CO_2 from industrial emissions rather than simply releasing these greenhouse gases into the atmosphere. The captured CO and CO_2 can be transformed into more useful and valuable chemicals, such as methane and methanol, which can also serve as alternatives to fossil fuels. The capture and utilisation of used carbon is necessary for achieving a closed carbon cycle, which is crucial in tackling global warming. This is especially important given that a substantial portion of the manufacturing and transportation infrastructure, including sectors such as aviation, heavy-duty, and marine transportation, will be difficult to electrify within the next 25 years and will likely continue to rely on carbon [5]. The necessity of establishing effective carbon capture and utilization (CCU) to achieve climate neutrality is already recognized by policymakers, as demonstrated e.g. in the “Key Principles of the Federal Government for a Carbon Management Strategy” published by the German government on February 26, 2024 [6].

A major topic in catalysis research has therefore been the conversion of CO and CO_2 to methanol, one of the world's most widely produced chemicals at a total annual production capacity of approximately 110 million tons [7]. Currently, around 2 million tons per year are produced from CO_2 with a demonstration plant in Iceland producing about 4,000 tons of methanol annually since 2012 [8]. A similar facility using the same technological core concept as the plant in Iceland has opened in Germany as well in 2019 [9]. The first industrial process for methanol conversion from CO_2 was established by BASF using a zinc/chromia based catalysts, which required a reaction pressure of 300 bars to reach sufficient methanol yields [10]. Four decades later Imperial Chemical Industries (ICI) commercialized the use of the Cu-ZnO-Al_2O_3 (CZA) catalysts, reducing the reaction pressure to 50-100 bar [10]. The CZA catalyst is the most used and researched catalyst for the conversion of CO/CO_2 to methanol to this day. In its most conventional form, the catalyst is composed of 50–70% CuO, 20–50% ZnO, and 5–20% Al_2O_3, achieving conversion efficiencies of approximately 30% and methanol selectivity ranging from 30–70% at temperatures of 220–300°C and pressures up to 50 bar.

The CZA catalyst presents an intriguing system for the investigation of heterogeneous catalysis in general, due to the interplay between a pure metal phase, copper, and an oxide phase, ZnO, described as the "strong metal-support interaction" (SMSI). The SMSI in the case of the CZA catalysts has been clearly shown to promote both the activity as well as the selectivity of the methanol conversion [11]. While Al_2O_3 was also shown to be crucial regarding the longevity of the catalyst in the industrial process, the phase is associated mostly with only a stabilising function [12]. Even though the CZA catalyst has been the subject of scientific research for several decades, the exact reaction mechanism is still not fully understood and debated. The commonly discussed active sites for carbon dioxide hydrogenation in a syngas mixture include: A) a surface copper–zinc alloy formed by the partial reduction of zinc oxide [13,14], B) metallic copper steps decorated with zinc atoms [11,15], and C) the formation of thin zinc oxide (ZnO_x) overlayers at the copper–zinc oxide interface, believed to contain oxygen vacancies [16,17]. It was observed that starting from an initial state where Cu and ZnO particles are separated, activation of the catalyst under reducing conditions (150–200 °C with H2/+CO at 50–100 bar) caused Zn species to migrate and form a graphitic-like ZnO_x overlayer on the metallic Cu surfaces, a process determined to be detrimental to the catalytic performance [18,19]. To resolve the general ambiguity regarding the active sites of the catalysts, a comprehensive understanding of

the molecular and atomic-scale processes occurring during catalytic reactions is crucial, which requires the application of various experimental techniques suited to investigate surfaces and interfaces of samples, a field of study known as surface science. In the investigation of catalysts, surface science faces two major challenges in catalysis research, known as the pressure gap and materials gap. The pressure gap describes the difference between the pressures range in which most of the experimental techniques of surface science can be employed, versus the pressure of the real-world industrial processes, which are usually several orders of magnitude larger. Especially spectroscopic methods such as XPS/XAS, EDX, IR, AES as well as imaging techniques such as SEM/TEM, AFM and STM are still mostly limited to ultra-high vacuum conditions, except for AFM and STM which can be used in ambient pressures. Development of new and improved experimental setups has allowed to increase the experimental pressure ranges of some of these techniques to a few hundred millibar recently [20,21].

The materials gap arises from the need to simplify the high complexity of real-world industrial powder catalysts, which often consist of a mixture of various components, with different particle sizes, shapes, and surface defects and facets, undercoordinated surfaces atoms as well as multiple active phases and support materials. These factors create a highly heterogeneous environment that is difficult to study systematically. To make these systems more manageable for scientific research, their complexity is reduced by using simplified model catalysts, typically consisting of well-defined surfaces, single crystals, or nanoparticles with a known surface structure.

Two tackle these two challenges, the aim of this work was to gather in-situ structural information about the CZA and Cu-Al_2O_3 catalyst at elevated pressures and temperatures using primarily surface sensitive X-ray diffraction. Since X-ray diffraction techniques are more suited to investigate samples at pressures considerably higher than 1 bar, in this work a special setup for operando surface XRD was employed and further developed to bridge the pressure gap. While the technical setup and improvement of the cell are discussed in chapter 5, the results of the performed operando experiment with the cell are described in chapter 7.

Furthermore, the preparation of model systems of the CZA catalyst in this work focused on preparing ordered epitaxial samples of the CZA catalyst with a controlled amount of metallic Zn to investigate the dynamic behaviour of Zn in-situ. For the controlled sample

preparation utilizing metallic Zn, a custom molecular beam epitaxy chamber for Zn deposition in ultra-high vacuum conditions was designed and commissioned as described in chapter 4 along with a description of all experimental setups used in this work. The dynamic behaviour of metallic Zn was investigated in different reaction gas mixtures at 1 bar total pressure in situ as described in chapter 6 utilizing two similarly prepared samples one with and one without Zn. The results are summarized and discussed in chapter 8.

2. Methanol synthesis from CO_2/CO syngas over Cu-Zn based catalysts

The hydrogenation of CO_2 from syngas, which refers to a mixture of CO_2, CO and H_2, is governed by two separate chemical reactions, namely the exothermic synthesis of methanol [22]:

$$CO_2 + 3H_2 \leftrightharpoons CH_3OH + H_2O \quad (1)$$

$$\Delta_r H_{298\,K} = -49.5\ {}^{kJ}/_{mol}$$

as well as the endothermic reverse water gas shift reaction [23]:

$$CO_2 + H_2 \leftrightharpoons CO + H_2O \quad (2)$$

$$\Delta_r H_{298\,K} = 41.2\ {}^{kJ}/_{mol}$$

CO can also be hydrogenated directly to methanol via the exothermic reaction:

$$CO + 2H_2 \leftrightharpoons CH_3OH \quad (3)$$

$$\Delta_r H_{298\,K} = -90.8\ {}^{kJ}/_{mol}$$

In order to overcome kinetic limitations, the hydrogenation of CO_2 is performed on an industrial scale at temperatures between 200-300° C, despite the decrease in equilibrium CO_2 conversion rates as well as methanol selectivity with temperature as seen in Figure 2.1. The reverse water gas shift reaction constitutes a competitive reaction to CO_2 hydrogenation with increasing temperature, but no clear consensus has yet formed on whether the reaction is beneficial to the catalytic activity due to a surface cleaning effect of the water [24,25], or whether it causes a deactivation of active sites [26]. The potential deactivation of active sites by water and other carbon-based reaction intermediaries was shown to be significant at temperatures below 210° C [27]. Furthermore, several studies employing isotopic labelling strategies find that the main source of carbon in the methanol synthesis from syngas mixtures is CO_2 [24,28].

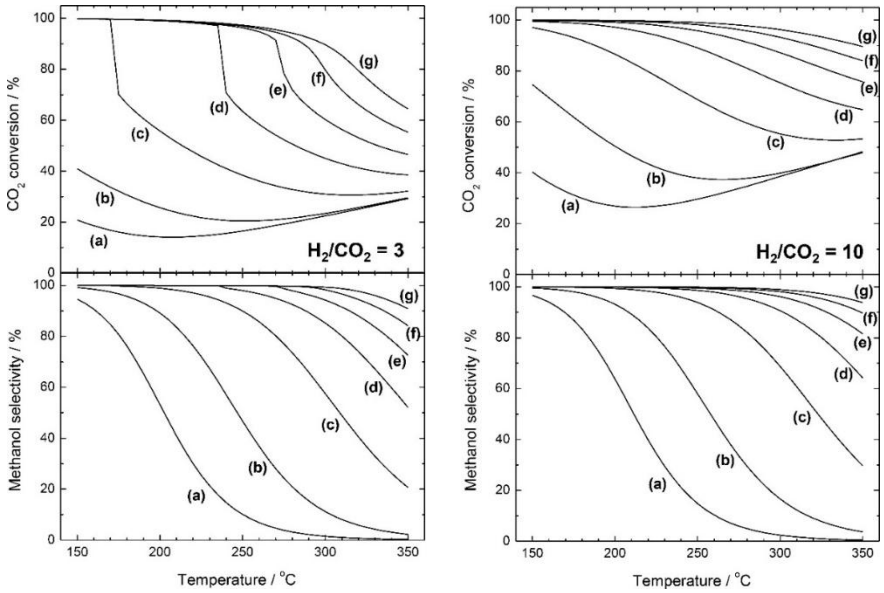

Figure 2.1. Equilibrium CO_2 conversion rates and methanol selectivity as a function of temperature with initial H_2/CO_2 ratios of 3 (left) and 10 (right) at pressures of (a) 10 bar, (b) 30 bar, (c) 100 bar, (d) 200 bar, (e) 300 bar, (f) 400 bar, and (g) 500 bar taken from [29].

2.1. The roles of Cu, Zn and alumina

In the research field surrounding the catalytic hydrogenation of CO_2 to methanol, Cu has been clearly established as the key element in the corresponding catalysts due to its high selectivity for methanol production [25]. In the steady-state of methanol synthesis from syngas, the variety of the electronic states of copper have been investigated and identified as crucial to the catalytic activity of the element, with the specific electronic state best suited for methanol synthesis even dubbed “methanol copper” by R. Schlögl [25]. This electronic state of copper is caused by a partial electron depletion of copper into a $Cu^{\delta+}$ state, which was determined to be caused by a partial oxidation of surface Cu by contact with oxygen either through surface adsorbates or proximity of oxide phases, e.g. ZnO [30–32]. A key question regarding the CZA catalyst is therefore, how the electronic state and the oxidation of Cu are linked, how these properties change under different reaction gas mixtures and pressures and how the state of Cu therefore effects the performance of the catalytic reaction. While the slow diffusion of oxygen into Cu at room temperature under exposure to air is already sufficient to cause the formation of Cu_2O and after prolonged exposure CuO for nanometre sized particles [33], significant and deep oxygen diffusion was observed at elevated temperatures, such as those needed for the activation of the catalyst prior to operation [30,34,35]. The oxidation state of Cu was shown to have a direct

impact on the ability to bind carbon species and facilitate the formation of specific reaction intermediaries, with a surface oxygen that forms without the formation of crystalline copper oxide being beneficial for the formation of C_1 compounds, while a copper oxide surface is beneficial for the formation of C_2 compounds [36,37].

The beneficial properties of catalysts containing Zn/ZnO have been attributed to various different effects. First of all, for the industrial powder catalyst the ZnO acts as physical spacer between Cu nanoparticles and facilitates the dispersion of the Cu phase, and consequently increases the Cu surface area [38]. As it was shown that ZnO was also directly involved in the catalytic activity, the dual-site mechanism was proposed in which the adsorption and dissociation of hydrogen are believed to occur on the Cu surface, while the CO_2 adsorption takes place on the ZnO, which is feed dissociated hydrogen from the Cu surfaces via spill-over [39–41]. More recently, the interaction of Cu and Zn/ZnO was identified to be more complex. Several studies report the formation of a Cu-Zn alloy when the catalyst is investigated under higher gas pressures and temperatures, closer to the conditions of the catalyst in the industrial application [11,15,42,43]. The surface copper–zinc alloy was believed to form through the partial reduction of zinc oxide [13,14], a result that is in line with more recent high pressure NEXAFS investigations of the catalyst, showing signal associated with reduced Zn^{2+} species under reducing gas conditions [42,43]. While the formation of Cu-Zn alloy can be detected by investigations at elevated pressures using techniques like NEXAFS or XPS via determination of the electronic state of Zn, very little is known about the actual structure and exact composition of the Cu-Zn alloy and regarding whether only a single alloy forms or whether multiple different alloy phases can be observed under different reaction gas mixtures. This is a fundamental question given, on the one hand, the observed reduction of ZnO to metallic Zn and, on the other hand, the complexity of stable brass phases as seen by the Cu-Zn phase diagram in Figure 2.2.

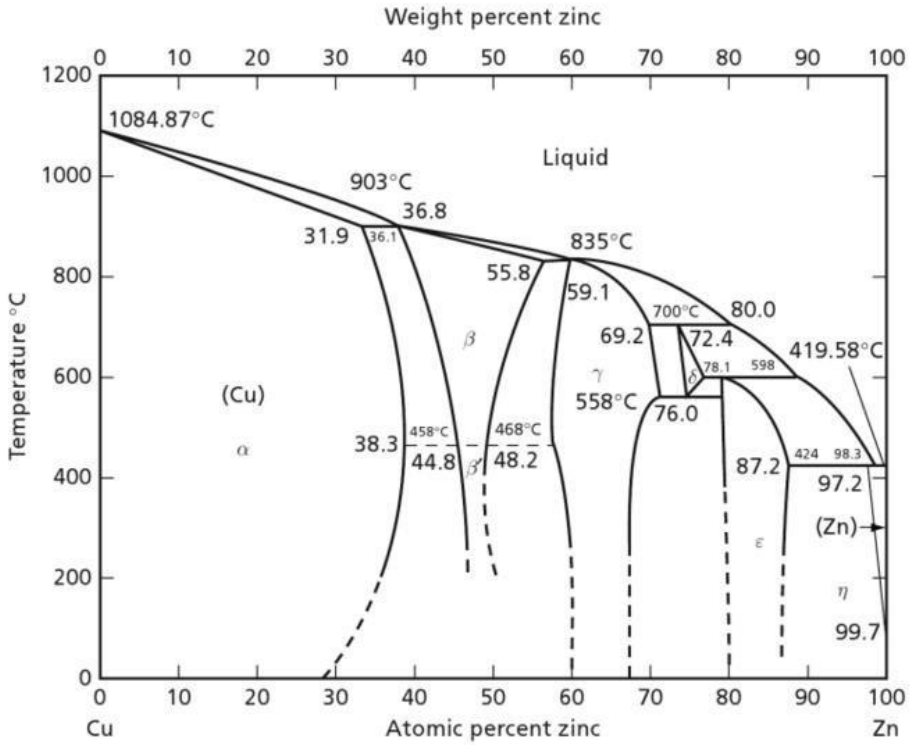

Figure 2.2. Equilibrium phase diagram of Cu and Zn taken from [44].

Furthermore, the possible formation of reduced Zn species from as prepared ZnO can cause a more dynamic behaviour of Zn under reaction conditions given the mobility of metallic Zn atoms compared to the much more stable ZnO. In fact, binding of metallic Zn to different reaction intermediaries was observed to enable even a gas-phase diffusion of Zn during methanol synthesis [17,20,45]. This mobility of Zn is key for additional theories regarding the active sites of the catalyst, with observations of metallic copper steps decorated with individual zinc atoms [11,15] pointing to the formation of a system that effectively constitutes an inverse catalyst with the possibly oxidized Cu acting as the support to the metallic Zn. Furthermore, migration of Zn to the surface of Cu particles under reaction gas mixtures containing oxygen sources caused the formation of thin zinc oxide (ZnO_x) overlayers, with the non-stochiometric sate of the ZnO being a result of the presence of oxygen vacancies in the layer [16,17].

The role of alumina within the CZA catalyst is a much less studied question for the system with the most common consensus being, that the phase acts as a structural promoter to increase the surface area of the Cu phase as well as improving the lifetime of the industrial powder catalyst [46]. Only in recent years, studies have started focusing more on the Al_2O_3 phase of the catalyst, investigating whether the oxide phase could influence the catalytic

activity as an oxide or even via promotion with metallic Al atoms. Promotion of defect structures within the ZnO phase through incorporation of Al^{3+} ions into the tetrahedral sides of the hexagonal ZnO phase, showed to improve the reducibility of ZnO and thereby improve the catalytic performance of the CZA catalyst for methanol synthesis [47,48]. These investigations used specially prepared catalysts that were not stable under industrial synthesis conditions however, and therefore the fundamental question of whether or not the aluminium oxide phase of the industrial powder catalyst remains stable under operando conditions still remains unanswered. With the rise of in-situ and operando investigations of the catalyst and corresponding model systems, some studies even suggest the formation of a $ZnAl_2O_4$ spinel structure and the possibility of a deactivation of the catalyst as a result of the Zn incorporation into such a stable phase [19,42,49]. Again, additional structural investigations of the catalyst under operando conditions are necessary to determine whether the formation of new phases incorporating aluminium is possible for the CZA catalyst and if so, how the preparation of the catalyst overall and the aluminium oxide phase in particular facilitate the growth of such structures.

2.2. Reaction pathway of methanol synthesis

The difficulty in understanding the catalytically driven methanol synthesis from syngas is not only based on the interplay between the different components of the catalysts, but also by the complexity of the reaction pathways from CO_2 and CO towards methanol and other possible products as seen in Figure 2.3. From the complex reaction network, four main reaction pathways are commonly investigated for the formation of methanol from CO and CO_2, namely two different variants of the formate pathway, the reverse water gas shift pathway as well as the trans-COOH pathway [25,50–52]. The most commonly discussed formate pathway starts from CO_2 absorbed as carboxylate on the catalyst surface, which is subsequently reacting with atomic hydrogen to form the formate intermediate. Formate is then hydrogenated first to H_2COO, then H_2COOH before being either cleaved to formaldehyde or further hydrogenated to methoxy (H_3CO) and then methanol. The reverse water gas shift route to methanol starts from CO, which is then hydrogenated to dioxymethylene, cleaved from the catalyst surface to form formic acid,

before being further hydrogenated to H_2COO and following the same path towards methanol from that point on, as the formate pathway.

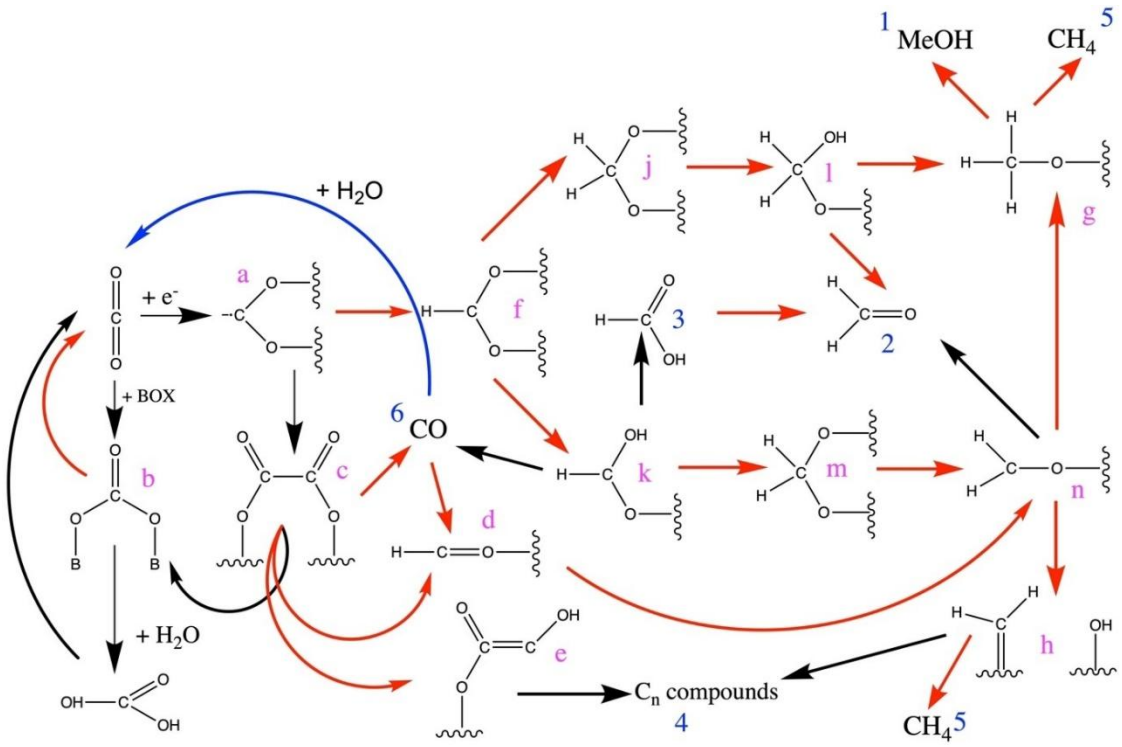

Figure 2.3. Possible reaction pathways for the reduction of CO_2 to various products including methanol. Reduction reactions are denoted in red, redox reactions in black and reverse water gas shift reactions in blue. Stable products are marked with blue numbers, intermediates with pink, lower case letters. Pink letters denote: carboxylate (a), carbonate (b), oxalate (c), formyl (d), carbonic acid (e), formate (f), methoxy (g), methylene (h), H_2COO (j), dioxymethylene (k), H_2COOH (l), H_2COO (m) and formaldehyde (n). Image taken from [25].

A third pathway can be seen as a combination of the formate pathway with the reverse water gas shift pathway, that is often referred to as an alternative formate pathway, in which the formate intermediate does not directly form H_2COO, but instead breaks the bidentate binding to form the dioxymethylene intermediate and from that point follow the same reaction path as the reverse water gas shift reaction. A final and fourth reaction pathway is the so called trans-COOH mechanism, in which CO_2 is first hydrogenated to hydrocarboxyl COOH–, which is then forming dihydroxycarbene COHOH under the presence of water. The carbene is then cleaved to COH, which is then hydrogenated to first HCOH and then H_2COH and finally methanol, similar to the pathways described above. This pathway is not included in Figure 2.3 but is illustrated instead in Figure 2.4.

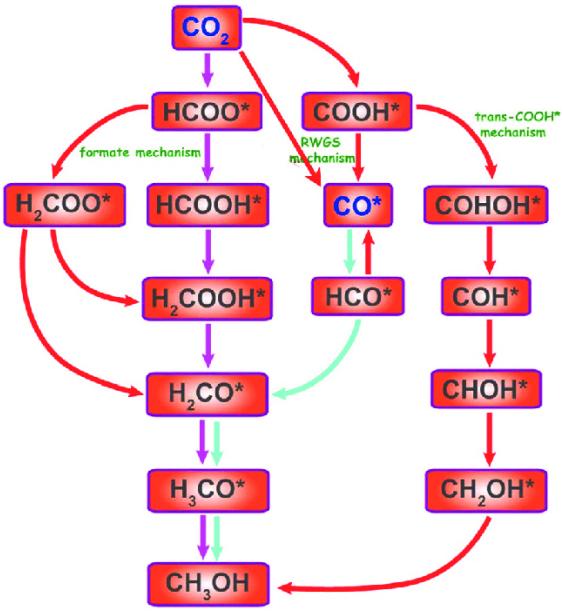

Figure 2.4. Alternative illustration of the different reaction pathways for methanol synthesis including the trans-COOH mechanism. Taken from [51].

3. Surface science methods

This chapter explains the theoretical and technical details about the different experimental techniques employed during this thesis. The main method of sample analysis was X-ray diffraction explained in detail, with shorter descriptions for X-ray photoelectron spectroscopy (XPS), auger electron spectroscopy (AES), low-energy electron diffraction (LEED) as well as Scanning electron microscopy (SEM) and energy-dispersive X-ray spectroscopy (EDX).

3.1. Fundamentals of X-ray interaction with matter

X-ray interaction with single electrons and atoms

The following overview of the general principles of X-ray diffraction is based on various textbooks of the topic [53–55]. Owing to the wave-particle dualism, X-rays can be described as electromagnetic waves as well as streams of particles called photons. The link between the particle energy and the corresponding wavelength is given in the equation:

$$E_\gamma = \hbar k = \frac{hc}{\lambda} \tag{4}$$

with the wavelength λ, the corresponding photon energy E_γ, Planck constant $h = 6.626 \times 10^{-34}$ Js, the speed of light $c = 2.998 \times 10^8$ m/s and the wavenumber $k = 2\pi/\lambda$. In general, when describing the interaction of X-rays with matter, both scattering as well as absorption of the incident beam have to be considered. In the case of absorption, the energy of the incident photon is being transmitted to the target material. If the energy of the photon E_γ fits to an energy difference between two distinct energy states in the atomic shell of the target material, the energy of the incident X-ray beam is absorbed, causing an electron to be lifted from the lower to the higher energy state. The energy difference between such states in an atom is referred to as an absorption edge in the context of X-rays interaction with matter.

For the discussion in this work, only weak scattering interaction of X-rays with the target material is assumed, so that multiple scattering events can be neglected and the kinematical approximation is valid. In the case of an elastic scattering event, no energy is being transmitted, but a wave is again emitted from the target material. This process can

be described by the classical description of X-ray scattering. In the classical description, the electric field of incident X-rays exerts a force on electrons within the target material, causing them to undergo acceleration and consequently to vibrate. A vibrating electron constitutes an electric dipole and in turn radiates waves in all directions. In the case of a pure scattering event without any loss, the scattering is called elastic scattering, and the wavelength of the waves emitted by the dipole is thus equal to the wavelength of the incident X-rays. The momentum transfer Q, defined as the difference between the incident k_i and scattered k_f wavevectors can be describes as:

$$\boldsymbol{Q} = \boldsymbol{k_f} - \boldsymbol{k_i} \tag{5}$$

With the simplification for elastic scattering of $|k_f| = |k_i|$. For scattering events, the energy-independent scattering amplitude for free electrons is given by the Thomson scattering length:

$$r_0 = \frac{e^2}{4\pi\varepsilon_0 m_e c^2} = 2.82 \cdot 10^{-5}\text{Å} \tag{6}$$

with the elemental charge e and the electron mass m_e, the vacuum permittivity ε_0 and again the speed of light c. With the scattering length of a single electron, calculating the scattering amplitude of an atom can be done by summing over all contributions of all of the atom's electrons. For an infinitesimal volume element dr, the contribution can be described by $r_0\rho(r)dr$. Additionally, to account for the different phases of the scattered waves, the phase vector e^{iQr} needs to be added, which yields the so-called atomic form factor f^0 (Q):

$$r_0 f^0(\mathbf{Q}) = r_0 \int \rho(\boldsymbol{r}) e^{i\boldsymbol{Q}\boldsymbol{r}} d\boldsymbol{r} \tag{7}$$

Since equation (7) is only valid for energies away from absorption edges, the atomic form factor needs to be corrected to account for so-called dispersion effects:

$$f(Q, \hbar\omega) = f^0(\mathbf{Q})(\hbar\omega) + if''(\hbar\omega) \tag{8}$$

With the X-ray beam frequency ω, $f'(\hbar\omega)$ describes the damping of the scattering electrons due to the binding force acting on the electrons in an atomic shell. Additionally, to account for the possibility of scattering and absorption taking place simultaneously, $f''(\hbar\omega)$ describes absorption reducing the form factor. For the considerations of this

chapter, it is important to note that both $f'(\hbar\omega)$ and $f''(\hbar\omega)$ become negligibly small if the X-ray energy is far larger than the closest adsorption edges of the target material.

X-ray scattering from crystals

In order to describe the scattering of X-rays by a crystal, again a summation of the atomic form factor is done. A crystal can be described as a lattice made up of unit cells. Therefore, the summation can be separated into these two contributions as a product of two contributing sums:

$$F_{crystal}(Q) = F_{unit\ cell} \cdot F_{lattice} = \sum_j f_j(\boldsymbol{Q}) \cdot \sum_{n_1,n_2,n_3} e^{i\boldsymbol{QR_n}} \tag{9}$$

with the lattice vector $R_n = n_1a_1 + n_2a_2 + n_3a_3$, base vectors a_1, a_2 and a_3 and integer values n_1, n_2, n_3. In the field of crystallography, the number of scattering unit cells is usually very large, so the lattice structure factor can be calculated for each dimension using the geometric series converging in β-functions:

$$F_N(Q) = \left|\sum_{n=0}^{N-1} e^{i\boldsymbol{Qna}}\right| = \frac{\sin\left(\frac{NQ_aa}{2}\right)}{\sin\left(\frac{Q_aa}{2}\right)} \tag{10}$$

with Q_a denoting the projection of the momentum vector **Q** along the direction **a**. Equation (10) has maxima at:

$$Q_a a_1 = 2\pi h, h \in Z \tag{11}$$

described as the Laue equation.

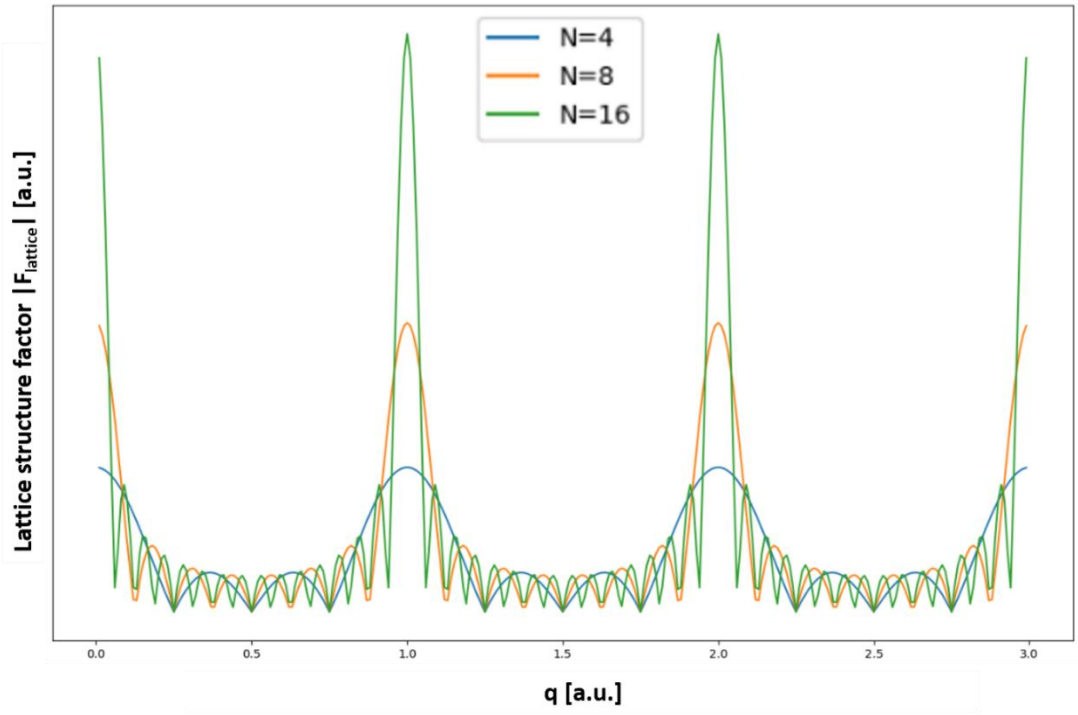

Figure 3.1. Illustration of the evolution of the lattice structure factor for increasingly larger numbers of unit cells N.

To illustrate how the Laue equation behaves for increasingly larger systems, Figure 3.1 is a plot of the equation for N=4, N=8 and N=16. As can be seen in the figure, converging toward larger N the maxima become sharper and more intense, yielding the so-called Bragg peaks in the crystallography of real crystals. Applying the same principle to the other dimensions similar to equation 11 gives:

$$Q_a a_2 = 2\pi k, k \in Z \tag{12}$$

$$Q_a a_3 = 2\pi l, l \in Z \tag{13}$$

To solve these equations, is has shown to be useful to use the concept of a reciprocal space, with reciprocal lattice vectors defined as:

$$\boldsymbol{a}_1^* = 2\pi \frac{\boldsymbol{a}_2 \times \boldsymbol{a}_3}{\boldsymbol{a}_1 \cdot (\boldsymbol{a}_2 \times \boldsymbol{a}_3)} \tag{14}$$

$$\boldsymbol{a}_2^* = 2\pi \frac{\boldsymbol{a}_1 \times \boldsymbol{a}_3}{\boldsymbol{a}_1 \cdot (\boldsymbol{a}_2 \times \boldsymbol{a}_3)} \tag{15}$$

$$\boldsymbol{a}_3^* = 2\pi \frac{\boldsymbol{a}_1 \times \boldsymbol{a}_2}{\boldsymbol{a}_1 \cdot (\boldsymbol{a}_2 \times \boldsymbol{a}_3)} \tag{16}$$

Combining equations 11-13 with the reciprocal lattice vectors, we can introduce the lattice vector G to describe the position of lattice points:

$$\boldsymbol{G} = h\boldsymbol{a}_1^* + k\boldsymbol{a}_2^* + l\boldsymbol{a}_2^* \tag{17}$$

Multiplying G with a real lattice vector gives

$$\boldsymbol{G}\boldsymbol{a}_{\boldsymbol{i}} = 2\pi(ha_1 + ka_2 + la_3) \tag{18}$$

And with that an obvious solution for the Laue equation can be found with:

$$\boldsymbol{G} = \boldsymbol{Q} \tag{19}$$

corresponding to the diffraction condition.

Another useful visualization of the Laue equation can be derived if the scattering crystal is viewed as a stack of parallel lattice planes:

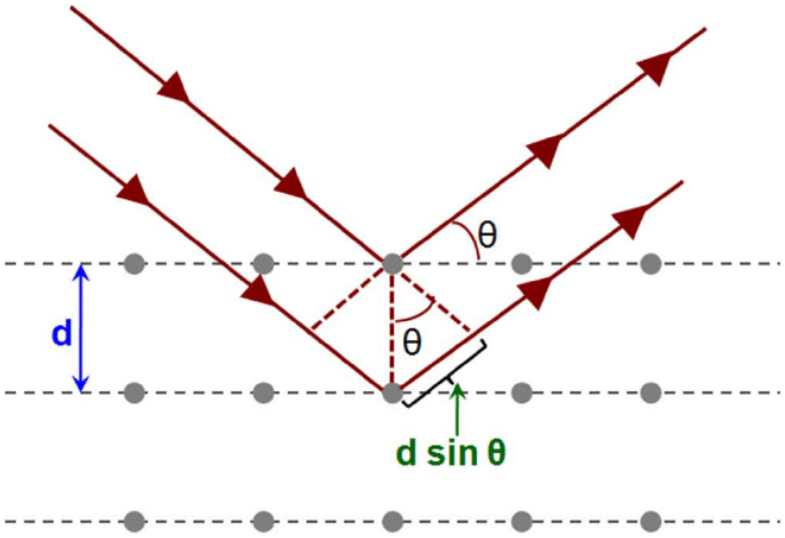

Figure 3.2. Illustration of Bragg's law taken from [56].

With this image, equation (19) can be turned to:

$$\boldsymbol{G} = \boldsymbol{Q} = \boldsymbol{k_f} - \boldsymbol{k_i} \Rightarrow |\boldsymbol{G}|^2 = (|\boldsymbol{k_f}| - |\boldsymbol{k_i}|)^2 \tag{20}$$

Which, using $|\mathbf{k_f}| = |\mathbf{k_i}|$ for elastic scattering, can be rewritten as:

$$2\boldsymbol{k_f} \cdot \boldsymbol{G} = |\boldsymbol{G}|^2 \tag{21}$$

Comparing this equation to Figure 3.2, **G** and **|G|** can be substituted to give:

$$2|\boldsymbol{k_f}||\boldsymbol{G}|\boldsymbol{sin}(\boldsymbol{\theta}) = |\boldsymbol{G}|^2 \tag{22}$$

$$2 \cdot \left(\frac{2\pi}{\lambda}\right) \cdot \left(\frac{2\pi n}{d}\right) \cdot \sin(\theta) = \left(\frac{2\pi n}{d}\right)^2 \tag{23}$$

with the distance between lattice planes d, the scattering angle θ, the wavelength λ and the integer n denoting the order of the diffraction.

Rearranging equation (23) yields Bragg's law:

$$2d \sin(\theta) = n\lambda \tag{24}$$

Ewald sphere construction

A useful illustration of the Laue condition is the so-called Ewald sphere. The construction of the Ewald sphere is most conveniently described in 2 dimensions as depicted in Figure 3.3.

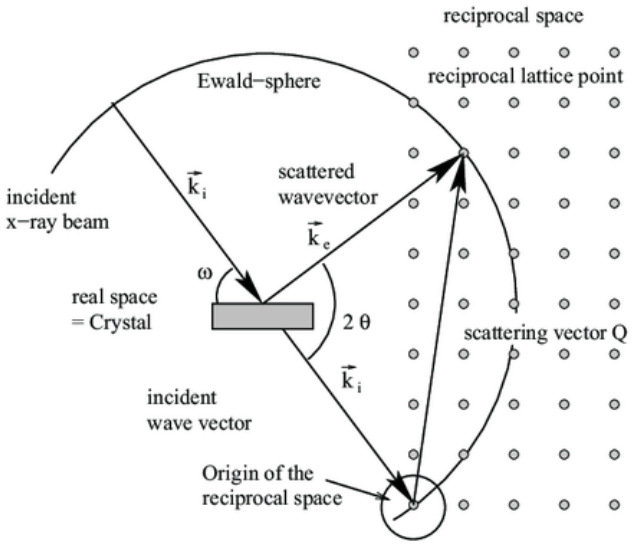

Figure 3.3. Construction of Ewald's sphere, taken from [57] .

Starting with the position of the sample in the centre, a circle with the radius of **|k|** is drawn around it. Then one point in the circumference of the circle is connected to the sample to constitute the incident X-ray beam with the corresponding wavenumber $\mathbf{k_i}$. Additionally, a scattered and a transmitted beam are added originating from the sample. The tip of the transmitted beam is set as the origin of the reciprocal space. The Laue condition in equation 19 is now only satisfied, when the scattered vector **Q** is equal to **G**,

which graphically translates into the reciprocal lattice point laying on the circle of the Ewald sphere.

In order to measure multiple lattice points, or rather Bragg peaks, two possibilities arise from the construction of the Ewald sphere. First, one could change the energy of the X-ray beam, thus changing the size of the incident wavevector and the radius of the Ewald sphere. Since adjusting the X-ray beam energy in a continuous way during the experiment is usually very inconvenient, diffraction experiments in the field of crystallography are performed so that the sample is rotated. Rotating the sample and thus the reciprocal space, can be illustrated with the Ewald sphere construction by rotation the sphere around the origin.

Since most structures discussed in this work belong either to cubic or hexagonal crystal structures, the corresponding formulas calculating the d-spacing of a specific HKL reflex for these structures are given as follows:

$$d_{cubic} = \frac{a}{\sqrt{h^2+k^2+l^2}} \tag{25}$$

$$d_{hexagonal} = \frac{1}{\sqrt{\frac{4}{3}\left(\frac{h^2+hk+k^2}{a^2}\right)+\frac{l^2}{c^2}}} \tag{26}$$

with a and c the lattice parameters.

3.2. X-ray photoelectron spectroscopy (XPS)

X-ray photoelectron spectroscopy (XPS) is a technique based on the photoelectric effect, used to analyse the surface chemistry of the sample by irradiating it with monochromatic X-ray photons and measuring the kinetic energy of the emitted electrons.

The principal of the photoelectric effect is that a material that is radiated with high energy photons, emits electrons, called photoelectrons. The kinetic energy of the emitted photoelectrons is discrete, as the electrons are ionized from the discrete atomic energy levels of the target material, called core levels. The energy necessary to ionize the electrons is the so-called binding energy. For electrons to be ejected, the incident photon energy must exceed the sum of the electron's binding energy plus a work function term for the specific surface of the material, which in real applications contains a correction by the work function of the instrument due to a certain contact potential. Therefore, to

describe the interaction of X-rays with matter for the case of the photoelectronic effect, the corresponding equation can be used:

$$E_{kin} = E_{\gamma} - (E_b + \phi) \tag{27}$$

With the E_{γ} is the energy of the incident photons, E_b the binding energy, E_{kin} the energy of emitted photoelectrons and φ the work function. The magnitude of the instrument's contribution to the work function strongly depends on the conductivity between the sample and the instrument. Since electrons are emitted from the target material during the measurement, a charge can build up on the sample surface, if the conductivity between the sample and the instrument is not high enough to allow for a sufficient replenishment of the sample surface with electrons. To combat the issue of insufficient conductivity for non-conducting samples a so-called flood gun can be used, which constantly bombards the sample surface with electrons during the measurement to compensate the charge.

For an XPS spectra the intensity of emitted photoelectrons is plotted against the kinetic energy of the photons. As the core level energies are specific for each atom, peaks in the spectra can be associated with specific atoms allowing for a determination of the chemical composition of the sample. Due to the strong interaction between electrons and matter, XPS predominantly probes the near-surface region of the sample, although adjustments in photon energy or detection angle can modify the escape depth of the electrons, enabling subsurface analysis. For typical XPS setups the penetration depth is usually around 1-10 nm.

In order to record a XPS spectrum, the instrument must be able to measure the intensity of electrons for each specific kinetic energy. For this purpose, the detector setup of XPS instruments first of all involves a set of electrostatic lenses that focus the electron beam through an entrance slit into a hemispherical analyser. In order for an electron to pass through the hemispherical analyser and reach the detector, it needs to be accelerated around the curvature of the analyser by an external electric field. With this setup, the energy of the electrons that reach the detector can be controlled through the energy of the electric field and the radius of the hemisphere.

A common computer program to analyse XPS spectra is *CasaXPS* [58]. Such a program allows to fit a superposition of theoretical peaks and a background to the core-level data.

In this work the fit peak were chosen to have a Gaussian-Lorentzian line shape and approximating of the background was done with the Shirley algorithm. Each component of the fit is described by its peak position, area, and the full width at half maximum (FWHM), providing quantitative and qualitative information about the sample's surface composition.

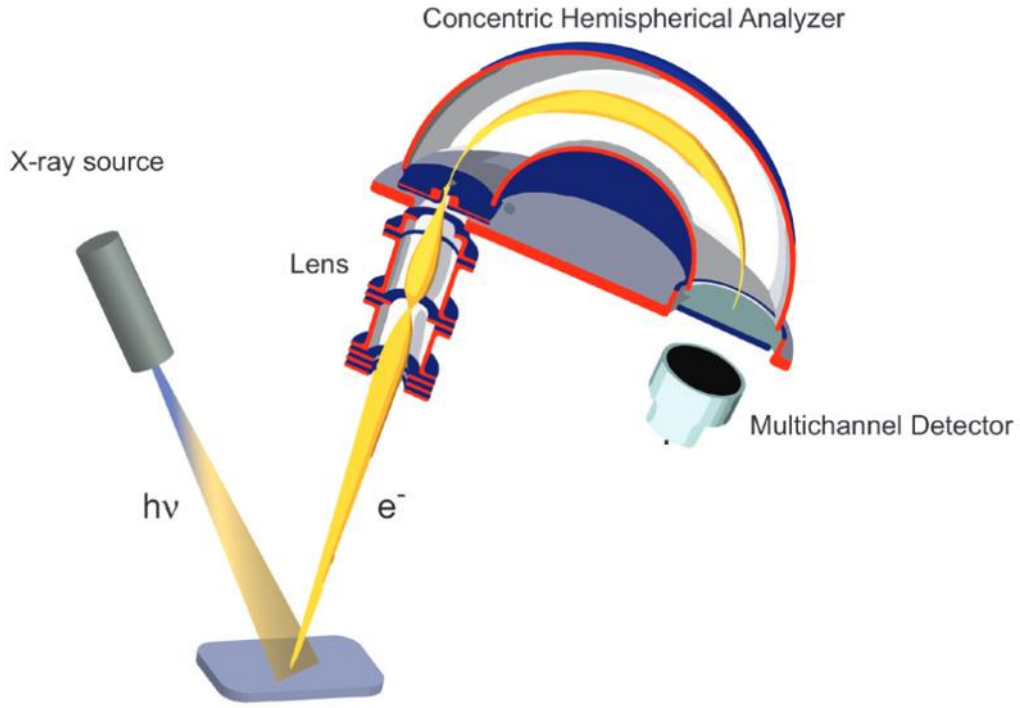

Figure 3.4. Illustration of the an XPS setup taken and adjusted from [59].

3.3. Auger electron spectroscopy

Auger Electron Spectroscopy (AES) is a technique for the chemical analysis of surfaces, leveraging the radiation less Auger process, which causes the emission of electrons from the sample with energies between 3 eV to 50 eV. These low energies limit the escape depth of the electrons to only a few nanometres, making the technique very sensitive to atoms located at the sample surface. Since the low energy of Auger electrons also necessitates ultra-high vacuum (UHV) conditions, AES is commonly used in UHV molecular beam epitaxy setups to determine the surface structure of the samples directly after the deposition.

For the AES analysis the sample is radiated with a beam of electrons. The incident electrons cause a core-level electron from a surface atom to be ejected. This event triggers

an electronic rearrangement within the atom, leading to a transition of an outer shell electron to the lower energy state of the ionized shell. In the Auger process the energy difference between the two shells can be coupled to a second outer shell electron, the auger electron, which is then emitted with a kinetic energy that is indicative of the target atom. These Auger electrons, when emitted from regions within a few angstroms of the sample surface, can escape with negligible energy loss.

The process can be described by the auger equation as illustrated in Figure 3.5:

$$E_A = E_z + E_y - E_x + \Phi_A \tag{28}$$

With the energy of the Auger electron E_A, the energies of the involved atomic core levels E_Z, E_Y, E_X from highest to lowest and φ_A a work function like term to account for the local chemical binding of the surface atoms.

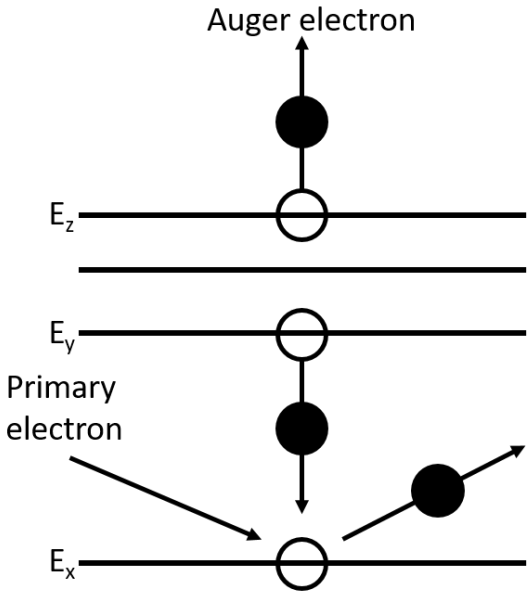

Figure 3.5. Schematic illustration of the Auger process. Radiation of the sample with electrons leads to an ejection of an electron from the atomic core level E_X. The hole in the core level is filled by an electron from a higher core level E_Y which also triggers the ejection of the Auger electron from the E_Z level. Taken and adapted from [60].

3.4. Low energy electron diffraction

Low Energy Electron Diffraction (LEED) is a technique used for the surface analysis of samples in UHV. For UHV setups it is common to employ one instrument that is capable of both LEED as well as AES. Therefore, similar to AES, the sample is radiated perpendicular with a beam of electrons, typically within the range of 20 to 200 eV. This

low energy range is chosen because the corresponding wavelength of the electron beams is in the order of the interatomic distances of solid samples, thereby giving rise to a diffraction pattern.

As the incident electrons interact with the outermost layers of the surface, they are elastically scattered by the atoms in the surface lattice. The diffraction is fundamentally similar to that for X-ray radiation as described in section 1.1, but for a precise description dynamical electron-diffraction theory needs to be employed. The electrons are scattered onto a fluorescent screen forming a series of bright spots. The LEED setup essentially acts as a real-world implementation of the diffraction described by the Ewald's sphere concept, where the reciprocal lattice of the surface being studied intersects with the Ewald sphere to reveal the diffraction conditions. Therefore, the technique is highly suitable to determine the surface crystallography of the samples.

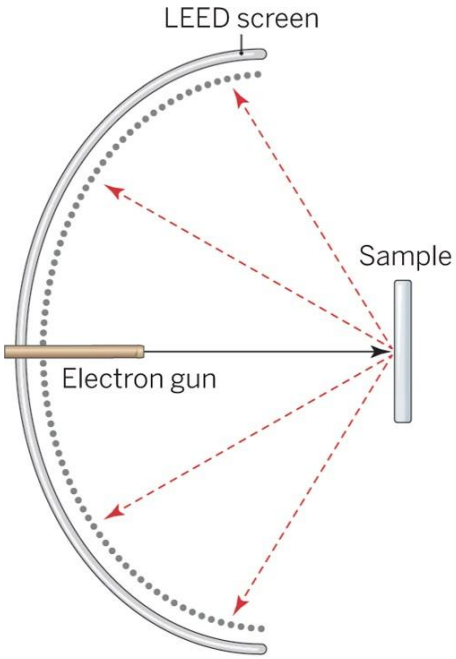

Figure 3.6. Schematic of a low energy electron diffraction setup with the scattered electron beams as red arrows. Taken and adapted from [61].

3.5. Scanning electron microscopy and energy dispersive X-ray spectroscopy

Scanning Electron Microscopy (SEM) is a technique for which the investigated sample is radiated with a focused beam of high-energy electrons in a raster pattern across the sample. Modern SEM instruments provide multiple modes for the detection of signal from the interactions of the electrons with the sample, providing different resolutions and

information about the sample's elemental composition. These interactions include secondary electrons, backscattered electrons, and characteristic X-rays among others [62].

Secondary electrons, emitted from the specimen's surface, provide topographical information due to their low energy and shallow emission depth, offering fine surface detail. Therefore, the secondary electron mode is the investigation mode used for all the SEM images shown in this work. X-ray signals generated by the interaction of the electron beam with the sample were utilized for energy dispersive X-ray analysis in this work, allowing to determine the elemental composition of the samples.

SEM requires that the investigated samples are electrically conductive to avoid unwanted interactions of local charge effects with the backscattered and secondary electrons. Given the fact, that all samples investigated in this work were made of Cu and Zn deposited on non-conductive Al_2O_3 substrates, the conductivity of sample "CZ-Al2O3" had be increased by coating half of the sample surfaces with a 3 nm carbon layer.

4. Experimental setups for sample preparation and characterisation

This chapter gives a detailed technical overview over all of the experimental setups used in this thesis as well as details about the sample preparation and pre-characterization.

4.1. Ultra-high vacuum laboratory for sample preparation and characterization at CXNS

Ultra-high vacuum chambers

All sample for this thesis were prepared in the Ultra-high vacuum (UHV) laboratory of the CXNS. In laboratory consists of multiple chambers and instruments all connected via a tunnel system allowing sample transport within the whole system without exposing the sample to air. The chambers and connecting tubes are all made from stainless steel and connections between different parts are sealed with copper gaskets, which are physically deformed when tightening the connector screws, allowing for very low leakage through the gaskets. The low base pressure of the laboratory is achieved through a combination of several different pumps, including pre-pumps, turbomolecular pumps, and sorption pumps. Initial evacuation to a rough vacuum ranging between 1×10^{-2} and 1×10^{-3} mbar is accomplished using membrane or rotary pumps, starting from atmospheric pressure. The vacuum is further refined to between 1×10^{-9} and 1×10^{-11} mbar by turbomolecular pumps, which operate in the so-called molecular flow regime. The mechanism of turbopumps is fundamentally different to the pre-pumps as they work by using a series of rapidly spinning rotors and stationary stators that impart momentum to gas molecules, propelling them from the vacuum side to the exhaust side of the pump. For achieving even lower pressures, below the 1×10^{-11} mbar range, ion getter pumps and titanium sublimation pumps are necessary. Ion getter pumps work by ionizing gas particles and trapping them with electrostatic forces between two titanium plates, to which a high voltage of about 6 kV is applied. Titanium sublimation pumps use titanium filaments that are heated by high currents to the point of titanium sublimation every couple of hours, causing the then gas-phase titanium molecules to bind to residual gas molecules. Pressure measurements within each chamber are taken using cold cathode pressure gauges.

Molecular beam epitaxy

Molecular beam epitaxy (MBE) is a technique employed for the controlled growth of epitaxial thin films or nanoparticle structures on flat substrates. This method involves directing a beam of molecules or atoms towards the substrate from an evaporator. For the growth, usually ultra-pure source material is used and placed within the evaporator, where it is heated via resistance or e-beam heating to the point of sublimation.

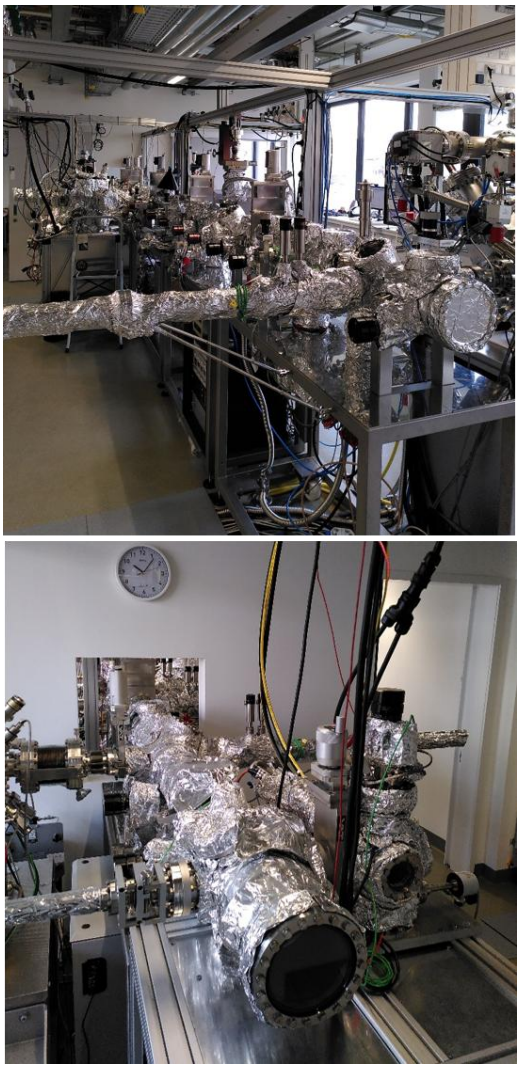

Figure 4.1. Top: CXNS UHV laboratory. The UHV system is setup around a long tunnel with two sample trolleys and each UHV chamber and instrument is connected directly to the tunnel. The tunnel is extended into the adjacent room through a cut-out in the wall. Bottom: The Zn chamber was attached at the end of the UHV tunnel in the second room being the chamber on the right side of the image.

MBE growth is performed in ultra-high vacuum (UHV) conditions, to ensure minimal collision of the evaporated particles and negligible adsorption of unwanted species onto the substrate surface.

Depending on the evaporated material, MBE requires specific substrate temperatures to control surface diffusion of the deposited materials in order to facilitating the formation of thin films or nanoparticles with precise control over thickness and height. Additionally, the growth rates in MBE processes are characteristically slow, generally on the scale of monolayers per second. This deliberate pacing allows for the atoms to settle and migrate across the substrate surface without interference from subsequently arriving particles. If a crystalline substrate is used, as was the case for each sample in this study, MBE growth allows for a formation of crystalline structures on the substrate, which align in some way to the substrate's lattice structure, leading to highly ordered and defect-free thin films. The orientational relationship between the substrate and the film/nanoparticle structures is referred to as epitaxy and is a crucial tool for the preparation of crystalline samples and especially model systems for characterization with X-ray diffraction.

MBE growth chambers, such as the ones used in the CXNS Nanolab, are usually combined with various instruments to investigate the grown samples in UHV, typical Auger electron spectroscopy (AES) and low-energy electron diffraction (LEED).

Argon sputtering

For argon sputtering in UHV, argon gas (in the order of 1e-6 mbar) is exposed to a strong electric field, leading to an ionization of the argon atoms, which are subsequently accelerated by the electric field towards the sample. The sample surface is bombarded with argon ions, removing any contaminants as well as a certain amount of sample material. This action effectively cleans the surface but also induces a certain degree of roughness. Typically, the sputtering process is complemented by an annealing phase. This subsequent step involves heating the sample to high temperatures for a brief duration, usually a few minutes. The high temperatures greatly enhance the mobility of the surface atoms, facilitating the repair of defects and smoothing of the surface. The cycled application of argon sputtering and annealing is a typical process during UHV sample preparation.

Sample heating in UHV

Within (UHV) chambers, sample heating is achieved through two principal methods: resistive heating or electron beam heating (e-beam heating). For resistive heating a high electrical current is applied to a tungsten filament behind the sample holder. Resistive heating in UHV with the used molybdenum sample holders and sapphire substrates of this

thesis is sufficient to reach up to about 900 K. For higher temperatures, e-beam heating is necessary. For e-beam heating an additional electric voltage is applied between the filament and the sample holder. Upon exceeding a certain voltage threshold, the energy of the electric field is strong enough, to cause electrons to be accelerated from the filament to the substrate. The energy of the impacting electrons is converted to heat. Since high currents need to flow through the electric wires of the heating station, ideally with very low electrical resistance, the wires for heating stations used in UHV are usually made of pure Cu.

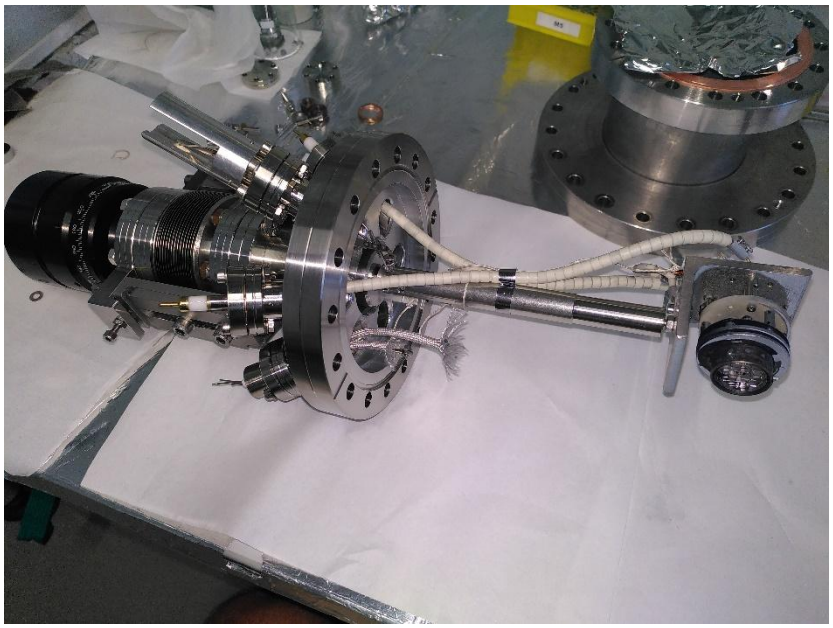

Figure 4.2. Sample manipulator and heating station for the sample stage from the Zn evaporation chamber. The high voltage copper wires for the heating station are encased with ceramic beads to protect from shorting with the chamber walls.

4.2. X-ray diffraction laboratory at the CXNS

The six-circle diffractometer at the CXNS X-ray laboratory consists of an area detector mounted on the diffractometer arm along with two sets of detector slits, the diffractometer cradles with the sample stage, and the X-ray source as seen in Figure 4.3. The sample stage enables precise control of the sample position, allowing for both horizontal and vertical translation, as well as rotation around the surface normal and along two perpendicular horizontal axes for optimal sample alignment. Additionally, the angle of incidence of the X-ray beam is adjustable. The detector arm is capable of both horizontal and vertical movement, allowing for the collection of data across a wide area

in reciprocal space. The X-ray source emits Cu $K\alpha_1$ radiation with a wavelength of 0.154 nm.

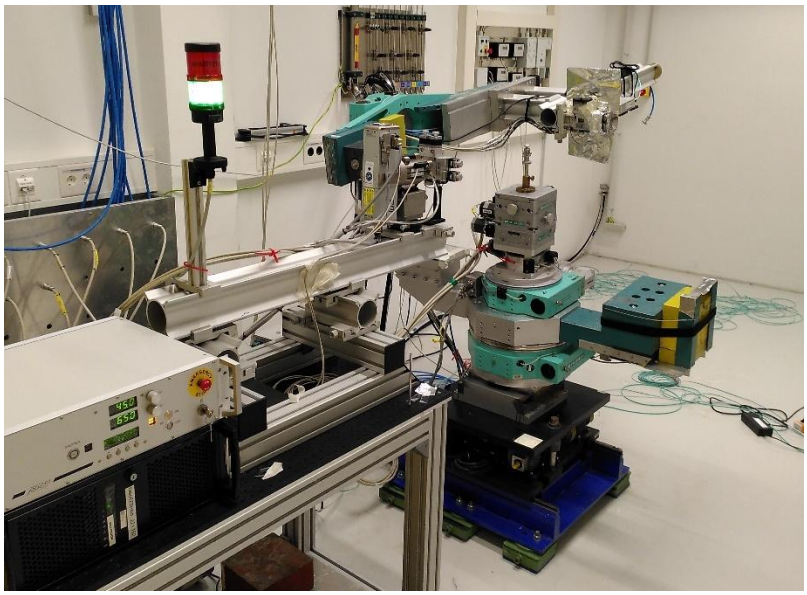

Figure 4.3. Six circle diffractometer setup at the XRD laboratory of CXNS consisting of a X-ray source, Huber table and an area detector mounted on the movable detector arm able to cover large parts of reciprocal space.

4.3. Scanning electron microscopy setup at the CXNS laboratory

SEM and EDX measurements in this work were performed by S. Kulkarni or A. Jeromin of the CXNS. SEM images were taken using the field emitter-based FEI Nova NanoSEM™ 450 instrument with a lateral resolution of ~1 nm, using a concentric back-scattered (CBS) detector as seen in Figure 4.4.

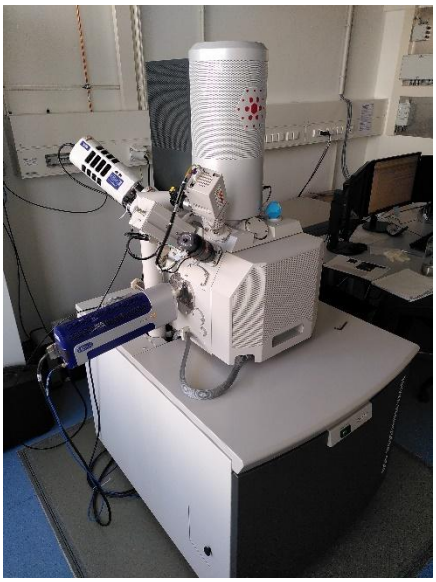

Figure 4.4. Scanning electron microscope FEI Nova NanoSEM™ 450 in the CXNS laboratory.

4.4. MBE chamber for the preparation of Zn thin films and nanoparticles

In order to prepare model systems of the industrial Cu-ZnO-Al_2O_3 (CZA) catalyst that are best suited for investigation of the catalyst in operando conditions with X-ray diffraction, it was necessary to be able to grow crystalline, epitaxial samples containing all three material phases. Since the Cu and Zn/ZnO phases and possible alloys of the two are believed to be the primarily active phases of the catalyst, it was vital for this work, to be able to control the amount of deposited Cu and Zn for the model systems. Therefore, the most useful approach for the model systems of this work was to use crystalline Al_2O_3 substrates and grow both Cu and Zn onto these substrates via molecular beam epitaxy in UHV.

While the general approach of particle and thin films growth on crystalline substrates is well established in the CXNS-Nanolab, the selection of materials is limited to metals with relatively low vapor pressure. Materials for which the growth via MBE is established at the CXNS-Nanolab include: platinum (Pt), palladium (Pd), copper (Cu), rhodium (Rh), gold (Au), iron (Fe), and cerium (Ce). To illustrate the difference in vapor pressure between these elements and Zn the Clausius-Clapeyron equation [63] can be used to estimate the dependence of vapor pressure versus temperature:

$$\ln\left(\frac{p_1}{p_2}\right) = -\frac{\Delta H_{vap}}{R}\left(\frac{1}{T_2} - \frac{1}{T_1}\right) \tag{29}$$

With ΔH_{vap} the enthalpy of vaporization, P_1, P_2 pressures and corresponding temperatures T_1 and T_2 at two distinct states 1 and 2. A comparison of the enthalpy of vaporization for the listed elements can be found in Table 4.1. Boiling points and enthalpy of vaporization for selected elements. Data taken from [64]. to highlight the significant difference in vapor pressure of Zn compared to the other metals:

Element	Boiling point [K]	Enthalpy of vaporization [kJ/mol]
Au	3243	342
Ce	3743	398
Cu	2868	305

Fe	3134	354
Pd	3233	380
Pt	4100	510
Rh	4000	531
Zn	1180	115

Table 4.1. Boiling points and enthalpy of vaporization for selected elements. Data taken from [64].

Given the much higher vapor pressure of Zn compared to the other mentioned metals, the only feasible way for MBE growth of Zn in the CXNS-Nanolab was to design and build a special and separated growth chamber for Zn. Not only were the MBE evaporators of the growth chamber of the CXNS-Nanolab not suited for low temperature evaporation, but the danger of potential contamination of the chamber with Zn was too high, since such a contamination could have seriously impacted the research work of the whole CXNS group. Since the growth chamber was only to be used for Zn growth, the chamber itself was designed to be much smaller compared to the other two growth chamber of the CXNS-Nanolab. The small design was also suitable, since the high vapor pressure of the Zn also causes a high dispersion of the Zn flux profile between the evaporator orifice and the sample, which makes it necessary to decrease the sample-evaporator distance as much as possible. A design was created in which the whole chamber is based on a cross of stainless-steel tubes suitable for UHV, and all the necessary instrumentation is located at one tube of the cross using a cluster flange with 3 flanges as seen in Figure 4.5:

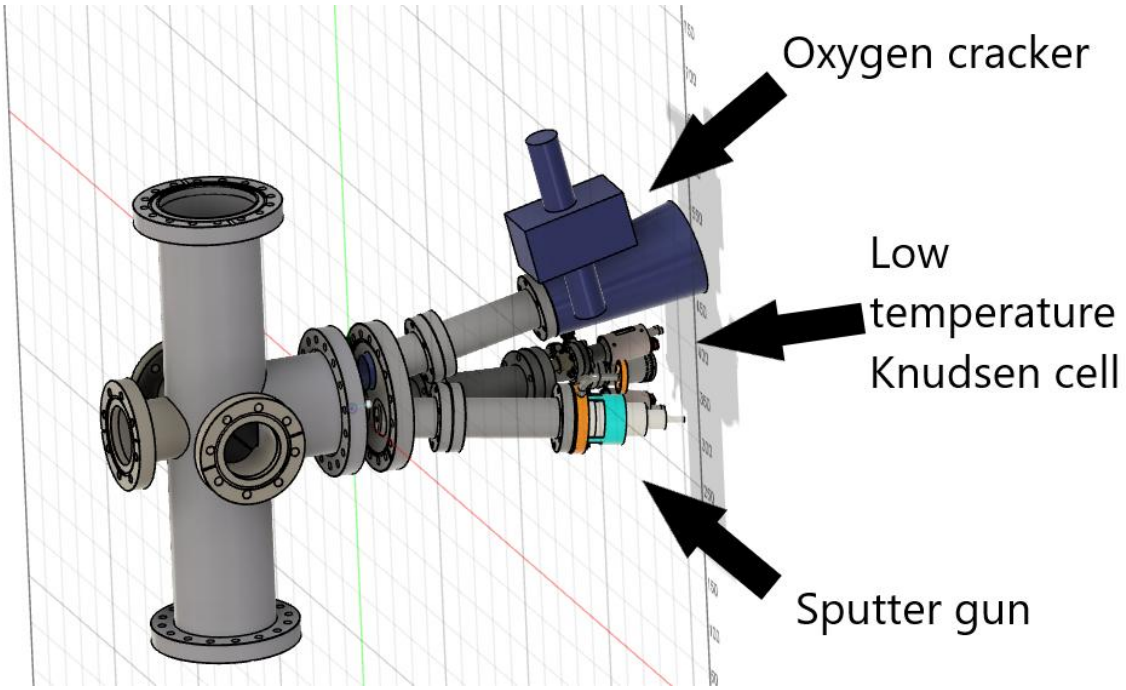

Figure 4.5. Original design of MBE growth chamber for Zn.

The instruments needed for the chamber were a low temperature Knudsen cell as the evaporator for the Zn, an Ar-sputter gun for sample cleaning as well as an oxygen cracker for oxygen treatment of the sapphire substrates as well as oxidation of the metallic Zn. Different from the evaporator of the other growth chamber in the CXNS-Nanolab, the Knudsen cell for the Zn chamber was designed for much lower evaporation temperatures and is equipped with two separate heating circuits. The first heating circuit directly heats the crucible with the high purity Zn material. The second heating circuit is located near the orifice of the evaporator, a so-called hot-lip construction, to prevent any form of re-deposition of the evaporated Zn at the orifice of the evaporator, potentially causing a blockage of the orifice. The chamber also needed a heating station for the sample with both resistance as well as e-beam heating, a manipulator to adjust the sample height within the chamber as well as enabling a rotation of the sample stage to turn the sample towards the instrument cluster for preparation as well as towards the flange connected to the UHV tunnel of the CXNS-Nanolab for the sample transfer. Two of the flanges of the cross were used for windows and at the bottom flange of the chamber is connected to a combination of a turbo-molecular pump and a rotary pre-pump. Due to the small size of the chamber an additional ion getter or titanium sublimation pump was not needed, and the fully functioning chamber is able to reach a base pressure of about 1.5×10^{-10} mbar. The sputter gun and oxygen cracker are both also connected to gas lines via leak valves

for Ar and oxygen respectively. The gas lines are also connected via a T-connector to the pre-pump. The pre-pump's exhaust is connected to the gas exhaust system of the CXNS building capable of safely depositing both toxic and flammable/explosive gases. The chamber is also connected to the cooling water supply of the CXNS Nanolab, providing the necessary cooling for operation of the Zn evaporator and the thermal oxygen cracker. For both instruments, operation without cooling water significantly increases the temperature of the whole instrument, which would cause a large increase in chamber pressure.

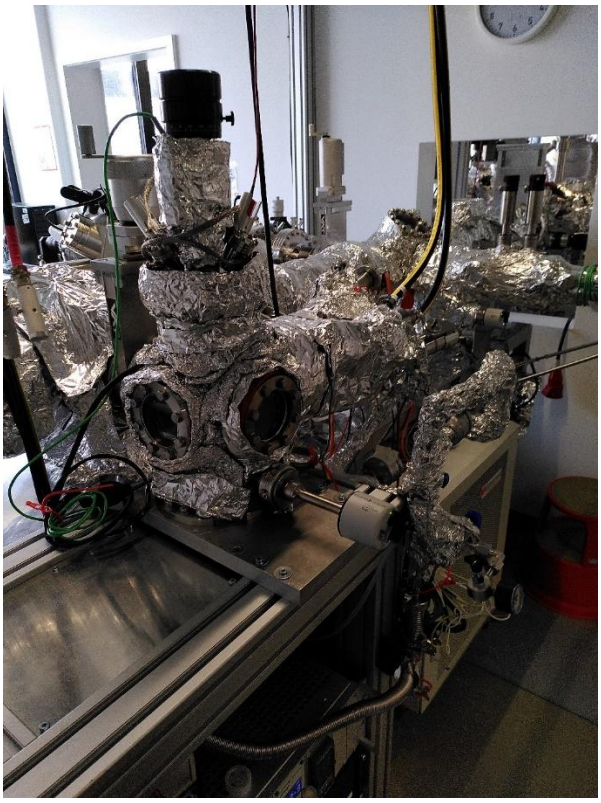

Figure 4.6. Finished Zn evaporation chamber connected to the UHV tunnel system of the CXNS Nanolab.

4.5. Zn growth in UHV

General difficulties for UHV Zn deposition

The specific challenge for the Zn evaporation within a UHV system is rooted in the comparably high vapor pressure of Zn especially compared to ZnO. As described in the previous section, the low temperature Knudsen cell for the Zn evaporation utilizes a crucible, which is loaded with shots of very pure Zn (Shots were purchased from Goodfellow GmbH with 99,9998 % purity and average shot diameter of 6 mm). The as-purchased Zn material is, however, covered with a layer of ZnO due to inevitable exposure to air. ZnO has a boiling point of 2,630 K, compared to Zn's boiling point at just 1180 K. Therefore, the first major challenge for the evaporation of Zn in UHV is to break up the ZnO layer surrounding the pure Zn material, without heating the shots to very high temperatures. Since, if a crack in the ZnO layer would form at high temperatures, the high vapor pressure of the Zn would cause the Zn to then evaporate extremely quickly, potentially contaminating the whole UHV chamber. To avoid the uncontrolled evaporation of Zn the crucible temperatures were held at 500 K with the hot lip at 600 K for all prolonged Zn evaporation. To create cracks in the ZnO layer, the temperature was increased for a short period of time to a max of 950 K with the hot-lip temperature at 1070 K. Additionally, the chamber was filled with pure H_2 gas up to a chamber pressure of 1×10^{-4} mbar with the evaporator running at a max temperature of 600 K. Even with these limitations in crucible and hot-lip temperature, Zn evaporation was impossible to achieve without visible contamination with Zn onto the chamber walls as depicted in Figure 4.7:

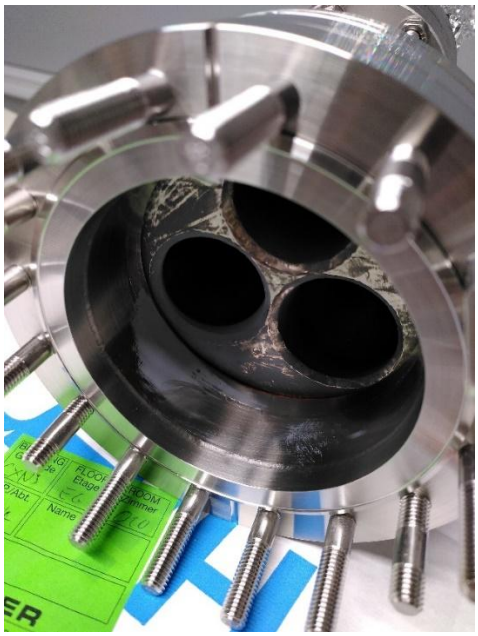

Figure 4.7. Dismounted cluster-flange of the Zn evaporation chamber showing contamination with Zn.

The contamination did not interfere with the function of the MBE chamber and the corresponding instruments however. Even after preparation of more than 20 samples containing Zn over a time period of 3 years, the Zn evaporation is still not easily controlled. One possible explanation for the inconsistency of the evaporation could be the large variation in Zn shot size. The effective reduction of the ZnO overlayer depends on the particle/shot size. Therefore, when commissioning the Zn evaporator, at some point the Zn evaporation was observed and steady for a certain time, and at a later point, Zn evaporation suddenly stopped, even though evaporation parameters such as crucible temperature, were kept constant. This effect could be explained, if smaller Zn shots reduced more quickly than larger ones, so that the evaporation stops as soon as the smaller shots are used up. The distribution of shots of different sizes within the crucible could also play a role, as the temperature gradient within the crucible might not be completely negligible. The inconsistency of the Zn evaporation also made it impossible to perform a reliable calibration for the Zn deposition.

4.6. P07 - The high energy materials science beamline of Helmholtz-Zentrum Hereon and DESY

Mapping of large area high energy reciprocal space maps was carried out utilizing a 2D detector at the DESY Petra III synchrotron end station `High energy materials science

beamline P07 [65]. For the 2D imaging a Varex XRD 4343R flat panel cesium iodide scintillator detector (Pixel Matrix: 2880 × 2880 at 150 µm pitch. Total Area: 432 mm × 432 mm) was used, while alignment and XRR measurements were carried out using a 0D Oxford Cyberstar NaI detector head. The photon energy of the incident beam can be adjusted at the beamline in the range between 30-200 keV and was set to 73.8 keV corresponding to a X-ray wavelength of 0.168 Å. The sample-detector distance was set to about 1.5 minutes.

4.7. P23 In situ X-ray diffraction and imaging beamline at DESY

Ambient pressure experiments were carried out at the P23 beamline at Petra III, DESY. The X-ray beam energy was set to 17.5 keV, corresponding to an X-ray wavelength of 0.70848 Å. The experiment was carried out in grazing incidence geometry with an incidence angle of 0.14° in close proximity to the critical angle of Al_2O_3. Data were collected using a LAMBDA 750 K GaAs area detector.

The sample enviroment consisted of a portable in-situ XRD cell connected to a gas supply and exhaust line, a ceramic heating cross onto which the sample is glued with boron nitride paste as seen in Figure 4.8 and covered with a beryllium dome that functions as an X-ray window.

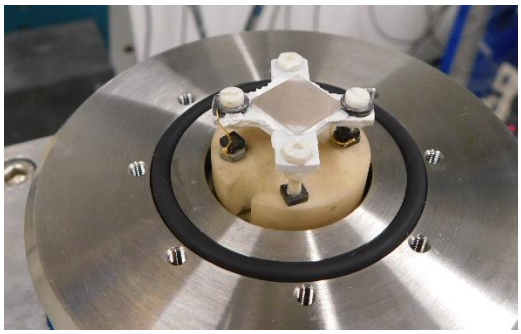

Figure 4.8. Sample mounting on ceramic heating cross using Boron nitride paste as utilized in the ambient pressure cell.

Gas was supplied using the gas cabinet as seen in Figure 4.9, providing individual gas flow controllers for each of the used gases (Ar, H_2, CO and CO_2) alloying to set exact gas reaction mixtures during the experiment under constant gas flow. The gas flow system and XRD cell is capable of being operated under vacuum conditions and up to ambient pressures limited by the stability of the thin walls of the beryllium dome.

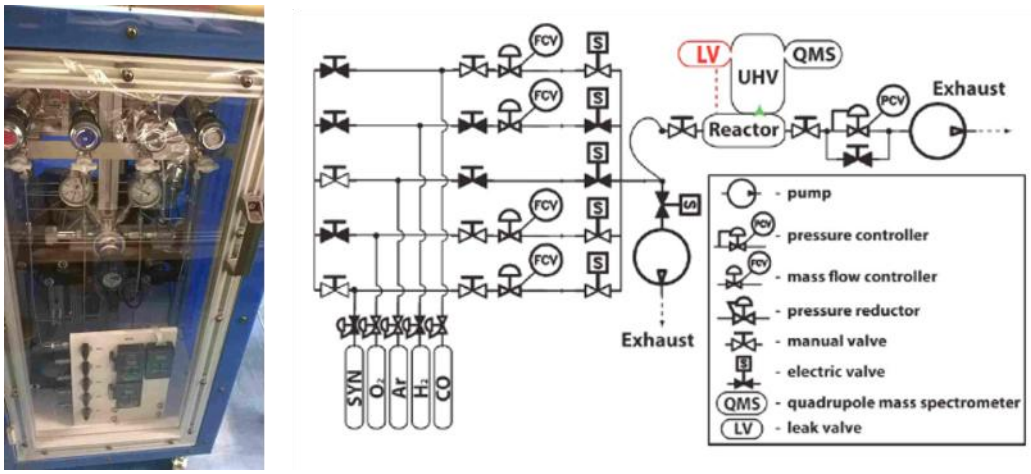

Figure 4.9. Gas cabinet (left) and corresponding gas flow scheme (right) as utilized in the ambient pressure experiments of this work.

4.8. Sample preparation and pre-characterization

All samples were prepared on single crystal Al_2O_3 (001) substrates produced by SurfaceNet GmbH. The substrates were first cleaned chemically with both acetone and iso-propanol using an ultrasonic bath. Afterwards the substrates were mounted onto molybdenum sample holders by spot-welding using tantalum clips before introduction into the DESY CXNS UHV system. To clean the surface from contaminations, especially water, the substrates were degassed at 970 K for 1 hour under ultra-high vacuum conditions. For the samples "Cu-Al_2O_3" and "CZ-Al_2O_3" investigated in near ambient conditions at the P23 beamtime, the Al_2O_3 substrates had been used as test samples for the Zn growth before. Despite the fact that no Zn signal could be detected on these substrates, for the re-use the samples were cleaned with two additional Ar^+ sputtering and annealing cycles, in which the sputtering was performed at an Ar pressure of $p_{Ar} = 1 \times 10^{-6}$ mbar at 1 keV beam energy for 15 minutes and subsequent annealing at 970 K for 15-25min. For all samples, these preparation steps were followed by thermal cracking under oxygen at $p_{O2} = 1 \times 10^{-6}$ mbar with a power of 60 W with the samples being held at 670 K for 20-30 minutes. Prior to the deposition of either Zn or Cu, all samples were sputtered again in $p_{Ar} = 1 \times 10^{-6}$ mbar at 1 keV beam energy for just 3-5min to roughen up the surface and create additional nucleation sites on the sample. A subsequent AES measurement conformed the clean surface of the substrate especially through a low carbon peak. Zn deposition always took place in the Zn evaporation chamber as described earlier, with the Zn evaporator set to an effusion cell temperature of 490 K and the hot lip

to 590 K for 20-40min, while keeping the sample itself at room temperature and the chamber at a base pressure of below 1×10^{-9} mbar. The successful deposition of Zn was conformed with AES. Deposition of metallic Zn was followed by a controlled oxidation of the Zn in $p_{O2} = 1 \times 10^{-6}$ mbar oxygen pressure at room temperature and a subsequent stepwise annealing to 673 K in oxygen. Both Cu growth directly onto the clean Al_2O_3 substrate as well as post Zn deposition was carried out with the same growth parameters of 674 K sample temperature, 300 nA Cu FLUX for 3.5 hours of deposition (Filament current = 1.86 A, Filament Voltage = 674 V, Emission current = 20.4 mA). A final AES measurement conformed the deposition of Cu on top of Zn as seen in Figure 4.10.

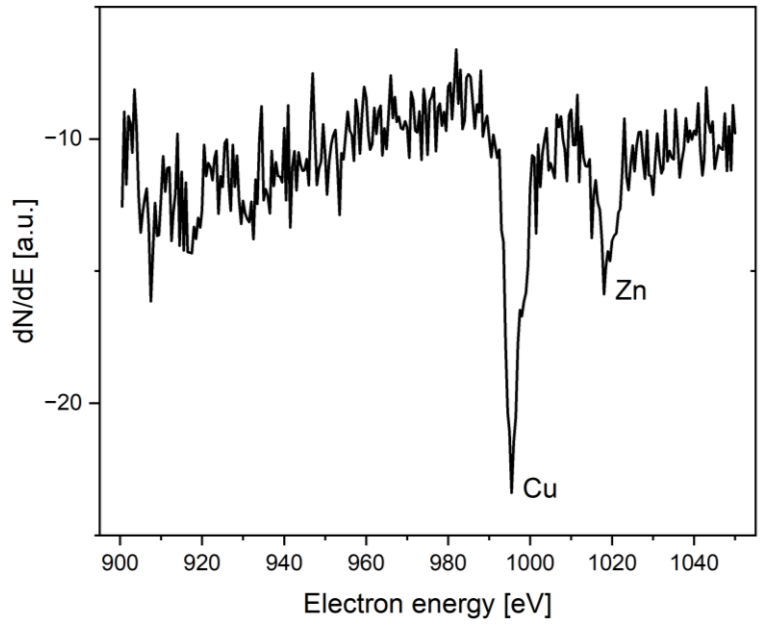

Figure 4.10. Exemplary Auger electron spectra taken under UHV conditions following the UHV sample preparation showing the clear Cu and Zn signal for sample "CZ-Al_2O_3".

5. Technical and safety aspects of a high gas pressure operando diffraction cell

This chapter introduces the high gas pressure reaction cell for heterogeneous catalysis, designed for the surface-sensitive investigation of samples using x-ray diffraction. The setup is capable of withstanding gas pressures of up to about 100 bar, using gas mixtures containing up to four different gases, as well as sample heating up to 800 K, and is therefore suitable for in-situ measurements of catalyst samples under industrially relevant conditions. The concept and first iteration of the operando SXRD cell was done by my colleague Robert Gleißner during his PhD. A description of this first iteration of the setup can be found in his PhD and the corresponding publication [66]. A second improvement to the setup was performed as a part of this thesis and is outline in the following chapter, as well as an outlook for further improvements to the setup for future use.

5.1. Fundamental working principle of the operando SXRD setup

The operando SXRD setup is comprised of two main parts, the system for supplying the reaction gas mixtures as well as the reaction cell. The reaction cell constitutes a single crystal aluminium oxide capillary, with two different inner diameters creating an edge for the sample sitting on top of a crown spacer as seen in Figure 5.1.

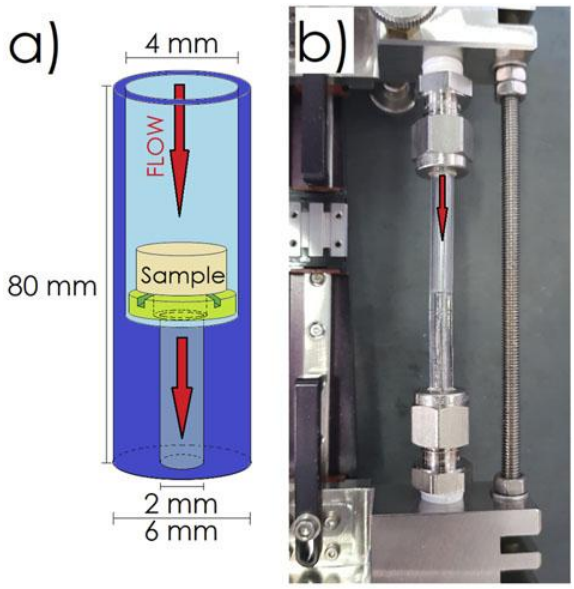

Figure 5.1. Overview of the gas-reaction cell of the operando setup. (a) Schematic drawing of the capillary with two different inner diameters to create a resting place for the crown spacer (green) underneath the sample. (b) Sapphire capillary installed within the capillary holder. Image taken and adjusted from [66].

The capillary is mounted into a specially designed capillary holder that provides the necessary connections for the gas inlet and outlet. Sealing of the capillary is done using Vespel® ferrules in combination with Swagelok® sealing mechanisms. A schematic drawing of the setup can be found in Figure 5.2. The gas handling system of the setup is designed to use high pressure gas provided from gas bottles. The mixing of the connected gases is controlled with a mass flow meter mounted into each gas line. An additional pumping and bypassing gas line is used to quickly reach a high pressure in the cell by bypassing the mass flow controllers, as well as to connect to a gas pump for cleaning of the system prior to operation. The gas handling system is connected to the reaction cell, which is equipped with a safety valve to close the gas line supply in case of capillary rupture.

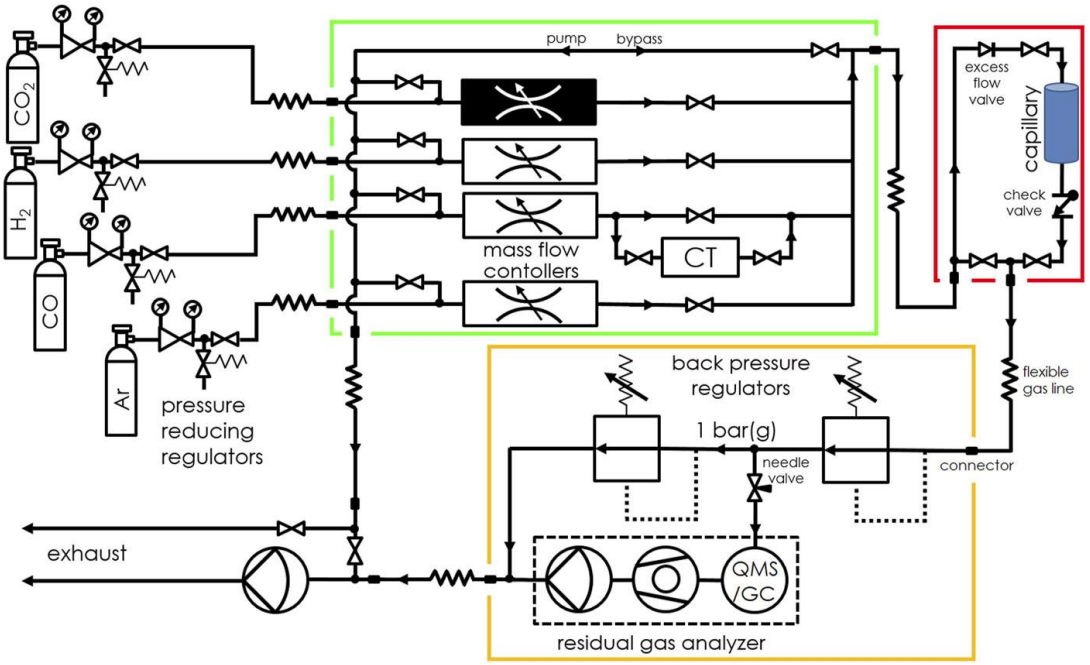

Figure 5.2. Schematic drawing of the full operando SXRD setup with the gas handling system (green), the reaction cell (red) and the pressure and mass spectrometry system (orange). Image taken from [66].

The pressure within the reaction cell is controlled with a back-pressure controller located downstream of the reaction cell. An additional back-pressure controller is used to set the pressure of the outlet gas stream to a value of around 1 bar necessary for the connected residual gas analyser.

5.2. Improvements to the original design

Following the analysis of the SXRD setup's performance, several critical improvements were identified, particularly in the gas handling system. Initially, increasing the pressure in the system to high levels (>1 bar), such as after a sample change or gas composition switch, was highly time-consuming, often taking several hours. This delay was due to the reliance on mass flow controllers, which regulate gas flow at relatively low rates (0.9–45 ml(n)/minutes). The low flow rate was selected to maximize the dwell time of gas molecules on the sample surface, improving the detection of reaction products via mass spectrometry downstream of the operando cell. This step is crucial for detecting reaction products in catalytic processes like methanol synthesis using a Cu-ZnO-Al_2O_3 catalyst, which has a low turnover frequency. Moreover, the single-crystal samples used in these experiments have a considerably lower surface area compared to powder samples typically employed in catalyst studies, further complicating product detection.

To address the slow pressure buildup, a new procedure was developed to rapidly achieve high pressures in the reaction cell by utilizing a bypass gas line. This method would allow the reaction pressure to be set directly to the inlet gas bottle pressure of the gas handling system, bypassing the mass flow controllers. However, this approach was limited to single-gas use, as precise gas mixtures could only be established through the mass flow controllers. Fortunately, the typical sequence of measurements for the Cu-ZnO-Al_2O_3 catalyst is compatible with this method, as the catalyst activation step involves pure H_2, followed by the gradual introduction of CO and CO_2 in increasing fractions.

Despite its potential benefits, the bypass method posed significant safety risks due to the configuration of the carbonyl trap in the CO line. Positioned downstream of the CO mass flow controller, the carbonyl trap was located on the low-pressure side of the system. This arrangement risked H_2 backflow into the carbonyl trap when high H_2 pressure was set in the reaction cell and the CO carbonyl trap's exit valve was opened. The active material within the carbonyl trap reacts violently with H_2, leading to material degradation, temperature increases, and, as indicated in the manufacturer's safety manual, the possibility of an explosion.

To mitigate this risk, the gas handling system was redesigned, relocating the carbonyl trap upstream of the CO mass flow controller, as shown in Figure 5.3. This adjustment places the carbonyl trap on the high-pressure side of the system, effectively preventing H_2 backflow as long as the H_2 pressure in the reaction cell remains lower than the CO bottle pressure. It is crucial to note that the selected CO bottle pressure remains stable only while there is sufficient pressure in the gas bottle. As gas is consumed, the bottle pressure will eventually decrease, potentially falling below the required operating pressure of the system.

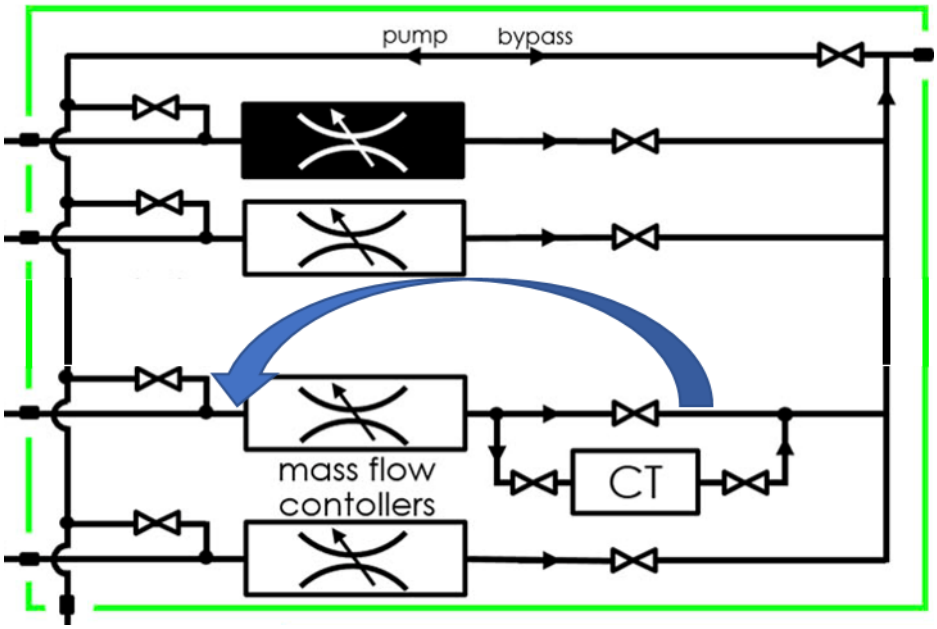

Figure 5.3. Illustration of the gas handling system of the SXRD setup highlighting the changed position of the CO mass flow controller and carbonyl trap. Original image taken and adjusted from [66].

Another critical improvement involved the Al_2O_3 capillaries used as the reaction cell. During the initial experiment, the supposedly single-crystalline capillaries exhibited polycrystalline reflection spots, indicating that the capillaries were not truly single-crystalline. To address this issue, a new supplier was contacted, and authentic single-crystalline capillaries were ordered. It is suspected that the initial set of capillaries was fabricated by gluing different parts with varying diameters, potentially leading to the observed polycrystallinity near regions where the inner diameter changed. Although the separate parts of the tube may have been single-crystalline, the gluing and heating process during manufacturing could have introduced polycrystallinity. This, however, remains speculative.

The new sapphire capillaries were produced from a single, solid crystal cylinder, which was meticulously bored by hand. To preserve the single crystallinity, this process was performed slowly to minimize heat buildup in the material, as even slight heating can disrupt the crystal structure. According to the manufacturer, this process requires approximately one week of continuous work per capillary, contributing to a prolonged delivery time of over three months. Subsequent measurements with the newly obtained capillaries confirmed their single-crystalline structure, resolving the issues observed with the original capillaries.

Additionally, the heating system used in the experiment required improvements. During the first test experiment, the heat gun employed to heat the capillary and the sample within was found to cause alignment issues. Given that the beam size for SXRD experiments at high-energy beamlines is typically 2–3 μm, even minor shifts in sample position or temperature fluctuations can affect alignment. Observations during the initial experiment suggested that the gas flow from the heat gun may not have been stable enough for the setup. To address this, the previously used Steinel® HG 2320E heat gun was replaced with a more stable hot gas blower from FMB Oxford.

A temperature calibration was conducted with the new system, in which a thermocouple was mounted directly onto a test sample within the operando cell as seen in Figure 5.4. The system was pressurized to 50 bars of Ar, with the cell outlet closed to prevent gas flow. The blower nozzle was positioned 5 mm from the capillary wall, and the blower was operated using pressurized air at 6 bar, pre-filtered to remove contaminants. Several test measurements confirmed that varying the nozzle distance up to 8 mm from the capillary wall did not result in a measurable change in sample temperature. Similarly, reducing the operating pressure down to atmospheric levels also had no significant effect on the sample temperature.

To ensure the Vespel® ferrules used to seal the capillary remained below their maximum operating temperature of 620 K, thermal investigations were performed using an infrared camera. These measurements indicated that the metal locking nuts of the ferrules reached a maximum temperature of approximately 425–455 K, well within the safety limits for the Vespel® components.

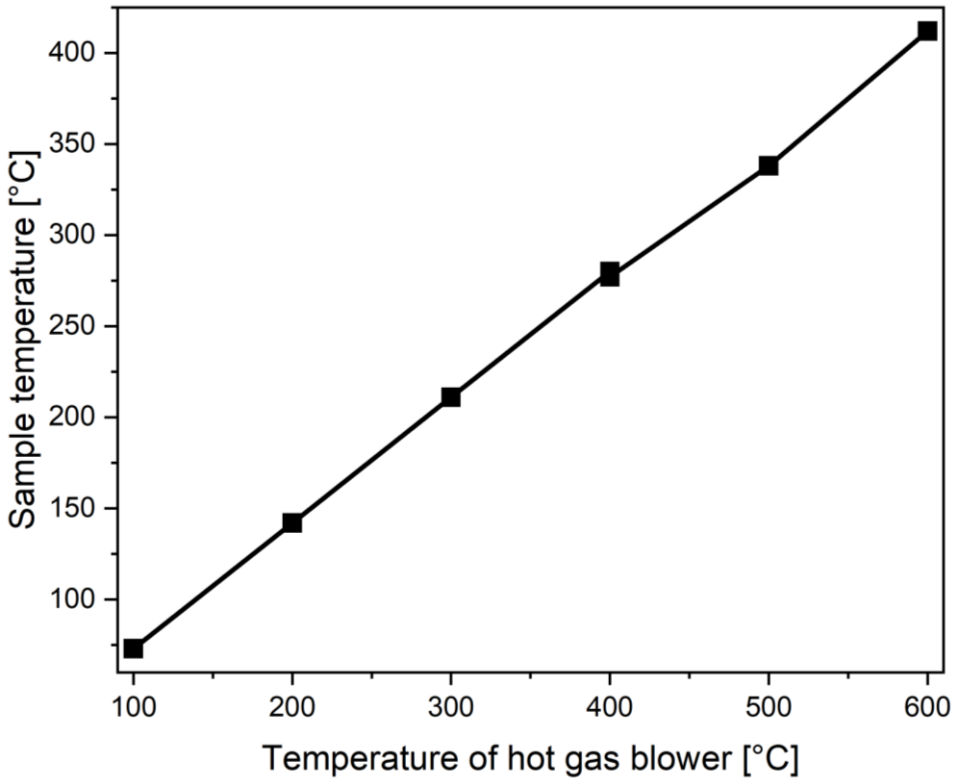

Figure 5.4. Temperature calibration of the FMB Oxford hot gas blower as used in the SXRD operando setup. Measurements were done at 50 bar cell pressure of Ar without air flow, and 5 mm distance between the nozzle outlet and the capillary wall.

5.3. New design of the operando cell for future experiments

I. Capillary material

A number of additional improvements to the reaction cell are described in this chapter to address the design flaws of the current setup as described in chapter I.B of the supporting information. The main issue with the operando SXRD stage is the connection between the capillary and the gas lines. The issue mainly arises due to the material of the capillary, as the sealing mechanism of Swagelok connections is absolutely gas tight up to hundreds of bars if stainless steel gas pipes are used. Therefore, a sensible first approach on improving the current setup is to look for alternative capillary materials. Regarding a metal capillary the main issue is however, that the capillary materials needs to have a high transparency for X-rays and it must be catalytically inactive. As a result, the only metal that is commonly used for experimental X-ray cells and catalysts is beryllium. Using a beryllium capillary might work in principle, but given the toxicity of beryllium, especially beryllium dust in case of capillary rupture, is less than ideal for a high-pressure setup. To overcome this issue, the walls of a beryllium capillary would have to be very thick, which makes this

likely a very expensive option. While there certainly are polymers that can withstand high pressures up to 100 bars as would be necessary for the setup, and others that can withstand high temperatures, it is very hard to find one that can withstand both. This is especially true, since the capillary has to withstand up to 800-1000°C from the heat blower, since in order to reach a certain temperature of the sample in the capillary under high pressure gas flow, the heat blower needs to be set to a significantly higher temperature. That leaves only ceramics like the sapphire capillary that is already used. One alternative out of the family of ceramics would be silica glass. The linear photoelectric attenuation coefficient of silica is very comparable to that of Al_2O_3 as seen in Figure 5.5.

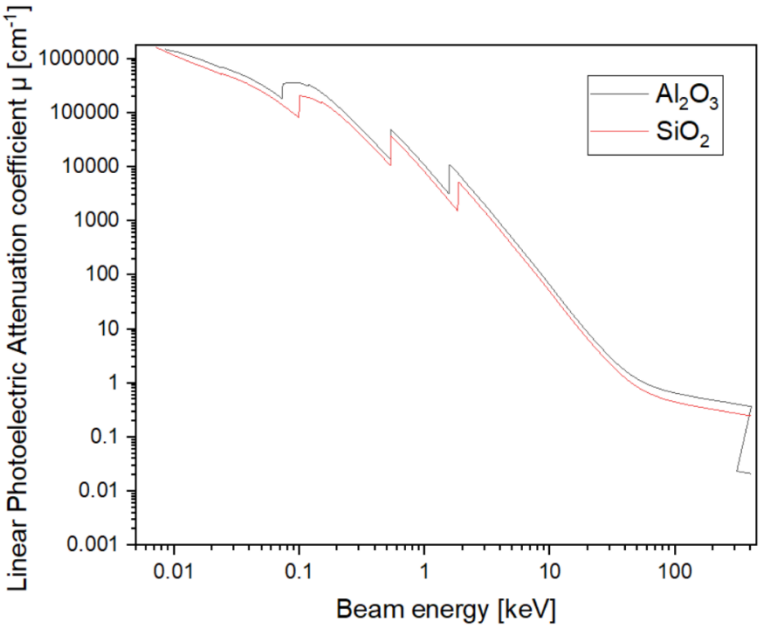

Figure 5.5. Linear Photoelectric attenuation coefficient of Al_2O_3 (black) and SiO_2 (red) as a function of beam energy.

Additionally, using glass capillaries instead would render the setup of the experiment somewhat easier, as the amorphous glass would not create any Bragg reflexes that have to be covered with beam stops. Other advantages are the much lower expected cost of glass capillaries due to the less complicated manufacturing process and with that also much shorter delivery times.

II. New capillary holder/operando cell design

For the design of an improved operando cell without a change of the capillary material, multiple adjustments were done to overcome the issue of connecting the capillary to the gas lines. First of all, the shape of the capillary has been changed to a dome or cylinder

with a closed end at the top as seen in Figure 5.6. All design schematic and technical drawings were created with the *Onshape* software.

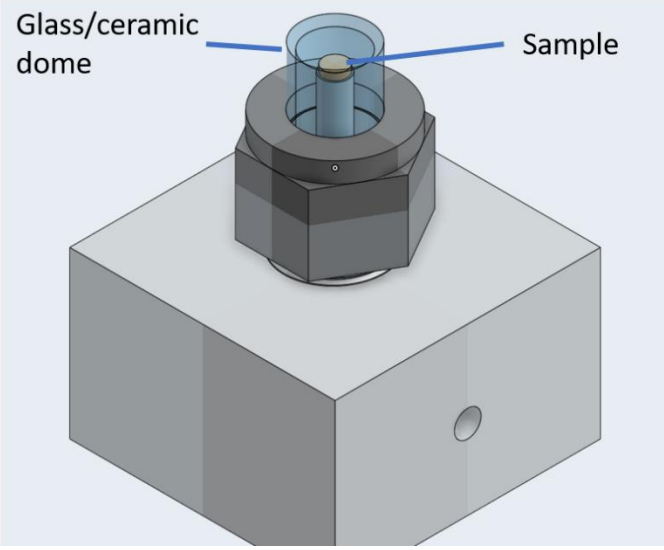

Figure 5.6. Isotropic view of the re-designed operando SXRD cell. For reference the block has side lengths of 40 mm and a height of 25 mm. The glass/ceramic dome is marked in blue, the sample in orange.

This shape has the advantage, that only one end of the capillary has to be sealed. Additionally, this design allows the hot gas blower to be mounted on top of the dome, which should reduce sample alignment issues during sample rotation. Furthermore, if the hot gas blower would be mounted on top of the operando cell, the setup would allow a full free 360° rotation of the sample during measurements. To prevent the glass/ceramic dome from experiencing any sheer force during tightening of the nut, the diameters of the setup have been changed as seen in the cross-sectional view in Figure 5.7.

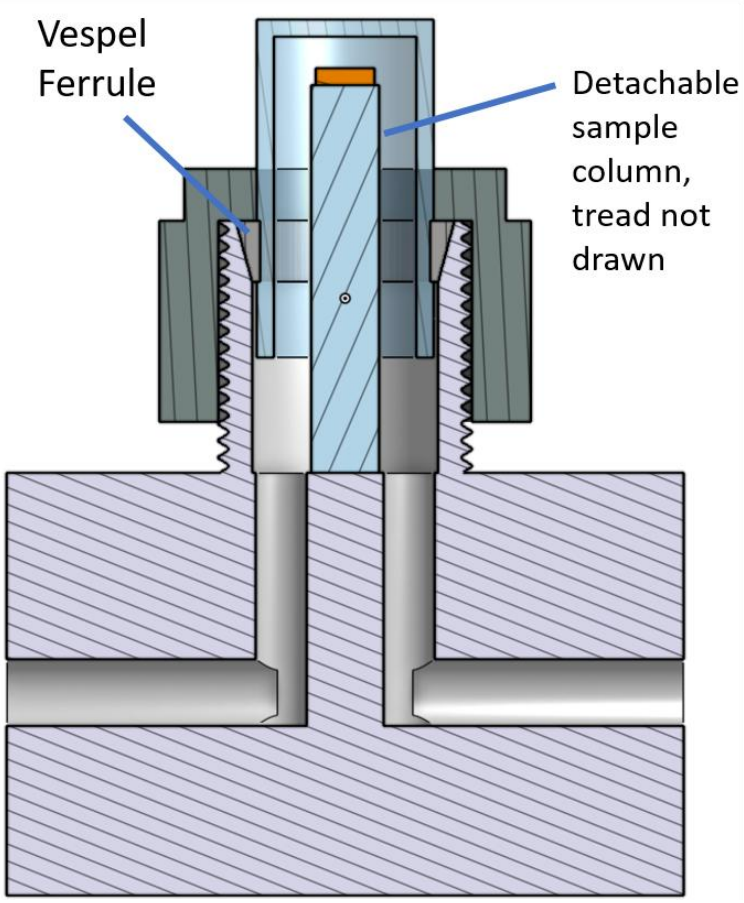

Figure 5.7. Cross-sectional view of the re-designed operando SXRD cell. For reference the block has side lengths of 40 mm and a height of 25 mm. The glass/ceramic dome is marked in blue, the sample in orange.

The sealing mechanism is designed to always leave a gap of 0.3 mm between the dome and the inner wall of the metal cylinder. This gap is large enough to prevent the dome from experiencing shear force from the metal wall even if a certain tolerance in the outer diameter of the dome is account for, while not being too large to significantly decrease the overall stability of the setup. Additionally, to prevent the Vesper ferrule from sliding on the dome during tightening, small notches are incorporated into the dome to fix the ferrule in place as seen in Figure 5.8. Another solution for this could be to also use a front and back ferrule made from Vesper, similar to the setup of the Swagelok metal ferrules. Given the gap between the dome and the tubing of the metal block however, fixing the ferrule perfectly in place should not be crucial anymore. The issue of the sample not being fixed in place in any way is solved by using a detachable sample column. The column can be screwed into the main block, with the thread not displayed in the drawing in Figure 5.7 for visual clarity. If the column is made of metal, the sample can be fixed by spot welding it onto the column using for example Ta clips, a well-established sample mounting method used in the CXNS UHV laboratory. Should the column be made of a ceramic to reduce the

amount of potentially catalytically active metal near the sample, the sample could be fixed using boron nitride paste, similar to the sample mounting described for the in-situ catalysis chamber.

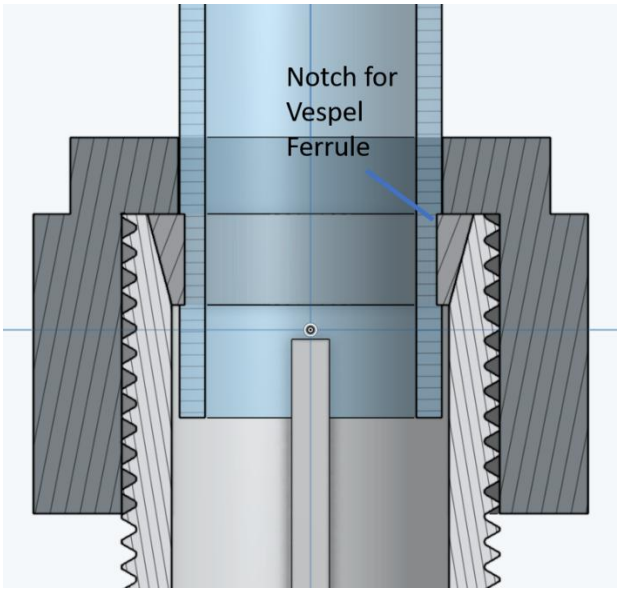

Figure 5.8. Close-up cross-sectional view of the operando SXRD cell revealing the small notches in the dome to fix the ferrule in place.

Since the shape of the cell is no longer a capillary with the gas inlet on one side and the outlet on the other side, some consideration had to made regarding the flow of the reaction gas. At least the majority of the gas flowing into the cell should cross the sample before exiting the cell on the opposite side. Since the sample is elevated from the entry and exit points of the gas, additional side walls are added to the setup as seen in Figure 5.9. To ensure that the sample column remains detachable and to reduce the manufacturing complexity of the cell, a small gap is left between the walls and the sample column. While gas will flow through this gap, the majority of the gas is still forced to flow over the sample. To reduce any unwanted catalytic activity of the walls, they should ideally not be made out of metal. This is especially important as the walls are close to the top of the sample column and therefore are expected to become hot during sample heating.

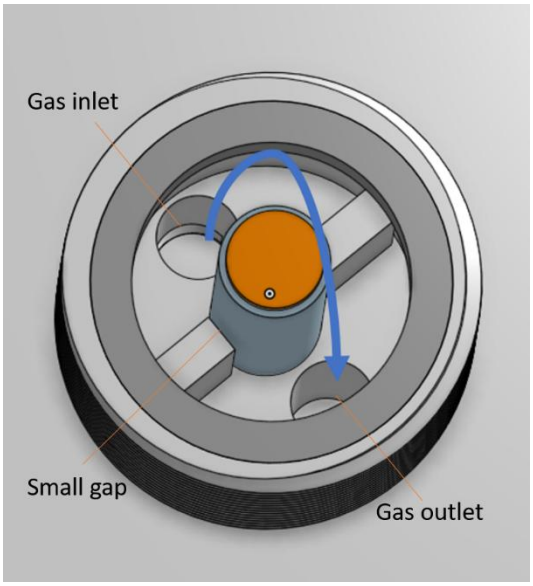

Figure 5.9. Isometric view of the operando SXRD cell from the top without the glass/ceramic dome. The flow of reaction gas is shown with a blue arrow.

5.4. Conclusion about the operando SXRD setup

In summary, while the high-pressure surface XRD setup underwent significant improvements and the conducted experiment yielded valuable data, several critical issues remain that require further attention. The encountered faults, such as gas handling malfunctions, sample alignment difficulties, and contamination, limited the amount of gathered data from the experiments. However, despite these challenges, the setup has demonstrated great potential for bridging the pressure gap in XRD studies. The data already collected clearly illustrates the system's capacity to deliver insightful results under high-pressure conditions, making it a promising tool for advancing research in surface-sensitive catalysis and other high-pressure applications. With the necessary refinements, this setup could become an invaluable instrument for future experiments.

6. ZnO-supported (CZA) and simplified (Cu-Al_2O_3) model catalyst at near ambient conditions: Dynamic oxidation and alloy formation

To gain insight into how the presence of ZnO in the model system changes the oxidation behaviour of the Cu phase in near-ambient conditions, measurements were carried with two distinct model systems of the Cu-Zn-Al_2O_3 (CZA) catalyst: a simplified form consisting of only Cu supported on Al_2O_3, and a more complex system of Cu on ZnO supported on Al_2O_3, denoted throughout this work as "Cu-Al_2O_3" and "CZ-Al_2O_3" respectively. Details regarding the sample preparation and pre-characterization can be found in section 4.8. By employing surface sensitive XRD, using synchrotron radiation with an X-ray energy of 17.5 keV, corresponding to a wavelength of 0.7085 Å, both samples were investigated in different reaction gases at up to 1 bar of total pressure and 575 K sample temperature utilizing the in-situ catalysis chamber described in chapter 4.7.

6.1. Structural analysis of the model systems

This chapter covers the structural changes of the Cu phase of the investigated model systems that occur between room temperature and up to 575 K in reducing gas-atmospheres. These conditions represent the typical activation procedure for this catalyst system, under which the analysis of the epitaxial orientation of Cu and copper oxides on the Al_2O_3 substrate as well as the formation of additional phases including Cu-Zn alloys is investigated. The structural differences between these systems are critical for understanding the catalytic behaviour during activation and reduction processes as described in the subsequent sections.

Native oxidation of the simplified model system "Cu-Al_2O_3"

As described in detail in section 4.8, both model systems were prepared using molecular beam epitaxy (MBE) under ultra-high vacuum (UHV) conditions to ensure precise control over the deposition of both Cu and Zn. Multiple X-ray reflectivity (XRR) measurements were performed to investigate the stages of native oxidation by tracking the ratio between Cu_2O and metallic Cu phases, consistent with prior studies on native oxidation of Cu in comparable model systems [67]. All the scans were fitted using a two-layer model system of a metallic Cu layer on top of the sapphire substrate, followed by a Cu_2O layer. Fitting of

the data was performed using the GenX software [68]. The XRR data set and fit parameters can be found in section I.C of the supporting information.

Despite the Ar^+ sputtering and annealing cycles performed during the sapphire preparation as well as the shorter pre-sputtering step to roughen the surface of the substrate in order to generate additional nucleation sides, the XRR results show that the Al_2O_3 surface remained flat given the measured roughness of the substrate of 1.47-1.65 Å for sample "Cu-Al_2O_3" and 4.36 Å for sample "CZ-Al_2O_3". For the simplified model system "Cu-Al_2O_3", the average height of the Cu layer deposited directly onto the sapphire substrate was measured to be 28.1 Å with a high layer roughness of 25.6 Å and a surface coverage of 79.4% in the measurement conducted a few hours after the sample was removed from the UHV system. The high roughness of the Cu layer suggests a broad distribution of particles sizes. The Cu_2O layer on top of the metallic Cu layer was measured to have an average height of 9.37 Å, with a roughness of 9.08 Å and an electron density that fits to a full coverage of the sample surface with Cu_2O. The results fit to the presence of a Cu_2O powder on the surface, with the associated layer thickness of the oxidized layer pointing to a full oxidation of smaller Cu particles to Cu_2O during the short exposure to air, while larger Cu nanoparticles remained metallic in their core, forming a Cu-Cu_2O core-shell system.

Additional two weeks of native oxidation was shown to cause a significant increase in the layer thickness of the Cu_2O to 28.9 Å with a roughness of 11.7 Å while the surface coverage of the phase has reduced to 89.3%. These results fit to an advanced Cu oxidation and particle coalescence. The Cu oxidation is also observed in the Cu layer, which has decreased in thickness to 24.9 Å with a roughness of 20.1 Å and surface coverage of 69%. The XRR data gathered for the "CZ-Al_2O_3" sample were fitted using the same two-layer model for direct comparison with the simplified model system, despite the presence of Zn on the sample. The first layer was measured to have a thickness of 40.3 Å with a roughness of 8.04 Å with a surface coverage of 20.6% assuming a pure metallic Cu layer. The results suggest particles of roughly twice the height on the sample compared to the results for Cu deposited directly onto the sapphire substrate. Given the deposition of Zn on the sample, this first layer is associated with either pure Zn or a Cu-Zn alloy phase. Assuming a pure metallic Zn layer, the measured electron density of the first layer would results in a sample coverage of 27.1% given the lower electron density of Zn. Therefore, the actual sample coverage of the layer can be assumed to be between 20.6-27.1% depending on the ratio

between Cu and Zn. Similar assumptions apply to the second layer of the model measured to have a thickness of 43.64 Å with a roughness of 30.98 Å and a surface coverage of 109.9% assuming a Cu_2O layer. The high electron density of the phase is a clear indicator that the association of the phase with a Cu_2O layer is not valid. Again, assuming a Cu-Zn alloy phase would result in a surface coverage between 12.5%-16.4% depending on the Cu and Zn ratio. Furthermore, given the electron density of ZnO, associating the second layer with ZnO would results in a surface coverage of 25.7%. Increasing the complexity of the fitting model by introducing additional layers did not significantly increase the overall fit quality.

In summary, the XRR investigation shows a continuous, structured native oxidation process in both model systems, with a gradual growth of a Cu_2O layer atop metallic Cu. The results for the ZnO-supported model system, namely the measured electron densities of the layers on the sample fitting to a Cu-Zn alloy and not to Cu_2O, suggest the presence of a Cu-Zn alloy underneath a layer of ZnO, as further underlined with the following grazing incidence XRD investigation preformed in-situ at pressures between 500-1000 mbar. In order to confirm the structural integrity of the substrate on the "Cu-Al_2O_3" sample, a rotational in-plane scan for Al_2O_3 (110) at room temperature and under Ar gas flow at 500 mbar total pressure was performed as seen in Figure 6.1. The reflexes show the high symmetry direction of the sapphire substrate with their 60-degree in-plane symmetry as well as the integrity of the substrate surface following the Al_2O_3 preparation as described in section 4.8. To calculate the actual in-plane direction $\omega_{corrrected}$ of an in-plane reflex, the measured in-plane rotation angle ω has to be corrected for the detector angle of the given measurement following:

$$\omega_{corrected} = \omega - \frac{\gamma}{2} \tag{30}$$

with ω the in-plane rotation angle and γ the in-plane/horizontal detector angle.

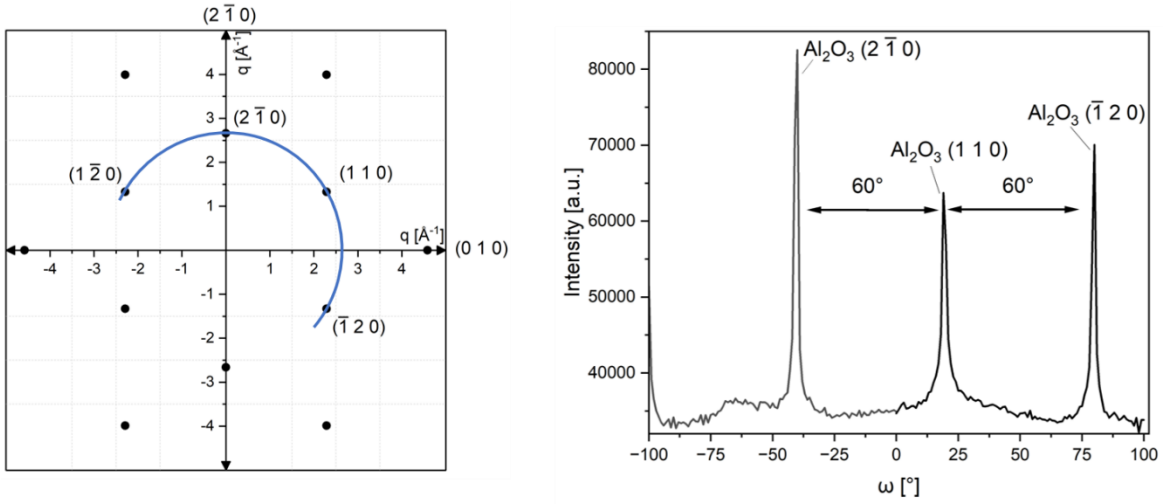

Figure 6.1. Left: In-plane reciprocal space map with the Al_2O_3 reflexes marked with black circles and the scan seen on the right illustrated as a blue line. Left: Azimuthal in-plane scan for Al_2O_3 (110) showing the high symmetry direction of the substrate and the 60-degree symmetry.

To investigate the state of Cu and Cu_2O particles and their orientations, additional azimuthal in-plane scans were carried out for each of the possible Cu and Cu_2O orientations for epitaxial particles. As can be seen in Figure 6.2, the angular position of the Bragg peaks of Cu_2O ($2\bar{2}0$) and Cu ($2\bar{2}0$)/Cu_2O ($1\bar{1}3$) corresponds to an alignment along the high symmetry direction of the sapphire substrate. Both of these reflexes show a broad full width at half maximum (FWHM), indicating a preferential in-plane orientation of these particles +- 5 degree off the high symmetry direction of sapphire. Since only these reflexes show a preferential orientation in-plane, it is concluded that the sample preparation yielded (111)-oriented Cu particles, that are partially oxidized to Cu_2O due to native oxidation. Furthermore, the oxidation did not change the epitaxial relationship of the particles with regard to the substrate, since only the same ($2\bar{2}0$) type reflex in-plane is observed for Cu_2O. To further investigate whether the signal of the other in-plane reflexes is to be interpreted as a powder signal or if it has to be regarded as background signal, radial scans along the high symmetry directions of the sapphire (110) as well as (300) directions were carried out.

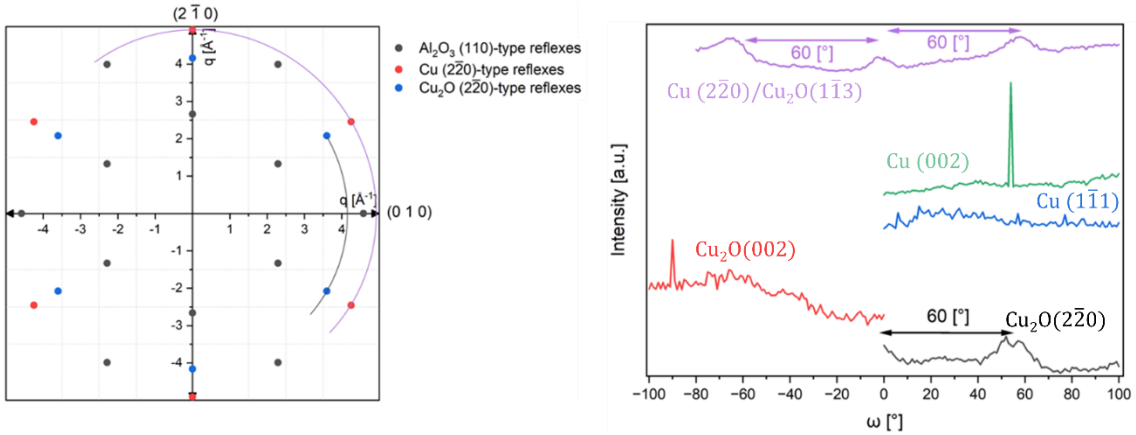

Figure 6.2. Initial azimuthal in-plane scans for Cu_2O (2$\bar{2}$0) (black), Cu_2O (002) (red), Cu (1$\bar{1}$1) (blue), Cu (002) (green) and Cu (2$\bar{2}$0)/Cu_2O (1$\bar{1}$3) (violet) at room temperature under Ar flow. Peaks indicating preferential in-plane order are only visible for Cu_2O (2$\bar{2}$0) and Cu (2$\bar{2}$0)/Cu_2O (1$\bar{1}$3).

Between the main peaks in Figure 6.3, which can be associated with Al_2O_3 (110) and (220), a total of 5 broad reflexes were observed, each of which can be associated with a Cu_2O phase, showing the presence of a Cu_2O powder on the sample after two weeks of native oxidation. Since no XRD data were gathered prior to the exposure to air, it cannot be determined, whether the sample already consisted of a mixture of Cu powder and Cu (111)-oriented particles in UHV post growth, or if the native oxidation of the Cu in air caused some particles to undergo structural degradation, resulting in the Cu_2O powder signal. Low energy electron diffraction measurements in UHV post growth, commonly used to determine the particle orientation of MBE grown samples prior to exposing the samples to air, were inconclusive due to a strong surface charge of the samples.

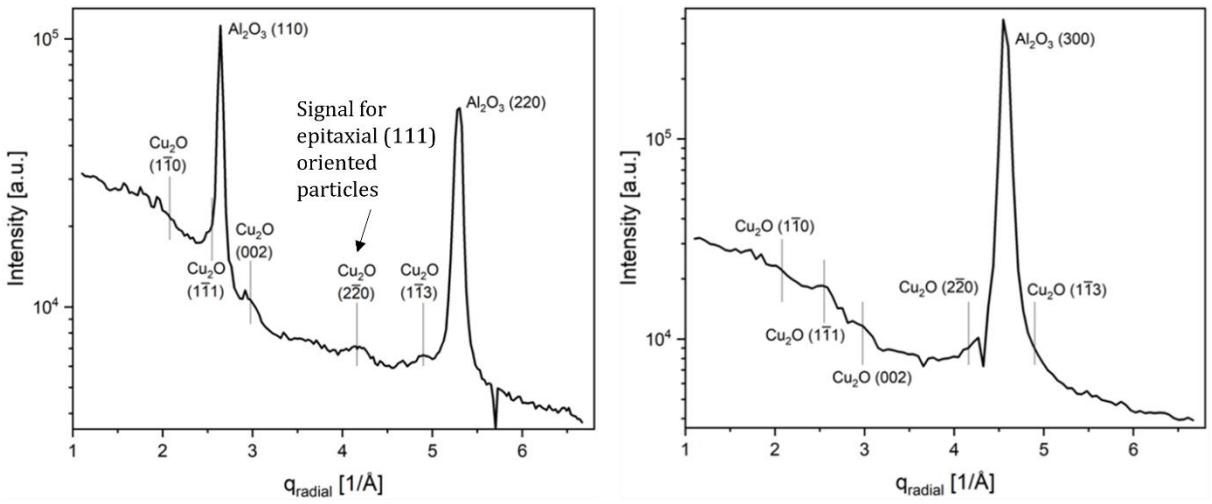

Figure 6.3. Radial in-plane scan along the Al_2O_3 (110) (left and (300) (right) direction showing broad nanoparticle signal, fitting to Cu_2O.

Orientation-dependent oxidation and reduction of Cu up to 575 K

To follow the oxidation at different temperatures, the azimuthal in-plane scans for Cu $(2\bar{2}0)$ /Cu_2O $(1\bar{1}3)$ and Cu_2O $(2\bar{2}0)$ were repeated after heating the sample to 325 K still under Ar flow, as seen in Figure 6.4. For both reflexes, even at these relatively low temperatures, a clear increase in the peak intensity relative to the background can be observed, indicating that an increasing number of particles adopt the epitaxial in-plane orientation. This effect can be seen, despite the most pronounced shift of the curves, which is the strong slope of the background signal, which is consistently higher for sample rotations in the negative ω-direction and lower for sample rotations around ω = 0. In retrospective, this change in the curves is due to the use of boron nitride paste for the sample mounting. As the sample temperature increases, the paste dries and slightly changes the tilt of the sample. This still happened during the measurements after the alignment of the sample. As a result, the tilt causes the sample to be practically better aligned at lower ω-values and slightly worse aligned around ω = 0. Nonetheless, the strong changes in the peak shape and intensity cannot be explained just by the slight misalignment due to the sample mounting.

The change is more pronounced for Cu_2O, which could be explained by the fact that the Ar gas used during the experiment contained trace amounts (~ 1 ppm) of water and oxygen, which were enough to oxidize the Cu. The oxidizing effect of the Ar gas became evident as well in additional measurements at higher sample temperatures (see e.g. Figure 6.7) and was also evident in later experiments such as the operando measurements described in chapter 7.

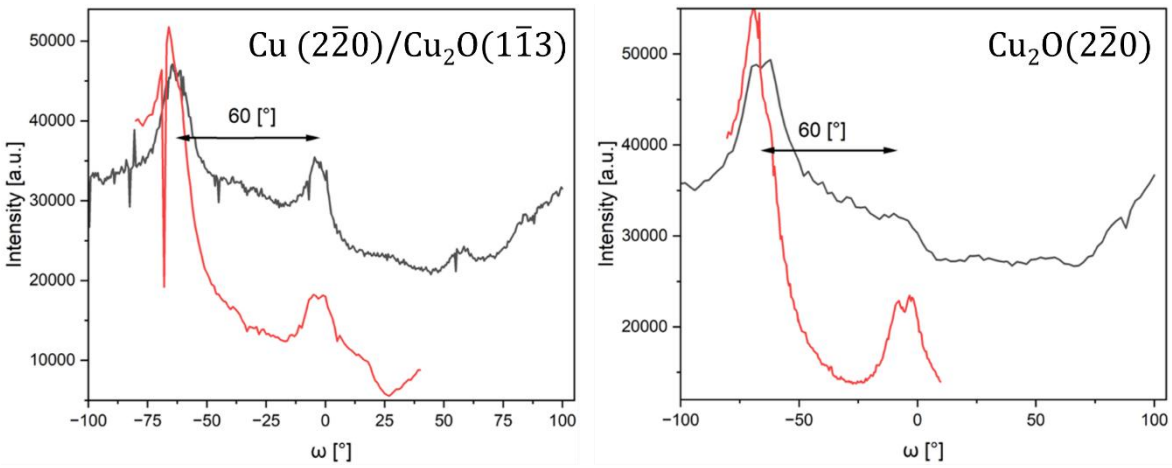

Figure 6.4. Left: Azimuthal in-plane scan for Cu $(2\bar{2}0)$/Cu_2O $(1\bar{1}3)$ in Ar at room temperature (black) and at 325 K (red). Right: Azimuthal in-plane scan for Cu_2O $(2\bar{2}0)$ in Ar at room temperature (black) and at 325 K (red).

Regarding the azimuthal in-plane scan for Cu $(2\bar{2}0)/Cu_2O$ $(1\bar{1}3)$, the change between the measurement at room temperature and 325 K is a definite reduction in the FWHM of the in-plane peaks which is assumed to be the consequence of an increase in the size of the corresponding crystallites. This assumed growth of the crystallites can be accounted for by two separate effects: First the growth of Cu (111) particles through the increased mobility of Cu atoms on the sample surface due to the increased sample temperature. Second, the advanced oxidation of the Cu powder and the formation and growth of (110)-oriented Cu_2O particles, oriented in-plane with the $(1\bar{1}1)$ direction along sapphire (110). A schematic illustration of the expected in-plane reflexes for (110)-oriented cubic nanoparticles can be found in Figure 6.5.

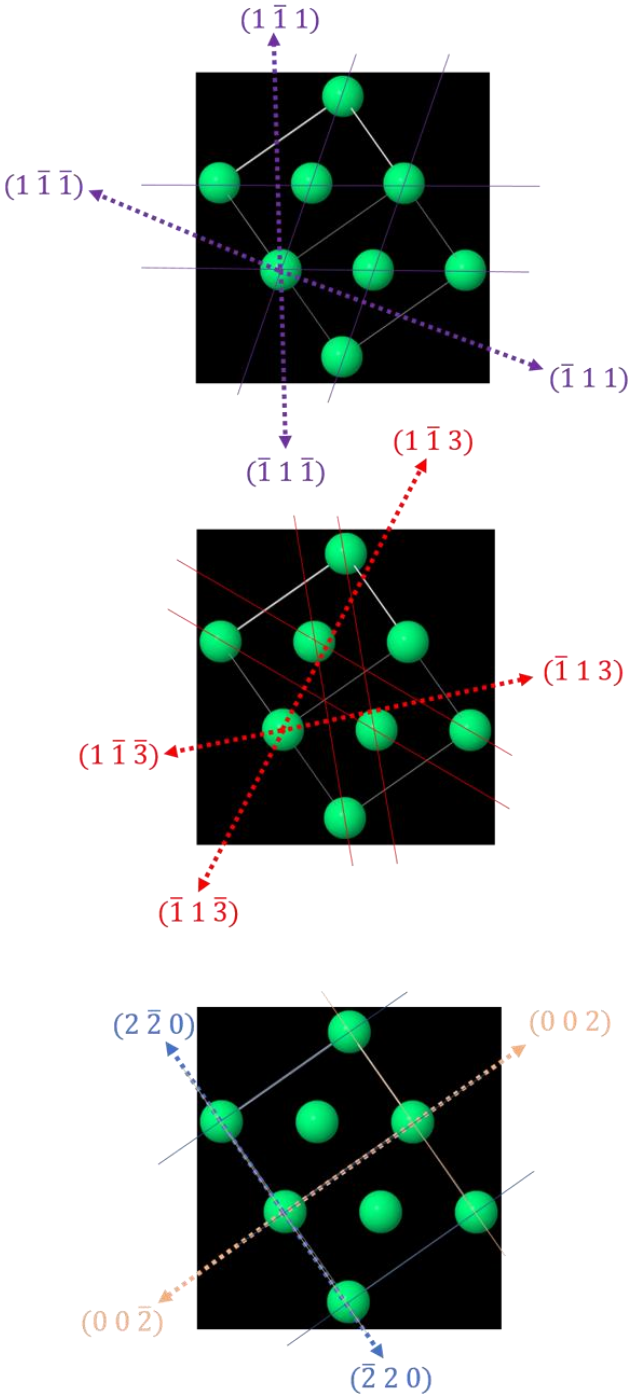

Figure 6.5. Schematic illustration of the top-down view of cubic particles oriented with their (111) direction out-of-plane. The atoms of a single unit cell are shown as green spheres, with the lattice planes indicated with straight lines and the corresponding in-plane crystallographic reflexes of the lattice planes indicated by a dotted line of the same color.

Since the Cu_2O (1$\bar{1}$3) reflex has a 12-fold symmetry in-plane for (110) orientation out-of-plane, peaks every 30 degree are expected for the Cu_2O (1$\bar{1}$3) reflex in-plane when (110)-oriented Cu_2O particles form. The angle between the (1$\bar{1}$1) and (1$\bar{1}$3) direction is 29.5°, as illustrated by the schematic drawing in Figure 6.6, therefore, the (1$\bar{1}$3) reflex is going to appear almost perfectly along the high symmetry direction of Al_2O_3, similar to the Cu

(2$\bar{2}$0) reflex of the (111)-oriented particles, as well as directly in the middle between the high symmetry directions.

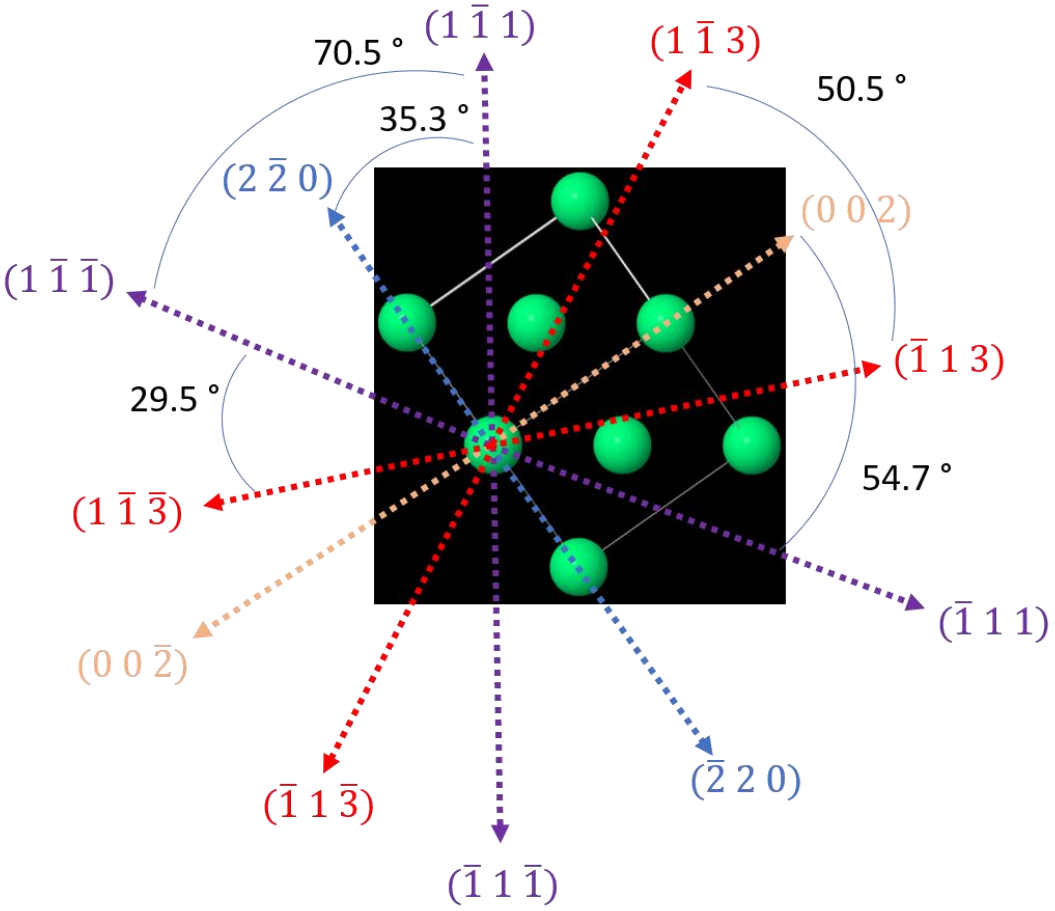

Figure 6.6. Schematic illustration of the expected angular difference between the different in-plane reflexes of cubic particles that are oriented with their (111) direction pointing out-of-plane. A single corresponding unit cell of such a particle is illustrated by green spheres, the corresponding lattice planes are illustrated for reference in Figure 6.5 using the same color coding.

Importantly, due to the 12-fold symmetry of the Cu_2O (1$\bar{1}$3) reflex, the performed scans are not suited to distinguish whether the (110)-oriented Cu_2O particles are oriented in-plane with the Cu_2O (1$\bar{1}$1) || Al_2O_3 (100) or Cu_2O (1$\bar{1}$1) || Al_2O_3 (110). For a precise determination of the epitaxial relationship of the Cu_2O particles to the substrate, measurements of additional reflexes would be needed.

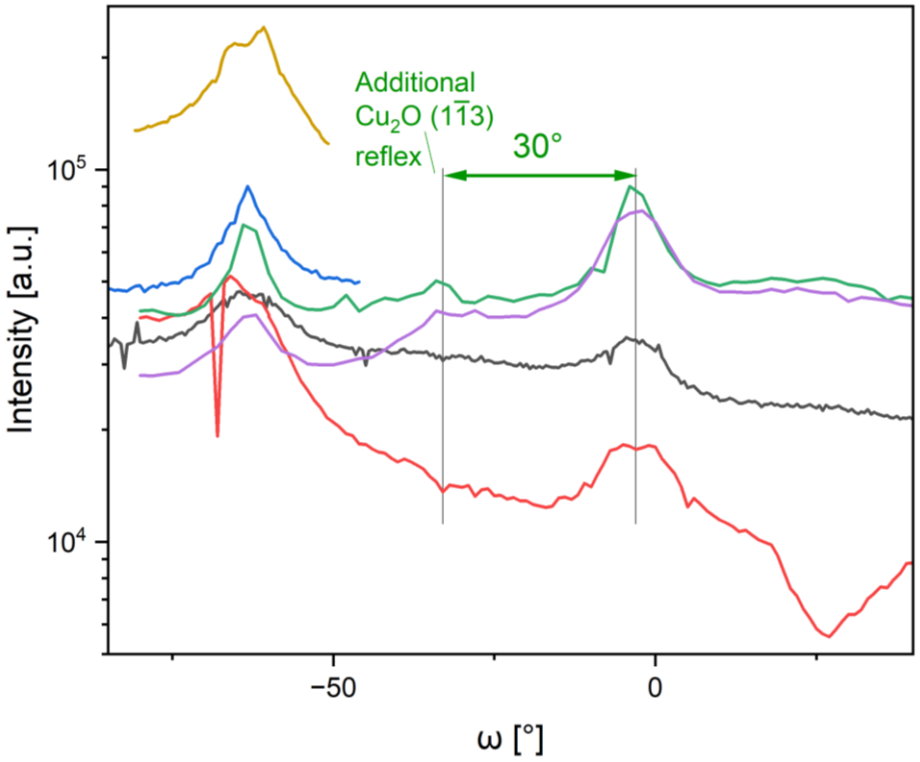

Figure 6.7. Evolution of Cu (2$\bar{2}$0)/Cu_2O (1$\bar{1}$3) reflexes measured in azimuthal in-plane scans under gas flow of: Ar at room temperature (black), Ar at 325 K (red), H_2:Ar (35:15) at 375 K (blue), H_2 at 375 K (green), Ar at 375 K (violet) and CO at 575 K (brown).

The formation and growth of both Cu (111) as well as Cu_2O (110) particles would be in accordance with the decreased FWHM of the peaks in the azimuthal in-plane scan and is further corroborated by the subsequent scans at even higher temperatures as seen in Figure 6.7. After reaching 375 K in a H_2:Ar (35:15) mixture, the peak in the scan has an even smaller FWHM and for 475 K in H_2 and Ar, an additional peak emerges between the main peaks. This additional peak can be associated with Cu_2O (1$\bar{1}$3) and therefore fits well to the formation of Cu_2O (110) particles as described above. Finally, the scan shows a double peak feature most clearly pronounced in the final measurement done at 575 K in pure CO. Before switching to pure CO, 5 cycles of switching between pure H_2 and Ar were carried out at 475 K at an increased total pressure of 1 bar which was kept for the remainder of the experiment. Afterwards, the gas mixture was switched to a (1:1) mix of H_2:CO and only afterwards the reaction gas was switched to pure CO.

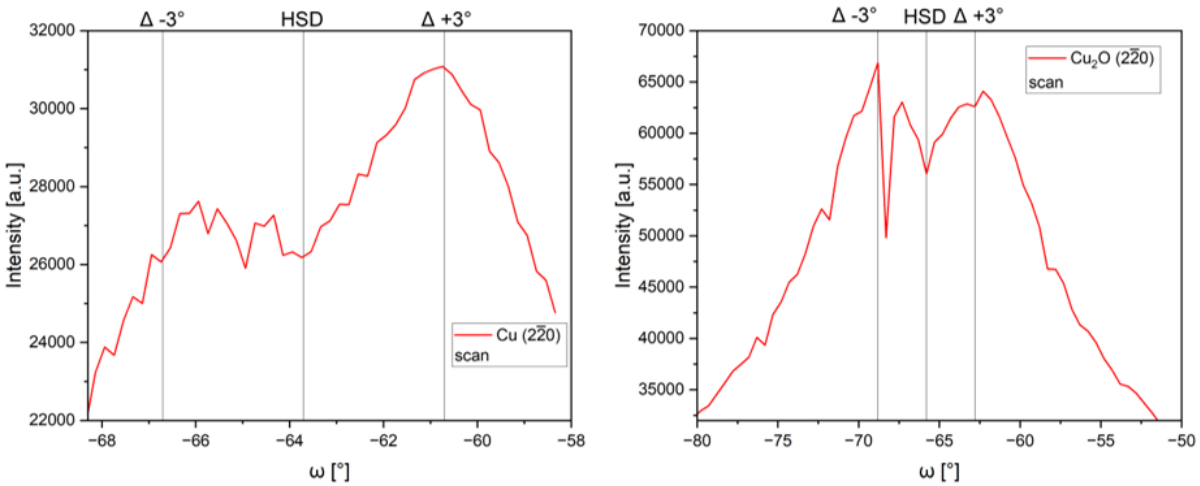

Figure 6.8. Azimuthal in-plane scans for Cu (2$\bar{2}$0) (top) and Cu_2O (2$\bar{2}$0) (bottom) at 575 K in pure CO showing the high symmetry direction (HSD) of Al_2O_3 (100) and the +-3° peaks corresponding to the Cu domains.

The double peak feature appears in a symmetrical way around the high symmetry direction (HSD) of the Al_2O_3 (100) in-plane direction, which corresponds to a formation of a coincidence site lattice of the Cu domains. Instead of showing a perfect in-plane orientation following Cu (1$\bar{1}$0) || Al_2O_3 (100), the two separate groups of domains are oriented +-3° off the HSD of Al_2O_3 as illustrated in Figure 6.8. This rotation around the surface normal was shown to be favourable for the growth of Cu (111) on Al_2O_3 (001) by Oh et. al. [69] and illustrated in Figure 6.9.

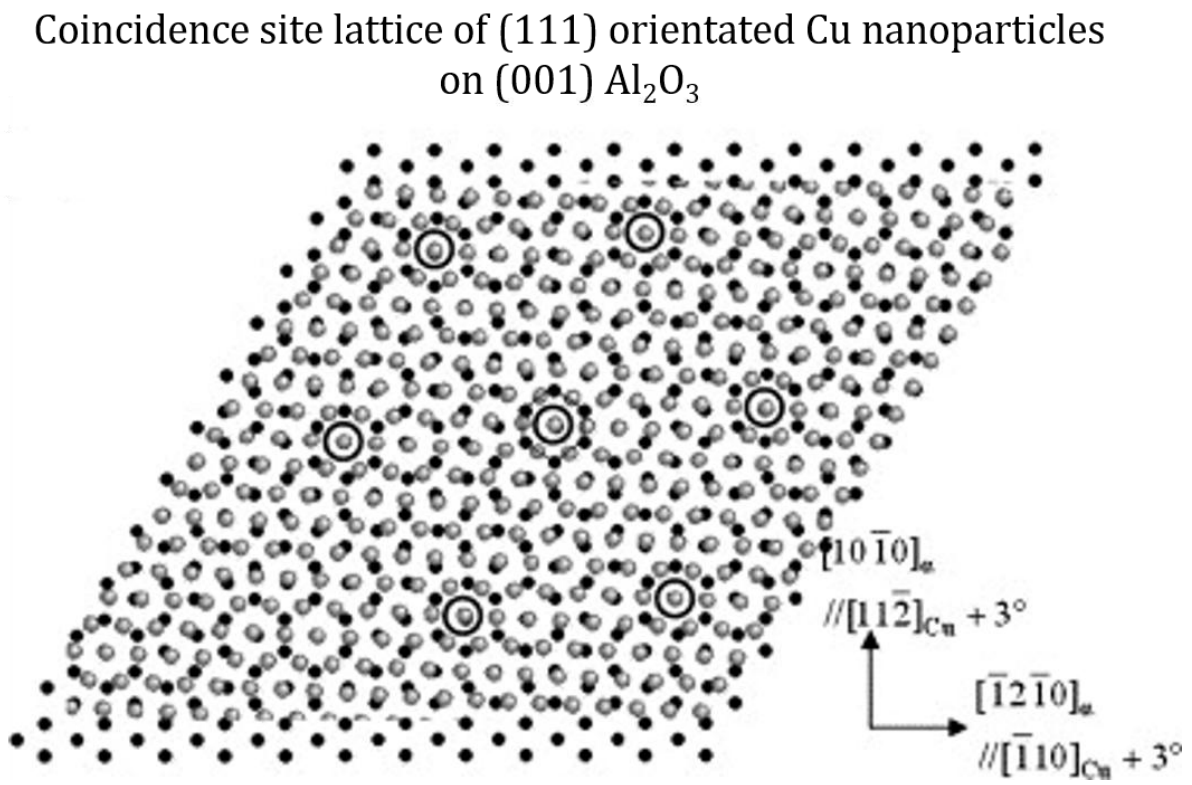

Figure 6.9. Lattice overlay of Cu on Al_2O_3 with Cu (111) || Al_2O_3 (001) in top/c-axis view. In the image, gray circles represent Cu atoms on the (1 1 1) plane, while black circles denote oxygen ions on the (0 0 1) sapphire surface. For clarity, Al ions and their associated OH groups have been omitted. Three distinct positions for Cu atoms are shown: atop the oxygen ions (represented by circles), atop the aluminum ions (represented by hexagons), and above the hollow sites (represented by triangles). The overlay shows, that the best fit regarding the lattice mismatch between the two phases is achieved, when the Cu ($1\bar{1}0$) in-plane direction is not aligned perfectly along Al_2O_3 (100) but with a rotation around the surface normal of 3°. The same coincidence side lattice is assumed for a rotation by -3°. Taken from [69].

Similar to the measurement at 575 K in pure CO in Figure 6.7, the sample heating caused the emergence of a double peak feature in the in-plane scan of Cu_2O ($2\bar{2}0$) as well as a decrease in FWHM as seen in Figure 6.10. This double peak feature is similar to that in the azimuthal in-plane scans of Cu ($2\bar{2}0$) and points to an oxidation of the Cu domains, for which the in-plane orientation of the domains is stable during the oxidation from Cu to Cu_2O, as the structure remains cubic.

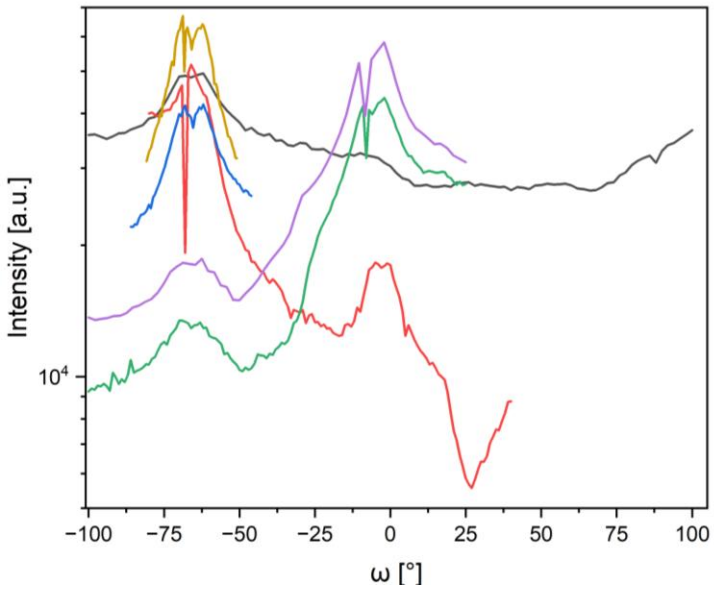

Figure 6.10. Evolution of the Cu_2O $(2\bar{2}0)$ reflex measured in azimuthal in-plane scans under gas flow of: Ar at RT (black), Ar at 325 K (red), H_2:Ar (35:15) at 375 K (blue), H_2 at 375 K (green), Ar at 375 K (violet) and CO at 575 K (brown).

Structure of Cu on the simplified model catalyst after activation

As seen in Figure 6.11, in order to investigate the state of Cu on the "Cu-Al_2O_3" catalyst, several radial in-plane scans were performed at 575 K. Clear in-plane signal for Cu $(1\bar{1}1)$, Cu (002) and Cu $(2\bar{2}0)$ were observed. For each of the reflexes, azimuthal in-plane scans revealed the in-plane orientation and epitaxy, with the measured in-plane direction angle corrected for the detector angle for the corresponding peak position using equation 30.

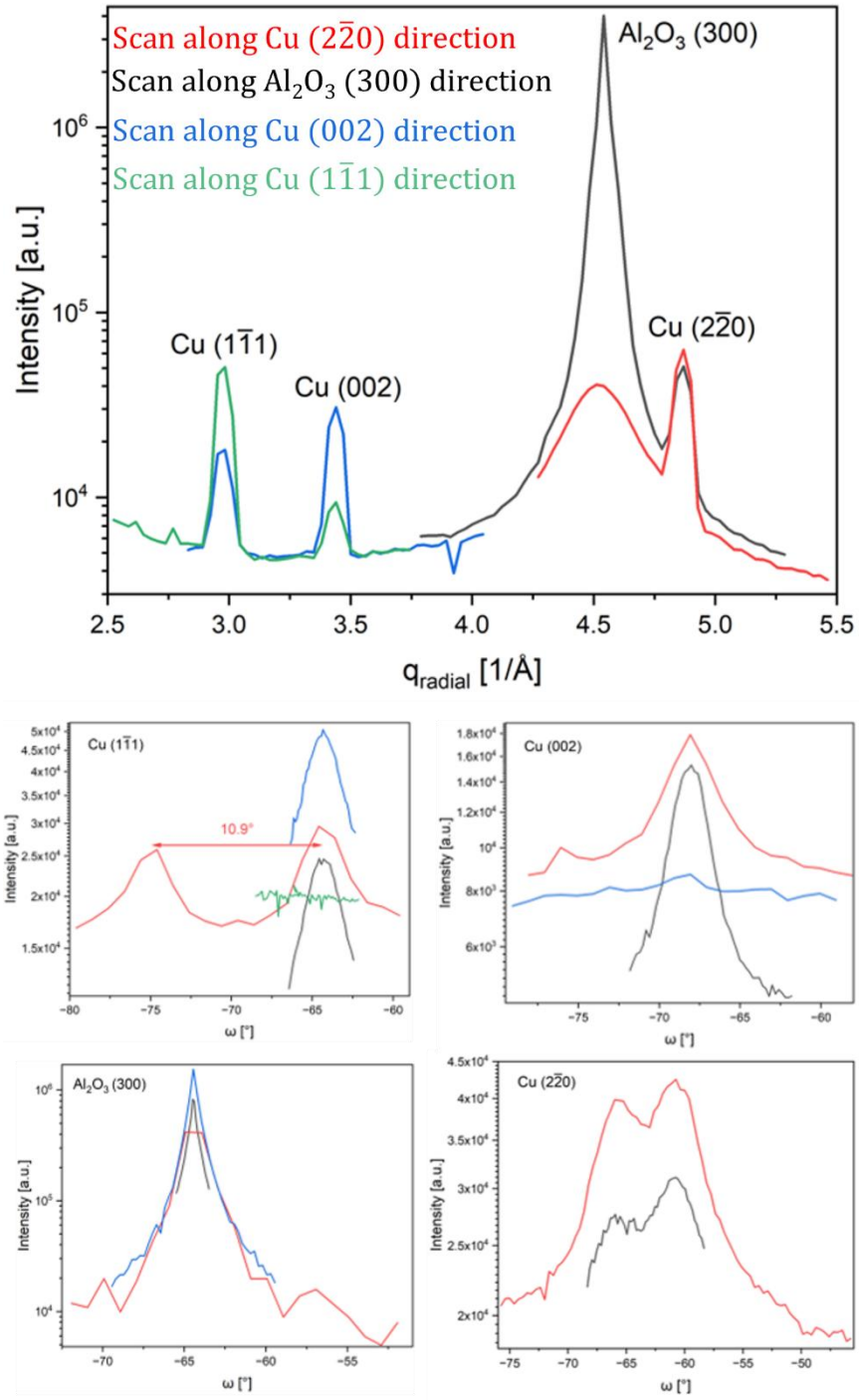

Figure 6.11. Cu supported on Al_2O_3 ("Cu-Al_2O_3" sample) investigated at 575 K and 1 bar total pressure under pure CO gas flow. Top: Radial in-plane scans for Cu (1$\bar{1}$1) (green), Cu (002) (blue), Al_2O_3 (300) (back) and Cu (2$\bar{2}$0) (red). Bottom: In-plane azimuthal scans for each of the reflexes at 575 K in CO (black), in Ar (blue), Ar:CO_2 (green) and in H_2 after CO_2 (red).

As listed in detail in Table I.5, the in-plane direction of the Cu (002) is aligned only 0.08° off the Al_2O_3 (300) in-plane direction. Furthermore, the difference in the in-plane directions of Cu (1$\bar{1}$1) and Cu (002) is 5.56°, which fits very well to the expected angle between the respective directions in an FCC lattice which is 54.7°, which, accounting for the 60° in-plane spacing between domains yields an expected angular difference of 60°-

54.7° = 5.3 °. A schematic illustration of the in-plane reflexes and their angular difference can be found in Figure 6.5 and Figure 6.6. Additionally, for the measurement under pure H_2 gas flow, the range of the Cu $(1\bar{1}1)$ radial in-plane scan was increased revealing another distinct peak at ω =-74.94°, 10.9° off the main peak position (red curve in Figure 6.11, left image in the middle). This second peak fits perfectly to the expected angular distance between Cu (111) and Cu $(1\bar{1}1)$ in-plane, which is 70.5°. This, again considering the 60° angle between domains, yields an angular difference between (111) type reflexes of 10.5° in the azimuthal in-plane scans for (110)-oriented particles. Therefore, the Cu $(1\bar{1}1)$ and Cu (002) in-plane peaks can be clearly associated with Cu (110)-oriented particles with the in-plane epitaxy described by Cu (001) || Al_2O_3 (100).

The Cu $(2\bar{2}0)$ signal cannot be explained by the same (110)-oriented particles, due to the radial in-plane position of the peaks. Since the (110)-oriented particles have an in-plane epitaxy of Cu (002) || Al_2O_3 (100), the Cu $(2\bar{2}0)$ reflex would be expected to appear at a 30° angle off the Cu (002) peak, so it would be aligned along the Al_2O_3 (110) direction, which was not measured. The in-plane radial position of the Cu $(2\bar{2}0)$ peak is instead consistent with the measurements at room temperature and above, fitting to (111)-oriented Cu particles with in-plane epitaxy of Cu (110) || Al_2O_3 (100) and the +-3° coincidence site lattice as described in the previous section. To further investigate the orientation and epitaxy of the Cu particles, out-of-plane L-scans were performed after setting an orientation matrix using the strong Al_2O_3 signals from the substrate. Figure 6.12 shows the L-scans performed starting from the Cu (002) and from the Cu $(2\bar{2}0)$ in-plane positions respectively. As a guideline, Figure 6.12 includes a simulated out-of-plane map, which shows all the expected reflexes for the Cu and Al_2O_3 phases.

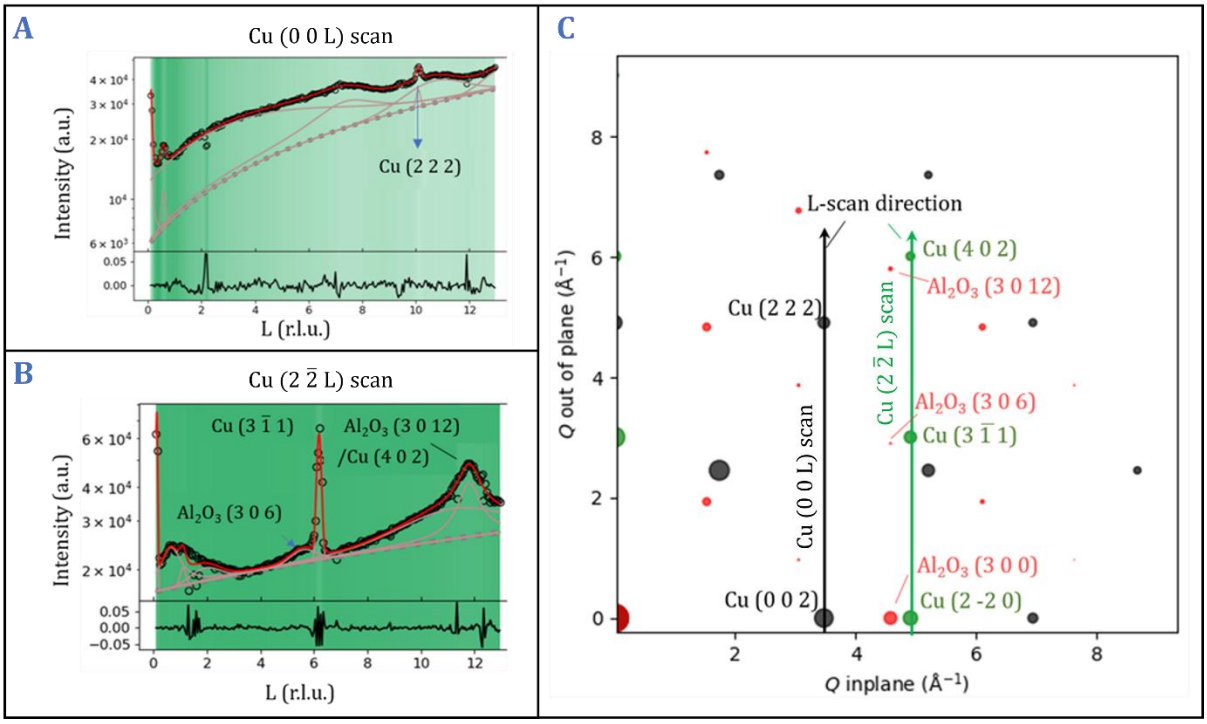

Figure 6.12. A&B: Out-of-plane L-scans performed using the Al_2O_3 orientation matrix in pure CO at 575 K and 1 bar total pressure (black) and corresponding peak fits (red). A: L-scan starting from the Cu (002) in-plane peak position. B: L-scan starting from the Cu (2$\bar{2}$0) in-plane peak position. C: Simulated reciprocal space plane for the corresponding L-scans showing the reflexes of the following planes (first direction is always out-of-plane, second is in-plane): Al_2O_3 (001)x(100) [red], Cu (111)x(1$\bar{1}$0) [green], Cu(110)x(001) [black]. Scan path of Cu (002) L-scan drawn in black, scan path for Cu (2$\bar{2}$0) L-scan in green. Reflexes are scaled according to their respective relative intensity.

All of the reciprocal space simulations in this work were prepared using the *xrayutilities* python package [70]. The Al_2O_3 plane that was used to create the simulations is defined by the (001) out-of-plane direction and the (100) in-plane direction. Since the in-plane epitaxy for the Cu particles can be described by Cu (110) || Al_2O_3 (100) for the (111)-oriented particles and by Cu (001) || Al_2O_3 (100) for the (110)-oriented particles, the planes for Cu used for the simulation were chosen accordingly to be: out-of-plane (111) and in-plane (1$\bar{1}$0) as well as out-of-plane (110) and in-plane (001). All reflexes occurring in any of these three planes are included in the simulation of Figure 6.12 in red for Al_2O_3, in black for (110)-oriented Cu particles and in green for (111)-oriented Cu particles. Comparing the simulation to the measured curves underlines the previously drawn conclusion based on the results illustrated in Figure 6.11 for the presence of both Cu (111) and Cu (110)-oriented particles at 575 K in pure CO. The L-scan starting from the Cu (002) in-plane position only shows one additional clear peak which can be associated with Cu (2$\bar{2}$0) as the next expected peak out-of-plane for (110)-oriented particles. Similarly, the main peaks in the L-scan starting from the Cu (2$\bar{2}$0) in-plane position shows two clear

peaks for Cu ($3\bar{1}1$) and Cu (402) respectively. Furthermore, additional signal from other peaks, one close to the Cu ($3\bar{1}1$) and a large peak underneath the Cu (402) are seen in the L-scan. Comparing the lattice spacings of these peaks with the simulated reciprocal space map shows, that these peaks can be interpreted as shoulders of Al_2O_3(306) and Al_2O_3 (3012) respectively. Figure 6.13 shows additional L-scans performed form the in-plane position of Cu ($1\bar{1}1$) as well as Al_2O_3 (300). The latter clearly shows the (306) and (3012) reflexes as expected and also underlines the vastly higher intensity of the substrate peaks, which fits to the assumption made above, that for the other L-scans, shoulder signal of close by substrate reflexes would still be sufficiently intense to be of comparable intensity to the particle signals. In order to understand all the measured peaks in the L-scan starting from the Cu ($1\bar{1}1$) position, additional reflexes from Cu particles with different in-plane orientations had to be included in the corresponding simulation compared to Figure 6.12 to account for shoulders of broad, close by Cu peaks in the scan. The additional orientations of the particles are simulated by adding the following hkl-planes to the simulation in Figure 6.13: (first direction is out-of-plane, second is in-plane): Cu (111)x($11\bar{2}$), and Cu(110)x($1\bar{1}1$). These additional planes were assumed based on to the small angle between the corresponding in-plane directions of Cu: (110)∢($11\bar{2}$) = (001) ∢($1\bar{1}1$) = 54.7°, which, again taking the 60° in-plane angular separation of domains into account, yields an effective angular difference of 60-54.7° = 5.3°. Additionally, the observed reflexes point toward a slight misalignment of the sample resulting in a slightly tilted L-scan. As can be seen by the simulated reciprocal space map of Figure 6.13, a perfectly straight L-scan starting from the in-plane position of the Cu ($1\bar{1}1$) reflex belonging to (110)-oriented particles marked with black circles, would miss the reflexes belonging to (111)-oriented particles marked with green circles. While a certain peak width of the corresponding peaks of (111)-oriented particles could also technically explain the presence of the Cu (002), ($2\bar{2}0$) and ($3\bar{1}1$) peaks in the scan, the absence of the ($1\bar{1}1$) reflex measured out-of-plane clearly points towards a slight sample misalignment.

Overall, the L-scans clearly underline the presence of distinct epitaxial crystalline domains of both Cu (111) as well as (110)-oriented particles. Furthermore, the presence of a Cu powder can also be excluded, since in the case of a powder, additional Cu signals would be expected in the L-scan performed from the Cu (002) and ($2\bar{2}0$) in-plane positions.

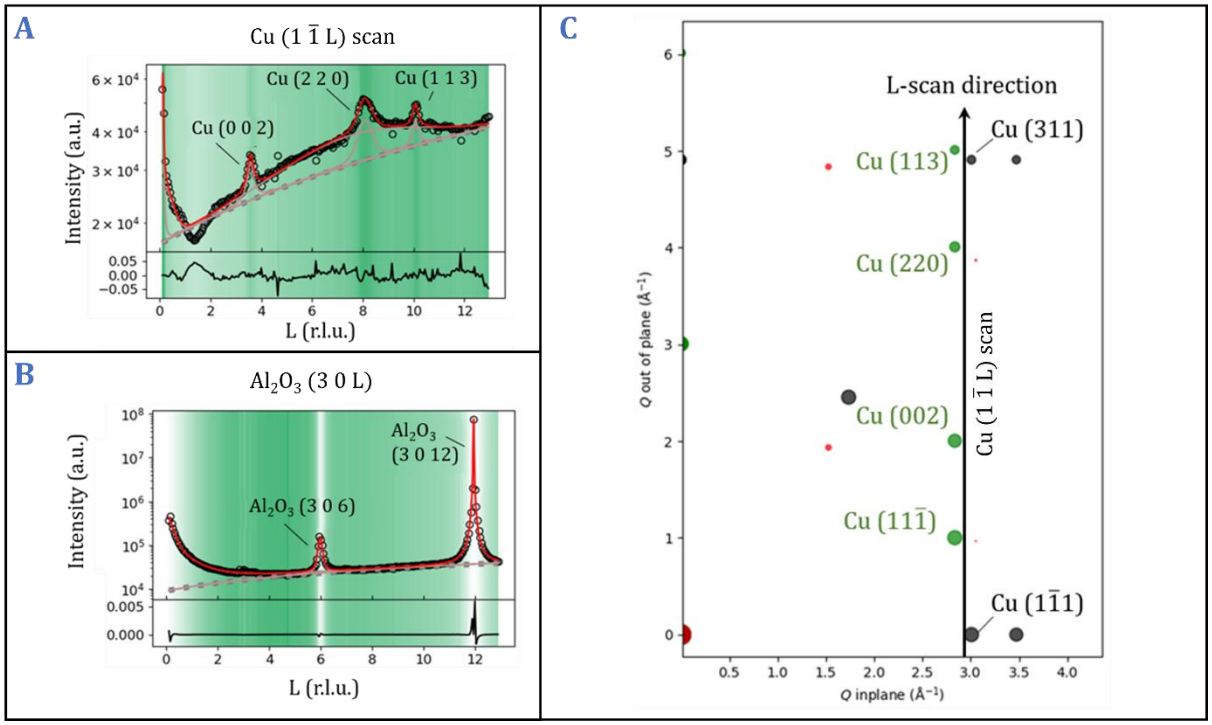

Figure 6.13. A&B: Out-of-plane L-scans performed using the Al_2O_3 orientation matrix under pure CO gas flow at 575 K and 1 bar total pressure (black) and corresponding peak fits (red). A: L-scan starting from the Cu (1$\bar{1}$1) in-plane peak position. B: L-scan starting from the Al_2O_3 (300) in-plane peak position. C: Simulated reciprocal space plane for the corresponding L-scans from the Cu (1$\bar{1}$1) in-plane peak position showing the reflexes of the following planes (first direction is always out-of-plane, second is in-plane): Al_2O_3 (001)x(100) [red], Cu (111)x(1$\bar{1}$0) and Cu (111)x(11$\bar{2}$) [green], Cu(110)x(001) and Cu(110)x(1$\bar{1}$1) [black]. Scan path of Cu (1$\bar{1}$1) L-scan drawn in black. Reflexes are scaled according to their respective relative intensity.

Structural analysis of the ZnO-supported model system after catalyst activation

As described earlier, during the ambient pressure experiments, the boron nitride paste used for sample mounting was continuously drying during the heating process from room temperature, causing slight changes in the sample alignment throughout all measurements below 575 K for "Cu-Al_2O_3". To avoid similar problems for the second sample, "CZ-Al_2O_3" was heated to 575 K before alignment and prior to any measurements. Therefore, no information about the catalyst at room temperature or below 575 K was gathered for this sample.

The integrity of the support surface after the sample preparation including Ar^+ sputtering as described at the beginning of this chapter, was confirmed by an azimuthal in-plane scan for the Al_2O_3 (300) performed under 1 bar total pressure and H_2 reaction gas flow at a sample temperature of 575 K as shown in Figure I.8. The 60° in-plane symmetry of the substrate is evident, with the high symmetry direction of the (300) type in-plane direction located at a corrected angle of $\omega_{corrected}$ = 10.22° (correction based on equation 30).

Azimuthal in-plane scans were performed for both Cu ($1\bar{1}1$) and Cu (002) revealing only negligible variations in intensity along the sample rotation, clearly pointing to the presence of in-plane randomly oriented Cu domains on the support (corresponding measurements are not shown in this dissertation). The random in-plane orientation of the Cu domains under the initial hydrogen flow for this sample is further underlined by the in-plane scans in Figure 6.14 and the corresponding fit parameters found in Table I.6. Clear signals were found for Cu ($1\bar{1}1$), Cu (002) and Cu ($2\bar{2}0$) in separate scans as well as in the radial scan performed along the in-plane direction of the Cu ($1\bar{1}1$) reflex. The corrected in-plane directions of the separate Cu peaks show no correlation to the high symmetry direction of the sapphire substrate being located at $\omega_{corrected,111}$ = -74.51°, $\omega_{corrected,002}$ = -71.2° and $\omega_{corrected,220}$ = -59.02°. Similarly, the radial scan along the Cu ($1\bar{1}1$) direction shows signals for Cu ($1\bar{1}1$), (002), ($2\bar{2}0$) and ($1\bar{1}3$) reflexes along the same radial direction again underlining the assumption that the Cu domains have either a textured- or powder-like orientation in-plane. It is noteworthy though, that at least in the initial H_2 conditions, the relative intensity ratios between the Cu reflexes do not fit to the expected ratios of a perfect Cu powder as described in the literature [71,72], as for example, the Cu ($2\bar{2}0$) reflex is measured to be of higher intensity than the Cu (002). This is true for the separate scans with the following intensities for the Cu reflexes: 711 ($1\bar{1}1$), 263 (002) and 376 ($2\bar{2}0$) as well as for the radial scan: 1058 ($1\bar{1}1$), 351 (002), 620 (002) and 176 ($1\bar{1}3$). The ratio of the intensities changes after the sample was exposed to different reaction gases and undergoing Cu oxidation and reduction, as in the final H_2 conditions the intensity ratios do match well to the expected ratios for a Cu powder. Therefore, the results in the initial conditions indicate, that the Cu on this sample had formed preferentially oriented particles during the growth in UHV similar to "Cu-Al_2O_3", while the heating process up to 575 K, caused the Cu domains to form in-plane randomly orientated domains as well as fully powder-like particles. Assuming that the Cu particles have grown in a similar fashion on "CZ-Al_2O_3" as they have on "Cu-Al_2O_3", predominately Cu (111)-oriented particles would be expected on the sample at room temperature. This assumption is accordance with the measured intensity of the Cu ($2\bar{2}0$) reflex, seen to be higher than the intensity of the Cu (002) reflex, with the signal for the Cu ($2\bar{2}0$) reflex including contributions of out-of-plane (111)-oriented domains.

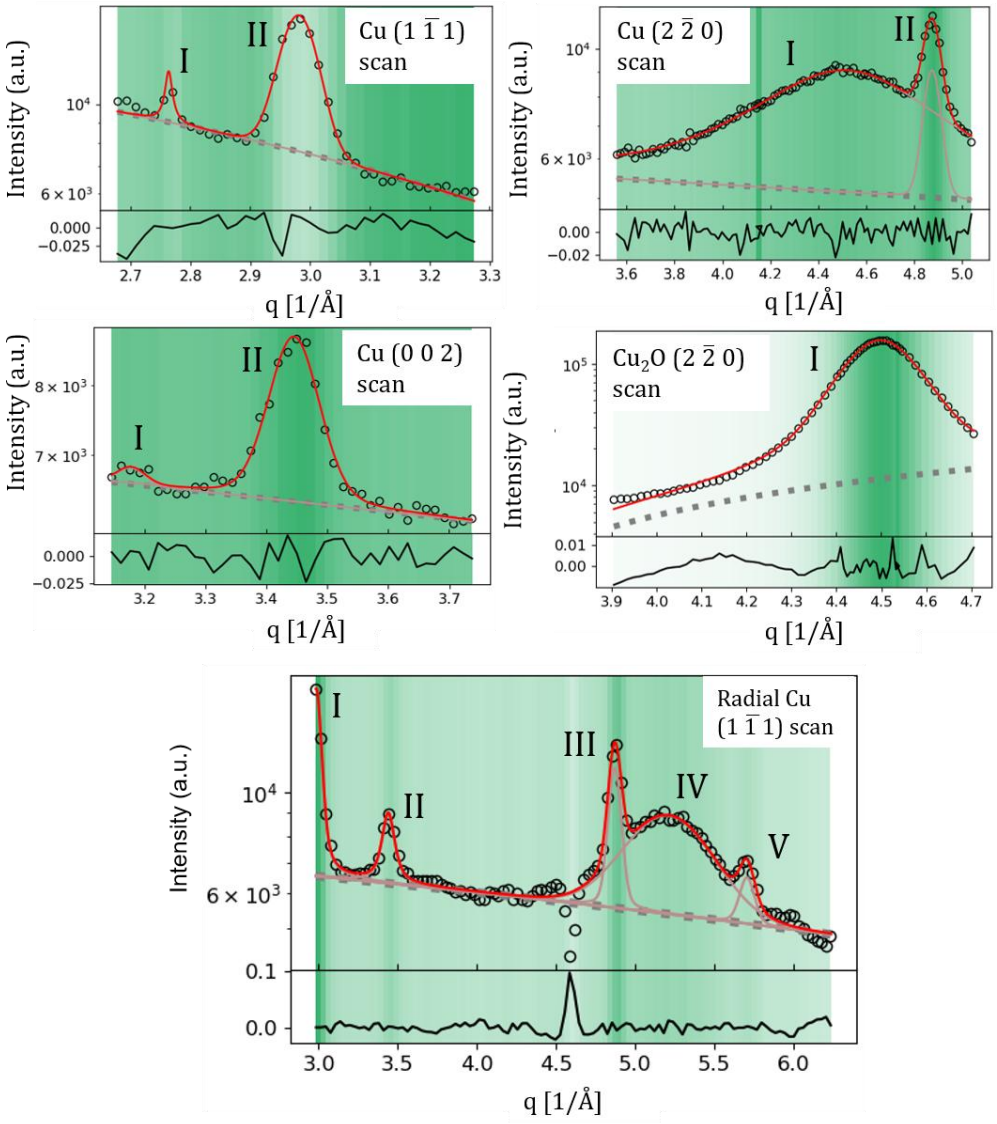

Figure 6.14. In-plane q and radial scans (black dotted lines) and corresponding fits (red lines) for "CZ-Al_2O_3" taken in initial H_2 conditions at 575 K at 1 bar total pressure. Peaks associated with roman letters as well as the fitting details can be found in Table I.6.

Furthermore, the in-plane scans show a number of additional reflexes associated with different phases. As discussed in detail in chapter 6.7, reflexes from an additional phase were observed during these measurements, whose chemical composition could not yet be determined. This phase is therefore referenced throughout this work as *unknown structure 1* (US1), assumed to have a cubic lattice structure with a lattice constant of 7.1149 Å, oriented with the (111) direction along Al_2O_3 (001). Another peak is observed in the Cu (1$\bar{1}$1) scan not only for "CZ-Al_2O_3" but also "Cu-Al_2O_3", which has been associated with the molybdenum (110) reflex caused by diffraction with the molybdenum screws used in the experimental setup. This association also fits well to the fact, that for both samples, this particular reflex does not change in either position nor intensity throughout

the exposure to various different reaction gases. Similarly, a peak is observed in the Cu (002) scan which can be assigned to the Be (110) reflex from the beryllium dome used in the experimental setup.

Finally, the scan used to investigate the Cu_2O $(2\bar{2}0)$ reflex, shows no peak in the corresponding q-range in the initial H_2 condition, revealing a full reduction of the Cu at 575 K similar to the results seen for "Cu-Al_2O_3" upon reaching 575 K.

6.2. Oxidation of activated model systems at 575 K

Formation of (111)- and (110)-oriented Cu_2O domains

The oxidation and reduction of the different Cu particles was investigated in different oxidizing and reducing gas atmospheres at 575 K. Figure 6.15 shows L-scans in different gas atmospheres for the simplified model catalyst ("Cu-Al_2O_3"), that were done using the Al_2O_3 orientation matrix and measuring the L-range for the Cu (220) and the Cu (113) reflexes in the L-scan along the direction of the Cu $(1\bar{1}L)$ position. As derived in the previous section, the corresponding peaks can be clearly associated with Cu (111)-oriented particles. As the changes in the scans are subtle, the exact fitting results for all scans are listed in Table I.7. As mentioned in the previous section, the Ar gas was observed to have an oxidizing effect on the samples, which is associated with the presence of a small amount of water and oxygen in the gas in the 1 ppm range. The Cu$(1\bar{1}L)$ scans performed in Ar (A) and an Ar:CO_2 (1:1) mixture (B) respectively were both measured exactly 35 minutes after switching the reaction gases. As can be seen, there is only negligible change in the curves. Furthermore, the fitting parameters are also very similar to the L-scan performed in pure CO. On the other hand, clear changes are observed for the Cu$(1\bar{1}L)$ scans, which were performed in pure H_2 and only 15 minutes (C) and 25 minutes (D) after switching the reaction gases, respectively. The most pronounced change in the peaks is the change in the FWHM, but a clear change in the lattice position can be observed as well. While in Ar/Ar:CO_2 the lattice spacings for Cu (220) were q=8.05 1/Å ≡ d=1.283 Å and for Cu (113) q = 10.08 1/Å ≡ d=1.100 Å, in H_2, the averaged lattice spacings shift to q=8.02 1/Å ≡ d=1.286 Å for Cu (220) and q = 10.14 1/Å ≡ d=1.096 Å. Even more pronounced are the differences in the FWHM of the peaks, reducing from an average of 0.236 1/Å for Cu (220) and 0.090 1/Å for Cu (113) in Ar/Ar:CO_2 to just 0.088 1/Å for Cu (220) and 0.077 1/Å for Cu (113) in H_2.

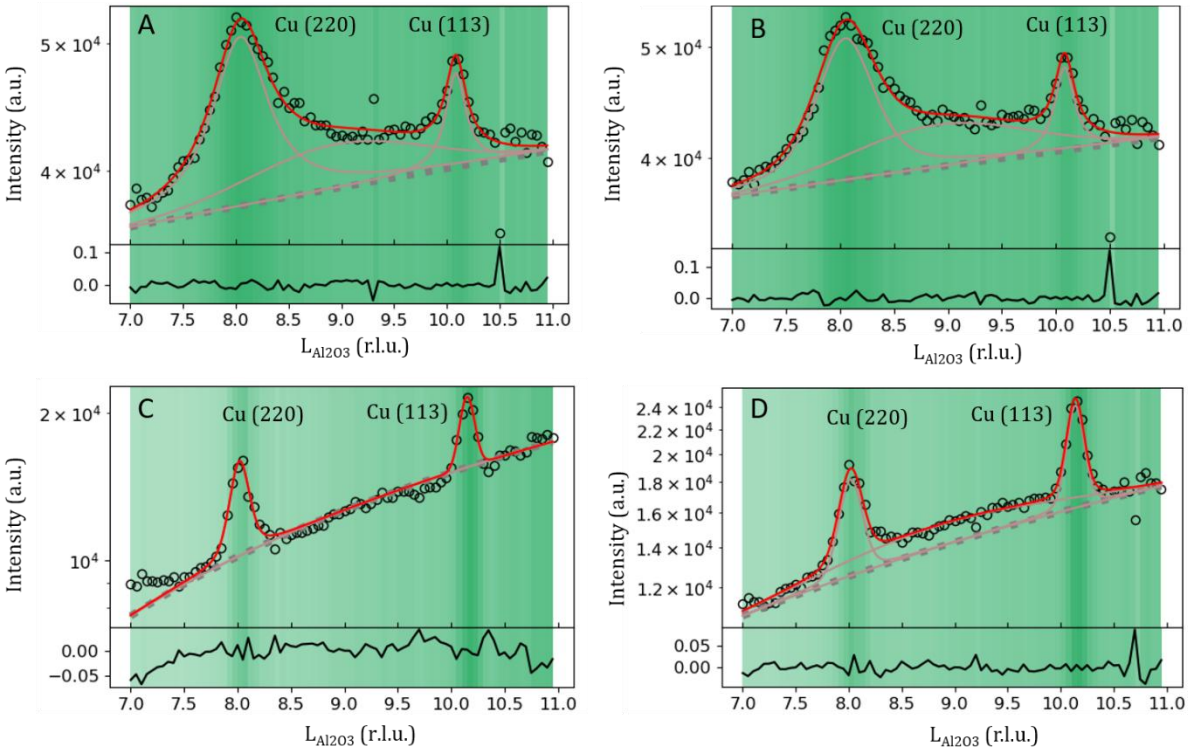

Figure 6.15. Out-of-plane L-scans along the L-direction of the Cu ($1\bar{1}1$) in-plane reflex of the "Cu-Al_2O_3) sample, around the range of the Cu (220) and Cu (113) reflex at 575 K: after 35 minutes in Ar (A), after 35 minutes in Ar:CO_2 (1:1) (B), after 15 minutes in H_2 (C) and after 25 minutes in H_2 (D).

To understand the changes in the peak position and width in Ar/Ar:CO_2 compared to H_2, another simulation of the corresponding reciprocal space planes is shown in Figure 6.16. Compared to the simulated reciprocal space maps shown in the previous section, the map in Figure 6.16 now also includes reflexes belonging to both (111) and (110)-oriented Cu_2O particles with the same in-plane epitaxy as the previously discussed Cu (111)- and (110)-oriented particles. With this addition, the large peak width can be explained by an overlap of the Cu (220) peaks with the nearby Cu_2O (222) and (311) peaks of (110)-oriented Cu_2O particles. Comparison of the scans under pure Ar to the scans under Ar mixed with CO_2 reveals no visible changes in the curves caused by the presence of CO_2 (Figure *6.15* A vs. B).

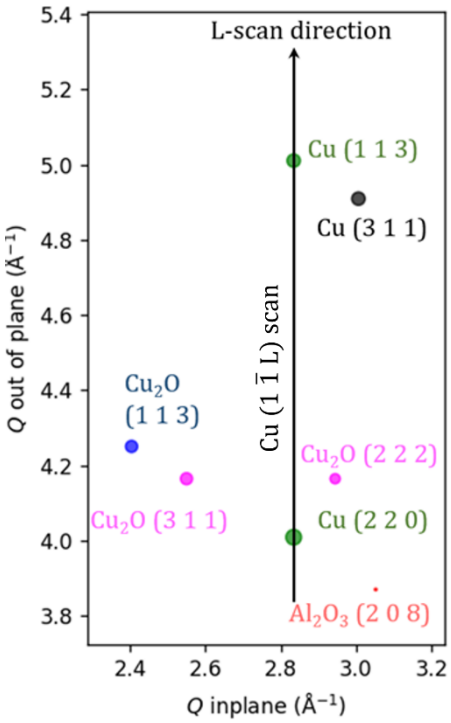

Figure 6.16. Reciprocal space map corresponding to the L-scans of Figure 6.15, showing the reflexes of the following planes (first direction is always out-of-plane, second is in-plane): Al_2O_3 (001)x(100) [red], Cu (111)x(11$\bar{2}$) [green], Cu(110)x(001) and Cu(110)x(1$\bar{1}$1) [black], Cu_2O(110)x(001) and Cu_2O(110)x(1$\bar{1}$1) [magenta], Cu_2O (111)x(11$\bar{2}$) [blue]. Scan path of L-scan drawn in black. Reflexes are scaled according to their respective relative intensity.

Following the oxidation of Cu under Ar gas flow, the reaction gas was switched to H_2, resulting in the reduction of the Cu_2O (110)-oriented particles. In the L-scan the previously broad peaks attributed to the superposition of Cu_2O signals appear much sharper as a result of a significant decrease in the intensity of the overlapping Cu_2O (222) and (311) peaks. Additionally, for the measurements in H_2, the lattice spacing of Cu (220) matches perfectly with the temperature corrected literature lattice spacing for Cu (220) at 575 K, which is $d_{220,575K}$ = 1.286 Å [71,72]. The changes in the Cu (113) peak are less pronounced, but can also be explained by an overlap of the peak with the nearby Cu (311) reflex. Specifically, the reduction of the peak width as well as the increase in the lattice spacing are in line with a more pronounced increase in the signal of the Cu (113) reflex associated with (111)-oriented Cu particles, compared to the increase in the Cu (311) signal associated with (110)-oriented particles, resulting in a measured lattice spacing fitting almost perfectly to the temperature corrected expected lattice spacing of Cu at $d_{113,575K}$ =1.097 Å.

Cu-Zn alloying and ZnO formation under oxidizing gas flow

Similar to the oxidation observed for the simplified model system "Cu-Al_2O_3", exposure of the ZnO-supported model system "CZ-Al_2O_3" to Ar gas flow caused a full oxidation of the Cu as shown in Figure 6.17 and corresponding Table I.8. All of the reflexes associated with Cu disappeared and reflexes for Cu_2O are seen instead, namely Cu_2O (002) and $(2\bar{2}0)$. The Cu_2O (002) peak appears along the corrected in-plane direction $\omega_{corrected,002}$ = -74.37°, while the $(2\bar{2}0)$ reflex was measured in several different scans corresponding to in-plane directions of $\omega_{corrected,220}$ = -56.59°/11.46°/-74.53°. The $(2\bar{2}0)$ reflex is always observed near an Al_2O_3 (300) reflex and it shows by far the highest intensity in the scan that is nearest to the actual Al_2O_3 (300) in-plane direction at $\omega_{corrected,220}$ = 11.46°. Therefore, the in-plane scans for Cu_2O show the presence of both fully randomly oriented domains as well as, domains with a preferential orientation along the Al_2O_3 (300) direction.

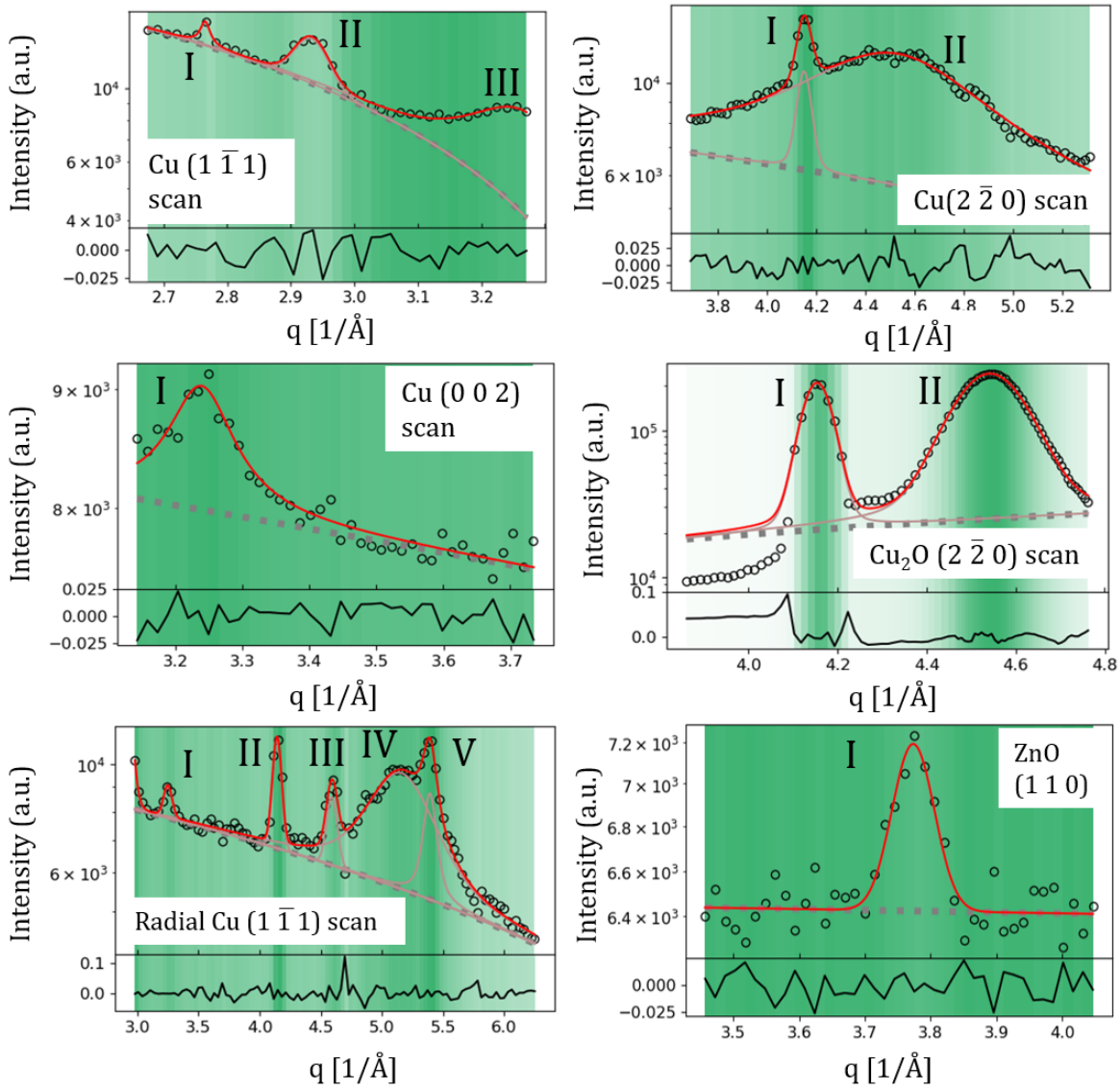

Figure 6.17. In-plane q and radial scans (black dotted lines) and corresponding fits (red lines) for the ZnO-supported model catalyst "CZ-Al_2O_3" taken under Ar flow at 575 K at 1 bar total pressure. Peaks associated with roman letters as well as the fitting details can be found in Table I.8.

Additional peaks emerged under oxidizing reaction conditions, associated with a Cu-Zn alloy formation, namely the $Cu_{0.64}Zn_{0.36}$ phase, specifically the $Cu_{0.64}Zn_{0.36}$ (002) reflex which can be associated to peak III in the Cu (1$\bar{1}$1) scan, peak I in the Cu (002) and peak I in the radial scan along Cu (1$\bar{1}$1) as well as the $Cu_{0.64}Zn_{0.36}$ (113) reflex associated with peak V in the radial scan. For details see Table I.8. The association of the measured peaks to this particular phase was further corroborated in the high energy X-ray measurements in air discussed in detail later in this chapter. In Ar, signal from the (002) reflex of $Cu_{0.64}Zn_{0.36}$ was observed in three different scans with fitted reciprocal d*-spacings of 3.27 1/Å, 3.24 1/Å and 3.25 1/Å, while the corresponding (1$\bar{1}$3) reflex was measured in one scan with a d*-spacing of 5.39 1/Å. Comparing these values to the literature lattice of the

$Cu_{0.64}Zn_{0.36}$ phase [73] yields an in-plane strain of the lattice of +4% after accounting for the thermal expansion of the phase, giving a reciprocal d*-spacing of 3.25 1/Å for the (002) reflex and 5.39 1/Å for the $(1\bar{1}3)$. The in-plane orientation of the reflexes associated with the $Cu_{0.64}Zn_{0.36}$ phase show that the phase either has in-plane randomly orientated domains, or at least two different in-plane orientations are present. As is discussed in more detail later in this chapter, the Cu-Zn alloy phase showed predominately (111)-oriented domains, but a weaker powder-like signal was observed as well. As shown in Figure 6.18, azimuthal in-plane scans were performed for ZnO (110) in both H_2 as well as Ar conditions. In H_2 a detector scan was performed at ω=-43.07° showing that the broad peaks are shoulders of Al_2O_3 (300) reflexes. In Ar gas however, a number of very small and sharp peaks appeared, and performing detector scans at the corresponding sample rotation positions revealed that these belong to ZnO (110), as seen in the bottom scan of Figure 6.17. Given the UHV preparation pathway for the ZnO on the Al_2O_3 substrates, the formation of (001) oriented ZnO domains was certainly expected for this sample [74], and the appearing of the (110) reflex as the strongest expected in-plane peak for c-oriented ZnO points towards the formation of such domains after exposing the sample to Ar. A total of 7 in-plane peaks were measured in the azimuthal scan, which can be associated to two distinct in-plane orientations of ZnO domains, each showing the characteristic angular 60° in-plane spacing as seen in Table I.9.

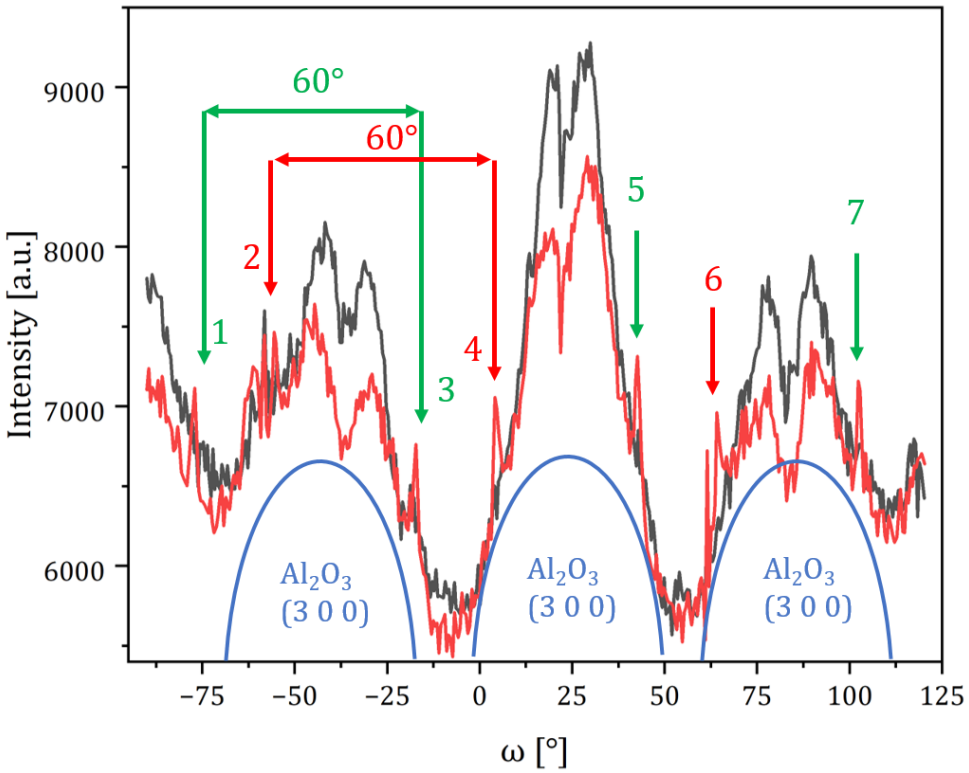

Figure 6.18. Azimuthal in-plane scans for ZnO (110) at 575 K in initial H_2 conditions (black) and in pure Ar (red). Very small additional reflexes were observed to emerge in Ar displaying two separate domains of (001) oriented ZnO. The corresponding peaks are numbered from 1 to 7, details for the peak position can be found in Table I.9.

Comparing the two domains to the in-plane directions of the Al_2O_3 (100) direction, the first ZnO domain corresponding to the peaks number 1,3,5 and 7, shows an angle of 9.77° to the Al_2O_3 (100) direction. The second ZnO domain corresponding to the peaks number 2,4 and 6 shows an in-plane angular distance of 11.9° to the Al_2O_3 (100), with an angle of 21.67° between the two ZnO domains.

6.3. Reversible reduction of Cu at 575 K

Further investigations of the simplified model system, 'Cu-Al_2O_3,' revealed that the oxidation of Cu and the reduction of Cu_2O at 575 K and 1 bar total pressure are not equally facile. After switching from pure CO to Ar, followed by Ar:CO_2(1:1), and allowing 35 minutes for stabilization after each gas change, the L-scans of the Cu reflexes showed only negligible changes. In contrast, clear changes were observed just 15 minutes after switching from the oxidizing reaction gases back to H_2. To further explore the oxidation and reduction processes, additional measurements were performed, focusing on the in-plane Cu signal, as shown in Figure 6.19. Both the Cu (002) and the Cu ($1\bar{1}1$) in-plane reflexes were measured in different gas atmospheres and showed the complete

reversibility of the oxidation. The strong Cu (002) and (1$\bar{1}$1) signals observed under H_2 gas flow decreased significantly during 45 minutes of Ar exposure and vanished completely after 60 minutes. The Cu (1$\bar{1}$1) scan measured under Ar flow also shows the emergence of a Cu_2O (002) reflex. Due to the small angle between the (002) and (1$\bar{1}$1) direction of 5.3°, the appearance of the Cu_2O (002) peak in the detector scan for Cu (1$\bar{1}$1) is not a clear sign of a different epitaxy of Cu_2O particles compared to the Cu particles however. Following another exposure to H_2 for 30 minutes, both in-plane peaks re-emerged, attaining at least 50% of their original intensity. This reduction step was followed by a 15-minute exposure to pure CO_2, but as the intensity of the reference peak did not stabilize under CO_2, the reaction gas was switched to Ar again for another 45 minutes and resulted in the complete oxidation of Cu, as evidenced by the disappearance of the in-plane peaks. Additionally, radial and azimuthal in-plane scans, as presented in Figure 6.11, confirm that the Cu particles retained their structural integrity during the oxidation and reduction processes, as seen by the consistent in-plane orientation observed under reducing conditions.

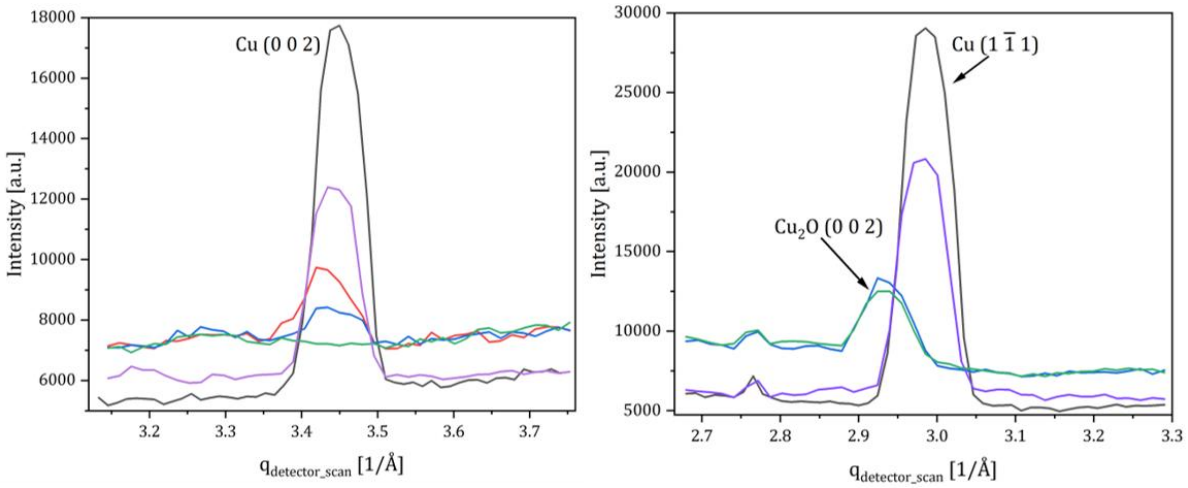

Figure 6.19. In-plane detector scans for the Cu (002) and Cu (1$\bar{1}$1) reflexes in different gas atmospheres all at 575 K and 1 bar total pressure in pure H_2 (black), in Ar after 45min (red), in Ar after 60min (blue), back in H_2 after 30 minutes (violet) and in Ar post CO_2 (green).

Comparing the L-scan of Figure 6.15 with the in-plane scans of Figure 6.19, a different reduction and oxidation behaviour is observed. While for the re-oxidation of the Cu the in-plane scans show a consistent decrease in peak intensity over time with a full disappearance of Cu peaks after 1 hour for both pure Ar as well as mixed exposure to pure CO_2 followed by Ar, only negligible changes are observed in the L-scans after switching from pure CO to Ar and afterwards Ar:CO_2 (1:1). The combined exposure time of the sample to either Ar or Ar:CO_2 was 70min without any change in the reflexes for the L-

scans. Exposure to pure H_2 yielded pronounced changes in the peaks after only 30 minutes for both measurements however. While the signal of the out-of-plane measurements of Figure 6.15 can be solely associated with Cu (111)-oriented particles, the in-plane Bragg peaks of Figure 6.19 belong to Cu (110)-oriented particles. The observed differences in oxidation and reduction behaviour may be attributed to the varying thermodynamic stability of the differently oriented Cu particles with respect to oxidation. While CO and H_2 differ in their effectiveness as reducing agents under the given conditions, the sample had already been exposed to both pure H_2 and H_2:Ar mixtures at 575 K before the introduction of pure CO. Thus, the differences in the reducing capabilities of the gases alone cannot account for the observed behaviour. Additionally, prior to the switch to pure CO, the sample underwent five cycles of switching between H_2 and Ar at 475 K to ensure surface cleaning. This makes it unlikely that surface contamination played a significant role in the variations observed between the out-of-plane and in-plane scans.

To investigate the reversibility of the reduction and oxidation of the Cu on the ZnO-supported model system "CZ-Al_2O_3", the sample was exposed to H_2 again after the observed oxidation under Ar flow. As can be seen in Figure 6.20 and the corresponding Table I.10, the signal corresponding to Cu_2O has disappeared and instead the reflexes from Cu are observed again. The radial scan along the Cu $(1\bar{1}1)$ in-plane direction includes the Cu $(1\bar{1}1)$, (002), $(2\bar{2}0)$ and $(1\bar{1}3)$ reflexes, still consistent with a powder-like orientation of the Cu domains in-plane. The intensity ratio between the reflexes in the radial scan remains inconsistent with literature values. For instance, the $(2\bar{2}0)$ reflex still exhibits higher intensity than the (002) reflex. However, the (002) reflex does show an increase in intensity compared to the initial measurement under H_2 conditions. Therefore, the intensity ratios of the Cu peaks are closer to those expected for a perfect powder compared to the measurements under the initial H_2 conditions, pointing to a more complete formation of Cu powder instead of preferentially oriented domains, through multiple oxidation and reduction cycles.

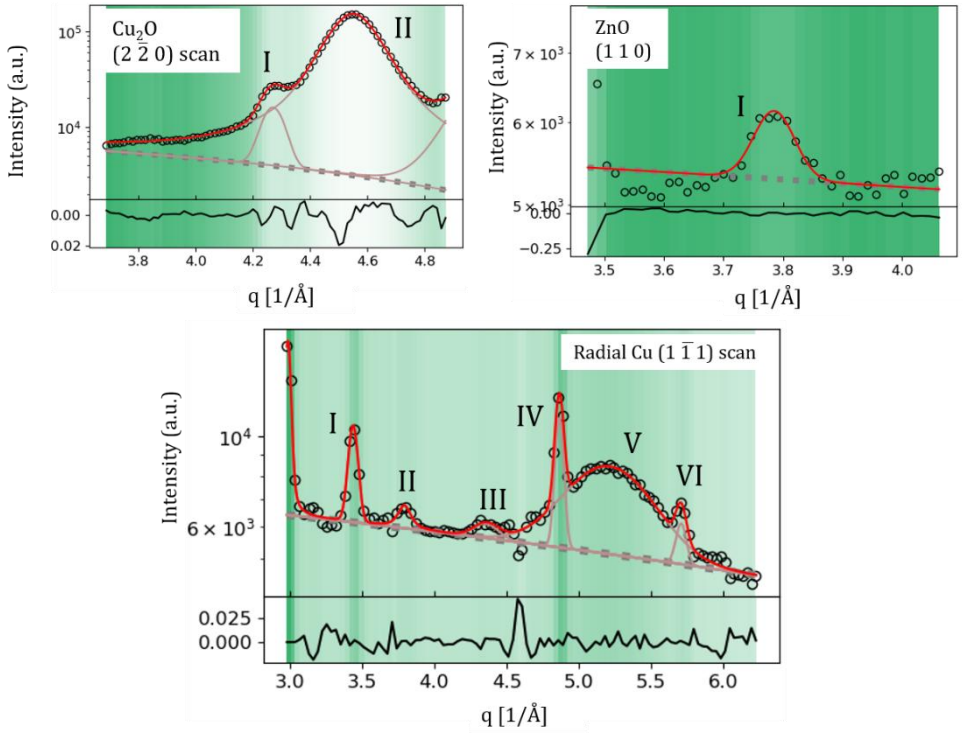

Figure 6.20. In-plane q-detector and radial scans (black dotted lines) and corresponding fits (red lines) for "CZ-Al_2O_3" taken in second H_2 conditions after oxidation in Ar at 575 K at 1 bar total pressure. Full fitting details can be found in Table I.10.

Furthermore, the radial scan shows additional peaks compared to the previous measurements belonging to the ZnO and US1 phase. For the latter structure the $(2\bar{2}0)$ and (440) reflex were already observed in the initial H_2 conditions and reappear under the H_2 gas flow following the Ar exposure. In these conditions, the radial scan along the Cu $(1\bar{1}1)$ direction also shows the (440) reflex again as well as an additional peak at q=4.36 1/Å. This additional peak is also observed in the Cu_2O $(2\bar{2}0)$ scan at q=4.27 1/Å. And is associated with the US1 (224) signal with detailed discussion in chapter 6.7. While the oxidation of the Cu was observed to be fully reversible at the given temperature and pressure, the ZnO reflex, first observed in the previous Ar condition, is still present after switching of the reaction gas back to H_2, and the peak even shows an increase in intensity of about 16%. Furthermore, the peak is now also observed in the radial scan along the Cu $(1\bar{1}1)$ direction.

To further investigate the reduction of Cu in different reaction gases, CO was introduced into the reaction gas feed, at a ratio of H_2:CO (3:1), without relevant changes observed compared to pure H_2 gas flow. Additional out-of-plane scans were performed using an orientation matrix for the Al_2O_3 substrate, with the out-of-plane L-scan starting from the

previously determined in-plane position of the Cu ($1\bar{1}1$) reflex shown in Figure 6.21 and corresponding fitting details in Table I.11.

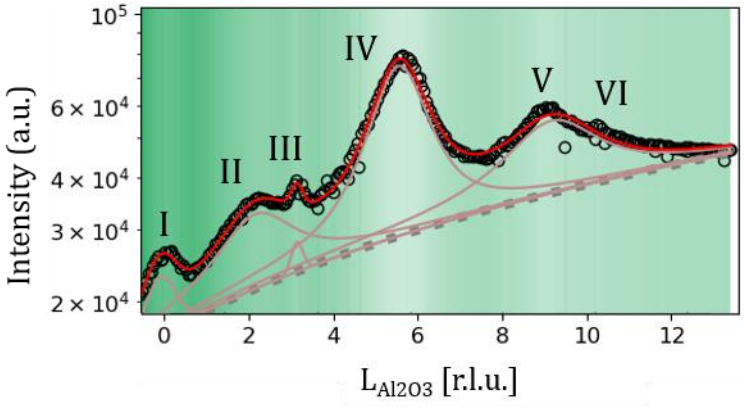

Figure 6.21. Out-of-plane L-scan starting from the in-plane Cu ($1\bar{1}1$) position (black dotted lines) and corresponding fits (red lines) taken in second H_2 conditions after oxidation in Ar at 575 K at 1 bar total pressure. Full fitting details can be found in Table I.11.

The scan shows a number of peaks associated with Cu and ZnO, as already observed in-plane. The in-plane signal can be associated with preferentially oriented particles, showing that the randomly oriented Cu domains observed in-plane belong to either textured domains or a weaker powder signal that is superimposing the signal from epitaxial Cu domains. Assuming an orientation of the Cu domains following Cu (110) || Al_2O_3 (001), an out-of-plane L-scan starting from the ($1\bar{1}1$) in-plane position is expected to only show the Cu (200) and Cu (113) reflex out-of-plane, just as observed in the scan, whereas for a perfect powder, the Cu (220) reflex would be expected between the (200) and (113) reflex as can be seen in Figure 6.22. The peaks would not be expected to be oriented at the exact same in-plane angle however, so a certain degree of out-of-plane tilt of the particles needs to be assumed. Additionally, if all the (110)-oriented Cu domains would have the same in-plane orientation, only either the Cu (111) and (113) reflexes or only the Cu (200) reflex would be expected to appear in one L-scan, as the in-plane angle between the corresponding domains corresponds to ($1\bar{1}1$) $\measuredangle$ (110) = 35.3°. This observation can be explained by either of two scenarios. First, while (110)-oriented Cu domains exist, two distinct in-plane orientations for these are observed 30° apart from another, e.g. Cu (111) || Al_2O_3 (110) and Cu (111) || Al_2O_3 (100). Second, while the Cu domains do show a clear preferential (110) out-of-plane orientation, they are in-plane preferentially randomly oriented, a so-called fibre-like texture. For such a case, the in-plane scans would show powder like signals, while only out-of-plane at least more of a preferential orientation is observed.

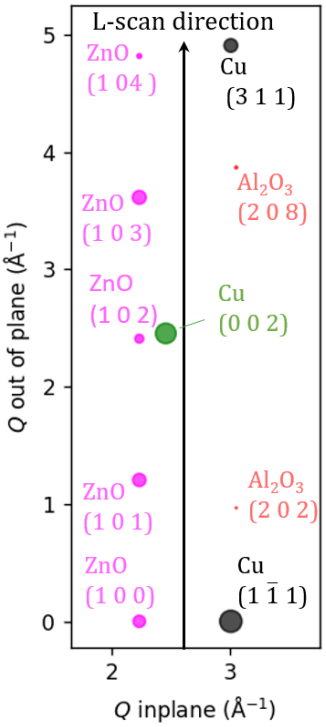

Figure 6.22. Reciprocal space map corresponding to the L-scans of Figure 6.21., showing the reflexes of the following planes (first direction is always out-of-plane, second is in-plane): Al_2O_3 (001)x(100) [red], ZnO (001)x(100) [magenta], Cu(110)x(1$\bar{1}$0) [green] and Cu(110)x(1$\bar{1}$1) [black]. Scan path of L-scan drawn in black. Reflexes are scaled according to their respective relative intensity.

Similarly, for the ZnO reflexes, a large number of additional reflexes would be expected in the out-of-plane scan in the case of a powder-like orientation and only a c-orientation ZnO matched the observed peaks. As was already discussed above, the reflexes for ZnO in Figure 6.18 showed at least two domains of distinct in-plane orientation for ZnO, which can now clearly both be associated to ZnO oriented with ZnO (001) || Al_2O_3 (001). This assumption is further underlined by the results of another out-of-plane scan performed starting from the in-plane position of the ZnO (110) reflex as seen in Figure 6.23 and the corresponding data set in Table I.12.

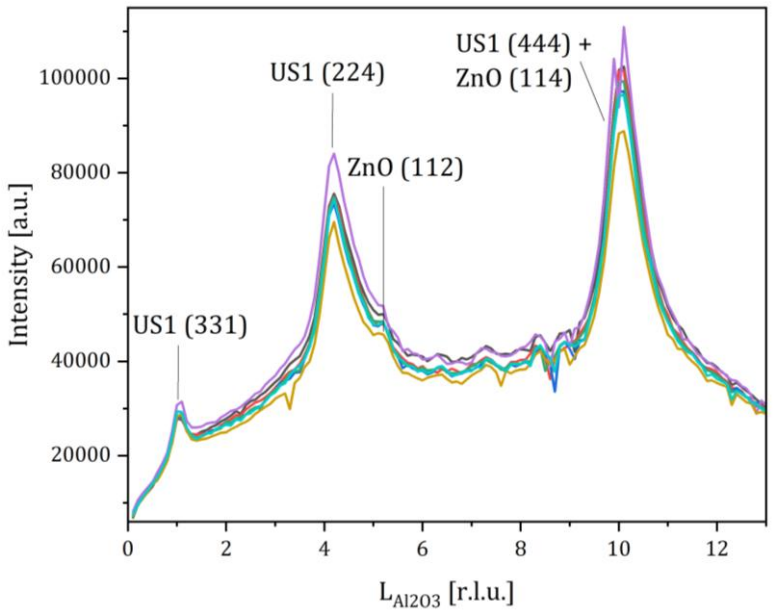

Figure 6.23. Out-of-plane L-scans started from the in-plane ZnO (110) position at 575 K at 1 bar total pressure in various different reaction gases. Full fitting details can be found in Table I.12.

As expected for an out-of-plane scan starting from the in-plane position of ZnO (110) for c-oriented ZnO, both the ZnO (112) as well as the (114) reflexes are observed in the scan. The most pronounced peaks in the scan however, fit only to the US1 structure with two separate orientations of US1 domains as discussed in detail in chapter 6.7. For the (110)-oriented US1 domains, the reflexes (224), (444) and (460) are observed as well, with the (444) reflex forming a superposition with the ZnO (114) peak. This L-scan was performed in all reaction gas mixtures containing various ratios of CO, CO_2 and H_2 but no relevant changes in the scan were observed as seen in Figure 6.23, showing the high stability of the US1 phase.

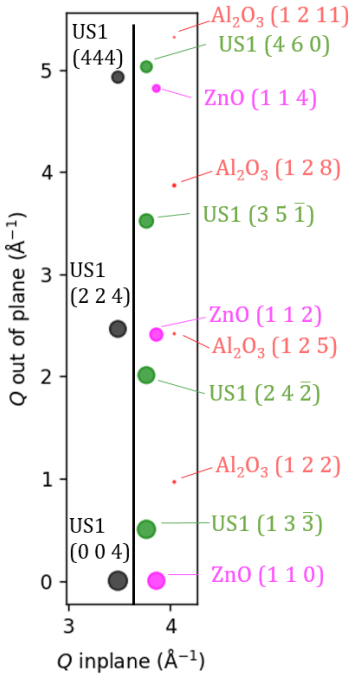

Figure 6.24. Reciprocal space map corresponding to the L-scans of Figure 6.23., showing the reflexes of the following planes (first direction is always out-of-plane, second is in-plane): Al_2O_3 (001)x(120) [red], ZnO (001)x(110) [magenta], US1(111)x(14-5) [green] and US1(110)x(001) [black]. Scan path of L-scan drawn in black. Reflexes are scaled according to their respective relative intensity.

6.4. Cu particle diameter of the simplified model system during reduction and oxidation

To determine the average diameter of the Cu particles deposited directly onto the Al_2O_3 substrate for the simplified model system "Cu-Al_2O_3", during the repeated exposure to oxidizing and reducing reaction gases, the average size of the corresponding crystal domain was extracted by determining the FWHM of the corresponding in-plane Bragg reflex. As can be seen in the data set in Table I.13, the results for the Cu particle diameter are consistent along the Cu $(1\bar{1}1)$ and Cu (002) directions, further underlining the assumption, that these two reflexes originate from the same Cu (110)-oriented particles. Averaging over all in-plane scans performed under H_2 gas flow at 575 K, the diameter of the Cu particles along the $(1\bar{1}1)$ direction yields 10.53 nm and 9.63 nm for the (002) direction. The ratio between the calculated particle diameter along the $(1\bar{1}1)$ and (002) directions shows a similar ratio as the inverse ratio of surface energies of the corresponding Cu facets [75]:

$$\frac{avarage\ diameter\ along\ (002)}{average\ diameter\ along\ (111)} = \frac{9.63\ nm}{10.53\ nm} = 0.91$$

$$\frac{Surface\ energy\ (111)}{Surface\ energy\ (002)} = \frac{1.34\ {}^{J}/_{m^2}}{1.47\ {}^{J}/_{m^2}} = 0.91$$

This is an indication, that the ratio of the diameters along the two investigated in-plane directions is similar to that expected for Cu particles with Wulff's shape, under the experimental conditions in pure H_2, but for a more exact analysis the impact of the substrate on the Cu particle shape would need to be considered in detail. The particle diameters were measured at different points in the experiment, namely during three separate exposures to pure H_2, while the sample was always exposed to at least one oxidizing gas in-between each of the H_2 exposures. The duration of the exposure to H_2 prior to the corresponding scan is also listed for each measurement. By comparing the particle diameters between these exposures, a trend is visible were the particle diameter along the $(1\bar{1}1)$ direction is slowly decreasing from 10.73 nm for the first H_2 exposure, to 10.49 nm in the second and 10.17 nm in the third. On the contrary, the evolution of the diameter in the (002) direction is inverse, moving from an average particle size of 9.47 nm during the first exposure to 10.1 nm in the second. This inverse evolution of the two directions could indicate a change in the nanoparticle shape throughout the oxidation and reduction cycles, from a disc-like morphology to a shape with more pronounced facets. Table I.14 lists the particle diameter determination for the Cu $(2\bar{2}0)$ as well as the Cu_2O (002) in-plane reflexes. As described earlier, the in-plane reflex of Cu $(2\bar{2}0)$ at the given sample rotation angle can be associated to Cu (111)-oriented particles. This reflex was measured in pure CO and pure H_2 atmosphere respectively, yielding an average particle diameter along the $(2\bar{2}0)$ direction of 8.67 nm, with an observed decrease from 9.12 nm in CO to 8.25 nm in H_2. Overall, the measured particle diameter for the (111)-oriented Cu particles is very comparable to the size of the Cu (110)-oriented particles, which implies, that the difference in the oxidation and reduction behaviour of the two different particle orientations cannot be linked to a difference in particle size. The measurements for the Cu_2O (002) in-plane reflex, were taken from the peak emerging in the range of the scan of the Cu $(1\bar{1}1)$ reflex as seen in Figure 6.19. Both measurements were performed in Ar, the first prior and the second after the sample was also exposed to CO_2. The average particle diameter of the Cu_2O in the (002) direction of 9.65 nm is similar to the estimated size of the corresponding Cu particles in H_2 along the same direction, measured to be 9.63 nm.

Analysis of the peak positions yields an average lattice parameter of 3.644 Å ± 0.004 Å averaged over a total of four Cu ($1\bar{1}1$) and four Cu (002) in-plane reflexes measured at three different occasions during the experiment always under pure H_2 conditions. These reflexes are associated with (110)-oriented Cu particles. The resulting lattice parameter is increased compared to the temperature adjusted lattice constant of Cu of 3.6378 Å by 0.179% likely due to the lattice mismatch with the sapphire substrate. The measured value is used as a reference for the lattice constant of fully metallic (110)-oriented Cu particle supported on Al_2O_3 at 575 K within this work.

6.5. Cu particle diameter and alloying as a function of partial H_2 pressure for the ZnO-supported model system (CZA)

Cu particle diameter in different reaction gases

Similar to the analysis of the Cu particle size and lattice changes for the simplified model system described in the previous section, the FWHM of the Cu reflexes was analysed for the ZnO-supported model system "CZ-Al_2O_3", to determine the diameter of the Cu nanoparticles. The results from the out-of-plane L-scans were not used due to a large amount of superposition of the peaks.

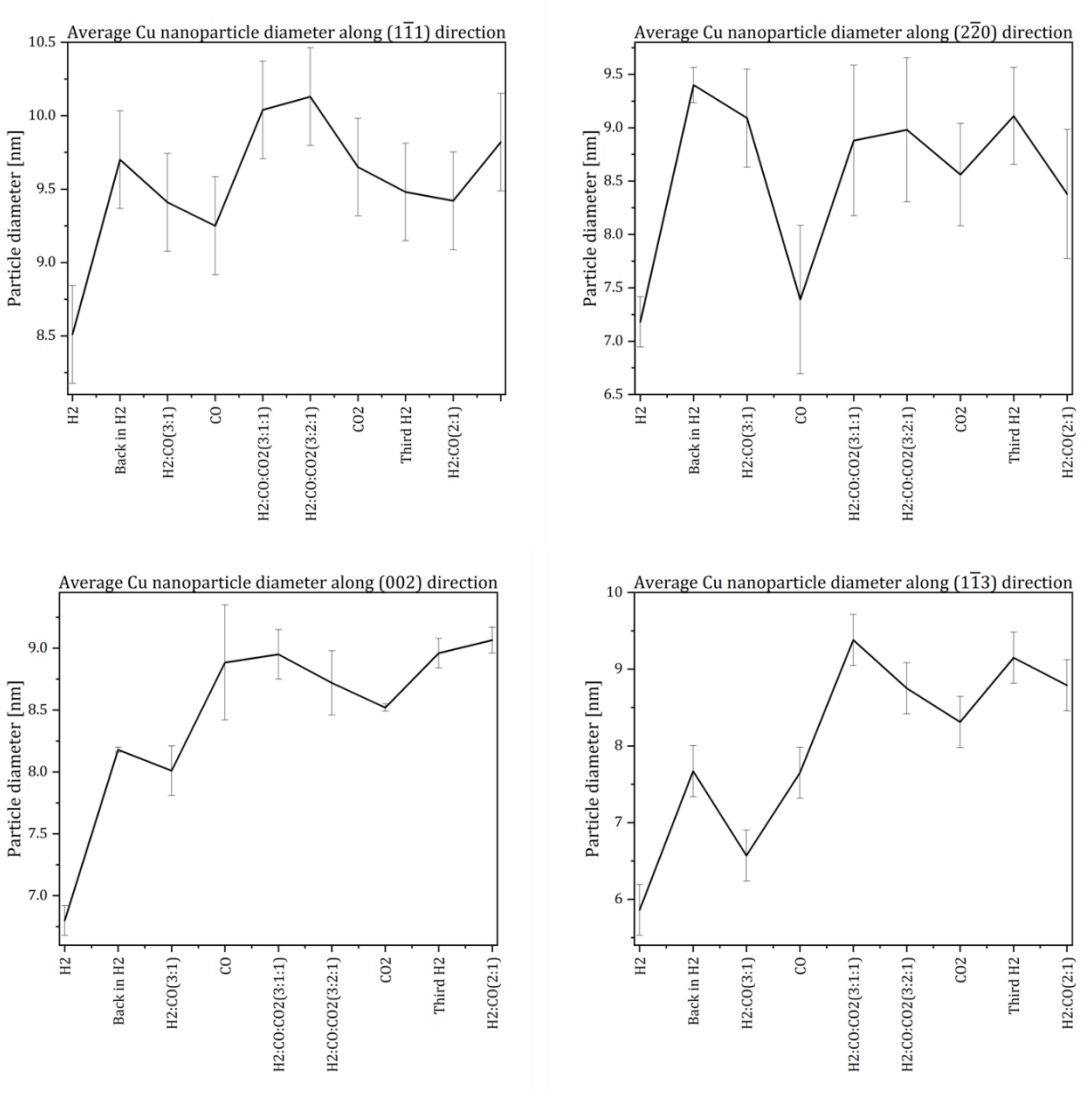

Figure 6.25. Cu nanoparticle diameter as calculated from the FWHM of the corresponding Bragg reflexes at 575 K as a function of the exposure to the different reaction gas mixtures. The averaged particles diameters are a result of averaging the given reflex from the detector scans with the same reflex measured in the radial scan for the (002) and (2$\bar{2}$0) reflexes, while for the other only one scan was measured. The error bars were therefore calculated using the mean deviation for the (002) and (2$\bar{2}$0) reflexes, while for the other reflexes the error bars were estimated to be equal to the average error of the (002) and (2$\bar{2}$0) reflexes.

As can be seen in Figure 6.25, the in-plane nanoparticle diameter was evaluated along the Cu (1$\bar{1}$1), (002), (2$\bar{2}$0) and (1$\bar{1}$3) direction respectively and yields slightly different results for each direction. Furthermore, the diameters increase dramatically from the first exposure to H_2 to the second, with the sample being exposed to Ar in between. The increase in particle diameter was measured to be 30.9% along the Cu (2$\bar{2}$0) and (1$\bar{1}$3) direction as well as 20.3% and 14.0% along (002) and (1$\bar{1}$1) respectively. Interestingly, the particle diameter is decreasing as the H_2 content of the reaction gas mixture decreases. Averaging the particle diameter over all measured directions as seen in Figure 6.26, more clearly reveals the overall evolution of the particles and shows that after the initial jump

between the first two exposures to pure H_2, the particles diameters always reach a local minimum when there is no H_2 in the reaction gas mixture, as is the case for exposure to pure CO and CO_2. Overall the Cu nanoparticle diameter for the ZnO-supported model system "CZ-Al_2O_3" is very comparable to the diameter of Cu nanoparticles measured on the simplified model system "Cu-Al_2O_3", with the averaged size between a minimum value of 7.09 nm in the initial H_2 condition and a maximum value of 9.31 nm in the H_2:CO:CO_2 (3:1:1) mixture.

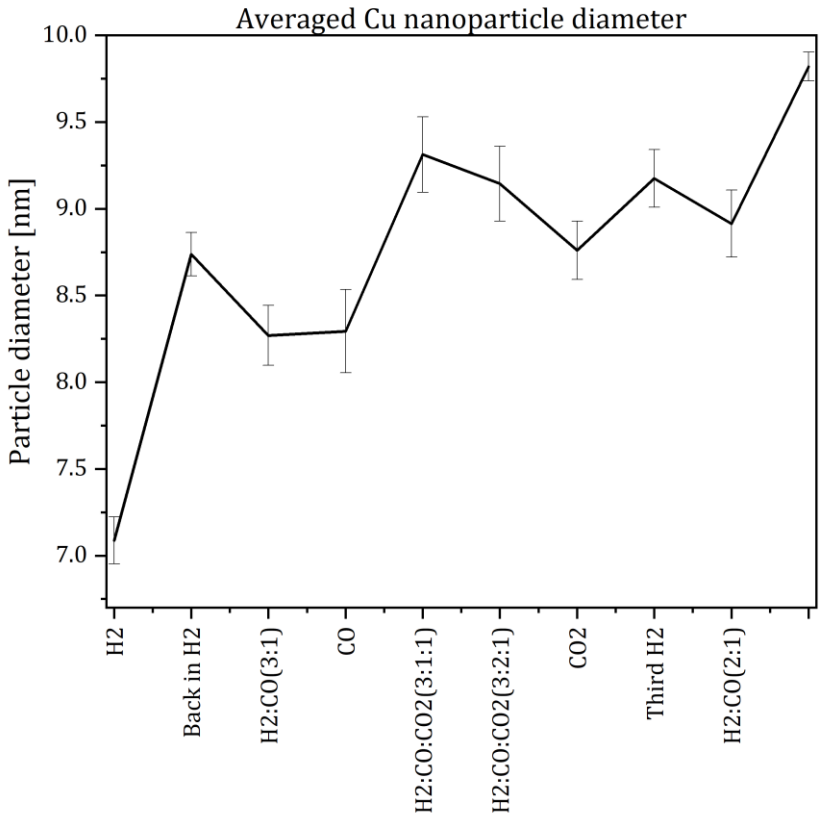

Figure 6.26. Cu nanoparticle diameter averaged over all measured Bragg reflexes as seen in Figure 6.25, at 575 K as a function of the exposure to the different reaction gas mixtures.

Zn incorporation into Cu particles

Throughout the experiment the sample was exposed to various different reaction gases including pure H_2, Ar, CO and CO_2 as well as different mixtures of H_2 with CO and H_2 with both CO and CO_2. For each reaction gas mixture, the same set of measurements was performed. Figure 6.27 shows the evolution of the reciprocal d^*-spacing measured for the different Cu reflexes both in- and out-of-plane as a function of the reaction gas mixtures. To investigate the small changes in the reciprocal d^*-spacing, the measured values used in this section were rounded to 4 decimal points, whereas for the more general analysis of the peaks in the previous sections, values were rounded to 2 decimal points. As can be seen, a clear dependency of the momentum transfer as a function of the H_2 content of the reaction gas is evident. For each of the measured Cu reflexes, the same general trend can be observed. Starting in the initial H_2 condition, a large reciprocal d^*-spacing is observed, after which the samples are exposed to Ar and a complete oxidation of the Cu to Cu_2O is observed. After switching the reaction gas then back to H_2 the observed lattice spacing of Cu was again very similar to the one measured in the initial H_2 condition. Introduction of CO into the reaction gas, first in a H_2:CO ratio of (3:1), causes a decrease in the reciprocal d^*-spacing, followed by an even stronger decrease after switching to pure CO. After the pure CO condition, the reaction gas mixture was changed to also include CO_2, starting with a mixture of H_2:CO:CO_2 (3:1:1), causing the reciprocal d^*-spacing to increase again. Raising the amount of CO in the mixture to (3:2:1) caused a slight decrease in the reciprocal d^*-spacing. Afterwards, the switch of the reaction gas to pure CO_2 caused a decrease in the reciprocal d^*-spacing similar to the decrease observed in pure CO. At this point the reaction gas was changed to pure H_2 for a third time, which caused a huge increase in the reciprocal d^*-spacing of the Cu reflexes, which reached the same values as in the previous H_2 conditions. Finally, CO was introduced again, in a mixture of H_2:CO (2:1) which caused a decrease in the reciprocal d^*-spacing similar to the beginning of the experiment.

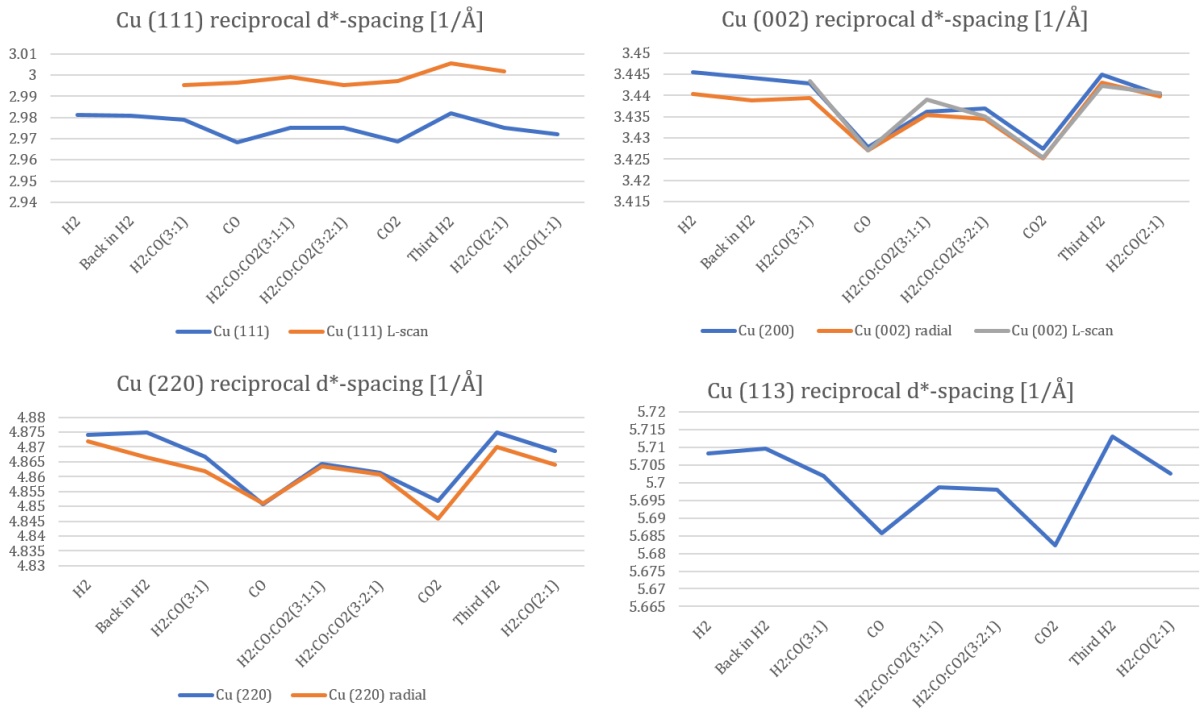

Figure 6.27. Reciprocal d*-spacing of all measured Cu reflexes in q-, radial- and L-scans in all reaction gas phases (excluding pure Ar) at 1 bar total pressure and at a sample temperature of 575 K.

The observed changes in the reciprocal d*-spacings of the Cu reflexes point to a direct dependency of the lattice parameter of the Cu on the H_2 amount in the reaction gas mixture. Surprisingly, the change of the lattice parameter of the Cu is similar regardless of whether the H_2 amount in the reaction gas is reduced by the introduction of CO or by CO_2. Furthermore, for each of the Cu reflexes the change in the reciprocal d*-spacing was averaged over all the performed scans, and then used to calculate the lattice spacing of the Cu in each reaction gas. These values were then compared to the expected Cu lattice parameter from literature adjusted for thermal expansion at 575 K, which yields $a_{Cu,\ 575\ K}$ = 3.6378 Å. The change in the lattice parameter in percent for each of the Cu reflexes is shown in Figure 6.28.

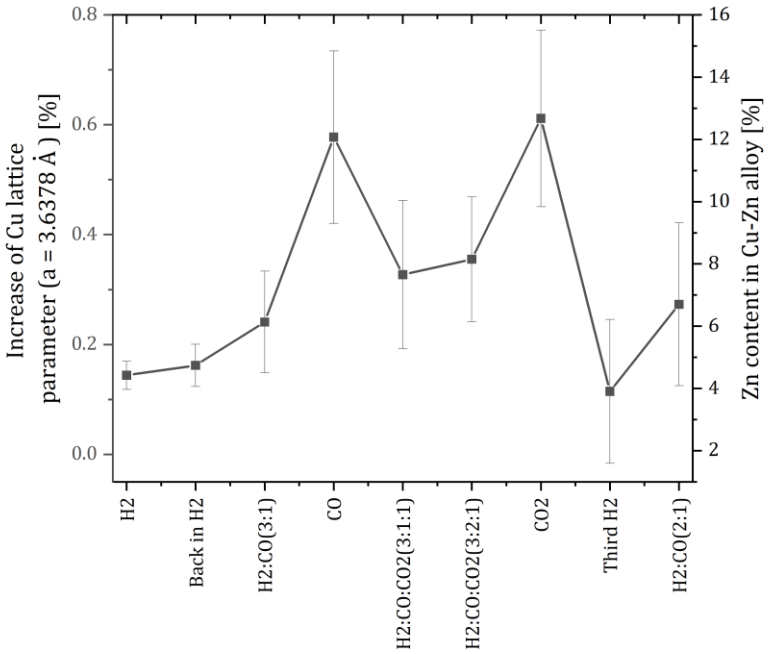

Figure 6.28. Average increase of the Cu lattice compared to the temperature corrected Cu lattice spacing at 575 K from literature (3.6378 Å) in percent as a function of the exposure to the different reaction gas mixtures. For each reflex, the data set was averaged over all measured scans (q-, radial- and L-scans), expect for the Cu (111), for which the results for the L-scan were excluded as the signal is assumed to be superimposed by another reflex. The error bars were calculated using the mean deviation of the measured data set. The right scale shows the Zn content of the phase based on the assumption, that the lattice increase is caused by incorporation of Zn into the Cu lattice.

The observed change in the lattice parameter is very consistent throughout the different measurements in the same experimental condition for all the different Cu reflexes. For this image, the data set of the Cu $(1\bar{1}1)$ L-scan was chosen to be excluded, as it seems to be superimposed by another peak, since the consistent trend in the measured lattice parameter of all other Cu reflexes was not observed for this reflex. The increase in the Cu lattice parameter is associated with Zn incorporation into the Cu constituting Cu-Zn alloy formation. The increase in the lattice parameter of Cu-Zn alloys up to a 38% Zn content can be estimated to be linear [76,77]. While the increase in the lattice parameter in the literature was calculated for room temperature measurements, the Zn content for the phase in this work is approximated using the Cu lattice constant at 575 K determined for the "Cu-Al_2O_3" sample of 3.644 Å as a first reference point. The second reference point is the lattice constant of the $Cu_{0.64}Zn_{0.36}$ phase adjusted for thermal expansion assuming a thermal expansion coefficient of 20.2×10^{-6} K^{-1} of 3.7192 Å. Linear approximation of the Zn content in the measured phase based on these two reference points was calculated and is shown in Figure 6.28.

The measurements performed on the sample in the reaction gas conditions of pure CO and pure CO_2 showed not only the strongest change in Cu lattices spacings as described in the previous section, but the emergence of additional peaks. These peaks appeared in the in-plane detector scans of Cu $(1\bar{1}1)$ and (002) as well as in the radial scan along the Cu $(1\bar{1}1)$ direction and can be associated with the Cu-Zn alloy phases of $Cu_{0.64}Zn_{0.36}$ as seen in Figure 6.29 and corresponding Table I.15. Determining the peak positions from the different scans yields reciprocal space vectors d* for the alloy phase of 2.83 1/Å for $(1\bar{1}1)$, 3.26 1/Å for (002) and 4.59 1/Å for $(2\bar{2}0)$, which match the phase well after accounting for thermal expansion and with the 4% in-plane lattice strain already observed earlier. The in-plane direction of the measured reflexes shows that the domains of the Cu-Zn alloy phase are in-plane randomly oriented, since all reflexes are observed very close to the same in-plane direction. The higher intensity of the $Cu_{0.64}Zn_{0.36}$ $(2\bar{2}0)$ reflex compared to the (002) reflex in the same radial scan however, could point the presence of additional domains with a preferential orientation following $Cu_{0.64}Zn_{0.36}$ || Al_2O_3 (001). This assumption is further corroborated with the high energy X-ray measurements performed in air after the exposure to various oxidizing and reducing gases, were predominately (111)-oriented $Cu_{0.64}Zn_{0.36}$ particles were observed, as discussed in detail in section 6.6. These peaks can be first seen in the Ar reaction conditions and afterwards are observed under pure CO and CO2 gas flow, clearly pointing to a connection of the emergence of the $Cu_{0.64}Zn_{0.36}$ alloy phase with the presence of an oxygen source in the reaction gas. Since it seems counterintuitive, that the $Cu_{0.64}Zn_{0.36}$ alloy phase would form under the most oxidizing reaction conditions, the presence and interplay of another Cu-Zn alloy phase was investigated as described in the following section.

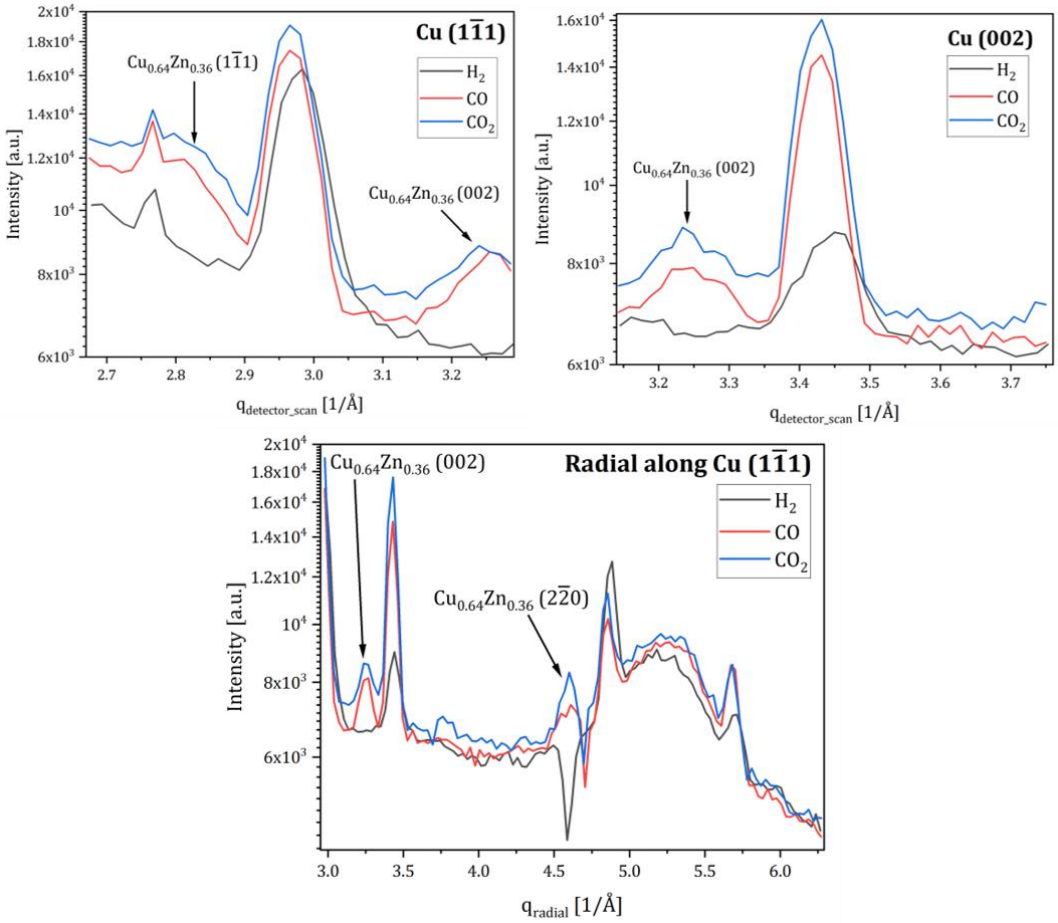

Figure 6.29. In-plane q and radial scans at 575 K at 1 bar total pressure in initial H_2 (black), pure CO (red) and pure CO_2 (green). Full fitting details can be found in Table I.15.

Indications for the presence of a $Cu_{0.2}Zn_{0.8}$ alloy phase

Given the preparation of the "CZ-Al_2O_3" as well as the additional XRD analysis, the presence of Zn on this sample is unambiguous. However, the data set shows only very weak signals for Zn-containing phases, specifically weak ZnO after exposure to Ar as well as $Cu_{0.64}Zn_{0.36}$ in Ar, CO and CO_2, as discussed in the previous section. While factors such as crystallite size, preferred orientation, or the distribution of Zn within the sample have a strong influence on the intensity of a measured reflex, these factors alone cannot fully account for the discrepancy between the observed data and the expected amount of Zn on the sample. Given the analysis of the Auger measurements performed in UHV conditions, as well as comparison to other experiments [78], it is expected that c-oriented Zn formed on Al_2O_3 and that after the oxidation of the Zn, a thin overlayer of ZnO formed on top of the Zn in a core-shell type system. Since no signal for metallic Zn was found and the weak ZnO signal is not sufficient to account for the expected amount of Zn on the sample, it is assumed that during the Cu deposition on ZnO/Zn in UHV, Cu already diffused into the Zn layer forming a Cu-Zn alloy. This alloy is further assumed to share the same hexagonal

crystal structure as that of Zn. With these assumptions, the $Cu_{0.2}Zn_{0.8}$ phase is a very likely candidate to account for the Zn on this sample, despite not being measured directly, as becomes evident when comparing the simulated reciprocal space maps of this phase with the Al_2O_3 substrate phase as seen in Figure 6.30. The figure shows that the reflexes of the $Cu_{0.2}Zn_{0.8}$ phase largely overlap with Al_2O_3 reflexes and were therefore not detected.

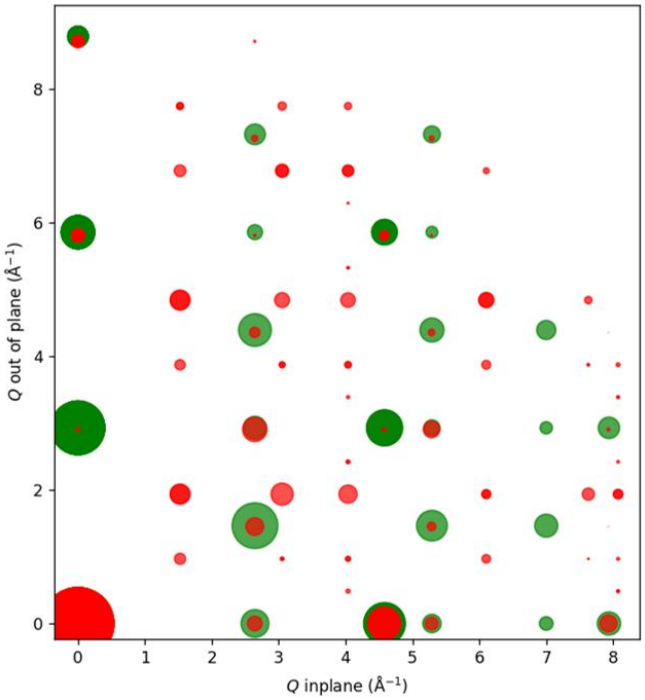

Figure 6.30. Simulated reciprocal space map showing all reflexes for $Cu_{0.2}Zn_{0.8}$ (green) as well as Al_2O_3 (red) in the q-range relevant for the performed experiments. Reflexes are scaled according to their respective relative intensity.

Nevertheless, a closer investigation of the measured Al_2O_3 reflex as seen in Figure 6.31, does indicate some changes during the exposure to different gas atmospheres. As can be seen, clear changes in the FWHM during the experiment are observed, first seen in the clear decrease in FWHM after the switch from the oxidizing Ar gas flow back to a pure H_2 reaction gas. Afterwards, the FWHM seems to stay relatively constant with a noticeably drop in pure CO_2. Assuming that the peak shape is a result of a superposition of a sharp Al_2O_3 substrate peak with a broad $Cu_{0.2}Zn_{0.8}$ nanoparticle peak, a decrease in the FWHM is associated with a decrease in the $Cu_{0.2}Zn_{0.8}$ peak. These results support the assumption that a large part of the deposited Zn on the sample formed the $Cu_{0.2}Zn_{0.8}$ during the sample preparation and or activation of the catalysts, while the phase remains stable throughout the exposure to various oxidizing and reducing reaction gases afterwards. The decrease in FWHM post Ar could indicate however, that Zn diffusion from this phase caused the formation of ZnO as well Zn incorporation into the Cu particles in the oxidizing

atmosphere. Therefore, it stands to reason that the ZnO formed on or at least close to the $Cu_{0.2}Zn_{0.8}$ domains, causing some of these domains to lose some of the incorporated Zn and in turn form the more Cu rich $Cu_{0.64}Zn_{0.36}$ phase.

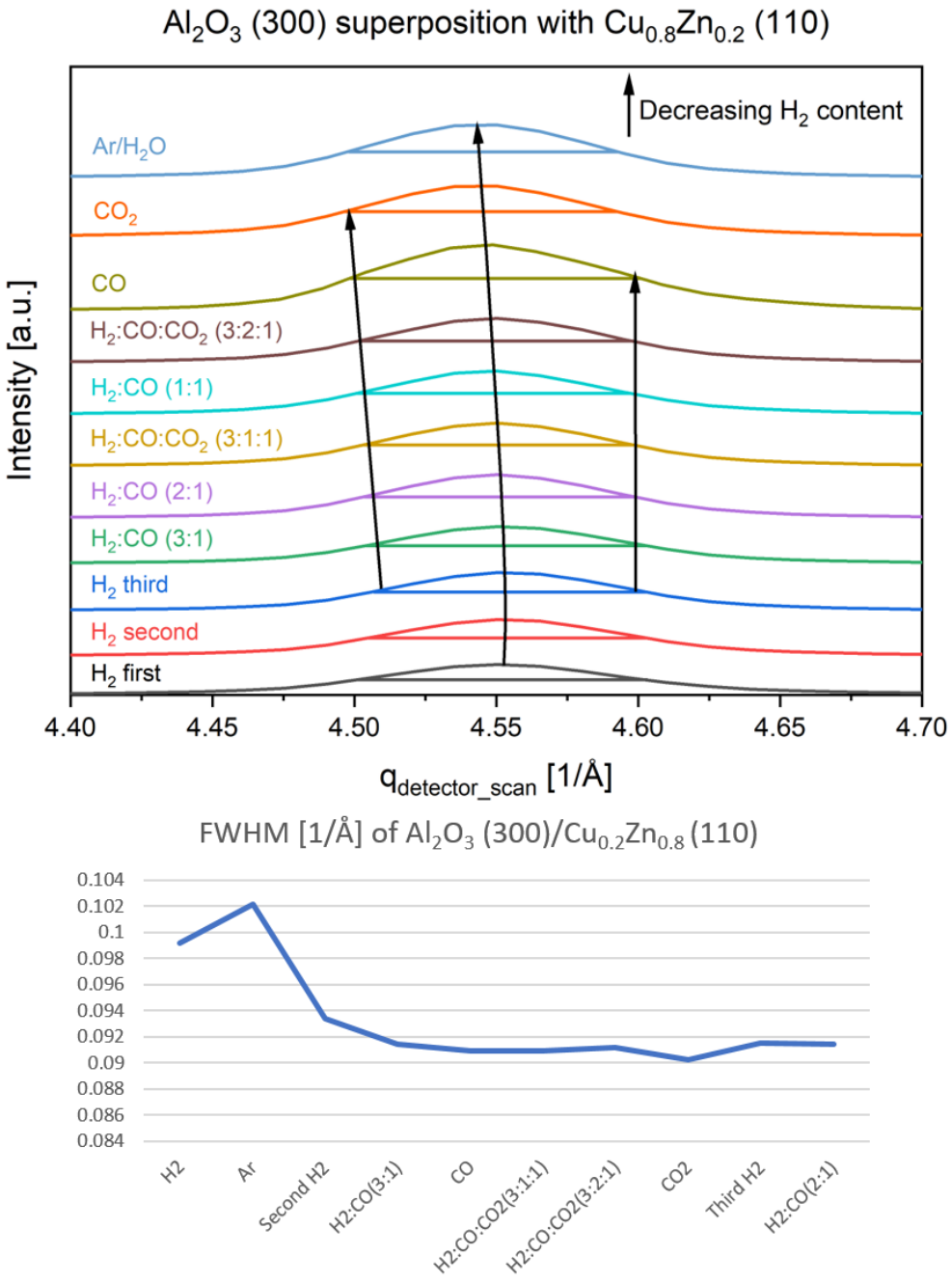

Figure 6.31. Top: In-plane detector scans for Al_2O_3 (300)/ $Cu_{0.2}Zn_{0.8}$ (110) in all measured reaction gases showing the clear change in FWHM of the peak. Bottom: Evolution of the fitted FWHM of the reflex in the different reaction gases.

6.6. Structural analysis in air post reaction conditions

Both model systems, "Cu-Al_2O_3" and "CZ-Al_2O_3", were further investigated in air and at room temperature after the exposure to various reaction gas mixtures a near ambient pressure and 575 K, utilizing high energy X-rays at the P07 beamline at DESY. The setup of the P07 beamline with a 2D detector allows for very fast measurements of large parts of reciprocal space. While each data set consists of a large number of detector images taken over a certain angular range of sample rotation, the images shown here are so called maximum pixel images. For such an image, for each pixel of the detector the measured intensity of that pixel is compared over the whole data set and only the maximum intensity is shown, regardless of the sample rotation position the maximum intensity was measured at. These maximum pixel images are useful to illustrate the presence of crystalline phases on the sample, while all the actual data analysis was done by a thorough integration separately for each reflex. For this integration, first a region of interest (ROI) was set around the peak as well as for a nearby region on the detector without any peaks used as a reference for the background signal. The intensity of the signal ROI was then plotted over the sample rotation angle and the corresponding peak positions were fitted. Using the fits of the peak over the sample rotation angle, the intensity of the signal and background ROI was integrated over all images that were determined to be inside of the FWHM of the analysed peak. The integrated intensity was then normalized with respect to the size of the ROI and the background intensity. Finally, in order to extract the structure factors from the measured intensity of the reflexes, the data sets were corrected for the stationary geometry of the sample and detector position using the Lorentz correction, while the polarization correction for the horizontally polarized X-ray beam of the synchrotron was found to be negligible. Additionally, the exact peak position inside the signal ROI was determined by fitting the intensity along the horizontal (q_{xy}) and vertical (q_z) direction. The data analysis including the reciprocal space transition, azimuthal integration and calibration of the sample position was done with custom python scripts utilizing the python packages *PyFAI* and corresponding *PyGix* [79], *FabIO* [80] and *xrayutilities* [70].

Structure of the highly ordered $Cu_{0.64}Zn_{0.36}$ structure in air

As mentioned in the previous sections, during the in-situ XRD measurements at ambient pressure, as discussed in the previous section, a number of reflexes were measured that can be associated with the Cu-Zn alloy phase of $Cu_{0.64}Zn_{0.36}$. In the additional measurements in air conducted using high energy X-rays and a 2D detector setup, the $Cu_{0.64}Zn_{0.36}$ phase can be clearly observed as seen in Figure 6.32.

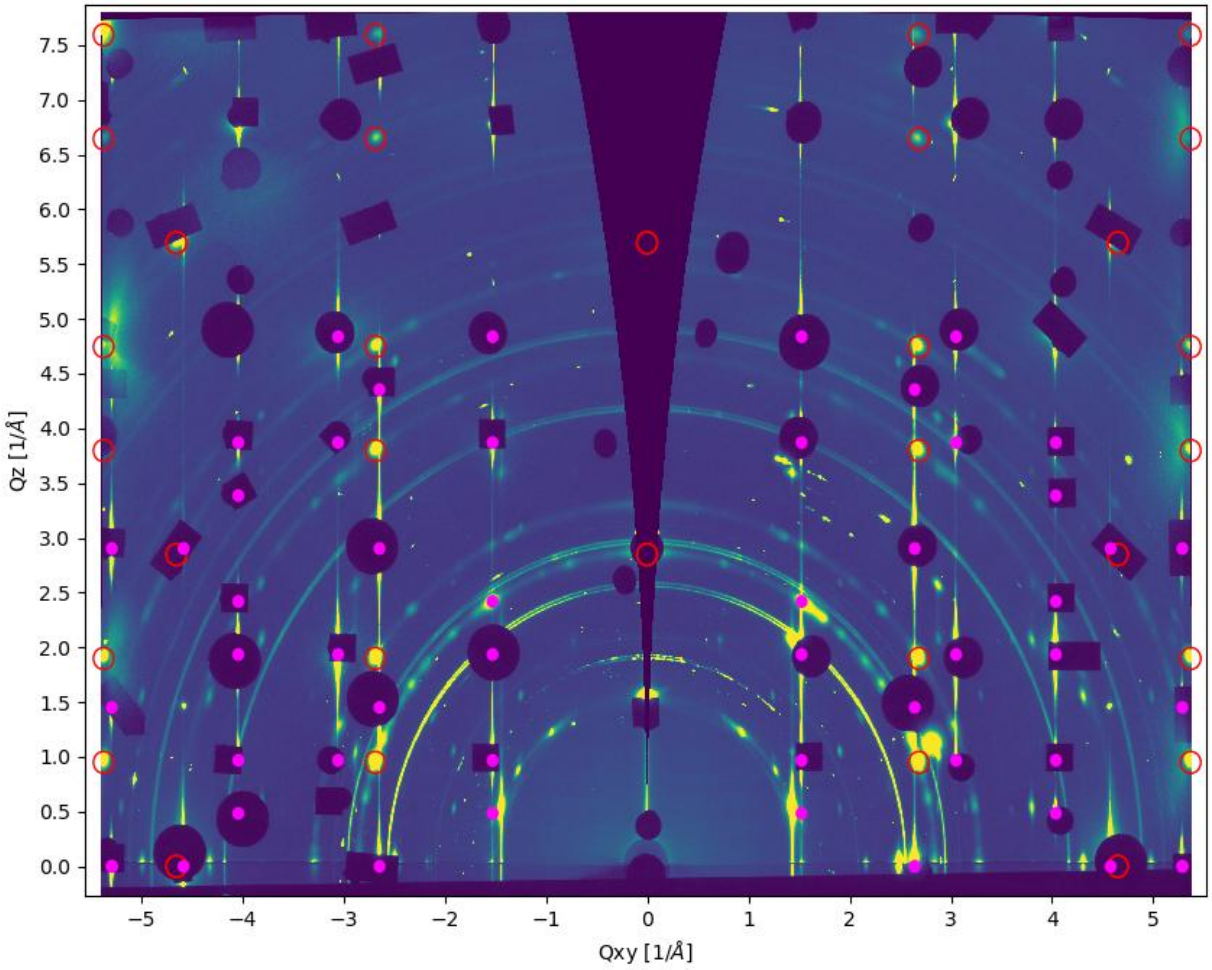

Figure 6.32. Maximum pixel image of the 2D detector data of "CZ-Al_2O_3" measured at room temperature in air over a 90° sample rotation. The red circles indicate the position of the reflexes corresponding to the $Cu_{0.64}Zn_{0.36}$ structure. Magenta dots show the position of the Al_2O_3 substrate reflexes, most of which are covered by beamstops.

Detailed analysis of each of the measured peaks was carried out following the procedure described above, resulting in the data set found in Table I.19. The reflexes can be associated with an FCC type lattice structure, with a lattice parameter of 3.822 Å ± 0.169 Å. However, a slight deviation from the ideal cubic structure was observed, as evidenced by a discrepancy between the measured reflection positions along the q_z and q_{xy}

directions compared to the expected positions based on the calculated lattice parameter, with the calculated lattice parameter showing the smallest overall deviation as shown in Figure 6.33.

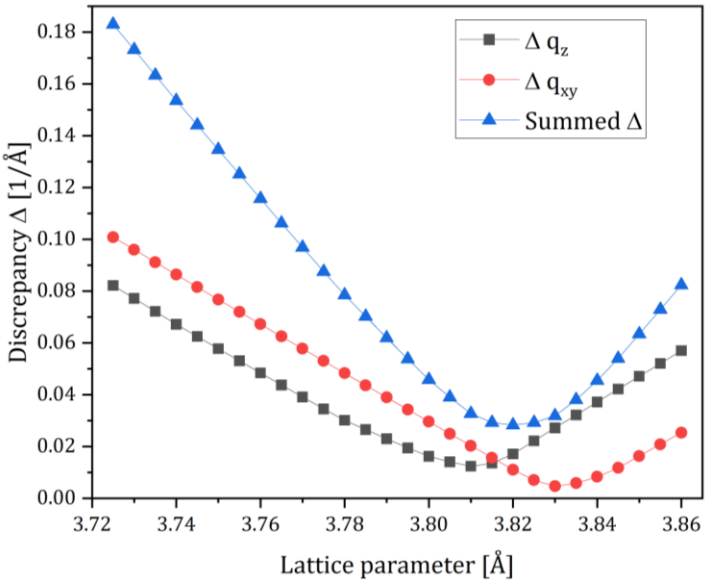

Figure 6.33. Calculated discrepancy between the calculated and measured reflex positions in q_z and q_{xy} direction as well as the sum of both as a function of the lattice parameter.

This lattice parameter yields average discrepancy along q_z of -1% and 0.27% along q_{xy}, where a negative value denotes a more compressed measured lattice compared to the calculated values. Given the assumed epitaxial relationship of the phase with respect to the support, a certain discrepancy between the reflex position along the in-plane and the out-of-plane direction can be explained by a certain strain in the phase. Comparison of the measured reflexes with the literature for the $Cu_{0.64}Zn_{0.36}$ structure shows that the measured phase has an increased lattice parameter, increased by 3.36% compared to the literature value, in good agreement with the measured increased lattice parameter of the phase in-situ under reaction gas flow at ambient pressure at 575 K as described in the previous sections. The change in the lattice parameter can be explained by a reduction of the lattice mismatch between the $Cu_{0.64}Zn_{0.36}$ phase and the Al_2O_3 substrate. To calculate the lattice mismatch for the (111)-oriented phase on the (001) oriented substrate, the lattice spacing of the Cu-Zn alloy phases along the in-plane direction is calculated using:

$$a_{in-plane} = \frac{\sqrt{3}\, a_{FCC}}{\sqrt{2}} \tag{31}$$

The resulting value can then be compared to the in-plane spacing of the Al_2O_3 substrate of 4.754 Å. The results can be found in the Table 6.1:

Phase	Lattice parameter [Å]	In-plane lattice parameter [Å]	Lattice mismatch [%]
Unstrained $Cu_{0.64}Zn_{0.36}$	3.6982	4.529	4.744
Strained $Cu_{0.64}Zn_{0.36}$	3.8223	4.681	1.536

Table 6.1. In-plane lattice mismatch between strained (as measured) and unstrained (111)-oriented $Cu_{0.64}Zn_{0.36}$ and the (001) oriented Al_2O_3 substrate.

As can be seen, the strain of the structure results in a considerable decrease in the lattice mismatch between the Cu-Zn alloy and the substrate. Additionally, the structure factor of the measured phase was calculated from the measured reflex intensities, which were both Lorentz- and Polarization-corrected. All of the determined structure factors are listed in Table I.19. For each reflex, multiple peaks, usually with different intensities, were measured at different angles of the sample rotation. Comparison of the resulting structure factors to the literature phase [73] showed that taking only the maximum measured intensity for each reflex for the determination of the structure factor, yielded a better match than averaging over all measured intensities. Therefore, Table I.19 also includes a list of only the maximum measured structure factors for each reflex denoted as "|F| max". Furthermore, the (111) reflex is located very close to an Al_2O_3 CTR and a strong discrepancy between the measured and reference structure factors of the phase lead to the assumption, that the measured intensity associated with the (111) reflex is affected by a superposition with signal of the substrate. Therefore, Table I.19 also includes a comparison of the structure factors without the (111) reflex. The true error in the structure factor is difficult to determine, therefore the measured background signal close to each reflex was used as a measure for the error instead. Figure 6.34 shows a comparison of the measured structure factors for both the case including as well as excluding the (111) reflex. Averaging over the discrepancy between the measured and literature values for each reflex yields an r-factor of 1.087 between the literature structure factors and the measured ones, while this discrepancy is reduced to an r-factor of just 0.114 if the (111) reflex is excluded. It is important to point out, that the investigation method used here is not ideally suited for a detailed determination of the structure factors of a crystalline phase on the sample. The literature values were measured using a powder sample and averaging over a much larger number of reflexes, using the Rietfield refinement method to yield the structures factors, while the total number of analysed reflexes for the structure in this work was just 58 peaks in total belonging to just 8 truly

different lattice reflexes. Therefore, a certain discrepancy between the measured structure factors and the literature is not unexpected. Additionally, the structure factors are of course affected by strain in the crystal phase, as the strain causes a slight change in the position of the atoms in the unit cell.

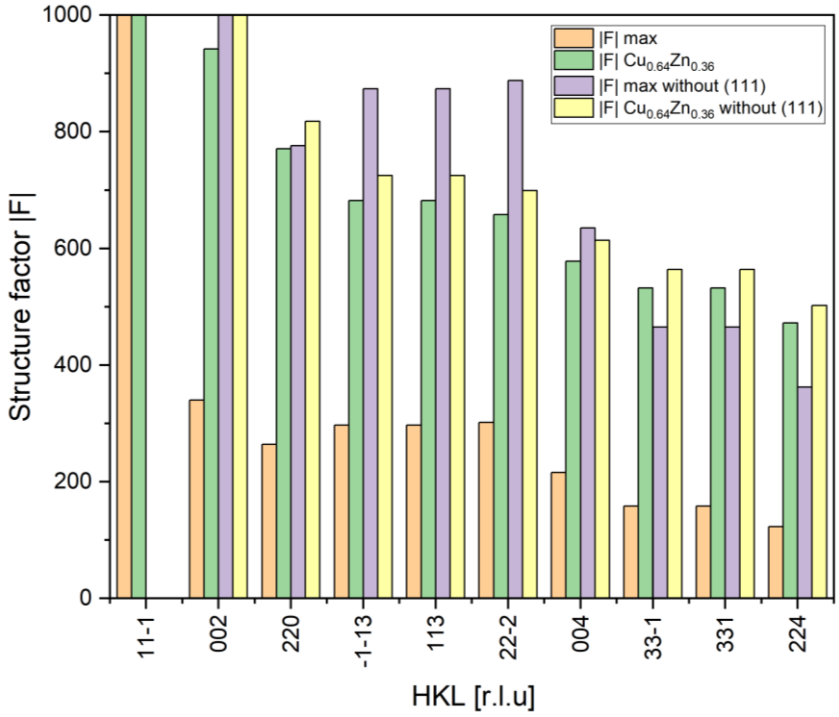

Figure 6.34. Comparison of the measured structure factor of the $Cu_{0.64}Zn_{0.36}$ phase compared to the literature phase. "|F| max" denotes the measured structure factor for which the most intense peak was selected from all the peaks measured at different sample rotation positions for a given reflex. The columns including "without (111)" refer to data for which the (111) reflex was taken out of the consideration due to the assumption of a possible superposition of the (111) reflex with an Al_2O_3 CTR signal.

Native Cu oxidation, tilted Cu-Zn alloy particles and ZnO in air on the ZnO-supported model system

In order to analyse the presence of powder-like signal on the ZnO-supported model system "CZ-Al_2O_3", an azimuthal integration was performed for all collected 2D detector images, resulting in a conventional powder diffraction pattern. The azimuthal integration was performed over the whole 180° angular range along the azimuthal direction of the images and the data for all images was summed and normalized. As can be seen in Figure 6.35, almost all of the peaks of the azimuthal integration can be associated with either Cu_2O or the previously discussed $Cu_{0.64}Zn_{0.36}$ phase. For the Cu_2O phase, no signal was detected that could be associated with any kind of crystalline order in- or out-of-plane, clearly showing that this copper oxide phase can be regarded as a perfect powder. As

during the in-situ experiment, only a very small fraction of the Cu on the sample was oxidized, the presence of the Cu_2O phase is a result of the native oxidation of the Cu following the exposure to air. The sample was exposed to air for a total of 17 days after the ambient pressure in-situ measurements, before the measurement at ambient pressure using high energy X-rays and a 2D detector setup were performed. Evidently, the oxidation of the Cu to Cu_2O also caused a disintegration of any crystalline structure of the Cu, which were previously observed during the in-situ measurements. For the $Cu_{0.64}Zn_{0.36}$ phase on the other hand, both crystalline and powder-like signal can be clearly observed. Figure 6.36 shows the results of plotting the measured intensity along the azimuthal angle following the Debye-Scherrer ring at the scattering vector corresponding to the four first reflexes of the $Cu_{0.64}Zn_{0.36}$ structure. The azimuthal scans were performed on each scan image and subsequently summed using a width of the integrated rings of ± 0.3 1/Å. While no clear correlation between peaks in the individual scans can be seen, three distinct azimuthal angles are more pronounced and could possible indicate a preferential out-of-plane tilt angle of the particles. These angles are 20°, 35° and 55° off the sample horizon.

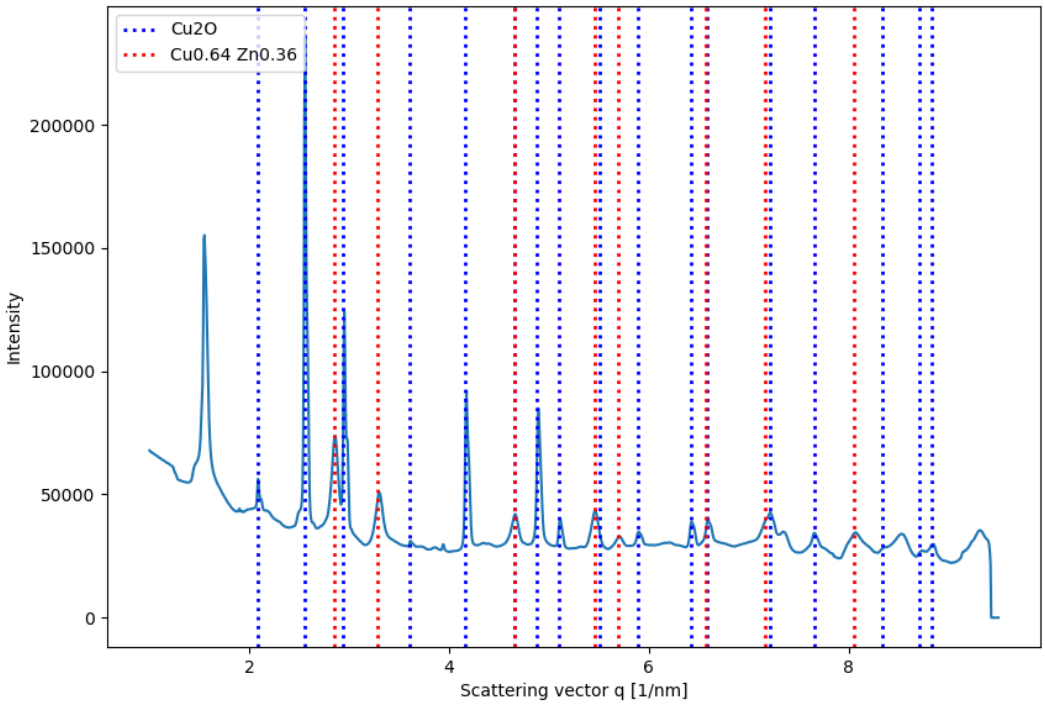

Figure 6.35. Results for the azimuthal integration of the 2D detector images measured of the ZnO-supported model system "CZ-Al_2O_3" as seen in Figure 6.37. The dotted vertical lines represent the expected scattering vectors for Cu_2O (blue) and $Cu_{0.64}Zn_{0.36}$ (red). While the scattering vectors for Cu_2O correspond to the literature lattice of Cu_2O at room temperature [81], the values of $Cu_{0.64}Zn_{0.36}$ correspond to the phase with an increased lattice parameter as described in detail in the previous section.

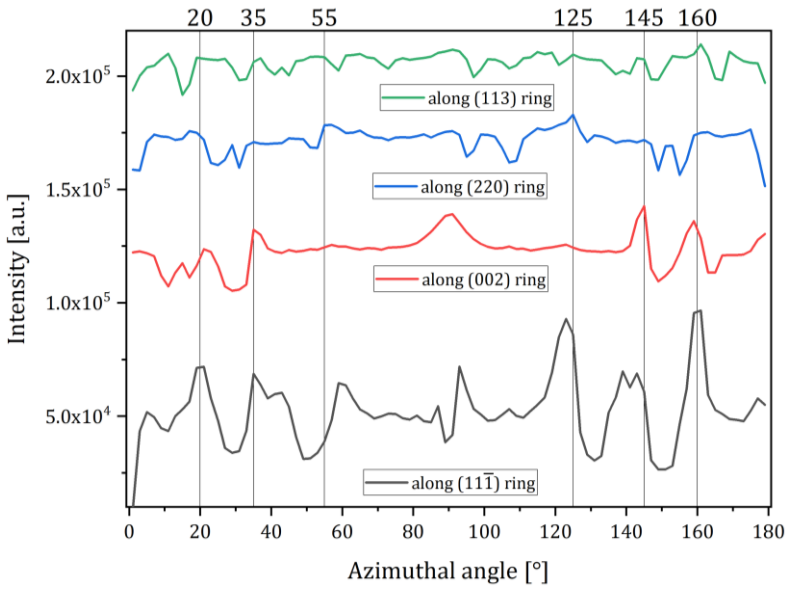

Figure 6.36. Scans along the azimuthal angle of "CZ-Al_2O_3" performed at a scattering vector corresponding to the $Cu_{0.64}Zn_{0.36}$ reflexes of (111) (black), (002) (red), (220) (blue) and (113) (green). For each scan, the integrated width of the corresponding ring was set to be ± 0.3 1/Å of the fitted scattering vector for the given reflex. Vertical lines indicate azimuthal angles at which a certain preferential orientation of out-of-plane tilted particles could be observed.

Since weak signals from (001) oriented ZnO particles were observed during the in-situ XRD experiment at ambient pressure, the data set from the high energy XRD measurements were also carefully analysed to see if any ZnO reflexes are visible. As can be seen in Figure 6.37, only signal from the (101) reflex of (001) oriented ZnO domains could be observed in the data. The corresponding in-plane reflex (100) is superimposed with a reflex of the unknown cubic structure US1 denoted as "1c" as discussed in detail in the next section, while all other reflexes of the ZnO are not visible, which can be explained by the overall low intensity of the phase. Accounting for the Lorentz-correction, the next highest intensity reflex of the phase would be the (110) reflex, which is already expected to have an intensity of only about ¼ of the observed (101) reflex. All other reflexes are of even lower intensity.

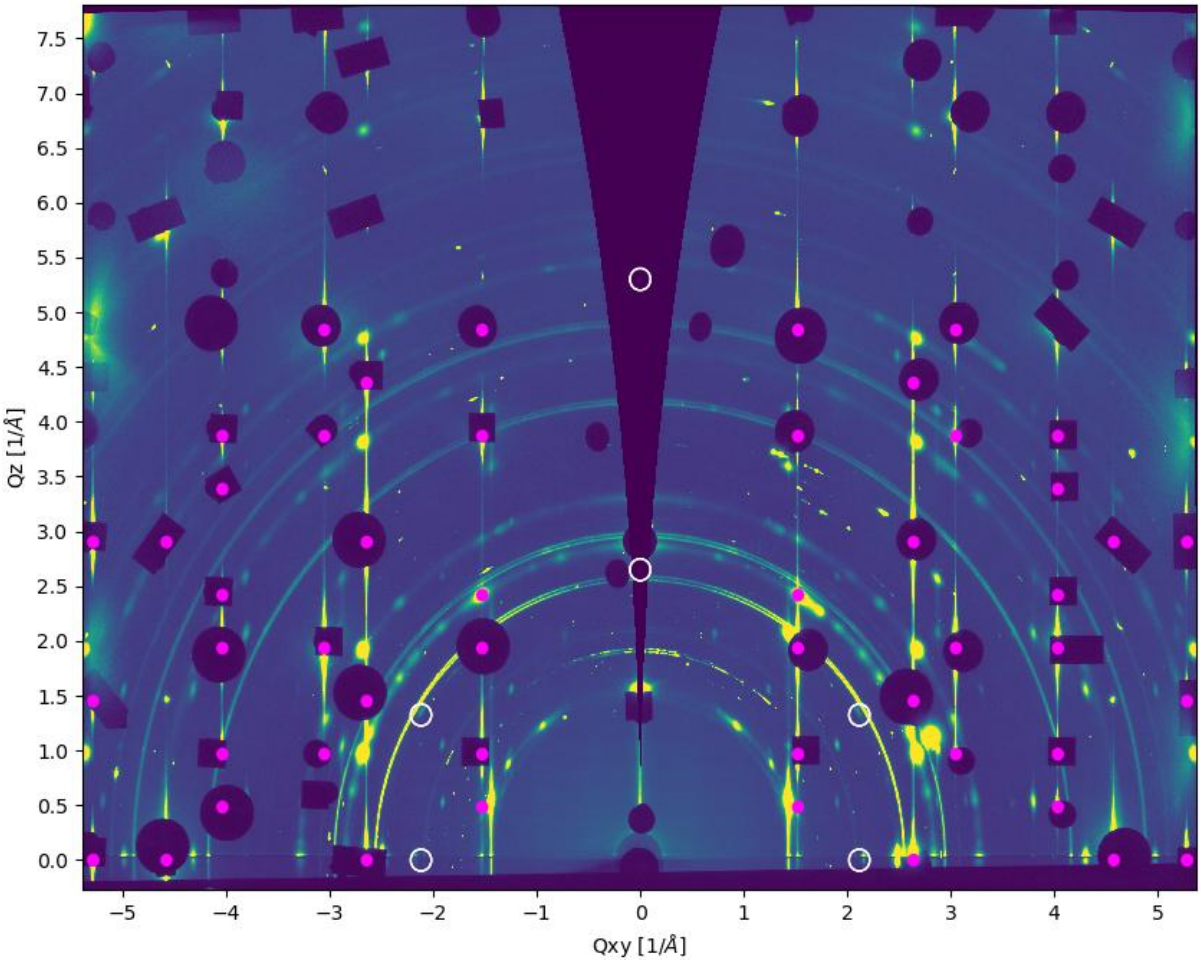

Figure 6.37. Maximum pixel image of the 2D detector data of "CZ-Al_2O_3" measured at room temperature in air over a 90° sample rotation. The white circles indicate the position of the first order reflexes corresponding to ZnO. Magenta dots show the position of the Al_2O_3 substrate reflexes, most of which are covered by beamstops.

The results of the peak analysis as seen in Table I.21, indicate, that there are at least two separate domains of ZnO on the sample, that share the same out-of-plane orientation, but exhibit different in-plane orientations. The angle between these reflexes is 12.59° which is very different to the angle between the in-plane domains observed in-situ at ambient pressure measured, measured at 21.67°. The change in the angle between the two separate in-plane orientations of the ZnO domains could be a result of a change caused by the difference in temperature between the in-situ measurement at ambient pressure and at 575 K and the measurements discussed here, which were conducted at room temperature. A change in the in-plane orientation driven by the reduction of the lattice mismatch to the sapphire substrate would also explain the slight change in the lattice parameter of the ZnO phase as described in Table I.21.

Stable Cu signal in air on the simplified model system ("Cu-Al_2O_3")

Similar to the proceedings described above for the "CZ-Al_2O_3" samples, images collected for the simplified model system "Cu-Al_2O_3" from the 90° sample rotation scan were integrated along the azimuthal direction as seen in Figure 6.38. Unfortunately, the "Cu-Al_2O_3" sample was not as flat as the sample of the ZnO-supported model system, yielding much less information from the same 90° sample rotation scan, since for most of the measured sample rotation angles, the sample alignment was inconsistent as a result. Therefore, certain sample rotation angles that showed signals were selected by eye and then the sample was measured at these selected angles again after re-alignment. While the intensity of the peaks for this sample is considerably lower for the reasons described, there are still a number of clear peaks visible. These peaks do not belong to Cu_2O, as was the case for the "CZ-Al_2O_3" system, but actually can be clearly associated with metallic Cu. This result is quite unexpected, given the identical growth procedure for the Cu particles for both samples, the very comparable experimental history, the fact that they both were exposed to the same reaction gases at the same temperature during the conducted experiments, and finally the same time being exposed to air between the in-situ measurements and the high energy X-ray measurements in air. Additionally, the nanoparticle diameter analysis during the in-situ experiment as described in chapters 6.4 and 6.5, shows that the Cu particles were also of very comparable diameter at elevated temperatures and under reaction gas conditions.

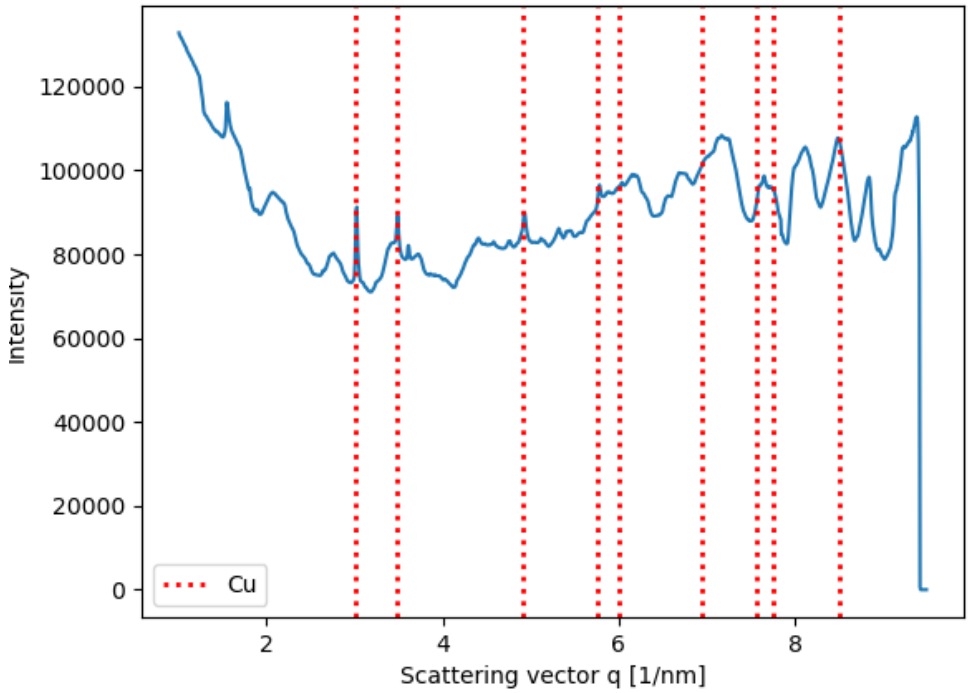

Figure 6.38. Results for the azimuthal integration of the 2D detector images measured of the Cu on Al_2O_3 "Cu-Al_2O_3" as seen in Figure 6.52. The dotted vertical lines represent the expected scattering vectors for Cu (red).

6.7. Analysis of an additional cubic phases with unknown chemical composition

A number of reflexes associated with a cubic structure of yet unknown chemical compositions were measured on both sample systems, the simplified ("Cu-Al_2O_3") as well as the ZnO-supported model system ("CZ-Al_2O_3"), referred to throughout this work as the "US1" structure. The $(2\bar{2}0)$ in-plane reflex of the structure was observed under gas flow of various different reaction gas mixtures on the simplified catalyst at 575 K close to the sapphire (110) reflex as shown in Figure 6.39. The corresponding azimuthal in-plane scans show, that this in-plane $(2\bar{2}0)$ signal cannot be associated with an in-plane powder-like signal, but evidently originates from ordered domains of US1 (111)-oriented particles, as the radial in-plane scan along Al_2O_3 (110) yielded a strong signal for US1 $(2\bar{2}0)$, which was not observed for the scan along a different radial in-plane direction.

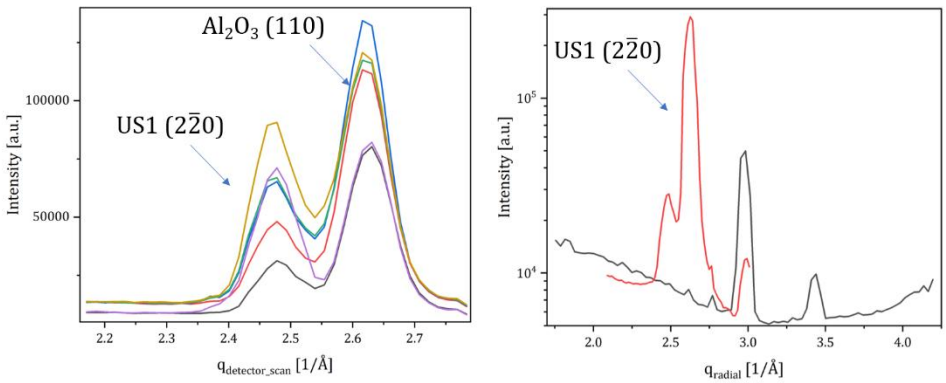

Figure 6.39. Left: detector scan for US1 (2$\bar{2}$0) (left peak) and Al_2O_3(110) (right peak) in different gas phases all at 575 K: Black in H_2, red in Ar, blue after being in Ar for about 1h 45min, green after switching back again to H_2. Violet after being in H_2 for 50 mins, brown back in Ar after being exposed to CO_2 for 30 minutes. Right: Radial in-plane scans for US1 (2$\bar{2}$0) at different in-plane azimuthal angles showing that the reflex is only visible at certain in-plane angles, and therefore the signal originates from an ordered domain and not a powder.

This assumption is further underlined by the measurements performed in air at room temperature, after the exposure to various reaction gases at 575 K, in which the phase was observed to consist of highly ordered (111)-oriented particles as discussed in detail later in this section. Since no corresponding radial in-plane scans were performed at room temperature for this phase, it cannot be unambiguously determined whether it has formed during the sample annealing during catalyst activation or if it was already present at room temperature or even under UHV conditions. However, the azimuthal in-plane scans performed for Cu_2O (111) at q=2.55 1/A in Figure 6.40 show an increase in the FWHM of the main peaks with increasing sample temperature. The main peak intensity here is associated with Al_2O_3 (110) at q=2.64 1/A, but the slight increase in FWHM could be the result of small changes in the underlying US1 (2$\bar{2}$0) reflex, as a change in the Al_2O_3 structure is unlikely. Regarding the ZnO-supported model system, azimuthal in-plane scans performed at 1 bar total pressure under H_2 reaction gas flow at a sample temperature of 575 K showed the presence of the same US1 (2$\bar{2}$0) reflex that was observed on the simplified model system ("Cu-Al_2O_3") as well, as seen in Figure 6.41 and the corresponding fitting details in Table I.16.

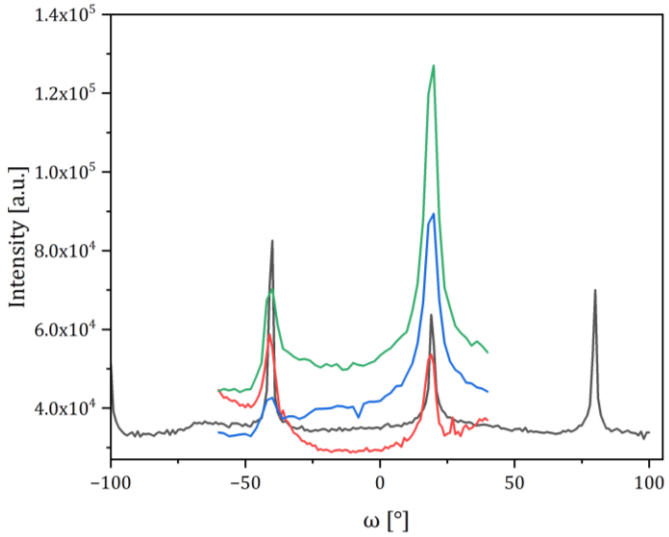

Figure 6.40. Evolution of azimuthal in-plane scan for US1 ($2\bar{2}0$) overlapping the sapphire (110) in different gas phases and temperatures: Ar at RT (black), Ar at 325 K (red), H2 at 375 K (blue) and Ar at 375 K (green).

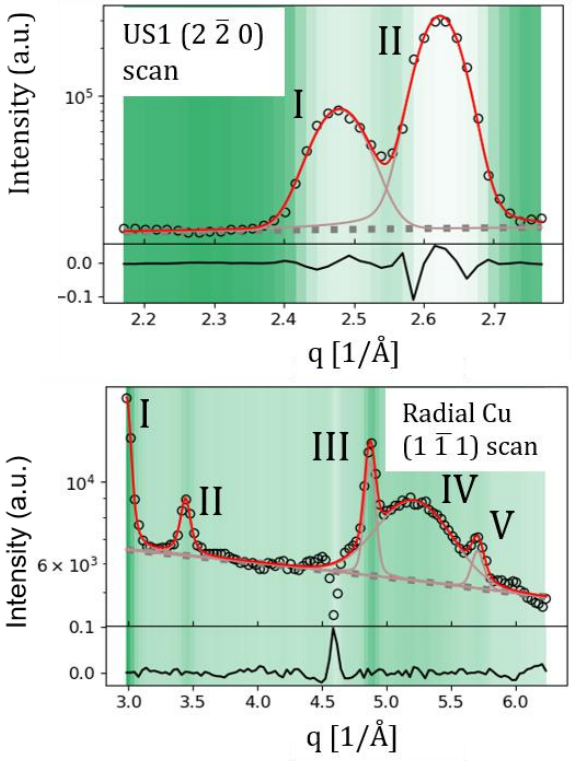

Figure 6.41. In-plane q-detector scan (top) and radial scan (bottom), with the measured data (black dotted lines) and corresponding fits (red lines) for "CZ-Al_2O_3" taken in initial H_2 conditions at 575 K and 1 bar total pressure. Peaks associated to the US1 structure and the corresponding the fitting details can be found in Table I.16, while the fitting details for the other reflexes can be found in section 6.1.

Since a larger part of reciprocal space was sampled for "CZ-Al_2O_3" compared to "Cu-Al_2O_3", additional reflexes associated with the US1 structure were observed for this sample. In the initial H_2 condition, a broad reflex is seen in the radial scan along the Cu ($1\bar{1}1$)

direction centred around q = 5.21 Å, a superposition of the close by reflexes US1 (440) with the Al_2O_3 (220) reflex. Assuming an epitaxial orientation of the US1 structure to the substrate following US1 (110) || Al_2O_3 (110), as was clearly observed in the measurements conducted in air after the exposure to various reaction gases, the US1 (440) reflex would be found along the same in-plane direction as the Al_2O_3 (220) reflex. Given the corrected in-plane direction of the radial scan, along the Cu ($1\bar{1}1$) direction of $\omega_{corrected,111}$ = -74.51°, and the closest corrected direction for the Al_2O_3 (222) of $\omega_{corrected,220}$ = -79.78°, results in an in-plane angular distance of the peaks of 5.27°, which explains the low intensity of these peaks in the radial scan. Regarding the observed reciprocal d*-spacing of this broad peak at 5.21 Å, a superposition of the US1 (440) at q = 5.00 with the Al_2O_3 (220) at q = 5.29 Å is reasonable. While the exposure of the activated catalyst to an oxidizing gas flow in the form of Ar with trace amounts of oxygen and water, caused the full oxidation of the Cu and the emergence of a number of additional peaks, the signals of the unknown structure US1, namely the ($2\bar{2}0$) and (440) reflexes, remain stable with only a minor shift of the respective reciprocal d*-spacings as shown in Figure 6.42.

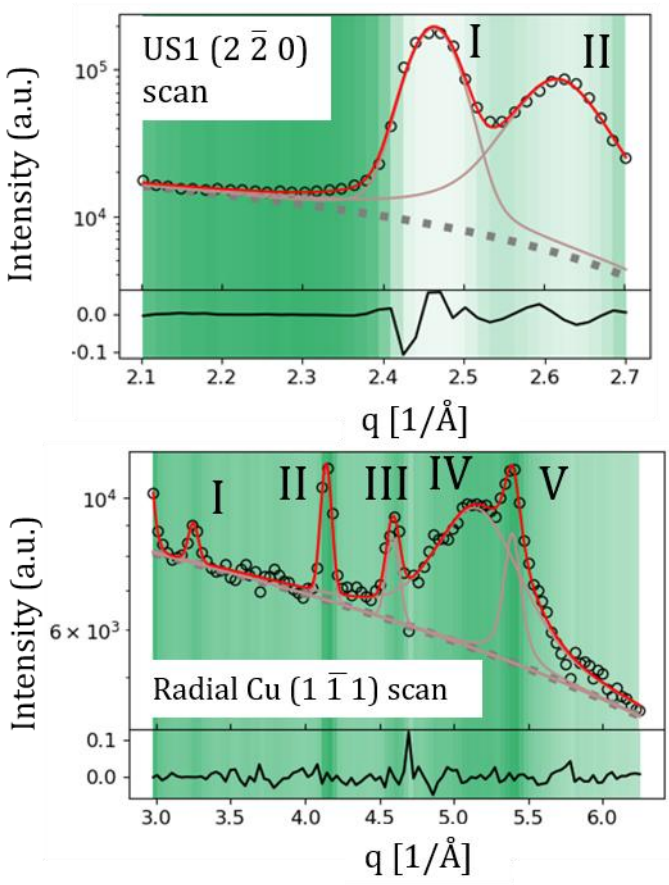

Figure 6.42. In-plane q-detector scan (top) and radial scan (bottom), with the measured data (black dotted lines) and corresponding fits (red lines) for "CZ-Al_2O_3" taken under Ar gas flow at

575 K and 1 bar total pressure. Peaks associated to the US1 structure and the corresponding fitting details can be found in Table I.17, while the fitting details for the other reflexes can be found in section 6.2.

In this condition an additional azimuthal in-plane scan was performed for the US1 ($2\bar{2}0$) peak as seen in Figure 6.43.

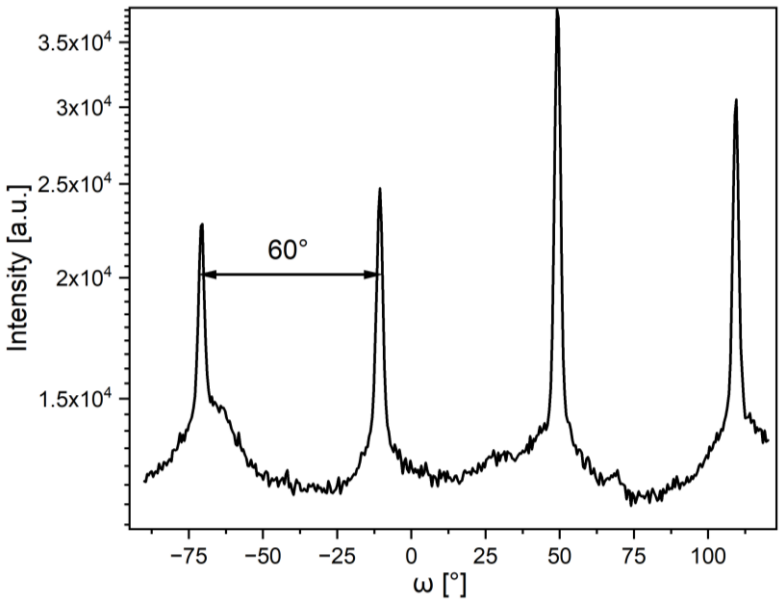

Figure 6.43. Azimuthal in-plane scans for US1 ($2\bar{2}0$) at 575 K in Ar condition.

The peaks show a perfect 60° angular separation of domains oriented along the Al_2O_3 (110) in-plane directions further conforming the epitaxial relationship of the US1 structure with the sapphire substrate. Following the exposure to Ar, switching the reaction gas flow to pure H_2 for a second time caused a clear increase in intensity of the US1 ($2\bar{2}0$) reflex compared to the Al_2O_3 (110) reflex next to it as shown in Figure 6.44, following the evolution of intensity ratios between the US1 and Al_2O_3 reflex of: $R_{I,initial\ H2}$ = 0.27, $R_{I,Ar}$ = 1.09, $R_{I,second\ H2}$ = 2.19. The radial scan along the Cu ($1\bar{1}1$) direction also shows the (440) reflex again as well as a new peak at q=4.36 1/Å. This peak is also observed in the Cu_2O ($2\bar{2}0$) scan at q=4.27 1/Å. Given the increased signal of the US1 phase in this condition, this new peak can be associated with the US1 (224) signal, as one of the three most intense in-plane peaks expected for this phase in case of an orientation of US1 (111) || Al_2O_3 (001).

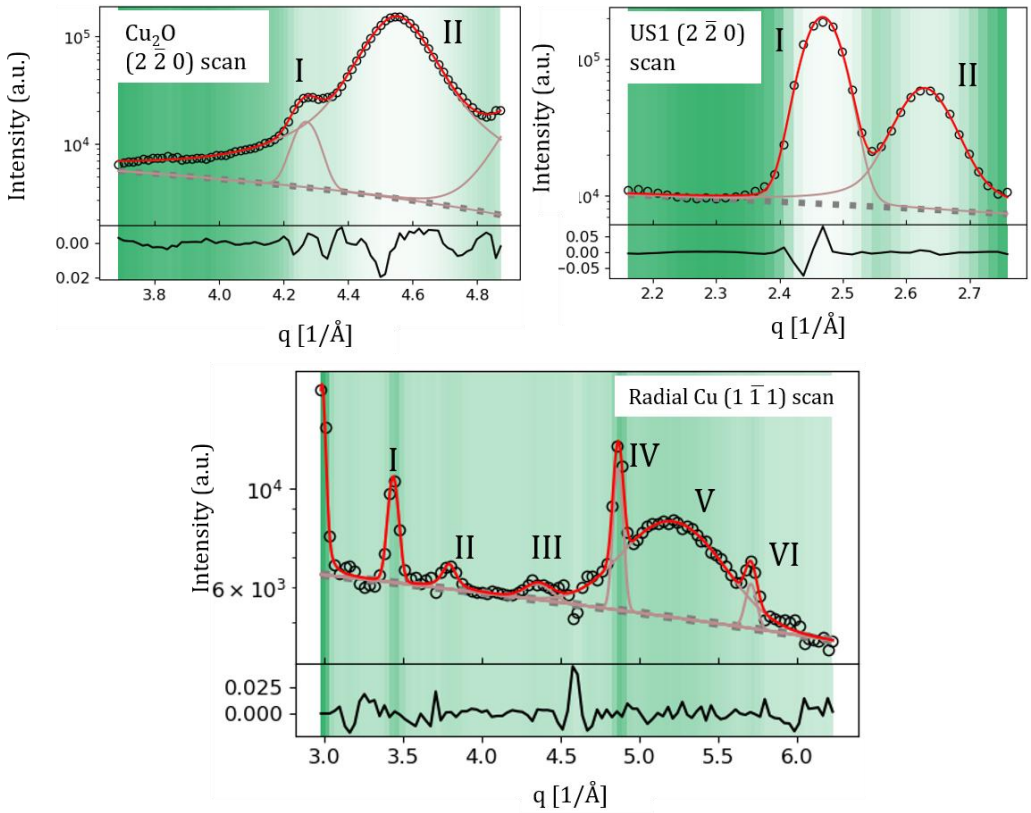

Figure 6.44. In-plane q-detector scan (top) and radial scan (bottom), with the measured data (black dotted lines) and corresponding fits (red lines) for "CZ-Al_2O_3" taken in the second H_2 condition at 575 K and 1 bar total pressure. Peaks associated to the US1 structure and the corresponding fitting details can be found in Table I.18, while the fitting details for the other reflexes can be found in section 6.3.

The in-plane direction of this peak points to a preferential orientation, as the much more intense signal observed in the Cu_2O $(2\bar{2}0)$ scan is observed along the corrected in-plane direction of $\omega_{corrected}$ = 9.19°, so only about 1° off the Al_2O_3 (100) HSD in-plane direction. This direction fits well to the in-plane direction of the US1 $(2\bar{2}0)$ reflex observed just 1.75° off the Al_2O_3 (110) in-plane direction. Both of these in-plane orientation of the US1 reflexes fit well to an epitaxial relationship following US1 (224) || Al_2O_3 (100). This assumption is further underlined by the results of the out-of-plane L-scan starting from the in-plane position of the ZnO (110) reflex shown in Figure 6.23 and the corresponding data set in Table I.12 in section 6.3, where the main conclusions of the measurements regarding the ZnO phase are discussed. Regarding the US1 structure the most pronounced peaks in the scan, are associated with the US1 structure, for which two separate in-plane oriented US1 domains have to be taken into consideration. The first peak in the scan can be explained by (111)-oriented US1 domains, for which the first peak would fit to the $(13\bar{3})$ reflex. As can be seen by the corresponding simulation of the reciprocal space planes in Figure 6.45, for the orientation of the (111)-oriented US1 domains, also the

(242) as well as the (351) are expected in the scan. While the latter cannot be distinguished in the scan, which is reasonable as its intensity is much lower than that of the other two reflexes, the (242) also fits to the peaks in the scan. For the (110)-oriented US1 domains, a reflex belonging to the (224) type is observed as well for the given orientation, as well as the (444) reflex. The latter fits well to the most intense reflex in the data as it would form a superposition with the ZnO (114) as well as the US1(460) peak from the (111)-oriented domains. This L-scan was performed in all following reaction gas mixtures but no relevant changes in the scan were observed as seen in Figure 6.23.

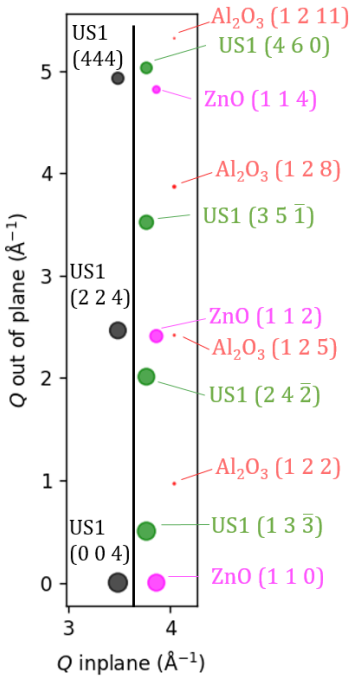

Figure 6.45. Reciprocal space map corresponding to the L-scans of Figure 6.23., showing the reflexes of the following planes (first direction is always out-of-plane, second is in-plane): Al_2O_3 (001)x(120) [red], ZnO (001)x(110) [magenta], US1(111)x(14-5) [green] and US1(110)x(001) [black]. Scan path of L-scan drawn in black. Reflexes are scaled according to their respective relative intensity.

Following the in-situ measurements at ambient pressure in which both model systems were exposed to various different reaction gas mixtures at 575 K, additional SXRD measurements in air at room temperature were conducted using a large 2D detector setup. These measurements yielded extensive reciprocal space maps of the samples which clearly show reflexes related to the unknown structure (US1) as seen for the ZnO-supported model system "CZ-Al_2O_3" in Figure 6.46. The strong substrate reflexes of the Al_2O_3 were mostly covered with lead beamstops as can be seen by the magenta points in Figure 6.46 showing the position of the sapphire reflexes. Two of the reflexes observed in the reciprocal space map were later also identified as Al_2O_3 reflexes, which were not

covered by beamstops due to their very low intensity compared to the other Al_2O_3 reflexes, namely the $(1\bar{1}1)$ and $(1\bar{1}5)$ reflex.

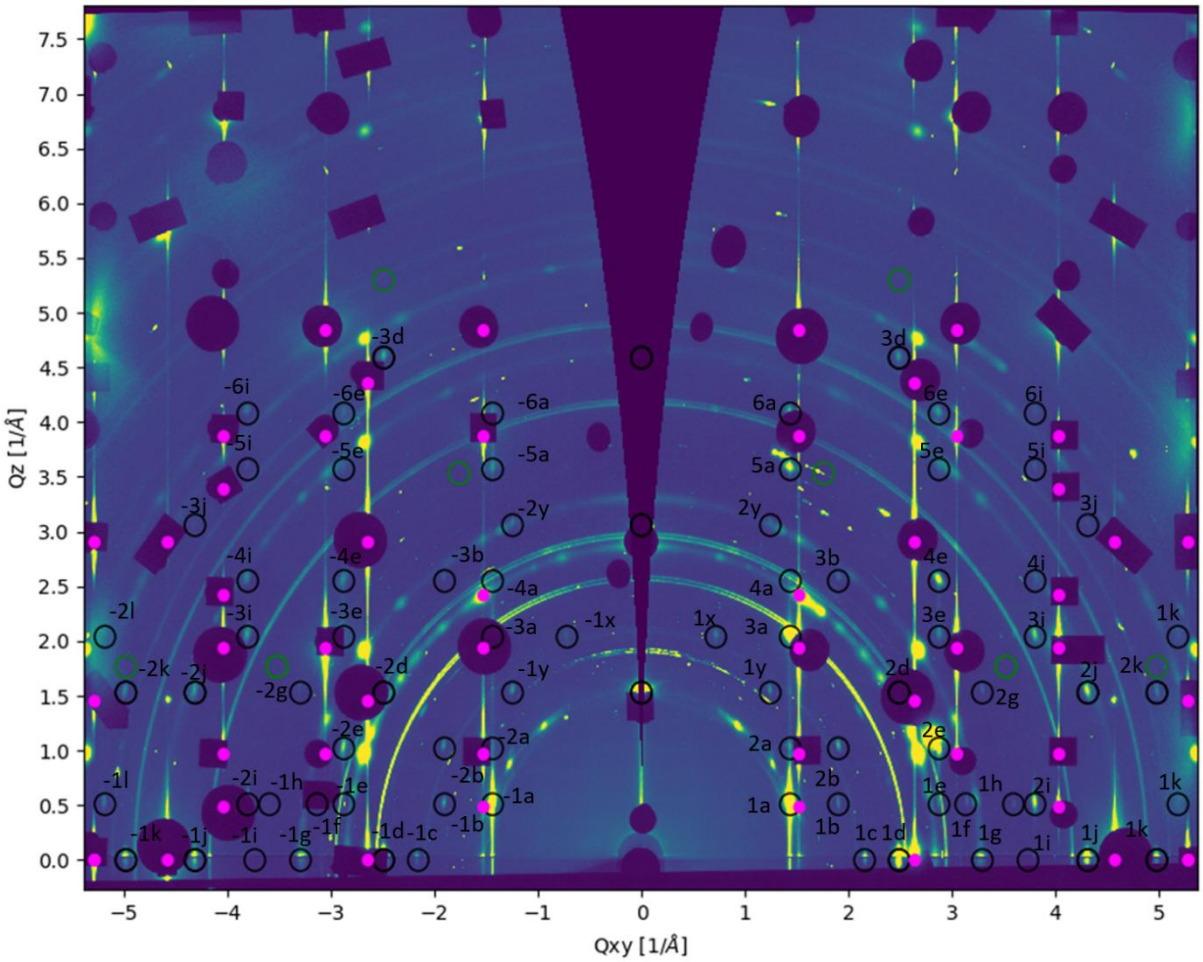

Figure 6.46. Maximum pixel image of the 2D detector data of "CZ-Al_2O_3" measured at room temperature in air over a 90° sample rotation. The black circles indicate the position of the reflexes corresponding to the US1 structure and each peak is named for further reference throughout this chapter. Magenta dots show the position of the Al_2O_3 substrate reflexes, most of which are covered by beamstops. Green circles indicate additional reflexes that would be expected for a lattice of the Fm3m space group, that were not observed for the crystal structure on the sample.

The position of the reflexes associated with the US1 structure are indicated by black circles in Figure 6.46, fitting to a cubic crystal structure with a lattice spacing of 7.1149 Å that is oriented with respect to the sapphire substrate according to US1 (111) || Al_2O_3 (001). The fact that this structure is based on a face-centred cubic (FCC) structure became quickly evident by the characteristic sequence and spacing of the reflexes along the out-of-plane direction denoted by the "a"-reflexes in Figure 6.46, starting from the $(1\bar{1}1)$ reflex named "±1a". When referring to an FCC lattice in this context, the space group in question is the Fm3m (space group number 225) as the simplest FCC space group. For an FCC structure with the (111) direction oriented out-of-plane, the spacings of the reflexes along

the out-of-plane direction starting from the $(1\bar{1}1)$ position, directly illustrate the presence of the two stacking orders ABC and CBA of close-packed planes in the FCC lattice. While the first stacking order produces the $(1\bar{1}1)$ (1a), the (220) (3a) and (331) (5a) reflexes, the CBA stacking represents the same type of lattice planes just rotated by 60° around the surface normal. Summing over the reflexes of a sample rotation of in this case 90°, both spacings appear, with the reflexes corresponding to the CBA stacking (002) (2a), (113) (4a) and (224) (6a). Both stacking orders show the same distance between each associated peak, which is equivalent to the length of the (111) vector, while the CBA stacking is shifted with respect to the reflexes of the ABC stacking by exactly 1/3 of the length of the (111) vector. This 1/3 length corresponds to the number of close-packed planes in the stacking orders, so in this case 3.

Based on the assumption of a cubic lattice, all reflexes were identified corresponding to the measured momentum transfer components along q_{xy} and q_z as seen in Table I.22. The calculated Δ values are based on the discrepancy of the measured reflexes to the corresponding reflexes of a cubic structure with lattice constant 7.115 Å ± 0.454 Å. This lattice constant was determined by calculating the average discrepancy in both q_{xy} and q_z for the calculated lattice constant, and then minimizing the overall discrepancy of the structure in both directions as illustrated in Figure 6.47.

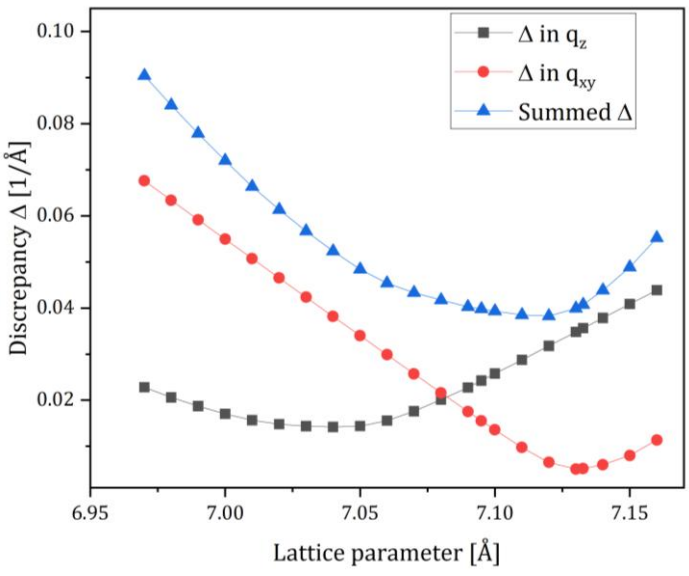

Figure 6.47. Calculated average discrepancy Δ of the measured reflex positions compared to the calculated positions in q_z and q_{xy} direction as well as the sum of both as a function of the lattice parameter.

Similar to the determination of the lattice parameter for the $Cu_{0.64}Zn_{0.36}$ phase as described in section 0, the discrepancy between the measured values and the expected

peak position based on the calculated lattice parameter are not perfectly identical along the in-plane and out-of-plane directions, with a discrepancy of -2.11 % along q_z, and 0.25% along q_{xy}. The negative discrepancy along q_z corresponds to a slightly increased lattices compared to the calculated values, while the opposite is true for the values along q_{xy}. These results would indicate a compression of the structure along the out-of-plane direction and a slight expansion in-plane. However, simulating the position of all expected reflexes for a structure with the Fm3m space group and a lattice constant of 7.1149 Å, yields additional reflexes that were not observed as indicated by the green circles in Figure 6.46. These circles refer to the (420), (442) and (622) type reflexes. For the Fm3m space group the structure factors for these reflexes would definitely be large enough to produce visible peaks in the measurements as the structure factors of these reflexes are almost identical to nearby reflexes that were observed. Specifically, the (420) reflex has a structure factor that is very close to that of the (331) type reflexes observed as peaks (8a, 4e), the (442) reflex has similar intensity to the (135) type reflexes observed as peaks (3d, 5i, 2k,1l), and the (622) reflex has a very similar structure factor to the (620) type reflexes observed as peaks (6i, 2l). Therefore, the absence of these peaks clearly proofs, that the crystal structure does not belong to the Fm3m space group.

In order to clearly identify the structure type of the measured structure, a vast number of material phases was examined in order to find a cubic structure for which the (420), (442) and (622) are either forbidden, or show a significantly lower structure factor than the surrounding reflexes. Additionally, the structure factors of the other reflexes of the phase also had to be taken into consideration. For example, the (113) reflex of the measured structure has a significantly lower intensity than the (002), (111) or (220) reflex, which is not the case for most cubic structures, for which the (113) reflex is usually the strongest or second strongest reflex. While the search for possible candidates for the given structure was initially limited to structures containing any combination of the expected elements, namely oxygen, aluminium, copper, zinc, carbon and hydrogen, eventually this limitation had to be abandoned since no fitting structures were found. Finally, a very fitting structure type was found with the cristobalite structure of SiO_2 measured originally by Barth et. al in 1932 [82] as illustrated in Figure 6.48.

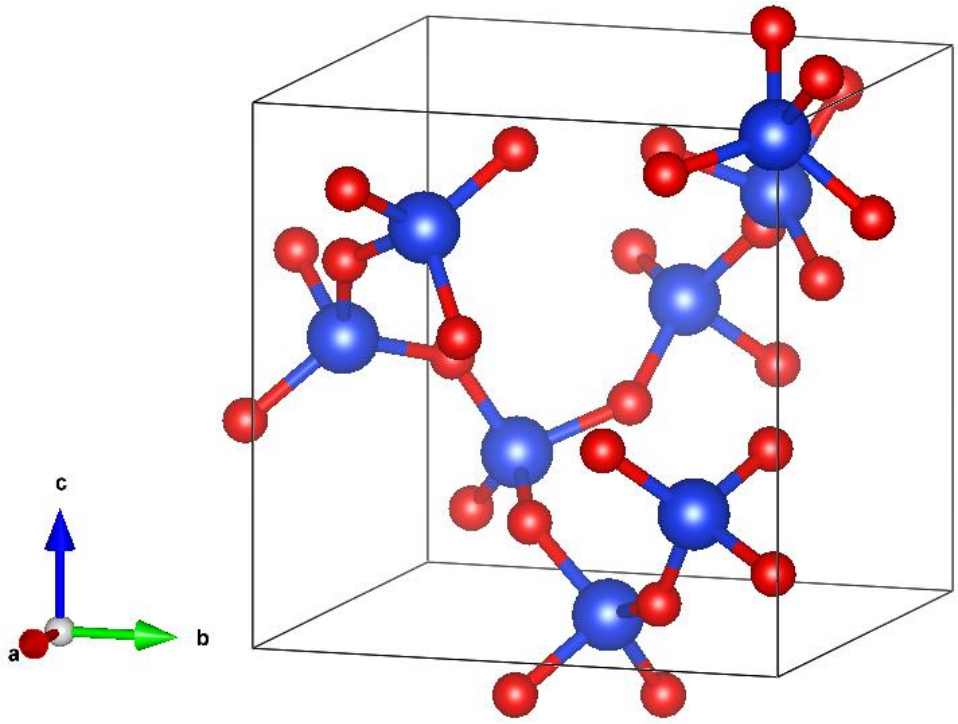

Figure 6.48. Illustration of the cristobalite structure of SiO_2 as described by Barth et. al. [82]. Blue atoms are Si, red atoms are oxygen.

The cristobalite structure of SiO_2 has the cubic space group P 21 3, space group number 198, with a lattice parameter of 7.16 Å, and was measured at room temperature and in ambient pressure. Using the cristobalite structure to describe the measured phase fits well especially because the phase shows a low relative intensity of the (113) reflex, very low intensity of the (420) and (622) reflex and the (442) reflex is even forbidden. Even the fit with the silica cristobalite structure type is not perfect however, since all measured reflexes can be explained with the structure, but the structure is expected to produce additional reflexes, that have not been measured. To fit the data, it has to be assumed, that certain reflexes were not measured, simply because their relative intensity is too low for a signal to be distinguishable from the background signal, as no crystal structure can perfectly explain only all the measured reflexes. For example, the first order of reflexes along the out-of-plane direction is supposed to contain the reflexes (110), (112), (221), (223), (332), (334) and (443) within the measured q-range. Only the (112) and (223) reflex could be clearly measured however. The relative intensities of the missing reflexes are comparably low however for SiO_2. Additionally, it is important to note that with a sample rotation of only 90°, some reflexes could have not been measured, especially given the general difficulty with the alignment of the samples, which could have influenced the measurement in specific angular ranges of the sample rotation. Finally, the true elemental

composition and the exact position of the atoms within the unit cell has a great influence on the relative intensity of the measured reflexes. So even though the cristobalite structure as observed for SiO_2 does fit reasonably well to the measured data, SiO_2 cannot explain the data due to a too large discrepancy between the relative expected intensity of reflexes that were not measured and because the presence of a significant amount of Si on the sample can be excluded with high certainty. This is evident as none of the pre- and post-beamtime investigations of the measured sample, or any of the other prepared samples of this work for that matter, have shown any signal of Si. Especially the spectroscopic measurement techniques like XPS, EDX and AES, would have shown any Si present on the sample. Having identified the cristobalite structure type as a potent candidate for the observed crystal structure, the search for a fitting material phase was extended to see if other materials that also form cristobalite could explain the data. A particularly interesting candidate emerged in $AlPO_4$ as it is described in the literature to from isotypic structures to those of SiO_2, for which simply half of the Si atoms have to be replaced with Al and P respectively [83,84]. As is described in more detail in the following section, phosphorus was actually observed on the sample in one of the EDX measurements following the ambient pressure experiments. While almost all of the structures observed for SiO_2 have also been reported for $AlPO_4$, the exact structure as described by Barth et. al. as mentioned above was not reported for aluminium phosphate. Instead, $AlPO_4$ was reported to form an orthorhombic structure that is only a very slight deviation from a cubic structure as seen in Figure 6.49 described as a low-cristobalite type structure.

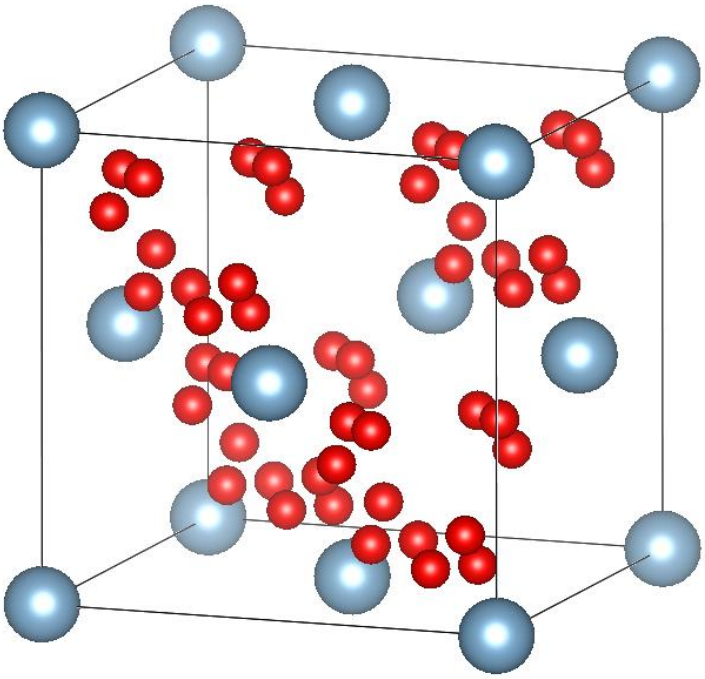

Figure 6.49. Illustration of the low-cristobalite structure of $AlPO_4$. Blue atoms are Si, red atoms are oxygen [83].

The low-cristobalite structure has lattice parameters of a=7.0843 Å, b=7.0823 Å and c=6.9989 Å, as measured again at room temperature and ambient pressure. The correlation between the $AlPO_4$ phase and the measured data is even better than with the cristobalite SiO_4 structure, since the relative intensities and forbidden reflexes fit much better to the measured data set as illustrated in the comparison in Figure 6.50.

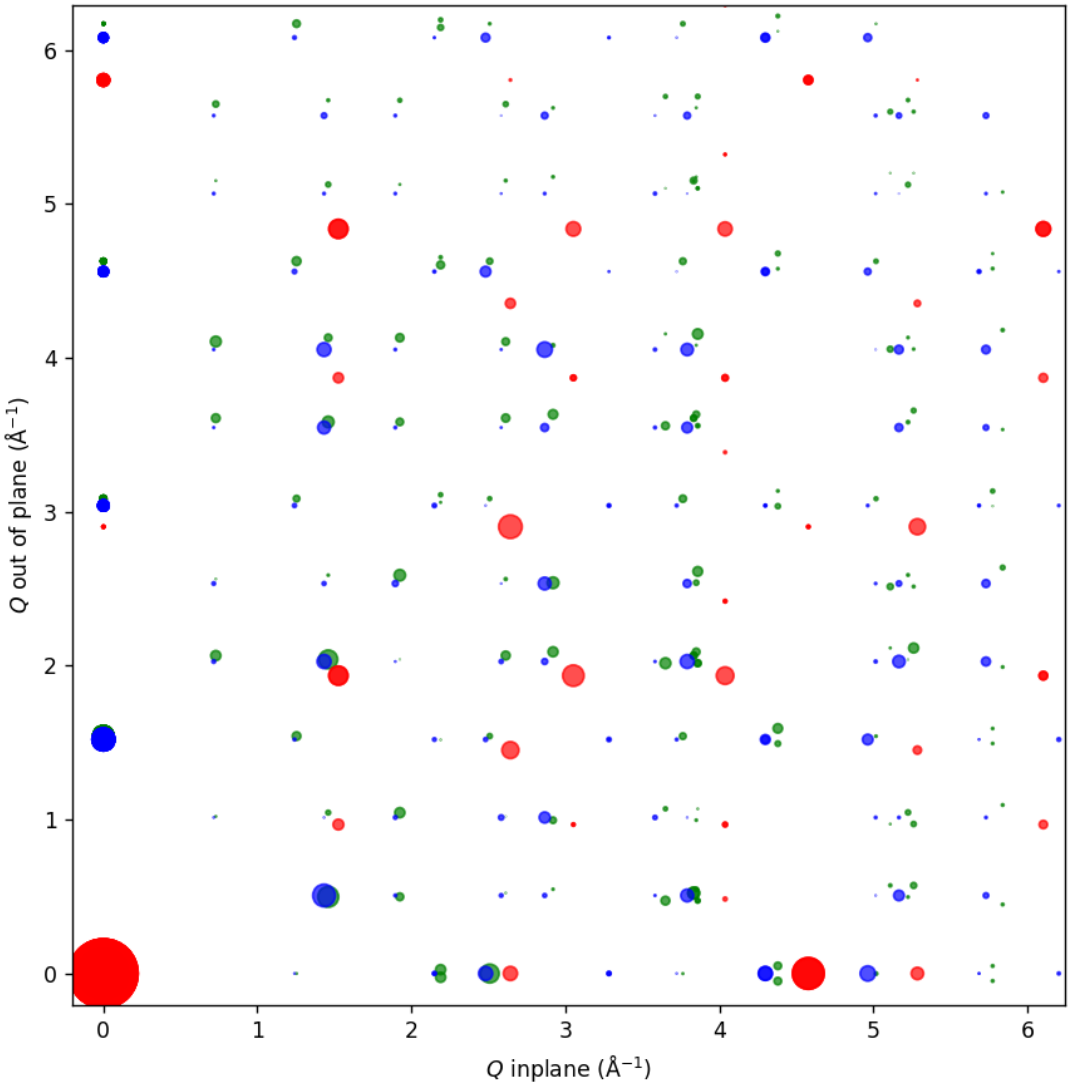

Figure 6.50. Simulated reciprocal space map showing all reflexes for the SiO_2 cristobalite structure (blue) as well as for the low-cristobalite $AlPO_4$ (green) in the q-range relevant for the performed experiments. Substrate reflexes of Al_2O_3 are shown for reference in red. All reflexes are scaled according to their respective relative intensity.

Comparing the relative intensities of the first order of reflexes along the out-of-plane direction for example, shows a much better fit of the measured data with the low-cristobalite structure, as the reflexes (110) and (221), both of which were not measured for the sample, have a significantly lower intensity for this structure. The relative intensity of the reflexes in the simulation does not account for the Lorenz-correction, which causes a decline in intensity with increasing momentum transfer of reflexes, which is why the high intensity of the signal of the low-cristobalite structure for the higher order reflexes (223), (332) and (443) is accounted for. It has to be noted however, that for the simulation in Figure 6.50, the same orientation of the low-cristobalite orthorhombic structure was chosen as for the cristobalite structure, meaning that the (111) direction is perfectly parallel to the substrates out-of-plane (001) direction. While for a cubic structure this

orientation is expected for particles on a hexagonal substrate, the argument is not quite as simple for an orthorhombic structure. The assumption of (111)-orientation is however, based on the fact that the $AlPO_4$ is reported to from a cubic structure at elevated temperature of 573 K [84], which is in the exact temperature range of the ambient pressure XRD experiment conducted, at which the structure is assumed to have formed. Therefore, it is reasonable to assume, that the low-cristobalite structure formed as a slight deviation from the previously present cubic phase, which happened without a substantial change in the particle orientation. This assumption is further underlined by the good fit of the data with the simulation of the (111)-oriented low-cristobalite structure. A full comparison of the structure factors of the $AlPO_4$ structure with the measured data set can be found in Table I.24. For the comparison, the measured peak intensity was averaged for each reflex. As can be seen, two comparisons were done, one with all measured reflexes and one without the data of the (111) reflex. This is due to the fact that the intensity of the (111) reflex is assumed to be superimposed with the $(1\bar{1}1)$ substrate reflex. With an average discrepency between the measured structure factor and the literature value of 24.25% ± 85.39% for the full comparison and 86.31% ± 132.72%, both of the comparisons are clearly dominated by some strong outliers. Other possible superpositions of the signal cannot be excluded as most of the measured reflexes are positioned very close to substrate reflexes. The general trend of the structure factor fits better to the data as the mean deviations suggest as can be seen in the comparison as bar diagrams in Figure 6.51.

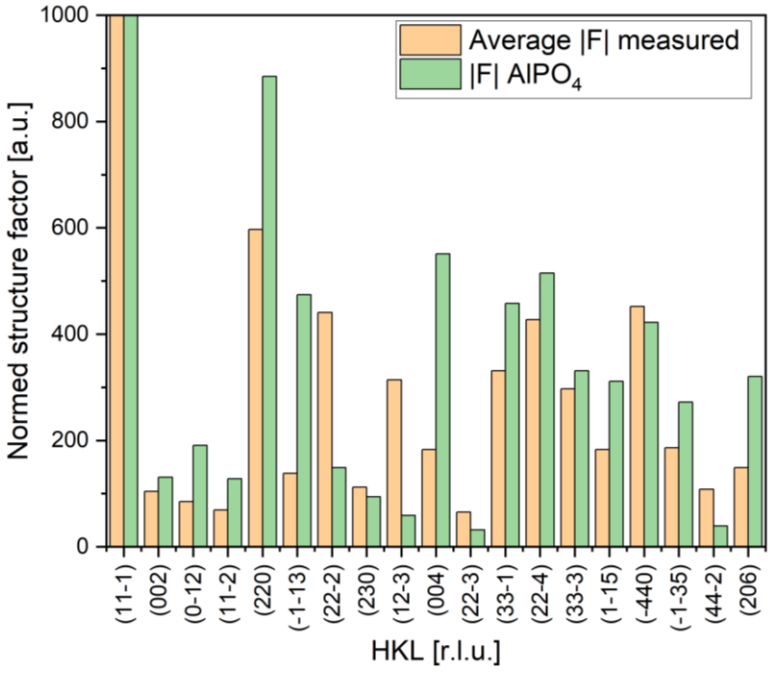

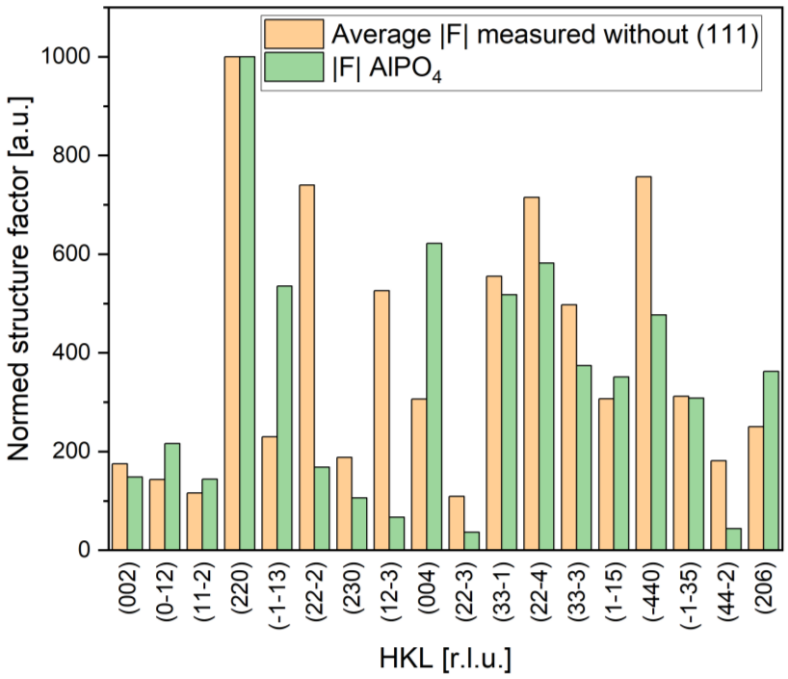

Figure 6.51. Comparison of the structure factor of the measured phase to the literature $AlPO_4$ phase [83]. Top: Comparison including all reflexes. Bottom: Comparison without the (111) reflex, which was taken out of the consideration due to the assumption of a possible superposition of the (111) reflex with the $(1\bar{1}1)$ Al_2O_3 substrate reflex.

Further analysis of the crystal structure of the US1 phase

For a more fundamental investigation of the measured structure, the data set was prepared in a way that resembles the data sets used for a classical structure analysis as done typically with single crystal samples. For this, each reflex was listed separately, including reflexes with the same momentum transfer that were measured at different angles of the sample rotation range. While the resulting data bank included a total of 116 reflexes, the number of reflexes is still very small compared to a structural XRD analysis. Additionally, the reflexes were indexed in hexagonal surface coordinates as shown in Table I.27. Mapping of the reflexes onto a hexagonal lattice structure yielded a certain discrepancy Δ between the calculated reflex positions and the measured in-plane angles of the peaks ω. The overall fit of the structure to a hexagonal lattice yielded an average Δ of 0.161° ± 1.16°. As can be seen in the data, most of the reflex can be described well within the context of a hexagonal lattice, while a few reflexes show high discrepancies to the calculated peak position. A first cell parameter refinement of the data has been performed and yielded lattice parameters of a=10.07 Å, b=10.05 Å, c=12.3 Å, α= 90.2°, β=90.36° and γ=119.9°. Further analysis of the data is underway but unfortunately beyond the scope of this work. The relatively high discrepancy between the surface coordinates and the measured peak positions which are also evident in the deviation of the hexagonal angles in the resulting fit of the structure, point to the presence of a hexagonal base structure with a cubic structural motif. This could be a result of a certain superlattice structure emerging from a certain oxygen/cation vacancy ordering.

Signal of the US1 Structure on the simplified model system

The investigation of the "Cu-Al_2O_3" samples using high energy X-rays with a 2D detector setup showed that the same unknown structure US1 also formed on this sample, proofing that the structure cannot be caused by the presence of Zn/ZnO on the ZnO-supported system. As discussed in the previous section, the "Cu-Al_2O_3" sample was not perfectly flat, yielding much less information from the same 90° sample rotation scan, since for most of the measured angles, the sample height was not correct. Therefore, specific sample rotation angles were selected by eye and measured again after re-alignment. Following this approach Figure 6.52 shows the result of the scan performed over the whole 90° sample rotation, while Figure 6.53 and Figure 6.54 show scans at two selected sample rotation angles.

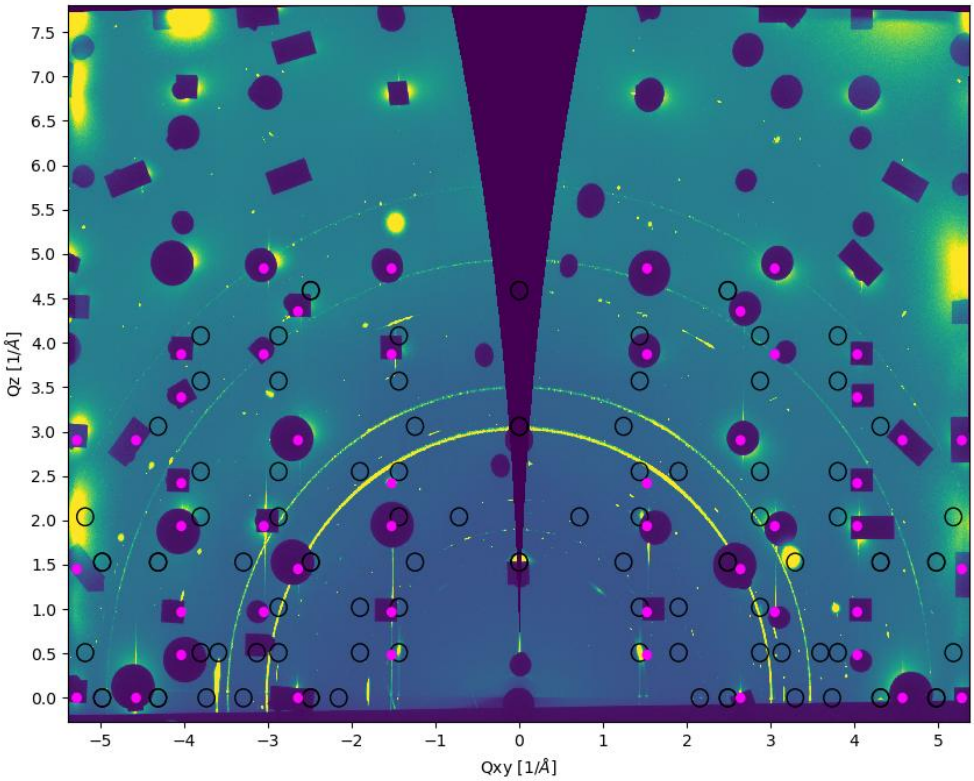

Figure 6.52. Maximum pixel image of the 2D detector data of "Cu-Al_2O_3", Cu on Al_2O_3, measured at room temperature in air over a 90° sample rotation. The black circles indicate the position of the reflexes corresponding to the US1 structure. Magenta dots show the position of the Al_2O_3 substrate reflexes, most of which are covered by beamstops. The sample height was inconsistent, causing alignment issues at most of the measured sample rotations angles during the 90° sample rotation scan, causing only a few reflexes of the US1 structure to be observed in the scan.

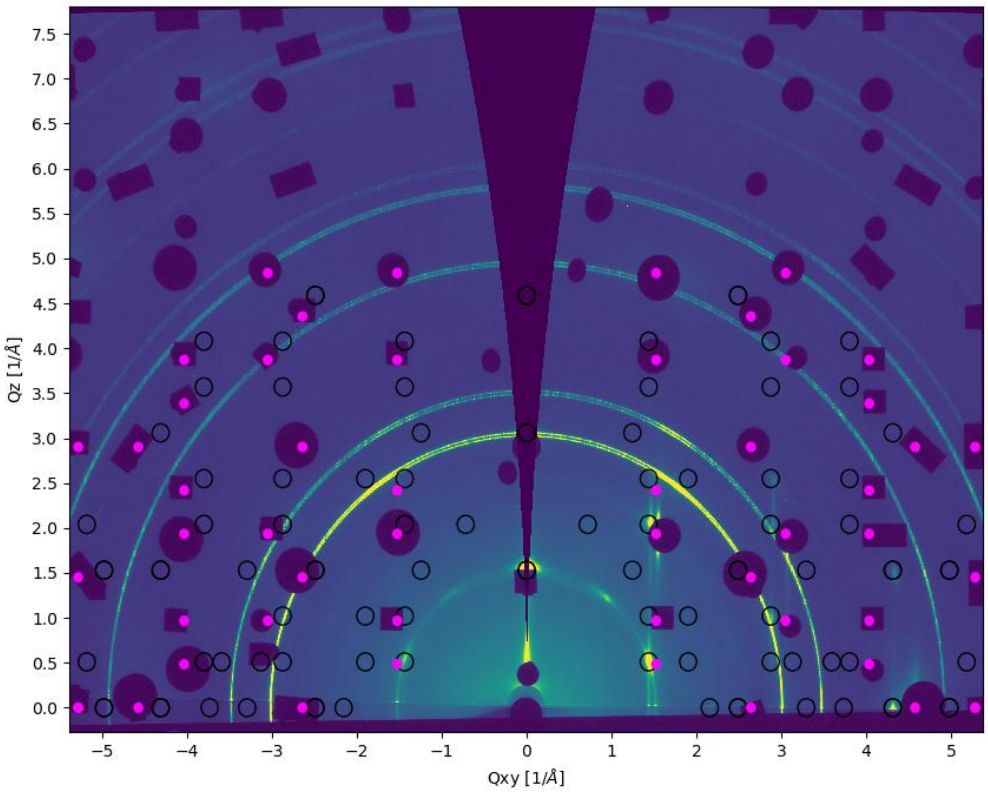

Figure 6.53. Maximum pixel image of the 2D detector data of "Cu-Al_2O_3", Cu on Al_2O_3, measured at room temperature in air at a steady sample rotation angle of 0°. The black circles indicate the position of the reflexes corresponding to the US1 structure. Magenta dots show the position of the Al_2O_3 substrate reflexes, most of which are covered by beamstops.

All the figures have the same overlay of black circles indicating the expected position of reflexes belonging to the unknown structure US1 as used in the previous section for "CZ-Al_2O_3". Despite the considerably lower amount of signal from the sample, each of the scans does show reflexes, all of which fit well to the unknown structure. Furthermore, the positioning of the strongest reflexes of the unknown structure directly next to the crystal truncation rods of the sapphire, clearly visible in both Figure 6.52 and Figure 6.53, are clear indications that the same structure observed for "CZ-Al_2O_3" is also present on this sample. Therefore, the conclusion can be made that the unknown structure formed on both samples, proofing that the presence of ZnO on "CZ-Al_2O_3" did not have an influence on its formation.

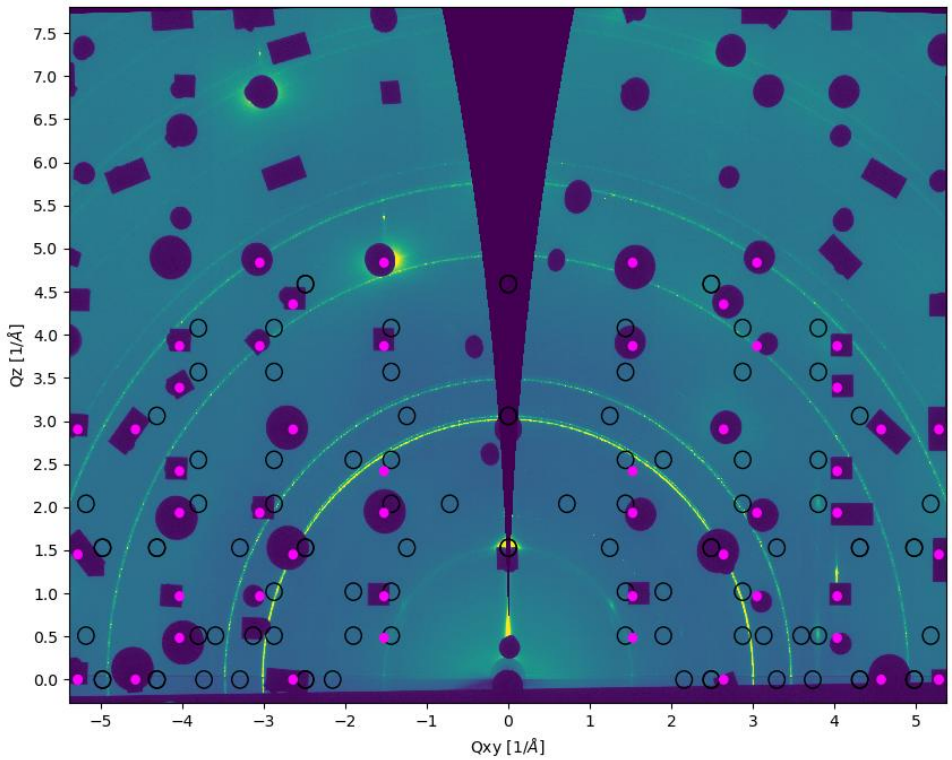

Figure 6.54. Maximum pixel image of the 2D detector data of "Cu-Al_2O_3", Cu on Al_2O_3, measured at room temperature in air at a steady sample rotation angle of 11.28°. The black circles indicate the position of the reflexes corresponding to the US1 structure. Magenta dots show the position of the Al_2O_3 substrate reflexes, most of which are covered by beamstops.

6.8. Particle agglomeration and Zn loss in air at room temperature

Based on the analysis of the data set collected for the ZnO-supported model system "CZ-Al_2O_3", a number of additional measurements were conducted in air and at room temperature following the exposure to various reaction gas mixtures at 575 K during the in-situ measurements, and are described in the following section.

Scanning electron microscopy (SEM) and energy dispersive X-ray analysis (EDX)

The first scanning electron microscopy measurements of "CZ-Al_2O_3" were conducted about 3 months after the XRD measurements, as seen in Figure 6.55. Only a limited number of images and magnifications could be measured as the sample was exhibiting significant electrical surface charging during the measurement. Nonetheless, a homogenous coverage of the sample with mostly elongated nanoparticles can already be observed. Despite the charging effects, nanoparticles size of 20 handpicked particles was analysed yielding an average size of 188.475 nm ± 73.295 nm. For the analysis, the length of each particle was measured along two different in-plane directions and the results were averaged. Smaller particles may also be present, but cannot be clearly differentiated from

the surrounding sample surface. Energy dispersive X-ray analysis (EDX) was performed on the sample, once directly atop one of the clearly visible nanoparticles (Figure 6.55, top), and once on the surrounding sample surface (Figure 6.55, bottom). While the latter spectrum showed mostly elements belonging to the sapphire substrate, namely oxygen and aluminium, with only a small amount of Cu of 3.79%, the spectra measured on one of the large nanoparticles shows a considerable amount of Cu of 34.54 % as seen in Table 6.2.

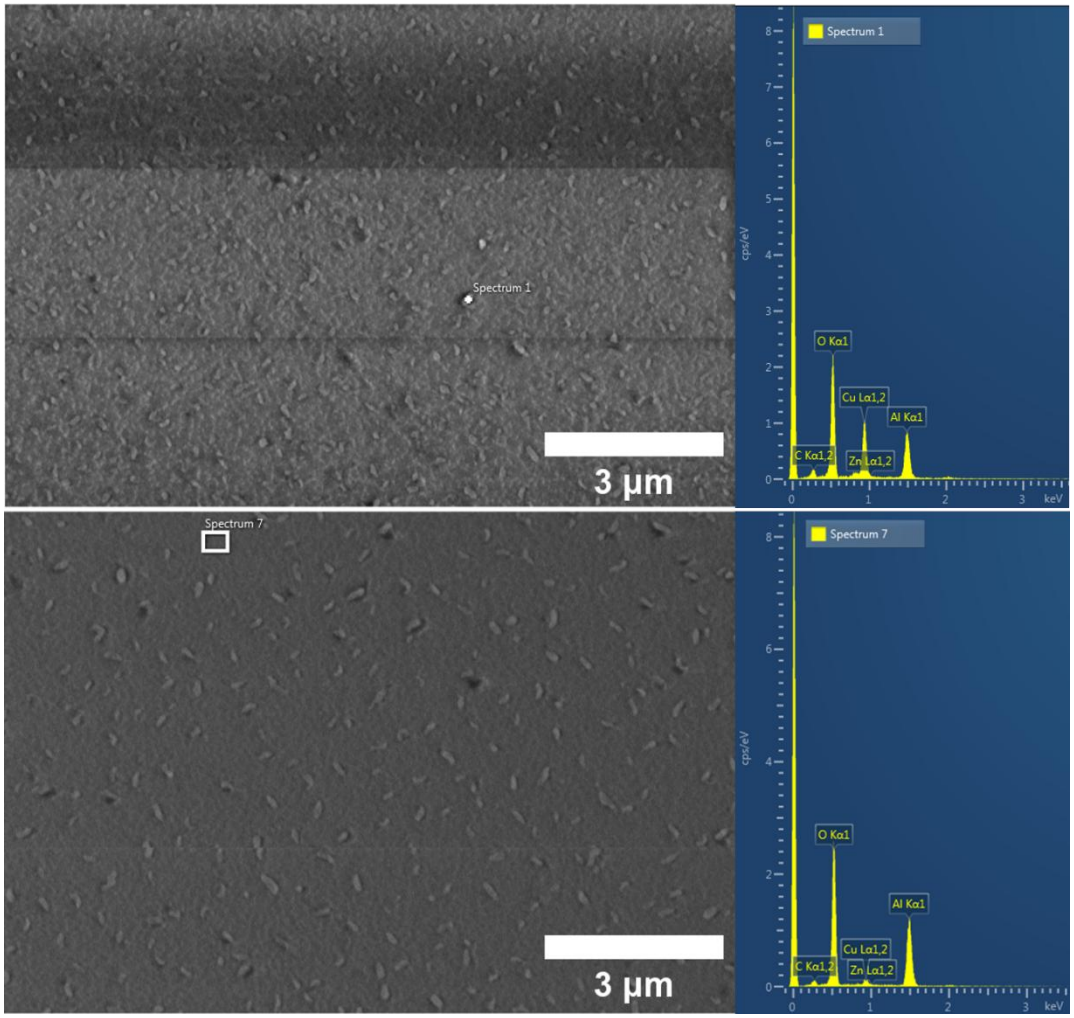

Figure 6.55. Left: SEM images of "CZ-Al_2O_3" as measured in the first post beamtime SEM measurement in air. Areas used for EDX analysis are marked in white. Right: Corresponding energy dispersive X-ray spectra (EDX) for each of the areas marked in the images on the left.

Spectrum Label	Spectrum 1 (nanoparticle)	Spectrum 7 (sample surface)
C	3.24	2.27
O	35.34	49.76
Al	26.87	44.18
Cu	34.54	3.79
Zn	0.00	0.00
Total	100.00	100.00

Table 6.2. Detailed elemental composition of the ZnO-supported model system in air as measured with EDX corresponding to Figure 6.55.

Signal from Zn was found in neither of the analysed areas on the sample. To reduce the amount of electrical surface charging and thereby improve the measurement, half the sample was covered by a 3 nm thick layer of carbon to promote electron mobility on the sample. Afterwards the measurements were repeated, about 8.5 months after the XRD measurements. As can be seen in Figure 6.56, again a homogenous coverage of the sample with mostly elongated nanoparticles can be observed. Again 20 of these particles were handpicked and their size analysed yielding an average size of 148.1 nm ± 47.065 nm. While a direct and detailed comparison of the different SEM measurements is difficult, it is unlikely, that the surface charging that effected the first SEM measurement, introduced a systematic error in the analysed size of the particles, especially in the order of the observed 27% decrease in particle size. Therefore, the SEM analysis shows a slow decrease in particle size with time, which could be a consequence of previously present Zn evaporating from the sample. Between the larger nanoparticles, additional smaller and more roundish particles can also be observed. Analysis of the size of these particles was difficult as the contrast between the particle edges and the surrounding sample surface was weak. The resulting size of the particles of 73.54 nm ± 13.14 nm can only be used as a rough estimation.

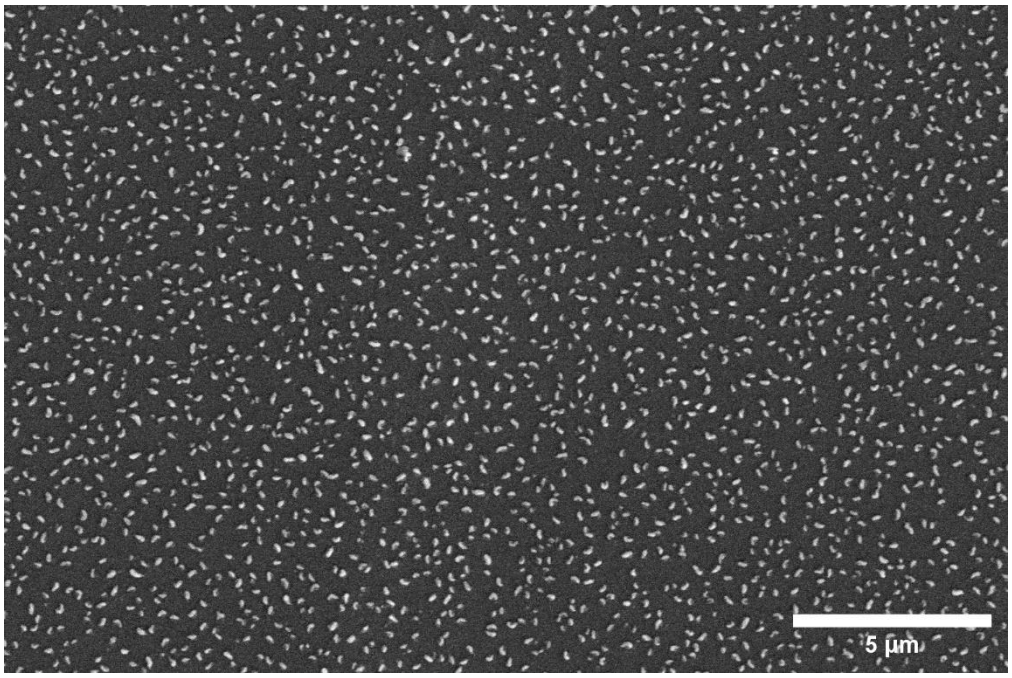

Figure 6.56. Scanning electron microscopy (SEM) image of "CZ-Al_2O_3", Cu on ZnO on Al_2O_3, taken about 9 months after the in-situ experiment and 8.5 months after the high energy X-ray measurements. The sample is covered homogenously with elongated nanoparticles.

Similar to the first measurement, during the second SEM measurement EDX measurements were carried out analysing the elemental composition of the larger particles versus the sample surface with the smaller particles as seen in Figure 6.57 and detailed composition in Table 6.3.

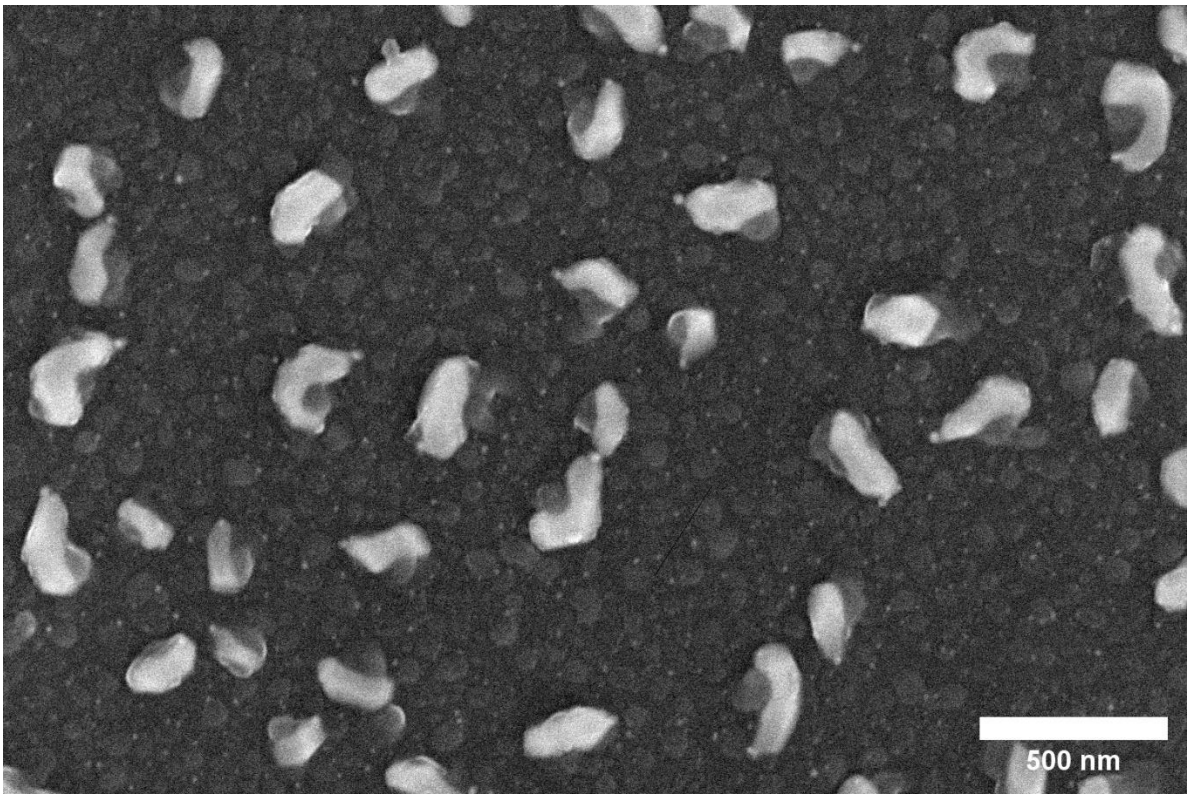

Figure 6.57. Scanning electron microscopy (SEM) image of "CZ-Al_2O_3", Cu on ZnO on Al_2O_3, taken about 9 months after the in-situ experiment and 8.5 months after the high energy X-ray measurements. This detailed view shows that the sample is covered with larger, mostly elongated particles, with smaller particles visible in-between the larger ones.

As expected, the elemental composition of all spectra shows a strongly increased amount of carbon compared to the first measurement as a result of the carbon layer that was added on half of the sample surface to reduce the surface charging effect (SEM measurements were carried out on the side of the sample that was not covered with carbon). The considerably higher amount of carbon for the spectra measured on the particles was not found to be consistent throughout all the analysed areas. Additionally, throughout all conducted SEM measurements a small amount of phosphorus is observed. As was also observed during the first SEM measurement, the clear difference in the elemental composition of the large particles and the surrounding sample surface can be seen in the amount of Cu in these areas. While the sample surface was measured to have a Cu content of just 0.76%, the spectra collected on the large nanoparticles yield an average of 49.2% of Cu. Since a native oxidation of the Cu is expected and oxidation of the Cu to Cu_2O was already clearly observed in the XRD measurements conducted 8.5 months earlier, the large nanoparticles can be assumed to be partially oxidized to CuO or Cu_2O. The comparably low amount of oxygen as measured in the elemental composition could suggests however, that the particles still exhibit a certain core-shell type structure with a

Cu_2O core surrounded by a CuO shell. Furthermore, while the carbon coating significantly improved the issue of surface charging and enabled the collection of much higher resolution SEM and EDX measurements, all of the analysed spectra of this sample showed again 0% Zn.

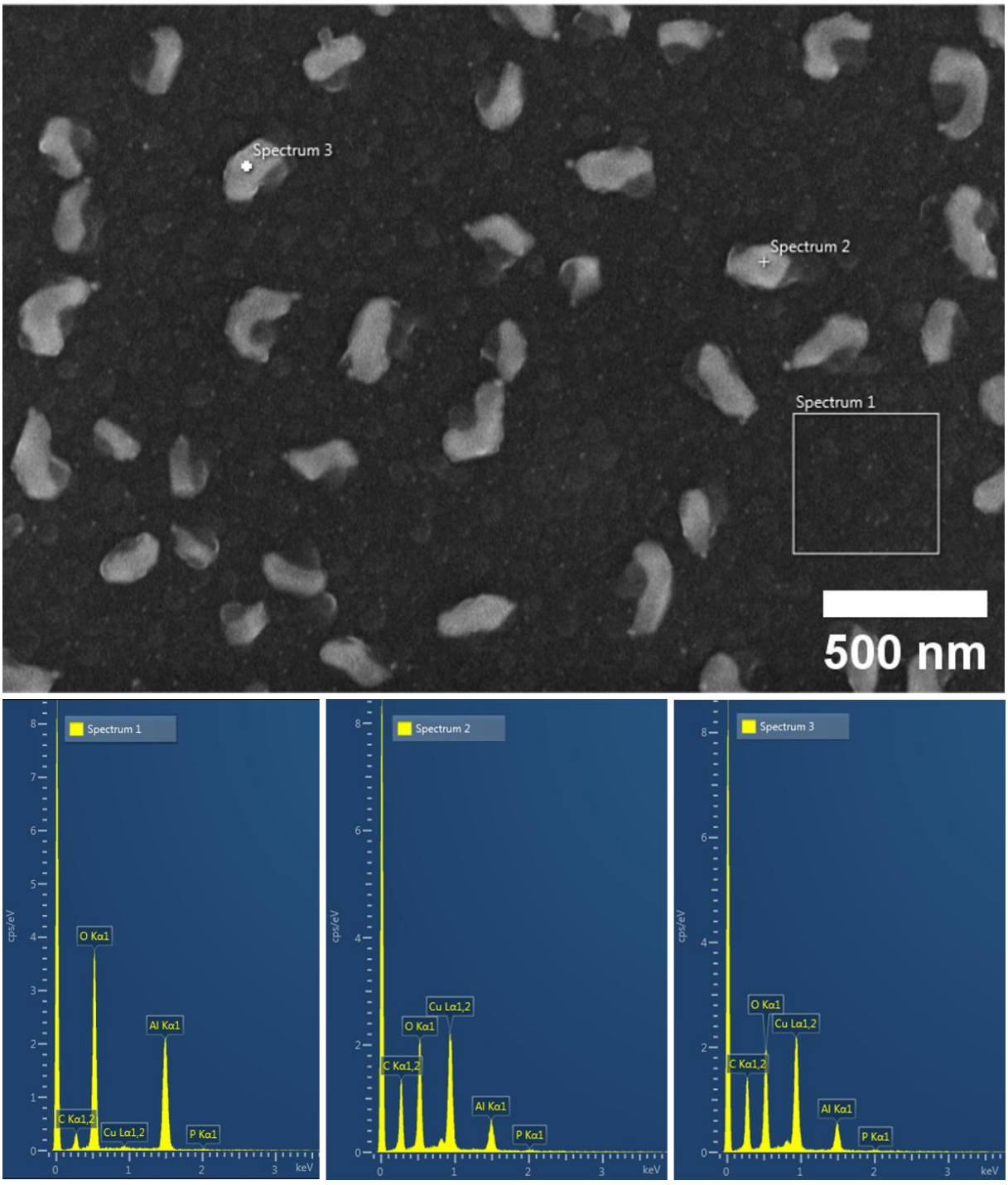

Figure 6.58. Top: Detailed SEM image of "CZ-Al_2O_3" post beamtime in air. Areas used for EDX analysis are marked in white. Bottom: Energy dispersive X-ray spectra (EDX) for each of the areas marked in the top image.

Spectrum Label	Spectrum 1 (sample surface)	Spectrum 2 (nanoparticle)	Spectrum 3 (nanoparticle)
C	4.08	15.05	16.45
O	43.70	22.37	21.86
Al	50.77	12.09	11.71
P	0.69	1.15	0.92
Cu	0.76	49.34	49.06
Total	100.00	100.00	100.00

Table 6.3. Detailed elemental composition as measured with EDX as seen in Figure 6.58.

Scanning auger microscopy

Since the results of the EDX measurements performed for the first and second measurements both showed 0% of Zn in the elemental composition of all analysed areas, scanning auger spectroscopy measurements were conducted as well. As can be seen in Figure 6.59, again different areas of the sample were investigated, distinguishing between the larger nanoparticles and the surrounding sample surface. The results for these measurements are again very consistent with the previously performed SEM and EDX measurements. While the large nanoparticles show a clear Cu and oxygen signal, the surrounding sample surface shows no Cu and mainly aluminium and oxygen. Clear carbon peaks are also observed for all areas due to the carbon coating, while again, scans for Zn showed no signal.

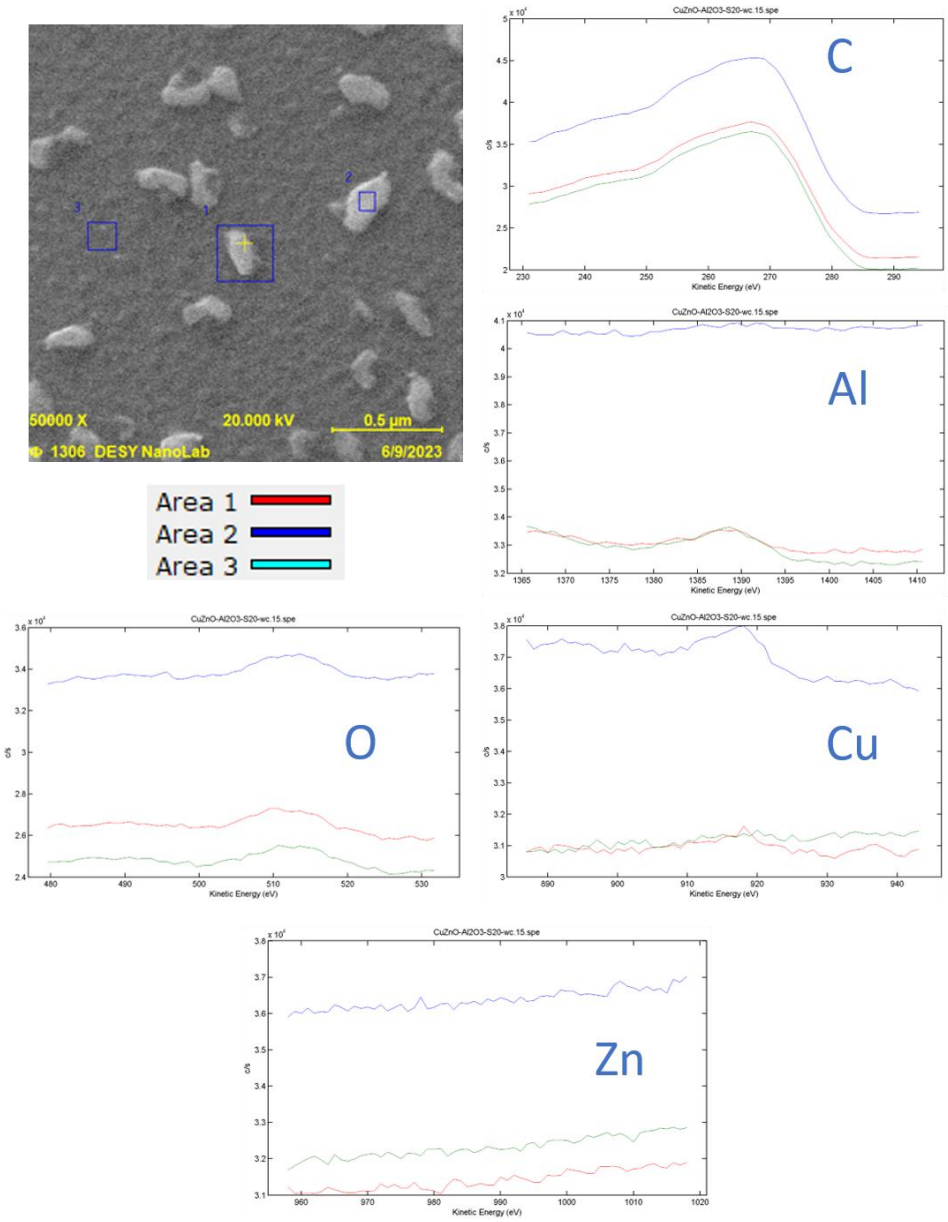

Figure 6.59. Scanning auger microscopy results for "CZ-Al_2O_3". The three analysed areas are marked in the image in the top left. The other images show the auger spectra in the range of carbon, aluminium, oxygen, copper and zinc respectively, corresponding to Area1 (red), Area2 (blue) and Area3 (green). About half of the sample was previously covered with a 3 nm thick layer of carbon to reduce electric charging for SEM and Scanning Auger measurements.

X-ray photoelectron spectroscopy (XPS)

To further analyse the elemental composition of "CZ-Al_2O_3", XPS measurements were carried out as well, 9 months after the XRD measurements. A survey scan of the sample at room temperature showed signal consistent with the results of the SEM and scanning Auger measurements as can be seen in Figure 6.60. Strong signal for oxygen and aluminium is seen as expected with clear signal visible for Cu and carbon as well. To investigate the oxidation state of Cu on the sample, the 2p core level of Cu was measured in detail and the resulting peaks were fitted using the XPS software Casa XPS [58] as

shown in Figure 6.61 and detailed fitting results in Table 6.4. The Cu 2p core level spectra are highly suited to determine the oxidation state of Cu and the measured data set fits very well to CuO [85]. The strong presence of satellite peaks in the spectra, which are of comparable intensity to the Cu 2p ½ peak clearly proof that at least the Cu near the sample surface has oxidized to CuO.

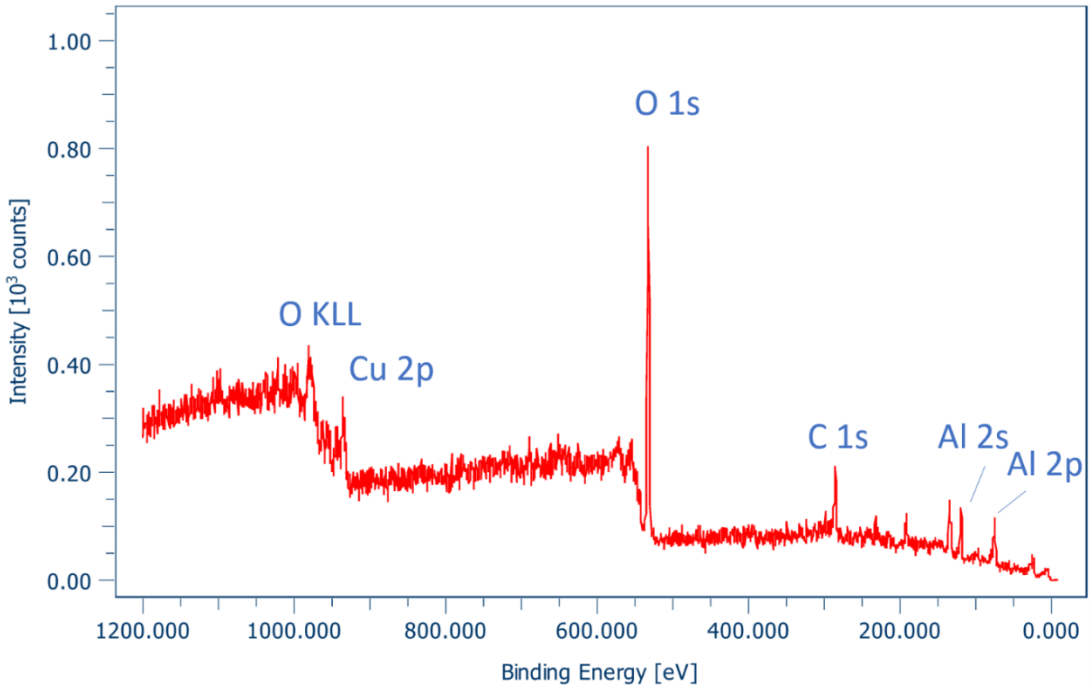

Figure 6.60. XPS survey scan for "CZ-Al_2O_3" measured post beamtime at room temperature. About half of the sample was previously covered with a 3 nm thick layer of carbon to reduce electric charging for SEM and Scanning Auger measurements.

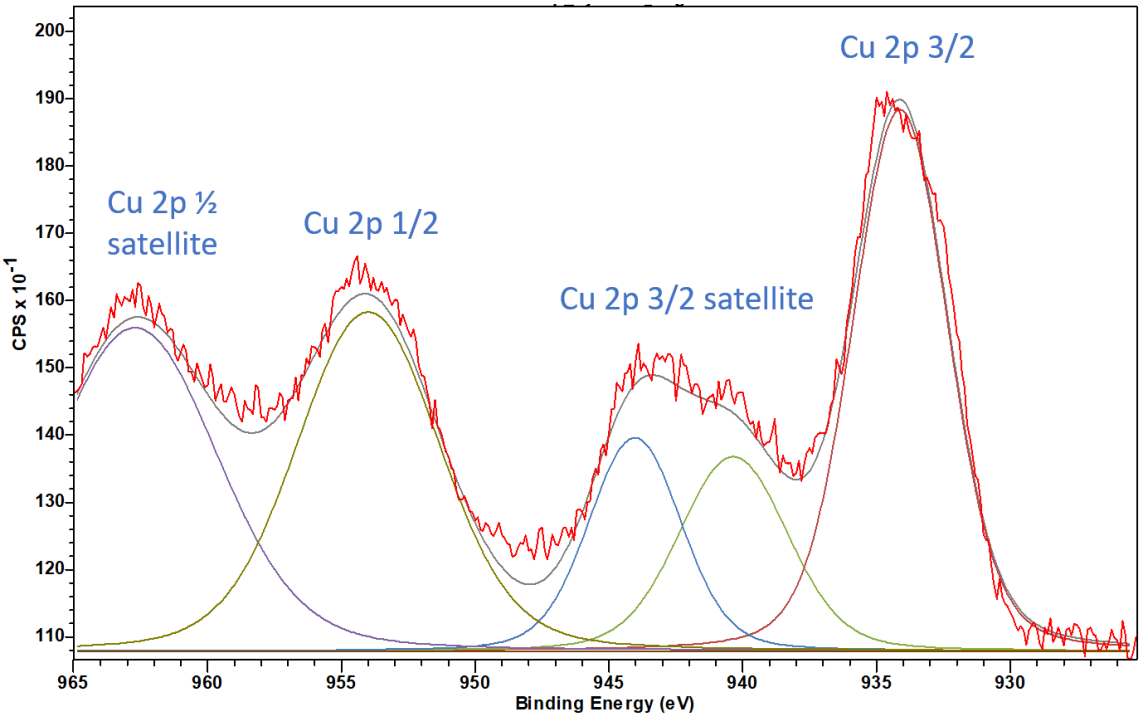

Figure 6.61. XPS spectra for Cu for "CZ-Al_2O_3" measured post beamtime at room temperature. The measured data set (red) was fitted with five separate components (violet, dark green, blue, light green, magenta) using the CASA XPS software. Detailed fit results can be found in Table 6.4.

Parameter	Cu 2p 3/2	Cu 2p 3/2 satellite	Cu 2p 3/2 satellite	Cu 2p 1/2	Cu 2p 1/2 satellite
Area	3898.2	1597.3	1492.5	3682.6	4025.5
FWHM	4.199	4.800	4.083	6.336	7.264
Position	934.11	940.35	944.03	953.99	962.71

Table 6.4. Detailed fitting results for the Cu XPS spectra of "CZ-Al_2O_3" as seen in Figure 6.61.

Finally, multiple spots on the sample were investigated and detailed scans for the Zn 2p core level were performed to see if any signal from Zn could be found. Despite comparably long measurement times, no clear Zn signal was found with the spectra shown in Figure 6.62, being the only spectra were a very small signal of Zn could possibly be seen. The data set is far from conclusive however, as the very slight peak in the spectra is hardly distinguishable from the level of background noise.

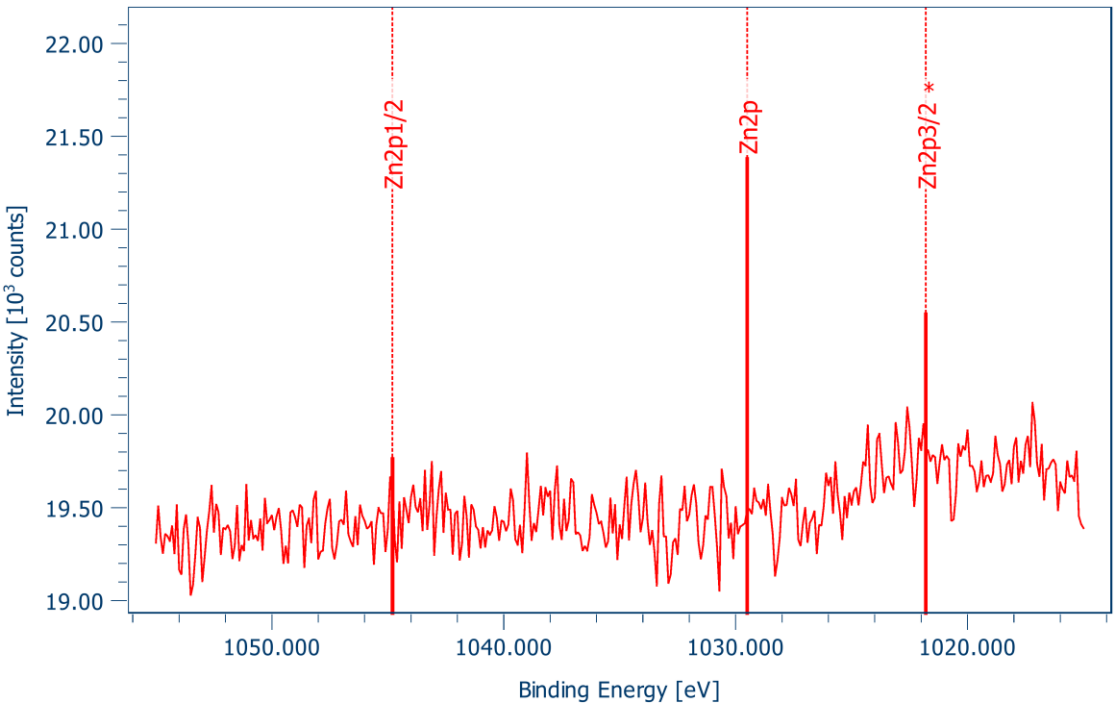

Figure 6.62. XPS spectra for Zn for "CZ-Al_2O_3" measured post beamtime at room temperature. Very slight peaks for Zn could possibly be identified here, but the data set is not conclusive. Multiple positions on the sample were analysed as well, revealing no visible Zn signal.

6.9. Summary and discussion

Stable (111)-oriented core-shell Cu-Cu_2O particles and formation of (110)-oriented particles below 575 K

The investigations of the simplified model system "Cu-Al_2O_3" show a clear evolution of Cu and Cu_2O phases in different reaction gas mixtures and at different temperatures. At room temperature in Ar, assumed to contain trace amounts of oxygen and water in the ~1 ppm range, prior to any activation procedure for the catalyst, clear signal for both Cu (111) and Cu_2O (111)-oriented particles as well as signal from a Cu_2O powder was measured, with the Cu_2O signal associated with native oxidation in air of the MBE grown metallic Cu particles. The particles show a clear epitaxial relationship with the sapphire substrate following Cu/Cu_2O (111) || Al_2O_3 (001) and Cu/Cu_2O (110) || Al_2O_3 (100). This epitaxial relationship of the Cu particles with the sapphire substrate was observed in previous studies using MBE growth of Cu on (001) single crystals of α-Al_2O_3 as well [69,86]. Given that only powder signal associated with Cu_2O powder was measured, the oxidation of the randomly oriented domains points to a smaller average size of these domains given the well-known size dependency of the copper oxidation of nanometre-sized particles [87]. Furthermore, in-plane signal of (111)-oriented particles is visible for both Cu and Cu_2O,

which clearly points to a core-shell type oxidation of the Cu particles, with a metallic Cu core being covered by a Cu_2O shell with the same crystal structure and orientation. Previous studies on ZnO substrates have also observed the oxidation of epitaxial Cu nanoparticles to Cu_2O without a change in the orientation of the particles [67].

With the stepwise increase of the sample temperature, changes in the in-plane signal for the different phases show the continuous growth of a Cu_2O phase with (110) out-of-plane orientation. As the in-plane signal for both Cu ($1\bar{1}1$) and Cu_2O ($1\bar{1}1$) remains stable, the formation of (110)-oriented particles could be associated with a rearrangement of the randomly oriented domains of Cu. This assumption is in accordance with later measurements at 575 K, for which the signal from powdered phases has vanished completely, pointing to a high mobility of Cu_2O at moderately elevated temperatures above 375 K. This formation of (110)-oriented domains on (001) Al_2O_3 at moderate temperatures is unexpected, given that the growth of epitaxial (110)-oriented Cu_2O particles on sapphire was only reported on c-plane sapphire with the utilisation of a buffer layer [88] or on a-plane sapphire [89]. Furthermore, an increasingly more pronounced splitting in the in-plane signal for both Cu ($2\bar{2}0$) and Cu_2O ($2\bar{2}0$) is observed with increasing sample temperature, which is in accordance with the formation of a coincidence site lattice of (111)-oriented particles on Al_2O_3, for which the Cu domains are in-plane rotated ±3° with respect to the high symmetry direction of the sapphire substrate. This coincidence site lattice was also observed by Oh et. al. for (111)-oriented Cu nanoparticles on (001) Al_2O_3 grown by MBE after annealing to 775 K in UHV [69]. The fact that this splitting is observed for both Cu and Cu_2O again points to the assumption of a core-shell type Cu-Cu_2O structure. This core-shell type structure remained stable below 575 K, in both Ar, observed to have an oxidizing effect due to trace amounts of water and oxygen estimated at about 1 ppm each, H_2 as well as CO including several cycling steps between pure Ar and H_2. The Cu_2O signal only disappeared after reaching 575 K in pure CO. At this condition both the (111) as well as the (110)-oriented particles were fully reduced without changing the epitaxial relation to the substrate and their out-of-plane orientation. These results indicate a stabilizing role of the sapphire substrate on the Cu_2O phase, as a previous study on very similarly prepared Cu nanoparticles on ZnO observed the full reduction of the Cu nanoparticles already at 500 K and under gas flow of a 4:1 ratio of Ar:H_2 under ambient pressure [67]. This stability could be a result of the formation of Cu-Al bonds as observed by Scheu et. al. for MBE grown Cu on α-Al_2O_3, observed in the

case that the support was cleaned with a number of Ar^+-sputtering and annealing cycles similar to the preparation of the supports in this work. Preparation without the Ar^+-sputter and annealing cycles were assumed to cause the formation of the less stable Cu-O-Al bonds instead, which were also proposed by Jensen et. al. [90]. In the latter study, the wetting-behaviour of Cu on Al_2O_3 is also linked to the presence of oxygen/hydroxyl-molecules on the surface, which for Cu growth on sapphire is assumed to improve the wetting, while for Cu growth on ZnO, the opposite behaviour is observed, were the presence of oxygen vacancies is assumed to improve the wetting behaviour [91,92].

Cu (110)-oriented particles show higher oxidation rate than (111)-oriented particles of the same size under the same reaction conditions

The in-situ ambient pressure measurements indicate that Cu particles with (110) orientation undergo oxidation and reduction more readily than Cu particles with (111) orientation at 575 K. This observed difference in oxidation behaviour cannot be attributed to variations in particle size, as analysis of the particle diameters during measurement reveals comparable sizes of 8–10 nm for both Cu (111) and Cu (110) domains. Additionally, the size of the (110) domains in the oxidized state remains consistent, with a notable increase in particle size upon prolonged exposure to oxidizing reaction gas. This increase aligns with a progressive oxidation process of the particles. These findings are consistent with the higher surface energy associated with Cu (110) facets compared to (111) facets, as established by Hansen et al. [91]. In their study, the morphology of copper nanocrystals was shown to dynamically adapt to variations in the reaction gas environment. Predominantly (111) facets stabilized under pure hydrogen, while exposure to an H_2/H_2O mixture promoted the growth of (110) and (100) facets, resulting in a more spherical particle shape. In this work, a similar evolution in Cu nanoparticle shape was observed by tracking the in-plane diameter of Cu particles under H_2 flow at various experimental stages. Initially, the particles exhibited a more disc-like morphology in the first H_2 condition, with progressively stronger signals from (110) and (100) facets as the number of reduction and oxidation cycles increased. Moreover, the stable preferential in-plane orientation of Cu (110)-oriented domains demonstrated that particle orientation remains stable through at least one oxidation-reduction cycle at these temperatures. Two separate domains with in-plane orientations following Cu (111) || Al_2O_3 (100) and Cu (001) || Al_2O_3 (100) were observed for the (110)-oriented particles following the reduction. The reaction gas dependent shape changes of Cu nanoparticles

as observed by Hansen et. al. were also observed for the Cu nanoparticles on the ZnO-supported model system "CZ-Al_2O_3" in this work. The analysis of the average Cu domain sizes shows a high mobility of the Cu atoms and particle sintering under oxidation and reduction cycles for the ZnO-supported model system at 575 K. Following the catalyst activation, the reduced Cu domains were fully oxidized to Cu_2O in Ar and then reduced again in H_2, causing an increase in the average Cu domains size of more than 20%. Additionally, the oxidation-reduction cycle resulted in the disappearance of the initially preferential (111)-oriented Cu domains, with a fully random in-plane orientation of Cu particles observed instead. Upon CO introduction into the reaction gas feed, preferential (110) orientation of Cu was observed, associated with the presence of two distinct Cu domains with different in-plane orientations, namely Cu (111) || Al_2O_3 (110) and Cu (001) || Al_2O_3 (100). The presence of two distinct in-plane oriented domains is similar to the observation made for the simplified model system "Cu-Al_2O_3", with the first set of domains oriented along the sapphire high symmetry direction and the second rotated with respect to the first around the surface normal. The rotation angle between the two types of domains is distinctly different between the two model systems however, with the observed angle of 5.3° for "Cu-Al_2O_3" and 35.3° for the ZnO-supported sample "CZ-Al_2O_3". The formation of 30° shifted domains on "CZ-Al_2O_3" can be associated with the comparably faster activation procedure of this catalyst model system under reducing conditions, since a similar phenomenon was observed by Oh et. al. [69]. In their paper from 2006, two separate in-plane orientations rotated by 30° with respect to each other around the surface normal were observed for (111)-oriented Cu nanoparticles on (001) Al_2O_3, depending on whether the Al_2O_3 surface termination was prepared to be -OH or -O. The domain that was shifted by 30° was observed to grow on -O terminated sapphire during a heat treatment at 675 K in UHV. Given the comparable sample preparation procedure of the study and this work, the presence of -O terminations on the support surface can be assumed, and the growth of the 30° shifted in-plane domain for "CZ-Al_2O_3" could be a result of the fast temperature increase during sample annealing under H_2, compared to the stepwise increase of the sample temperature under different and mostly oxidizing gases for "Cu-Al_2O_3". Furthermore, while the presence of two distinct in-plane orientations was also observed for ZnO for the ZnO-supported samples, the orientation of these domains is distinctly different to the ones observed for Cu, showing that the epitaxial Cu domains did not grow on top of the ZnO. For ZnO the out-of-plane signal

confirmed the assumption of c-oriented ZnO, with the two in-plane domains rotated by an angle of 21.67° around the surface normal with respect to each other. The in-plane orientations of these two ZnO domains are each about 10° off the sapphire high symmetry direction along (100) and are therefore unlikely candidates to explain the presence of the two distinct Cu in-plane oriented domains. The formation of ZnO is expected for the sample system, given that the oxidation of Zn to ZnO is highly exothermic with an approximated heat of formation for nanoscale particles of 3.456 ± 0.003 eV at 575 K (details in SI).

Oxidation of the metallic Cu domains was observed for both model system at 575 K under exposure to 1 bar of Ar gas flow, assumed to contain trace amounts of around 1 ppm of both oxygen and water. While the oxidation of Cu towards Cu_2O is exothermic at the experimental temperature, with a heat of formation of -1.74 eV, the activation energy of the oxidation can be approximated to be between 0.4-0.6 eV (details in SI). The chemical potentials of both O_2 and H_2 at 575 K and 1 bar total pressure were calculated to be between -0.3 to -0.6 eV for oxygen and -0.1 to -0.5 eV for H_2 depending on the partial pressure of the reaction gas as shown in Figure I.1. Therefore, the chemical potential of gas-phase oxygen is already sufficient to account for the Cu oxidation under the experimental conditions. The reduction of the Cu_2O phases to Cu however, can be approximated to have an activation barrier around 1.19 eV as determined for bulk phases, clearly showing that the chemical potential of H_2 from the gas phase cannot account for the reduction. Nonetheless, H_2 acts as a stronger reducing agent at 575 K for the simplified catalyst model system "Cu-Al_2O_3", compared to CO. Prolonged exposure to CO induced only negligible changes of the associated reflexes, whereas a switch to pure H_2 led to notable changes within 15 minutes. A full oxidation of the reduced (110)-oriented particles was observed after approximately 1 hour of exposure to Ar and CO_2 at 1 bar total pressure. Upon subsequent reduction in H_2, the Cu_2O signal disappeared after just 15 minutes, with Cu reflection signals reaching about half the intensity associated with fully reduced particles. Comparison of the simplified to the ZnO-supported model system reveal that the presence of Zn/ZnO did not affect the oxidation and reduction behaviour of the Cu domains for all of the different reaction gas mixtures used in the experiments, with the exception of exposure to pure CO_2. For the simplified model system, the Cu_2O signal did not stabilize under exposure to pure CO_2, suggesting rapid oxidation likely accompanied by particle sintering or rearrangement towards a powder-like structure.

Such a drastic structural degradation of the nanoparticles to a randomly orientated powder-like structure under CO_2 was also observed in a recent study for very similarly prepared Cu particles on ZnO substrates [67]. For the ZnO-supported model system, however, the Cu particles not only retained their structural integrity under pure CO_2, but no oxidation of the domains was observed. This difference in CO_2 reactivity is attributed to the incorporation of Zn into the Cu lattice and Cu-Zn alloy formation for the ZnO-supported system, as discussed in the following section.

Zn incorporation into Cu as a function of the reaction gas mixture

Analysis of the Cu reflexes under exposure to different gas atmospheres containing H_2, CO, CO_2 and Ar showed a change in the lattice parameter of Cu, that is dependent on the amount of hydrogen in the reaction gas mixture. The increased lattice parameter for Cu on the "CZ-Al_2O_3" sample can be associated with the incorporation of Zn into the Cu lattice. Given the similar experimental conditions as well as the Cu particle orientation, the lattice parameter determined for (110)-oriented Cu particles on the "Cu-Al_2O_3" sample can serve as a reference for the strain- and temperature corrected lattice parameter of metallic Cu. The measured increase in the lattice parameter comparted to this reference point for the "CZ-Al_2O_3" sample of up to 0.61% cannot be explained by either the incorporation of carbon nor oxygen into the lattice as the solubility of these elements in solid Cu is much too low [93,94]. Therefore, the incorporation of Zn is assumed as the cause for the lattice increase, reaching a maximum of 14.5% Zn into Cu in pure CO_2 at 575 K. Incorporation of Zn into the Cu lattice and the associated increase in the measured Cu lattice parameter was also suggested by Frei et. al. [95]. In their study, the increase of the bulk lattice parameter was observed to depend on the sample temperature during catalyst activation under hydrogen and was measured to reach about 10% for an annealing temperature of 673 K. While the Zn incorporation into the Cu domains during the activation of the catalyst under pure hydrogen was also observed in this work, the diffusion of Zn into the Cu domains is shown to change dynamically under reaction conditions, and was found to be a function of the amount of hydrogen in the reaction gas mixture. The strongest increase of the lattice parameter was observed under the absence of H_2 in pure Ar, CO and CO_2, and the smallest lattice constant measured in pure H_2. Additionally, signal form the $Cu_{0.64}Zn_{0.36}$ phase only emerged under reaction gas mixtures containing no H_2. From a thermodynamic standpoint, Zn incorporation into a Cu lattice is slightly exothermic with the heat of formation ranging from -0.01 to -0.09 eV, but the activation barriers involved

are relatively high, estimated between 1.244 eV to 1.814 eV for Zn contents between 5-34 at. % (details in Si). Therefore, the observed dynamic behaviour of the Zn incorporation as a function of the hydrogen content within the reaction gas mixture suggests a direct contact between the Cu phase and an adjacent phase of either a Cu-Zn alloy or ZnO, which is able to supply Zn with substantially lower activation barriers. Such a dynamic exchange of Zn between different crystal phases of the samples was further underlined by the measurements of the average Cu/Cu-Zn alloy crystal domain size in the different experimental conditions. The domain size showed a similar dependency on the amount of hydrogen in the reaction gas mixture, only inverse to the changes observed for the lattice parameter, as the domain size was determined to reach the lowest values in the absence of hydrogen and the highest under pure H_2 flow. For the Cu-ZnO-Al_2O_3 catalyst, a mobility of Zn under reaction gas conditions at elevated temperatures has been reported in numerous works, with a consensus that Zn diffusion between phases causes Cu-Zn alloy formation under reducing conditions and ZnO formation under oxidizing conditions [17,20,21]. Especially the works of Song et. al. [17] as well as Beck et. al. [43] can serve as direct comparison with this work, as they observed the formation of the same $Cu_{0.64}Zn_{0.36}$ phase on the surface of Cu after prolonged exposure of pure H_2. Furthermore, Song et. al. described the formation of a ZnO_x overlayer, when the sample was instead exposed to a 0.5% CO_2/H_2 mixture. While Amann et. al. [21] performed in-situ high pressure XPS measurements and therefore could not directly identify the exact structure of the Cu-Zn alloy phase, they report the formation of metallic Zn under CO reaction gas and ZnO under CO_2. Finally, Jensen et. al. [20] observed the presence of Cu-Zn alloy in H_2/CO_2, while only in gas mixtures containing CO, ZnO_x also emerged. A fundamental conclusion of these as well as other publications is that the formation of a Cu-Zn alloy phase is expected under reducing conditions of gas phases containing pure H_2, or H_2 and CO. The results of this work on the other hand show the emergence of the $Cu_{0.64}Zn_{0.36}$ phase only under reaction gas conditions free of H_2, so arguably in the most oxidizing conditions. One possible theory to explain this fundamental difference in the observed data is based on the presence of an additional $Cu_{0.2}Zn_{0.8}$ phase. The observed change in the FWHM of the Al_2O_3 reflex in different reaction gas mixtures in this work was therefore investigated, especially the pronounced decrease measured between the first and second exposure of the sample to pure H_2. Given the overall low intensity of the ZnO and $Cu_{0.64}Zn_{0.36}$ reflexes in stark contrast to the amount of Zn deposited on the sample during UHV sample preparation,

the presence of the $Cu_{0.2}Zn_{0.8}$ phase on the sample is considered. Given the lattice parameter of the $Cu_{0.2}Zn_{0.8}$ phase, the expected reflexes of this phase overlap almost perfectly with the Al_2O_3 reflexes, making it impossible to directly measure the presence of such a phase on the sample. Therefore, the observed changes in the FWHM of the sapphire reflex could be accounted for by a superposition of the reflex with a reflex of the $Cu_{0.2}Zn_{0.8}$ phase. This assumption is hard to validate further however, as the measurements of the Al_2O_3 reflexes were not adjusted to investigate the presence of a superposition with another reflex. The heat of formation for the $Cu_{0.2}Zn_{0.8}$ phase can be estimated to be around -0.06 eV, with a relatively low activation barrier for the phase reported around 0.69 eV (details in SI). The formation of the $Cu_{0.2}Zn_{0.8}$ phase is assumed to have occurred during the UHV sample preparation of the ZnO-supported model catalysts, specifically during the Cu deposition onto the previously deposited and oxidized ZnO. Within this context, Harikumar et. al. investigated the oxidation of metallic Zn as well as Cu diffusion through ZnO for sample systems that were prepared in a very similar procedure to the one used within this work [96]. They observed the formation of a dense ZnO layer of approximately 10 Å thickness during the oxidation of metallic Zn at 400–450 K, after which the layer thickness plateaued. Furthermore, the activation barrier for Cu diffusion through this 10 Å ZnO layer was measured to be 0.44 eV at 400 K, allowing significant Cu diffusion through the oxide shell and the formation of Cu-Zn alloy phases underneath this particle shell. While the study utilized mainly XPS measurements and thus could not determine the exact phase composition of the Cu-Zn alloy, its findings strongly implicate the formation of a Cu-Zn alloy on the ZnO-supported samples used in this work. Additionally, the $Cu_{0.2}Zn_{0.8}$ phase is thermodynamically the most likely Cu-Zn alloy to form under the described process for the model systems of this work, as its hexagonal structure offers the lowest lattice mismatch with the hexagonal structures of both the Al_2O_3 support and the c-oriented Zn and ZnO phases, compared to other stable Cu-Zn alloy phases. A general consensus within the literature regarding the dynamic behaviour of Zn within the CZA catalyst is that the exposure of ZnO on Cu to reducing reaction gas mixtures causes a reduction of the Zn and as a consequence a formation of a Cu-Zn alloy.

In-situ observed structures at ambient pressures and 575 K					Simplified model system Cu-Al_2O_3: "S"		ZnO-supported model system CZ-Al_2O_3: "Z"	
Measured phases→ / Reaction gas mixtures ↓	Cu		Cu_2O		US1	ZnO	$Cu_{0.64}Zn_{0.36}$	$Cu_{0.2}Zn_{0.8}$
H_2	S	Z			S	Z		Z
Ar + 1ppm O_2 and H_2O			S	Z	S	Z	Z	Z
CO	S	Z			S	Z	Z	Z
CO_2	S	Z			S	Z	Z	Z
Measured only for ZnO-supported model system CZ-Al_2O_3: "Z"								
H_2:CO (3:1)	Z				Z	Z		Z
H_2:CO (3:1)	Z				Z	Z		Z
H_2:CO:CO_2 (3:1:1)	Z				Z	Z		Z
H_2:CO:CO_2 (3:2:1)	Z				Z	Z		Z

Table 6.5. Overview of the measured material phases under the different reaction gas mixtures at ambient pressure and 575 K as observed for both the simplified and ZnO-supported model systems.

Exposure of the system to oxidizing atmospheres however, causes the opposite reaction, in which the Zn is preferentially oxidized, and an increased signal for ZnO/ZnO_x is measured. This general consensus cannot be applied to explain the appearance of the Cu-Zn alloy and ZnO phases of this work however. As is illustrated in Table 6.5, the appearance of the $Cu_{0.64}Zn_{0.36}$ as well as an increased signal of the ZnO phase is instead observed in the most oxidizing reaction gas mixtures which contain little to no hydrogen. To explain this observation, a possible mechanism of the interplay between the different phases of the sample is presented here and illustrated in Figure 6.63. Given the appearance of the $Cu_{0.64}Zn_{0.36}$ phase under oxidizing reaction gas mixtures, it is proposed that the presence of oxygen caused an oxidation of Zn from the outermost layers of the Zn rich $Cu_{0.2}Zn_{0.8}$ phase, which is covered by a thin layer of ZnO. The depletion of Zn from

these $Cu_{0.2}Zn_{0.8}$ domains could induce the transitions of these domains into the more Cu rich $Cu_{0.64}Zn_{0.36}$ phase.

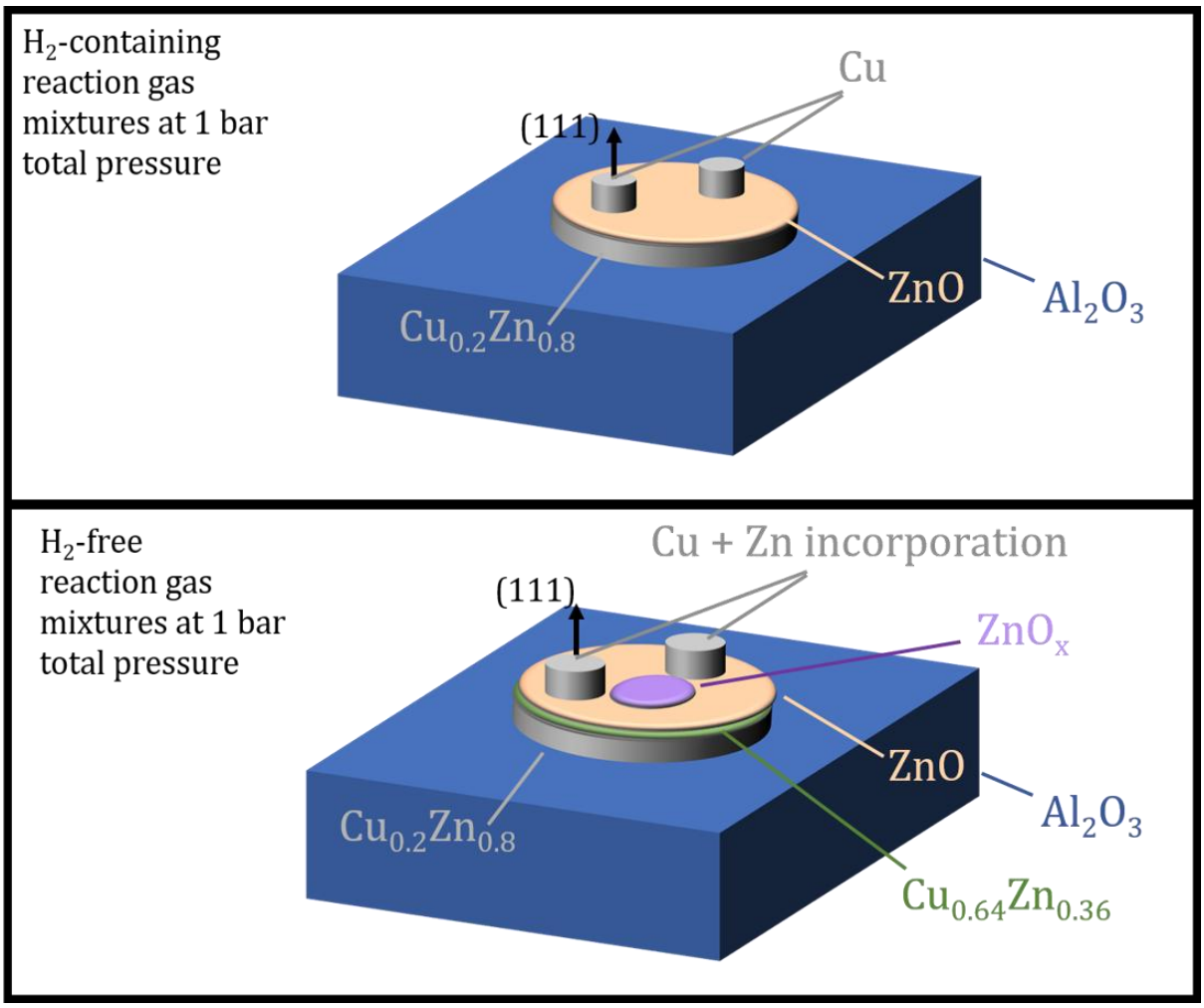

Figure 6.63. Schematic illustration of the proposed mechanism of Zn diffusion and the appearance of the different material phases of the ZnO-supported model catalyst under reaction gas flow containing H_2 (top) and free of H_2 (bottom) at 575 K and 1 bar total. Top: Under flow of hydrogen containing reaction gases the (001) Al_2O_3 support is at least partially covered by a (001) $Cu_{0.2}Zn_{0.8}$ phase encapsuled by a thin ZnO layer, on top of which disc-shaped metallic Cu particles were observed. Bottom: Under reaction gas flow containing no, or only trace amounts of hydrogen, Zn from the $Cu_{0.2}Zn_{0.8}$ phase is oxidized, forming ZnO_X at the surface. The depletion of Zn from the top layers of the $Cu_{0.2}Zn_{0.8}$ phase causes a transformation of these layers to the more Cu rich $Cu_{0.64}Zn_{0.34}$ alloy phase. Additionally, Zn from the $Cu_{0.2}Zn_{0.8}$ phase diffuses into the Cu nanoparticles either through the bulk or via the gas-phase and causes an increase in the lattice spacing of the Cu.

The transition of the phase simultaneously triggered the diffusion of Zn into the adjacent Cu nanoparticles, causing the observed lattice change of Cu in the different reaction gas mixtures. Additionally, The Zn from the $Cu_{0.2}Zn_{0.8}$ phase is oxidized, forming ZnO/ZnO_x phases at the surface. This proposed mechanism is based on the different observations made during the ambient pressure experiments, namely the measured signal for both

$Cu_{0.64}Zn_{0.36}$ and ZnO reflexes under the most oxidizing reaction gas mixtures, the dynamic variations of the Cu lattice parameter, as well as the change in the FWHM of the sapphire reflex assumed to be superimposed by the $Cu_{0.2}Zn_{0.8}$ phase. While the proposed mechanism for the dynamic diffusion of Zn between the two different Cu-Zn alloy phases of $Cu_{0.64}Zn_{0.36}$ and $Cu_{0.2}Zn_{0.8}$, has, to the best knowledge of the author, not been observed within the literature, a fundamentally similar mechanism was described by Xu et. al. [97]. Their study investigated the high-temperature oxidation behavior of a bulk Cu-Zn alloy with 38 at. % Zn, initially in the form of a single-phase α-brass alloy. During oxidation at temperatures ranging from 773 K to 1123 K, zinc atoms in the alloy diffused toward the surface, where they reacted with oxygen to form a ZnO shell. This process led to the formation of a Zn-depleted zone beneath the oxide shell, consisting of α-brass with a reduced Zn content due to selective oxidation. The oxidation kinetics followed a parabolic rate law, indicating diffusion control, and an activation energy of 1.82 eV was determined for this process. The mechanism described in the study is fundamentally similar to the mechanism proposed for the observations in this work, with the main difference being the scale of the Zn diffusion. While in the study of Xu et. al. the Cu-Zn alloy remained in its α-brass structure during the Zn depletion, the Zn diffusion in this work is assumed to be of a higher magnitude causing the transition of the $Cu_{0.2}Zn_{0.8}$ to the $Cu_{0.64}Zn_{0.36}$ phase as well as additional Zn diffusion into the adjacent Cu atoms. The increased diffusion observed in this work could be caused by the lower thermodynamic barriers for the removal of Zn from the $Cu_{0.2}Zn_{0.8}$ compared to the α-brass alloy as discussed above and in the supporting information.

Furthermore, the results of this work would suggest that for the investigated model system, not the presence of CO or CO_2 in the reaction gas mixtures is the determining factor in the oxidation of the $Cu_{0.2}Zn_{0.8}$ phase, but instead merely the absence of H_2. Assuming that the oxidation of the $Cu_{0.2}Zn_{0.8}$ phase causes the formation of $Cu_{0.64}Zn_{0.36}$, none of the reaction gas mixtures containing H_2 with CO, CO_2 or both, created a strong enough oxidation potential to oxidize the $Cu_{0.2}Zn_{0.8}$ phase. Only the absence of hydrogen in the reaction gases of Ar, pure CO or pure CO_2 enabled the oxidation of the $Cu_{0.2}Zn_{0.8}$ and in turn the increased signal of the $Cu_{0.64}Zn_{0.36}$ phase. The presence of the $Cu_{0.2}Zn_{0.8}$ phase was, to the best knowledge of the author, not reported before for the CZA catalyst system in the context of methanol synthesis.

Since no direct proof for the presence of this phase was observed, another theory for the observed alloy formation is discussed here. Assuming that the Cu and Zn interplay is fundamentally similar to the observations made in the other works mentioned above, meaning that the Cu domains are covered by a thin ZnO_x overlayer and Cu-Zn alloy formation is caused by the reduction of the overlayer, the role of hydrogen in the reaction gas mixture needs to be considered in more detail. The fundamental difference for the model system investigated in this work in this context is, that only reaction gas mixture free of H_2 would cause a reduction of the ZnO_x overlayer. Therefore, the reduction of the ZnO_x would mostly likely depend on the presence of H_2O on the sample, which is expected for all of the measured reaction gas mixtures containing H_2 due to the reverse water gas shift reaction. In his study [98], Spencer proposes, that for the Cu-ZnO catalysts, hydrogen dissociation on the ZnO phase only occurs under reaction gas conditions that cause a deficiency of adsorbed hydrogen on the Cu phase. In this context, the exposure to hydrogen-free reaction gas mixtures in this work may lead to oxidation of the Cu particle surface, thereby diminishing the ability of the Cu particles to absorb hydrogen from the ZnO phase via spill-over. This reduction in hydrogen uptake could trigger hydrogen dissociation directly on the ZnO surface, leading to the reduction of the ZnO phase. This process could explain the formation of the Cu-Zn alloy, which is observed only in hydrogen-free reaction gas mixtures.

Full transformation of Cu particles to (111)-oriented $Cu_{0.64}Zn_{0.36}$ in air

Additional investigations of the ZnO-supported model system "CZ-Al_2O_3" after a total of 17 days of exposure to air at room temperature, showed the formation of the $Cu_{0.64}Zn_{0.36}$ as the most prominent structure on the sample next to the unknown cubic structure US1, whereas no signal from epitaxial Cu or Cu_2O particles was observed. The prolonged exposure to air and therefore water, caused not only the formation of the $Cu_{0.64}Zn_{0.36}$ structure but also the full oxidation of the Cu to Cu_2O powder, similar to the changes observed at elevated temperatures under the exposure to Ar gas at 575 K assumed to contain trace amounts of H_2O. The simplified model system "Cu-Al_2O_3" sample, in contrast, still exhibited fully metallic Cu powder signal even after prolonged exposure to air. This is particularly notable, as room temperature measurements in Ar, conducted after just 2 days of air exposure prior to the ambient pressure experiment, clearly showed the presence of Cu_2O due to native oxidation. This suggests that exposure to the various

reaction gas mixtures at elevated temperatures likely resulted in the formation of an oxidized Cu shell around the metallic Cu cores. Once this shell reached a certain thickness, it significantly hindered further oxygen diffusion into the Cu core during air exposure. The formation of such a dense CuO shell surrounding a Cu core and preventing further oxidation of the core was observed for example by Fang et. al. in 2024 [99]. While the measured Cu domain size during the ambient pressure experiments were very comparable between "Cu-Al_2O_3" and "CZ-Al_2O_3", the difference in the oxidation behaviour could still be influenced by a difference in the particle size, which is known to be an important factor in the oxidation behaviour of nanometre-sized Cu particles [87]. Particle size analysis using SEM of the ZnO-supported model system "CZ-Al_2O_3", showed particles with an average size almost 20 times larger than the size determined during the ambient pressure measurements, with a size of 188 nm after 3 months and 148 nm after 8.5 months of exposure to air. Such coalescence of nanoparticles on substrates at room temperature is associated with Oswald ripening [100]. Similar measurements could unfortunately not be conducted on the simplified model system "Cu-Al_2O_3", so the influence of the Cu particle size on the oxidation behaviour in air for the investigated systems remains elusive. Nonetheless, the full oxidation of the Cu on the ZnO-supported model system further supports the assumption of the formation of a Cu-Zn alloy at the surface of the Cu particles, which fundamentally changes their oxidation behaviour and prevents the formation of a dense CuO shell around a metallic Cu core.

Loss of Zn from Cu-Zn alloy in air

The mobility and reactivity of Zn at room temperature in air is further underlined by the EDX measurements of the sample after both 3 and 8.5 months of exposure to air, which did not reveal any Zn signal on the sample. To gather more surface sensitive signal, the sample was then further investigated by both scanning auger as well as XPS. No clear Zn signal was detected in these measurements either, showing a near complete depletion of Zn from the sample. A depletion of Zn from Cu-Zn alloy particles was also mentioned in the literature as caused by Zn entering the gas-phase due to its high vapor pressure and was observed at pressures of only several hundred millibar and at moderate temperature of 318 to 418 K [17,21]. Such a depletion of Zn is only expected directly from the Cu-Zn alloy phase as Zn is known to form a stable ZnO layer in air, which is protecting the metallic core underneath from further oxidation [101,102]. Therefore, these results again

show that the Zn that was deposited onto the ZnO-supported model system readily formed Cu-Zn alloy phases, whereas only thin ZnO layers were formed.

Measurement of unknown crystal structure

Signal from a crystal structure with yet unknown chemical composition, referred to as *unknown structure 1* or US1, was observed for both the simplified "Cu-Al_2O_3" and ZnO-supported model system "CZ-Al_2O_3". The measurements indicate that the structure was already present either directly after the UHV sample preparation or after the 2 additional days of exposure to air, with only minor changes in the associated signal of the structure observed under different reaction gas mixtures. The US1 structure was identified as a cubic structure with a lattice parameter of 7.1149 Å, oriented with the (111) direction along Al_2O_3 (001). An extensive search for a fitting structure type for this phase was conducted with the most promising candidate being the low-cristobalite structure of $AlPO_4$. This structure matched best to both the presence of measured reflexes as well as the structure factors out of all the compared structures, but further analysis of the data is still needed and will continue beyond the scope of this work. Given the elemental composition of the phase and its presence on both "Cu-Al_2O_3" and "CZ-Al_2O_3", it is believed that the structure formed during the Al_2O_3 sample preparation in UHV and was caused by the Ar^+-sputtering of the sapphire substrates. This assumption is further underlined by the fact that the samples investigated under operando conations as described in the following chapter, were prepared in the exact same way as the ambient pressure samples, except for the Ar^+-sputtering and annealing cycles, which were omitted for these samples. In the investigation of the other samples under operando conations, no signal from the US1 structure was found. It is not clear at which point a possible contamination with P could have occurred, but trance amounts of phosphorus were also identified in the EDX measurements 3 months after the ambient pressure experiment. The formation of an $AlPO_4$ structure is not mentioned in the context of the CZA catalyst for methanol synthesis or the MBE-based preparation of single crystal sapphire.

7. Operando SXRD measurements: Reduction and sintering of Cu_2O particles at pressures over 20 bar

Similar to the measurements done at ambient pressure as described in the previous chapter, two different model systems, one with and one without ZnO/Zn were used during the operando measurements, denoted "Cu-Al_2O_3-operando" for the simplified model system and "CZ-Al_2O_3-operando" for the ZnO-supported one. Both samples were investigated at the DESY P07 beamline, already described in the previous chapter, utilizing high energy X-rays and a 2D detector setup in different reaction gases at up to 30 bar of total pressure and 685 K sample temperature. For the experiment, the operando SXRD stage as described in chapter 5 was used.

7.1. Reduction of copper oxide particles on Al_2O_3 (001)

Representing the simplified model catalyst, the sample "Cu-Al_2O_3-operando" - Cu nanoparticles grown directly onto a (001) Al_2O_3 single crystal substrate following the same growth parameters as for the "Cu-Al_2O_3" sample which was investigated in ambient pressure – showed clear signs of native oxidation of Cu at room temperature at a total pressure of 23 bar in pure Ar as can be seen in Figure 7.1. At this point of the measurement the sample had already been exposed to 23 bar of Ar pressure for about 20 hours.

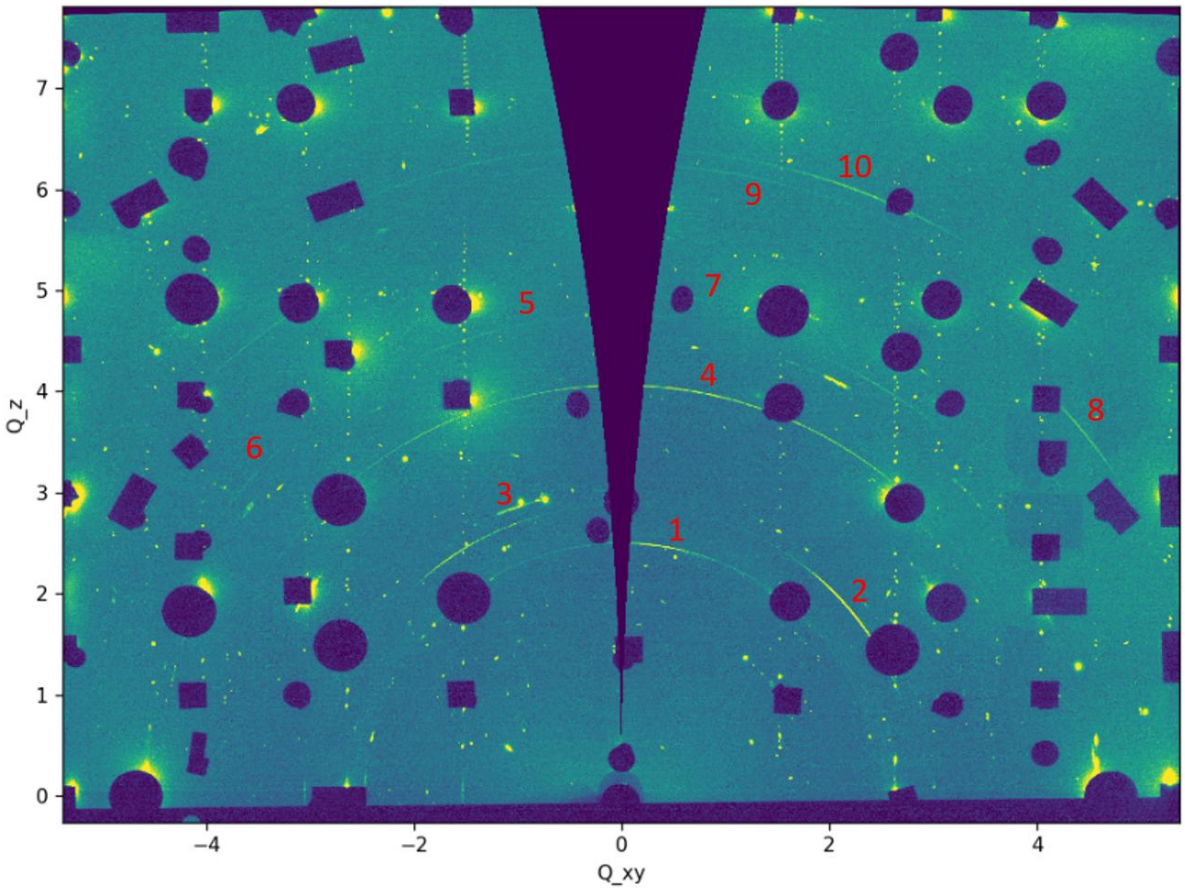

Figure 7.1. Maximum pixel image of the 2D detector data of "Cu-Al_2O_3-operando" measured at room temperature in Ar at a pressure of 23 bar over a 90° sample rotation. Visible powder ring sections are numbered in red, with the corresponding momentum transfer listed in Table I.28.

Under these conditions, several powder-ring sections were observed, as analyzed in Table I.28. Drawing from the results of the in-situ XRD measurements at ambient pressures, exposure to Ar gas, assumed to contain trace amounts of oxygen and water, is expected to oxidize the metallic Cu nanoparticles. Similarly, prior to the exposure to high pressure Ar gas flow, the sample was exposed to air for multiple days, which was shown in the previous chapter to cause the partial oxidation of the Cu particles to Cu_2O due to native oxidation.

As shown in Table I.28, the momentum transfer of the measured signals does not align directly with reflexes from either Al_2O_3 or Cu_2O. Although the measured values could technically be most closely matched to Al_2O_3 reflexes, this association comes with an average discrepancy of 0.91% ± 0.46%, and would only occur in case of the formation of an Al_2O_3 powder, for which numerous additional reflexes would be expected, none of which appear in the data. Furthermore, Al_2O_3 is known to be highly stable at the experimental temperature and under the range of reaction gases used in this work, making the presence of an Al_2O_3 powder unlikely. In contrast, the association with Cu_2O

is notably more consistent: while the average discrepancy is 2.28%, all measured reflexes closely align with the expected Cu_2O reflexes, and the discrepancy is uniform, suggesting a strain effect within the particles. This level of deviation falls well within the expected strain range for epitaxial particles with a lattice mismatch to the support. The peak labelled "3" aligns well with Cu (111), the most intense Cu reflex, clearly showing the presence of (111)-oriented metallic Cu particles on the support. Continued oxidation and increasing particle strain was observed upon an additional 1.5 hours of exposure to the high pressure Ar gas flow as shown in Figure 7.2 and Table I.29, with the momentum transfer being on average 0.38% ± 0.09% smaller than in the first measurement. For the second measurement the comparison with both Al_2O_3 and Cu_2O yields similar results as for the first measurement, in that the sapphire reflexes are much closer on average, but show a much higher inconsistency as seen by the equally high mean deviation of 0.46%. The Cu_2O reflexes now shown an on average 2.66% larger momentum transfer, but with a more consistent mean deviation of just 0.19%. The peak denoted with number “3”, again matches Cu (111).

Given the much higher consistency of the comparison with the Cu_2O reflexes, the data set points to the presence of an oxidized Cu_2O lattice, which is considerably strained. The lattice is slowly expanding with continued exposure to high pressure Ar gas, containing oxygen and H_2O impurities, pointing to a continuous advancement of the partial oxidation of Cu particles. The further the oxidation of the Cu particles advances, the more strain is induced, causing an increase in the measured lattice spacing. The signal fitting to the (111) reflex of metallic Cu shows the presence of an unstrained copper core underneath the Cu_2O.

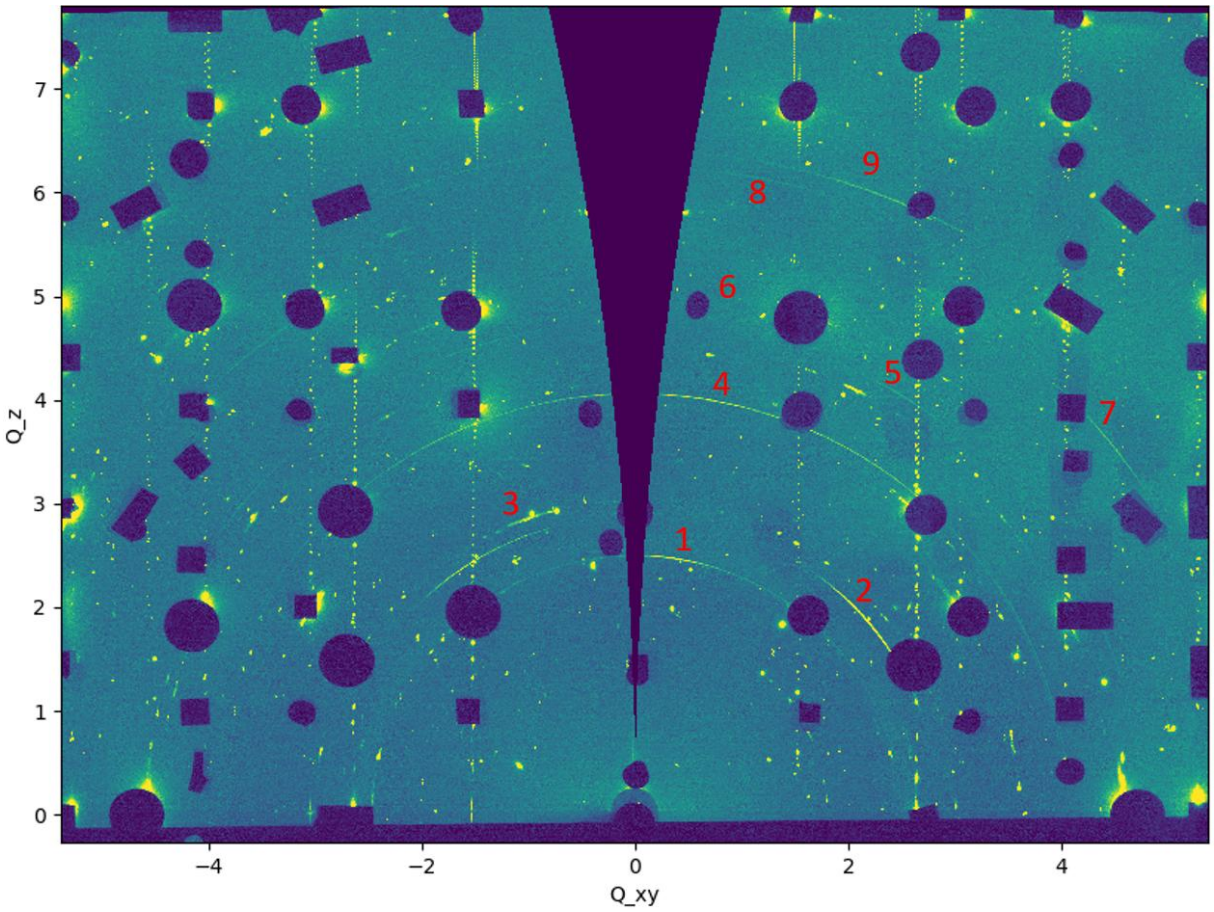

Figure 7.2. Maximum pixel image of the 2D detector data of "Cu-Al_2O_3-operando" measured at room temperature in Ar at a pressure of 23 bar over a 90° sample rotation, 1.5 hours after the previous measurement. Visible powder ring sections are numbered in red, with the corresponding momentum transfer listed in Table I.29.

Following the room temperature exposure to 23 bar of Ar, the sample temperature was increased to 685 K and the pressure was increased to 30 bar. The increased sample temperature caused a complete reduction of the previously observed oxidized Cu phase to a metallic Cu powder as seen in Figure 7.3. Additionally, an azimuthal integration was carried out for this measurement, which further underlines, that all signals observed in the scan can be associated with either metallic Cu or Al_2O_3.

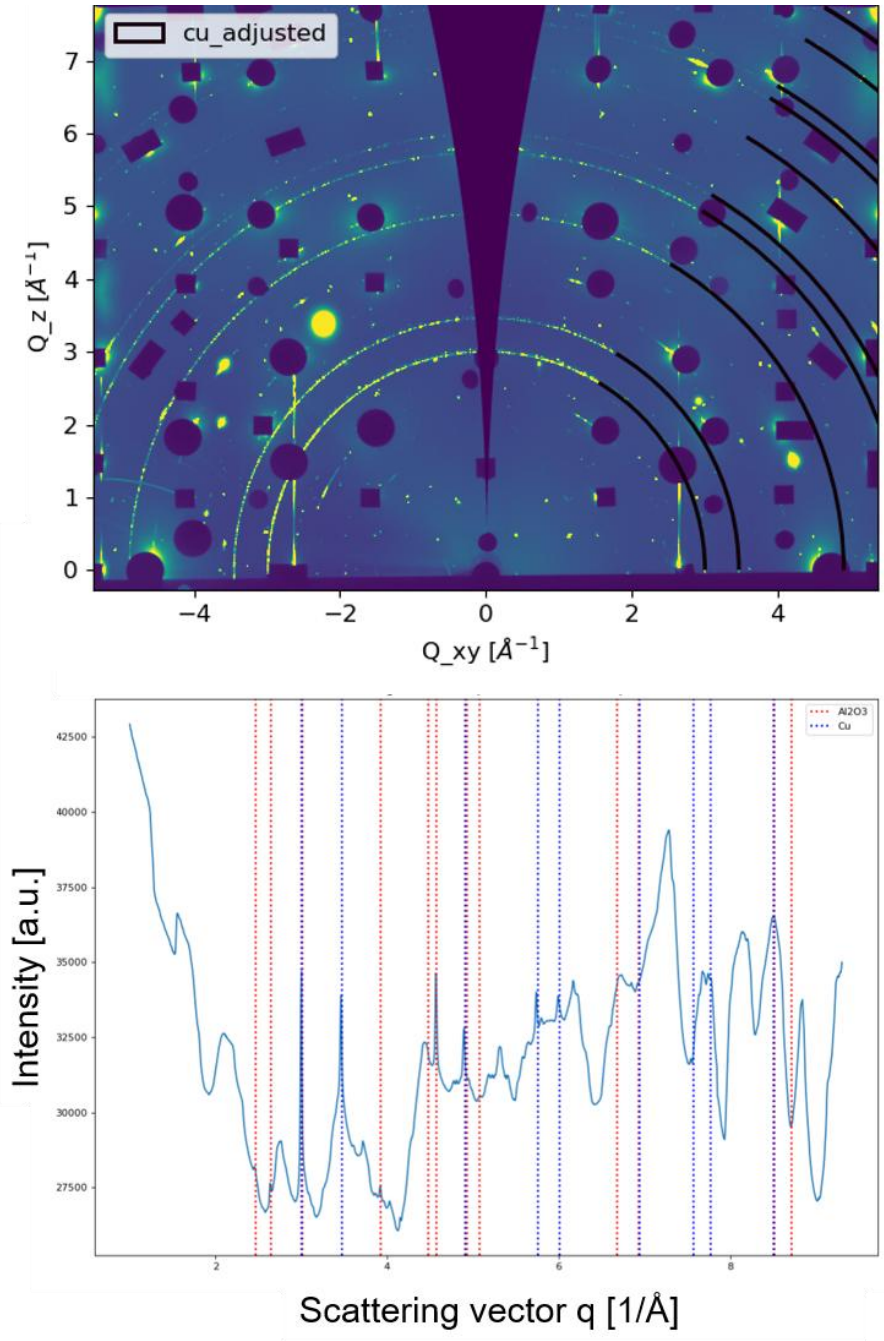

Figure 7.3. Top: Maximum pixel image of the 2D detector data of "Cu-Al_2O_3-operando" measured at 685 K in Ar at a pressure of 30 bar over a 90° sample rotation. Black lines indicate the position of Cu powder rings. Bottom: Azimuthal integration of the max pixel image and vertical lines indicating the position of Al_2O_3 (red) and Cu (blue).

Following exposure to pure Ar, introduction of H_2 in an H_2:Ar (4:1) mixture yielded very similar results as can be seen in Figure 7.4. The reduction of the Cu with H_2 evidently did not cause the formation of ordered particles, as no signal from ordered domains or any preferential orientation within the powder rings can be observed.

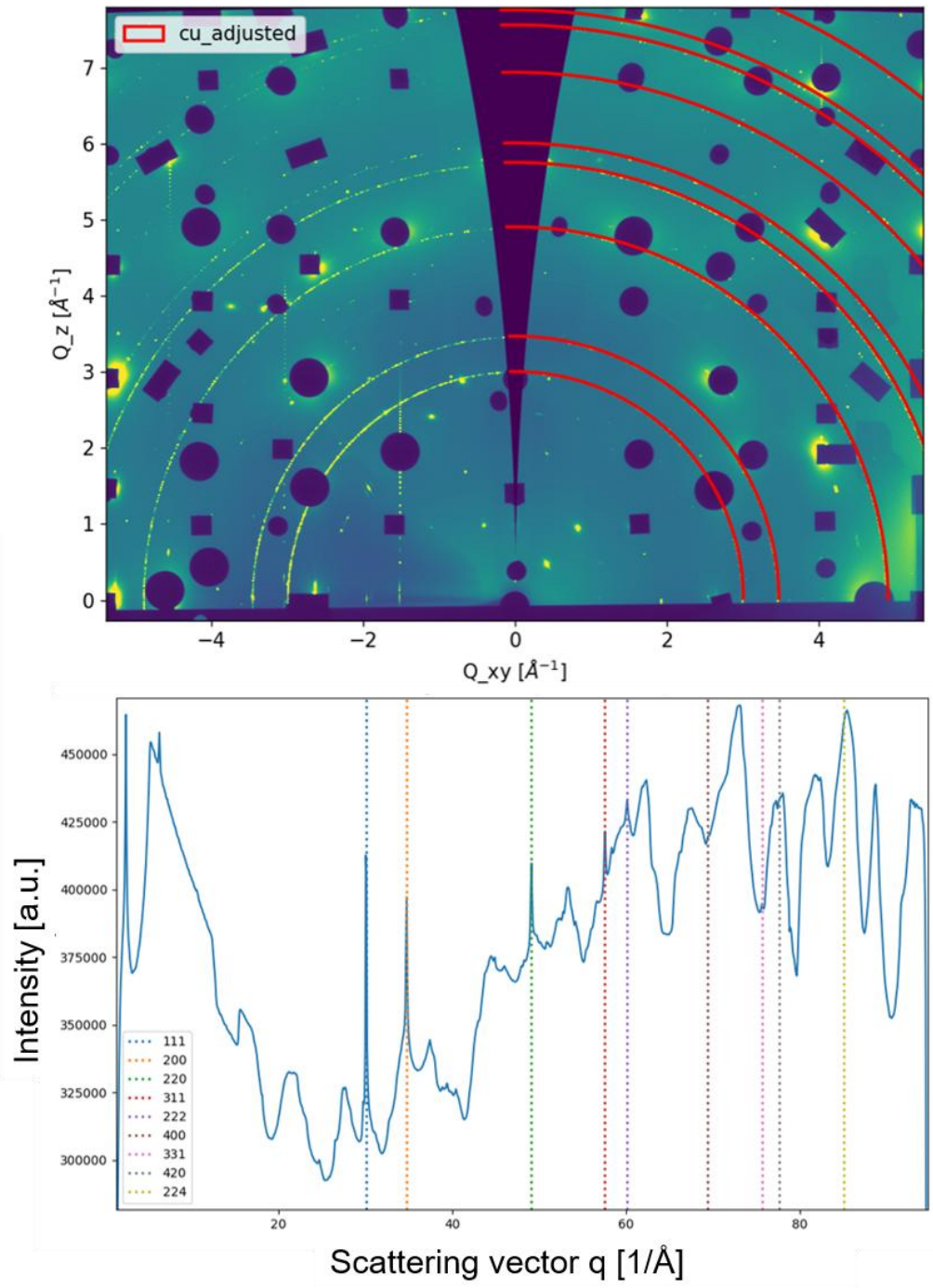

Figure 7.4. Top: Maximum pixel image of the 2D detector data of "Cu-Al_2O_3-operando" measured at 685 K in an H_2:Ar (4:1) mixture, at a total pressure of 30 bar over a 90° sample rotation. Red lines indicate the position of Cu powder rings. Bottom: Azimuthal integration of the max pixel image and vertical lines indicating the position the different Cu reflexes.

After the introduction of hydrogen, the next scans of the sample were performed in reaction gas mixtures containing CO. As the post beamtime analysis revealed, the installed carbonyl trap of the CO gas line did not function properly, and evidently the sample was exposed to Ni-carbonyls, which are still contained in CO gas even of very high purity. The signal of Ni was immediately observed in the first scan containing CO as seen in Figure

7.5. In the CO:H_2:Ar (1:4:1.25) reaction gas mixture additional powder rings of Ni can be seen, close to the powder ring of Cu.

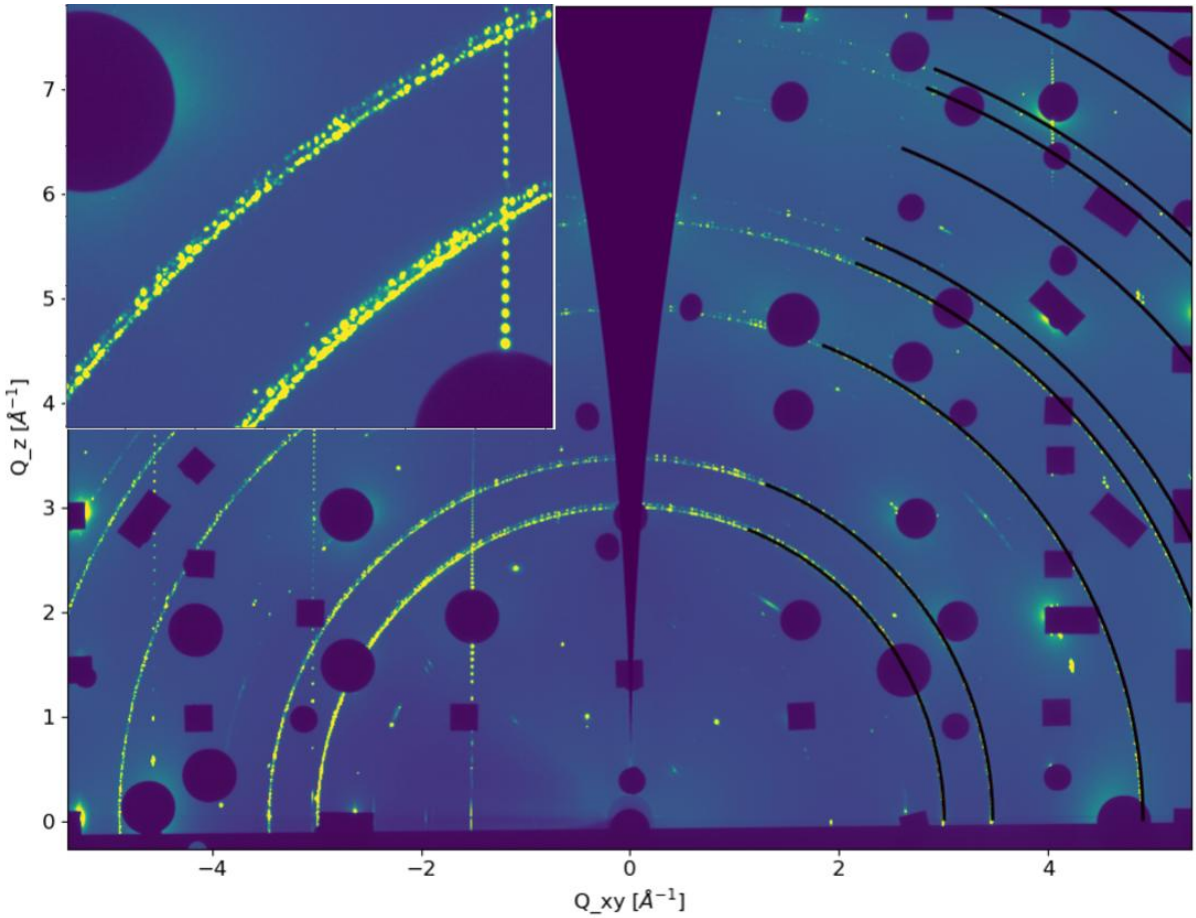

Figure 7.5. Maximum pixel image of the 2D detector data of "Cu-Al_2O_3-operando" measured at 685 K in an CO:H_2:Ar (1:4:1.25) mixture, at a total pressure of 30 bar over a 90° sample rotation. Black lines indicate the position of Cu powder rings. Inlet: Close-up on the first two powder rings revealing the presence of two distinct powder rings very close to another.

Following an increase of the CO fraction in the reaction gas mixture to CO:H_2:Ar (2:4:0.75), the Ni signal becomes considerably more intense and the co-existence of both Cu and Ni becomes even more evident as seen in Figure 7.6.

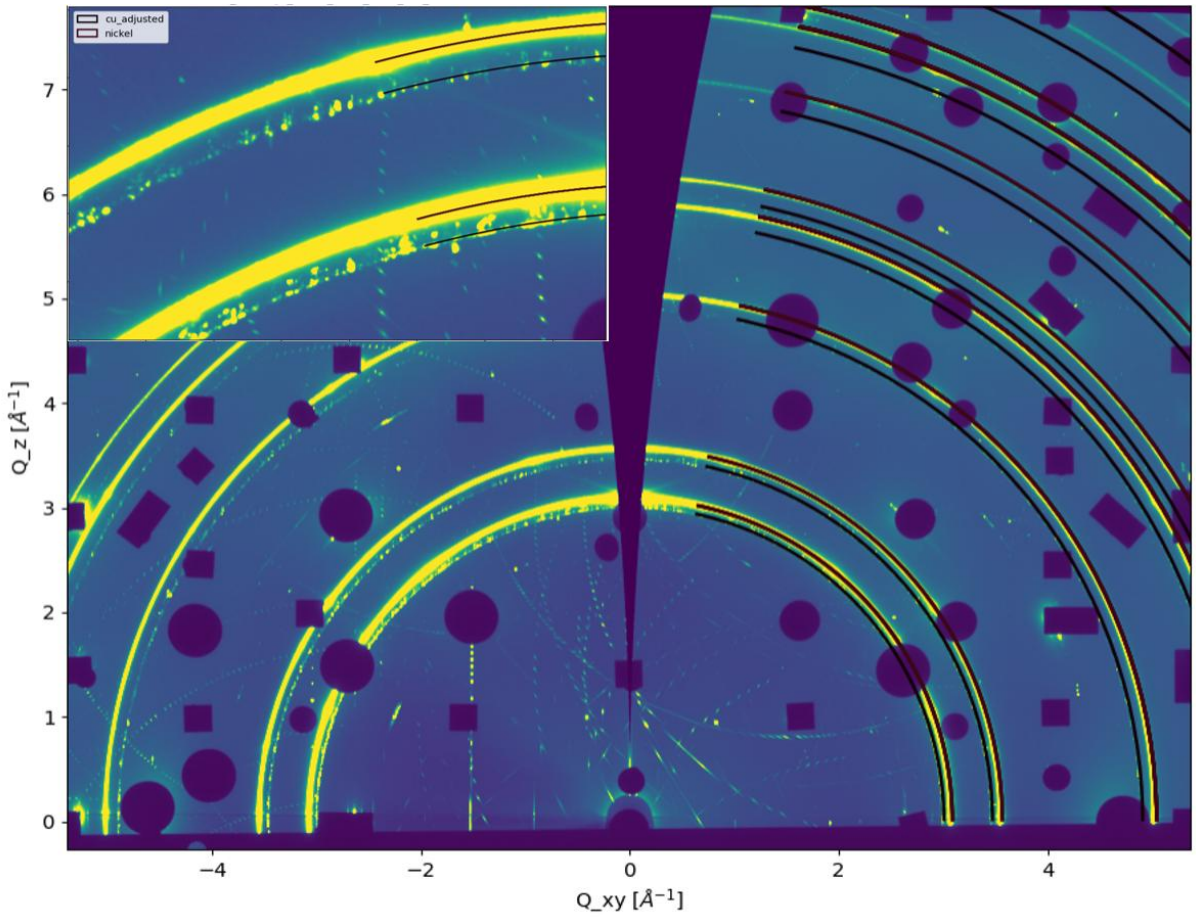

Figure 7.6. Maximum pixel image of the 2D detector data of "Cu-Al_2O_3-operando" measured at 685 K in an CO:H_2:Ar (2:4:0.75) mixture, at a total pressure of 30 bar over a 90° sample rotation. Lines indicate the position of powder rings of Cu (black) and Ni (red). Inlet: Close-up on the first two powder rings underlining the presence of both metallic Cu and Ni.

Despite the unwanted exposure of the sample with Ni, even in a reaction gas containing CO:H_2 in a ratio of 1:2, the spotty character of the Cu powder rings is still apparent. While the smooth Debye diffraction ring of Ni evidently shows that the Ni has formed a powder of individual nanoparticles, the spotty character of the Cu proofs a stable presence of larger Cu domains, associated with macroparticles [103].

7.2. Reduction and sintering of copper oxide on CZA model catalyst

As a more complete model system for the industrial Cu-ZnO-Al_2O_3 catalyst, "CZ-Al_2O_3-operando" was prepared in the same way as the "CZ-Al_2O_3" sample analysed in the previous chapter.

ZnO-supported model catalyst under 30 bar Ar pressure at room temperature

The first scan of "CZ-Al_2O_3-operando" was performed at room temperature and under 30 bar of Ar pressure as shown in Figure 7.7. A number of powder ring sections can be

identified in these conditions, which match well to the ones observed on the simplified model system "Cu-Al_2O_3-operando" at room temperature described above, as can be seen in the analysed momentum transfer in Table I.30. Again, one can find Al_2O_3 reflexes close to each of the measured values, with an average discrepancy of 0.64%, but the consistency of the comparison to sapphire is low as seen by the high mean deviation of 0.43%. Comparison to Cu_2O yields much more consistent results with an average discrepancy of 2.27% and a much lower mean deviation of 0.18%. The peak denoted with the number "3", is again associated with the (111) reflex of unstrained metallic Cu, showing the presence of a metallic core underneath the Cu_2O shell.

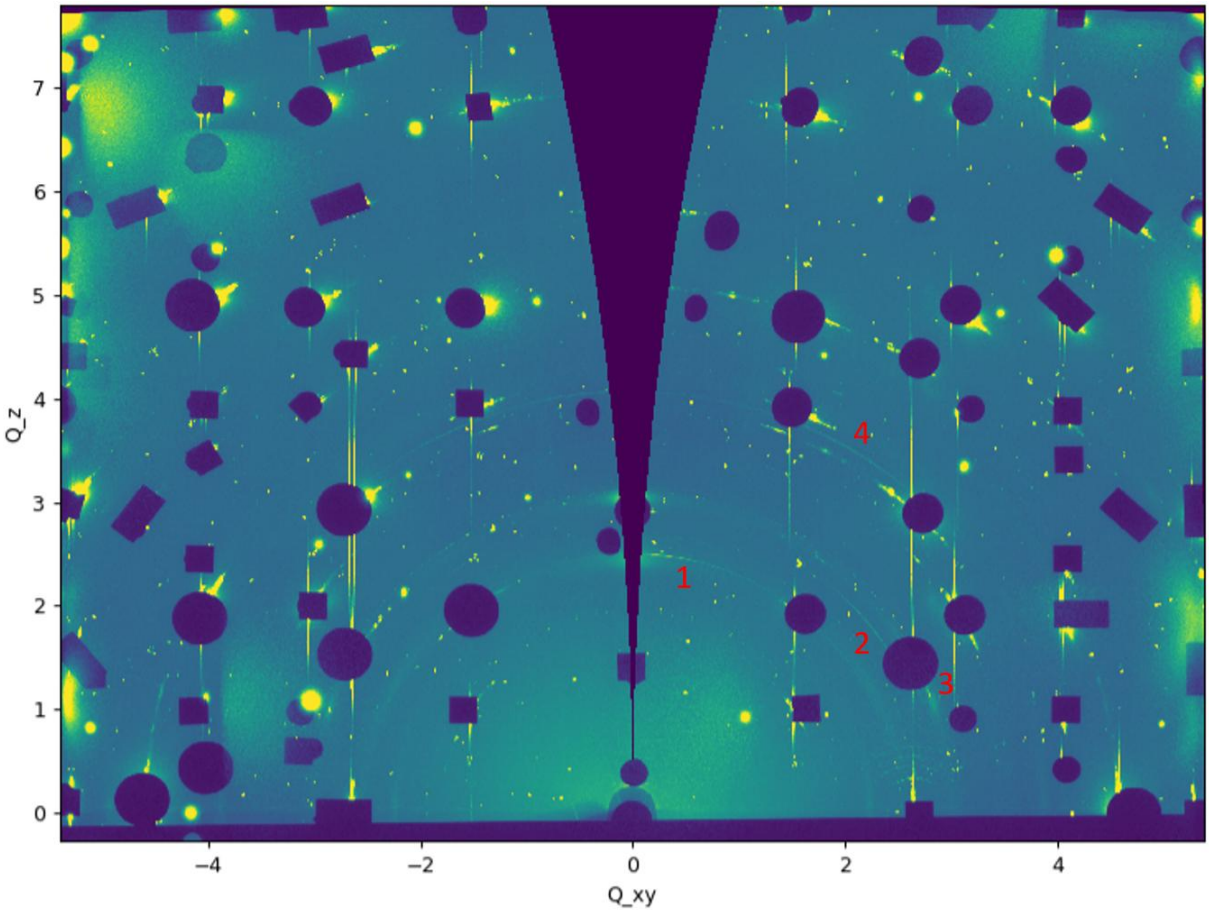

Figure 7.7. Maximum pixel image of the 2D detector data of "CZ-Al_2O_3-operando" measured at room temperature in Ar at a pressure of 30 bar over a 90° sample rotation. Visible powder ring sections are numbered in red, with the corresponding momentum transfer listed in Table I.30.

Investigation of specific angular ranges of the sample rotation revealed oriented domains as shown in Figure 7.8. In addition to the previously discussed powder rings, signal from preferentially oriented domains is visible as seen in the zoomed in view in the inlet of Figure 7.8. As shown in Table I.31, the peak matches to Cu (111). The position of the preferential orientation is also consistent with Cu nanoparticles oriented with the (111)

direction parallel to the substrates (001) direction. On the right-hand side of the detector the (220) Cu reflex can be observed as well as seen in Figure 7.9, further underlining the assumption of (111)-oriented Cu domains.

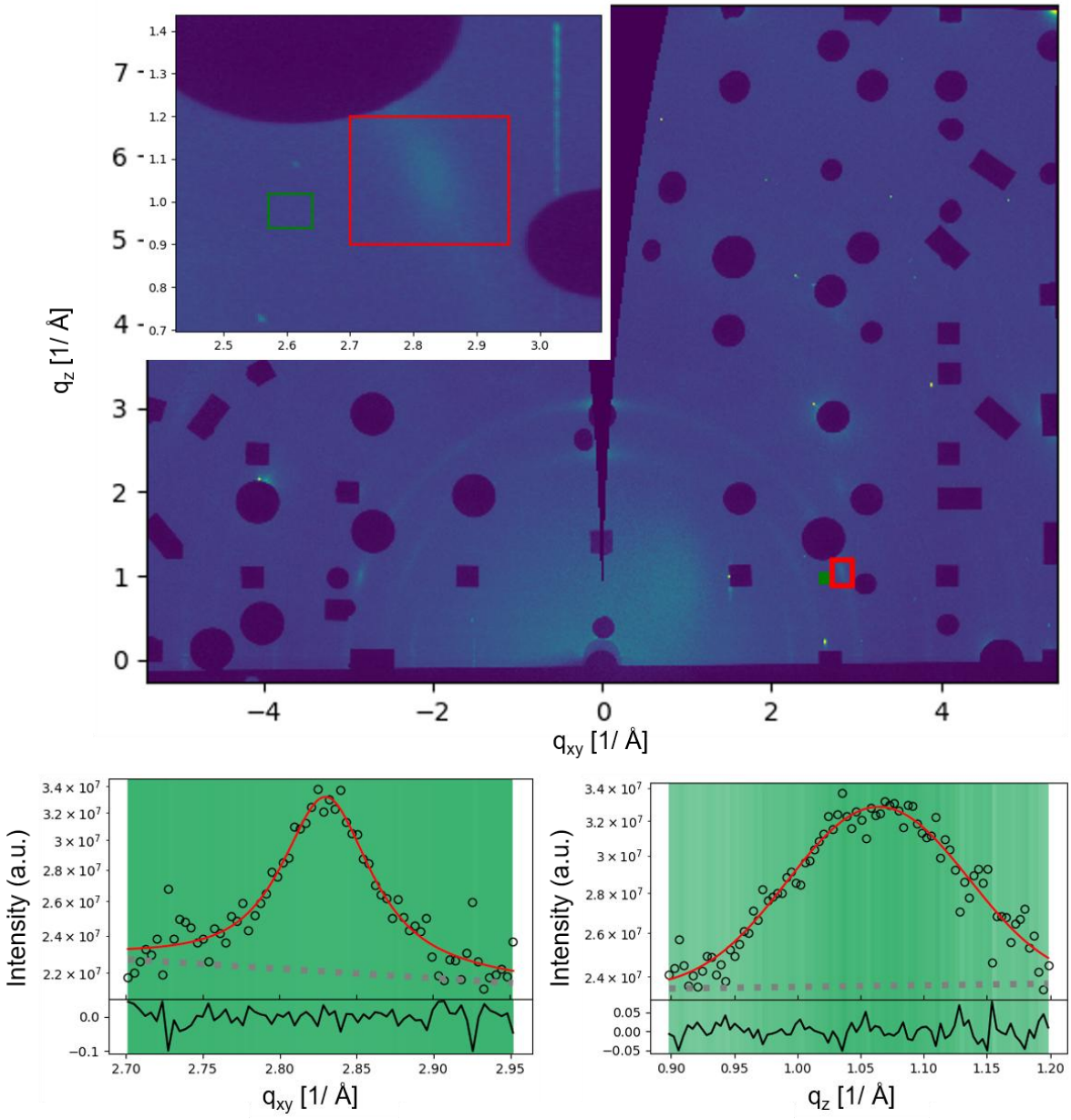

Figure 7.8. Top: Maximum pixel image of the 2D detector data of "CZ-Al_2O_3-operando" measured at room temperature in Ar at a pressure of 30 bar over a 6° sample rotation. The region of interest is marked in red. Inlet: Zoomed view of ROI. Bottom: Fit results for the signal in the red ROI with data found in Table I.31.

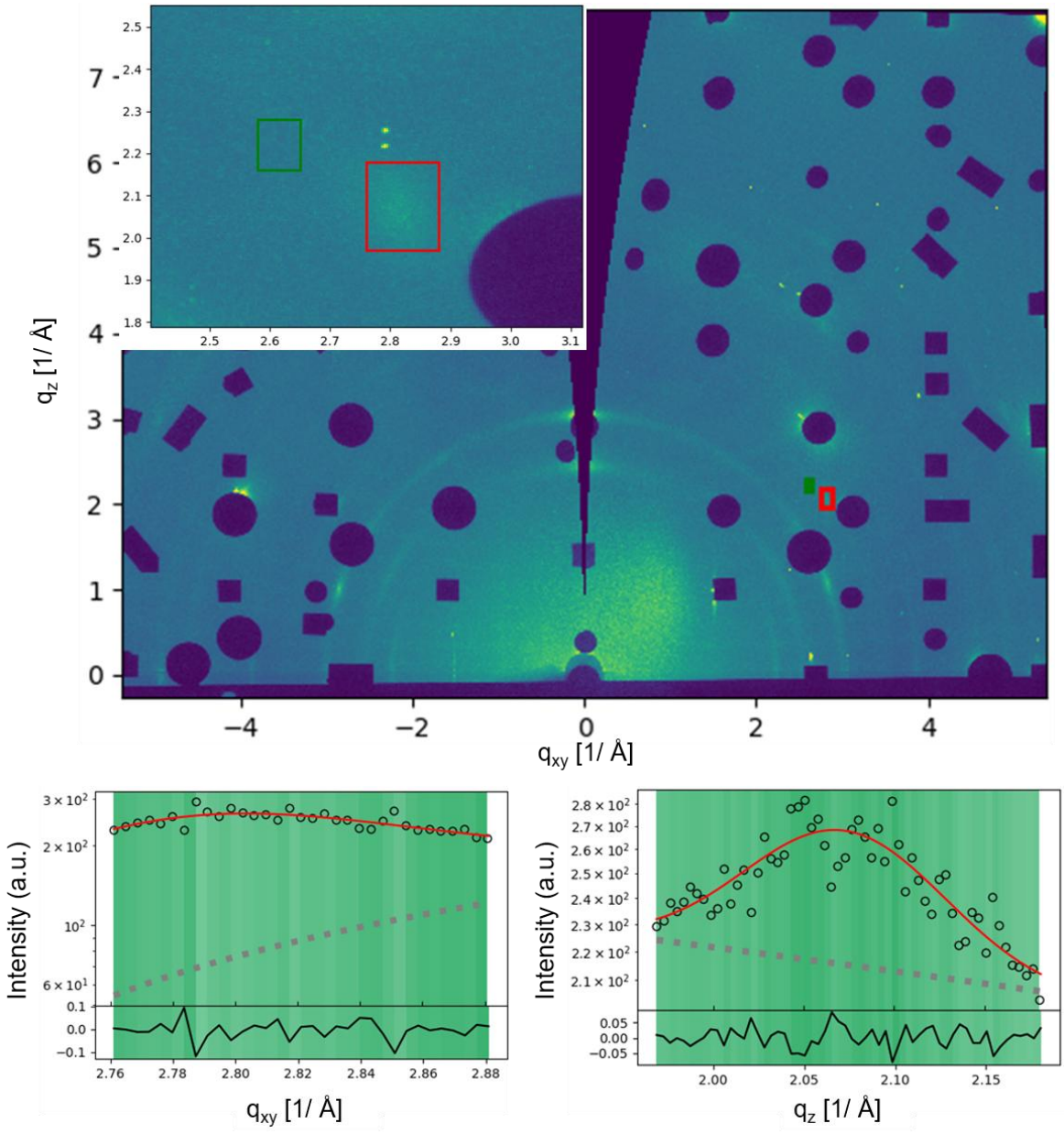

Figure 7.9. Top: Maximum pixel image of the 2D detector data of "CZ-Al_2O_3-operando" measured at room temperature in Ar at a pressure of 30 bar over a 6° sample rotation. The region of interest is marked in red. Inlet: Zoomed view of ROI. Bottom: Fit results for the signal in the red ROI with data found in Table I.31.

Additionally, a powder matching Cu_2O (111) is visible as seen in Figure 7.10. For all of the reflexes associated with (111)-oriented Cu and Cu_2O, the average FWHM of the peaks was determined, to calculate the domain size of the given reflex as an indication of the nanoparticle size. As shown in Table I.31, the size of the nanoparticles of Cu and Cu_2O is in the 4-6 nm range, which is comparable to the nanoparticle sizes determined for the similarly prepared samples measured in-situ at ambient pressure, as discussed in the previous chapter. Especially considering the presence of both Cu and Cu_2O, a 4-6 nm Cu

core with a 4 nm shell, matches very well to the domain sizes of the fully reduced Cu particles determined at ambient pressures, of 8-10 nm.

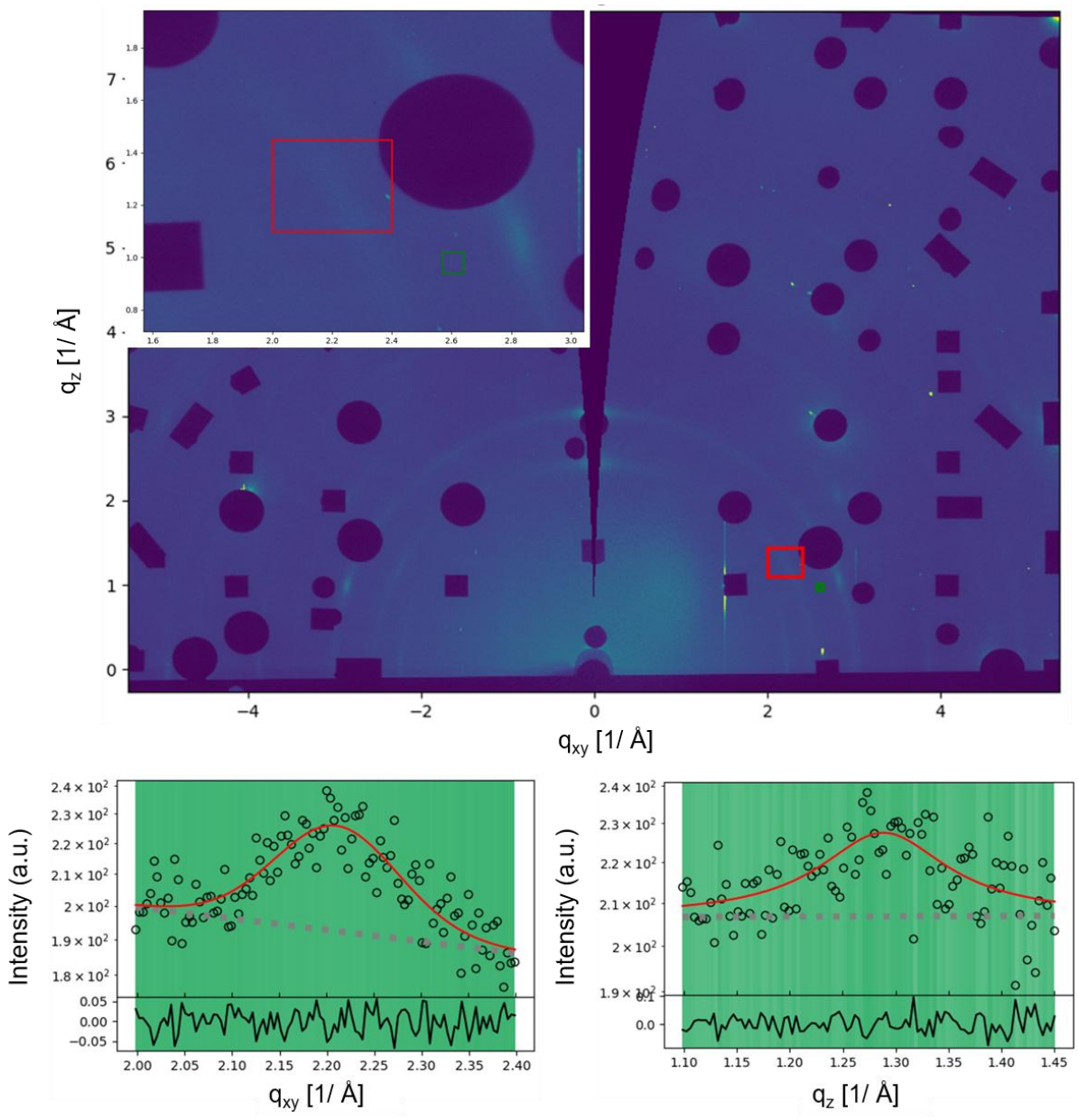

Figure 7.10. Top: Maximum pixel image of the 2D detector data of "CZ-Al_2O_3-operando" measured at room temperature in Ar at a pressure of 30 bar over a 6° sample rotation. The region of interest is marked in red. Inlet: Zoomed view of ROI. Bottom: Fit results for the signal in the red ROI with data found in Table I.31.

ZnO-supported model system at 30 bar Ar pressure at 550 K

Following the room temperature measurement, the gas composition and pressure were kept constant while the sample temperature was increased to 550 K. As can be seen in Figure 7.11, a large number of powder rings with a spotty appearance were observed, most of which are associated with Al_2O_3. On the ring fitting to the position of Cu (111) also multiple separated spots are observed, including one at the position of the powder ring at which the preferential orientation was observed in the previous scan, fitting to the signal expected for (111)-oriented particles, which was fitted and yielded an estimated domain/particle size of 25.86 nm as seen in Table 7.1. As the momentum transfer of the Cu (111) reflex is also very close to the Al_2O_3 (113) it cannot be determined with certainty, whether the observed signal does indeed belong to Cu (111). Similar to the measurements in the previous experimental condition, also smaller angular ranges of just a few degrees were analysed for this scan, but no additional signals were found.

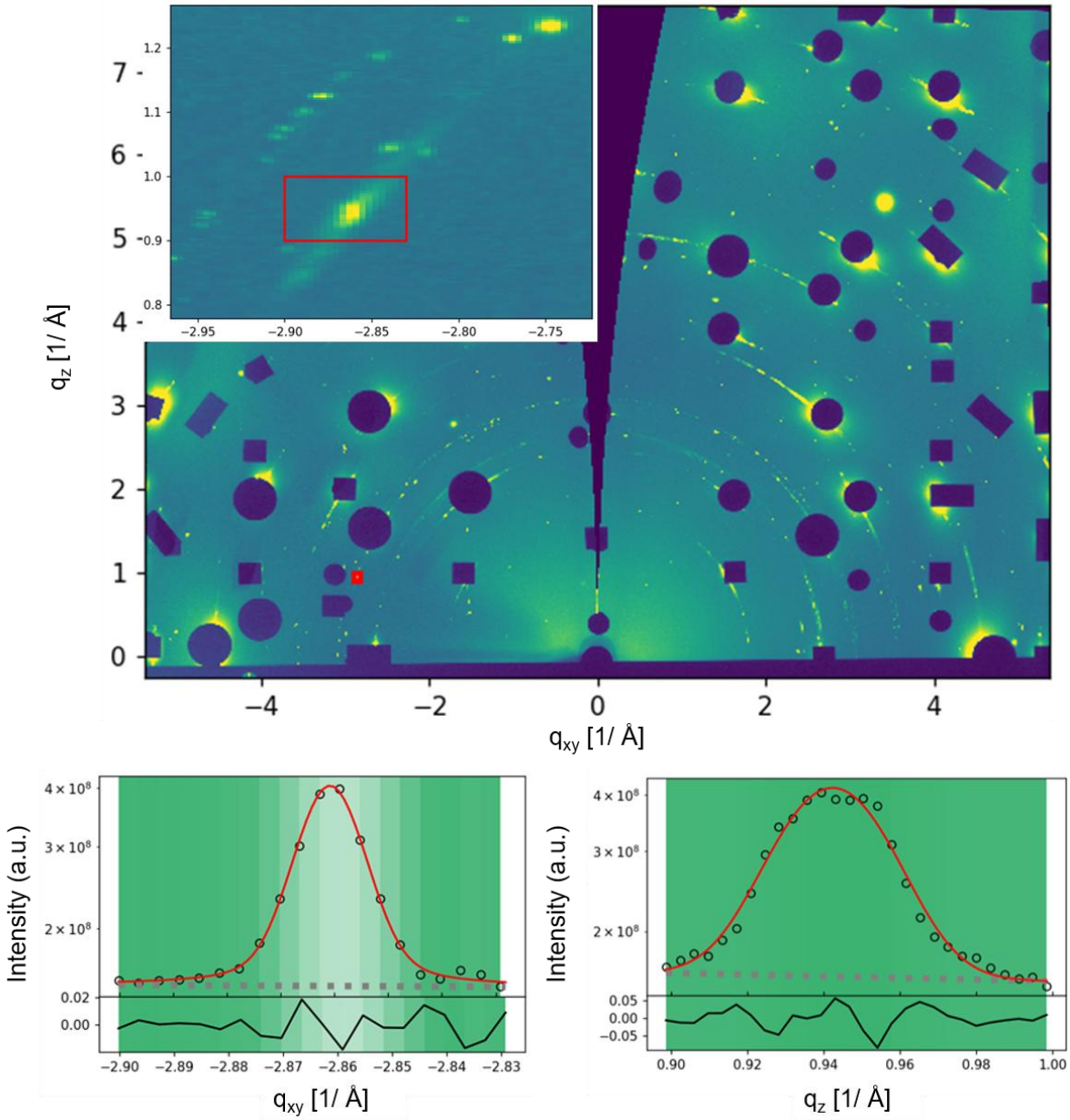

Figure 7.11. Top: Maximum pixel image of the 2D detector data of "CZ-Al_2O_3-operando" measured at 550 K in Ar at a pressure of 30 bar over a 90° sample rotation. The region of interest is marked in red. Inlet: Zoomed view of ROI. Bottom: Fit results for the signal in the red ROI with data found in Table 7.1.

Peak [#]	q_xy [1/ Å]	q_z [1/ Å]	q [1/ Å]	Reference [1/ Å]	Average FWHM [1/ Å]	Nanoparticle size [nm]
1	2.8608	0.9424	3.01202497	Cu (111) 3.01	0.0243	25.86

Table 7.1. Fit results and nanoparticle size calculations for the ROI in Figure 7.11.

Apart from the Cu nanoparticle signal, another spotty powder ring was observed as seen in Figure 7.12. The momentum transfer of this ring is clearly different from any of the close by Al_2O_3 reflexes, and a fit of one of the measured reflexes in the ring yielded a momentum transfer of 3.077 as seen in Table 7.2. Given the observations of the Cu-ZnO-

Al_2O_3 sample measured in-situ at ambient pressure, in which the presence of a $Cu_{0.2}Zn_{0.8}$ phase was assumed, the powder ring seen here could arise from a similar Cu-Zn alloys phase. For the $Cu_{0.2}Zn_{0.8}$, most reflexes are very close to Al_2O_3 reflexes and could be covered by the substrate signals to a large extend. The visible spotty powder ring is about 1.75% too large for the $Cu_{0.2}Zn_{0.8}$ however, as seen in Table 7.2.

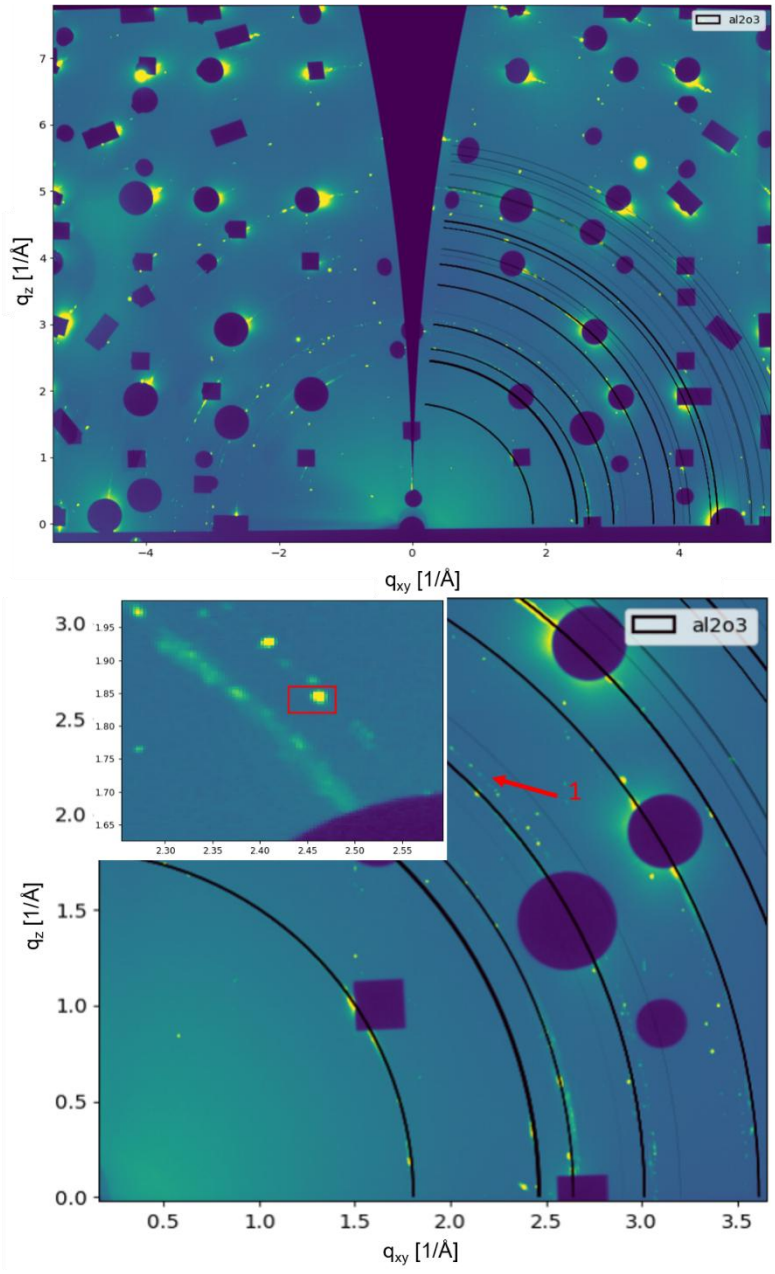

Figure 7.12. Top: Maximum pixel image of the 2D detector data of "CZ-Al_2O_3-operando" measured at 550 K in Ar at a pressure of 30 bar over a 90° sample rotation with black line showing the position of Al_2O_3 reflexes as Debye-Scherrer rings. The transparency of the rings scale with the relative intensity of the reflex. Bottom: Close-up view of the image showing the spotty Debye-Scherrer ring. Inlet: Close-up of the spotty Debye-Scherrer ring with the analysed spot marked with a ROI in red. Fit results for the signal in the red ROI can be found in Table 7.2.

Peak [#]	q_xy [1/ Å]	q_z [1/ Å]	q [1/ Å]	$Cu_{0.2}Zn_{0.8}$ Reference [1/ Å]	Δ [%]
1	2.462	1.845	3.077	3.024 (101)	1.75

Table 7.2. Fit results for the ROI in Figure 7.12.

ZnO-supported model system under 30 bar H_2 pressure at 550 K

A malfunction of the setup caused a delay as well as the sample to be turned up-side down. The delay was used to switch the reaction gas to pure H_2 keeping the sample temperature at 550 K. As can be seen in Figure 7.13, after the delay and the switch to hydrogen, very clear and smooth Debye-Scherrer rings for Cu are visible. Very few small spots can still be seen on the first (111) Cu ring, but these cannot be clearly associated with larger macroparticles as the position of the spots is inconsistent and does not fit to the previously observed preferential orientation. An azimuthal integration of the scan was performed as well, clearly proofing the presence of a Cu powder.

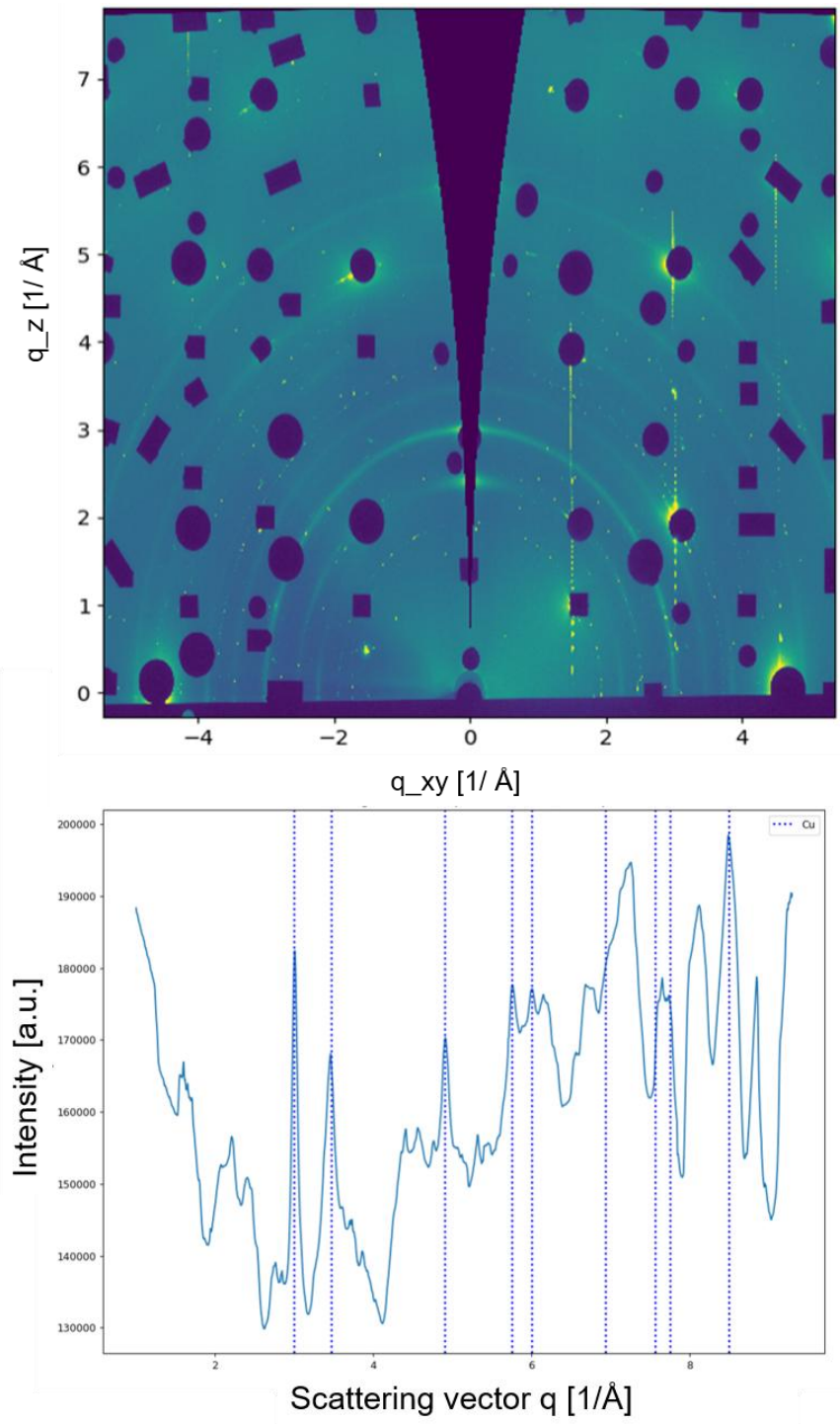

Figure 7.13. Top: Maximum pixel image of the 2D detector data of "CZ-Al_2O_3-operando" measured at 550 K in H_2, at a total pressure of 30 bar over a 90° sample rotation. Bottom: Azimuthal integration of the max pixel image and vertical lines indicating the position the different Cu reflexes.

Similar to the previous measurement, additional spotty Debye-Scherrer rings appeared as shown in Figure 7.14. The analysis of the momentum transfer of the rings in Table 4.7, and the comparison to the close-by Al_2O_3 reflex positions shows an average discrepancy of 2.13% and a very high inconsistency of the comparison as seen by the mean deviation

of 2.65%. The results clearly point to a phase that is not closely related to the crystal structure of sapphire. Additionally, the spotty Debye-Scherrer ring observed in the previous measurement is not visible under the H_2 conditions.

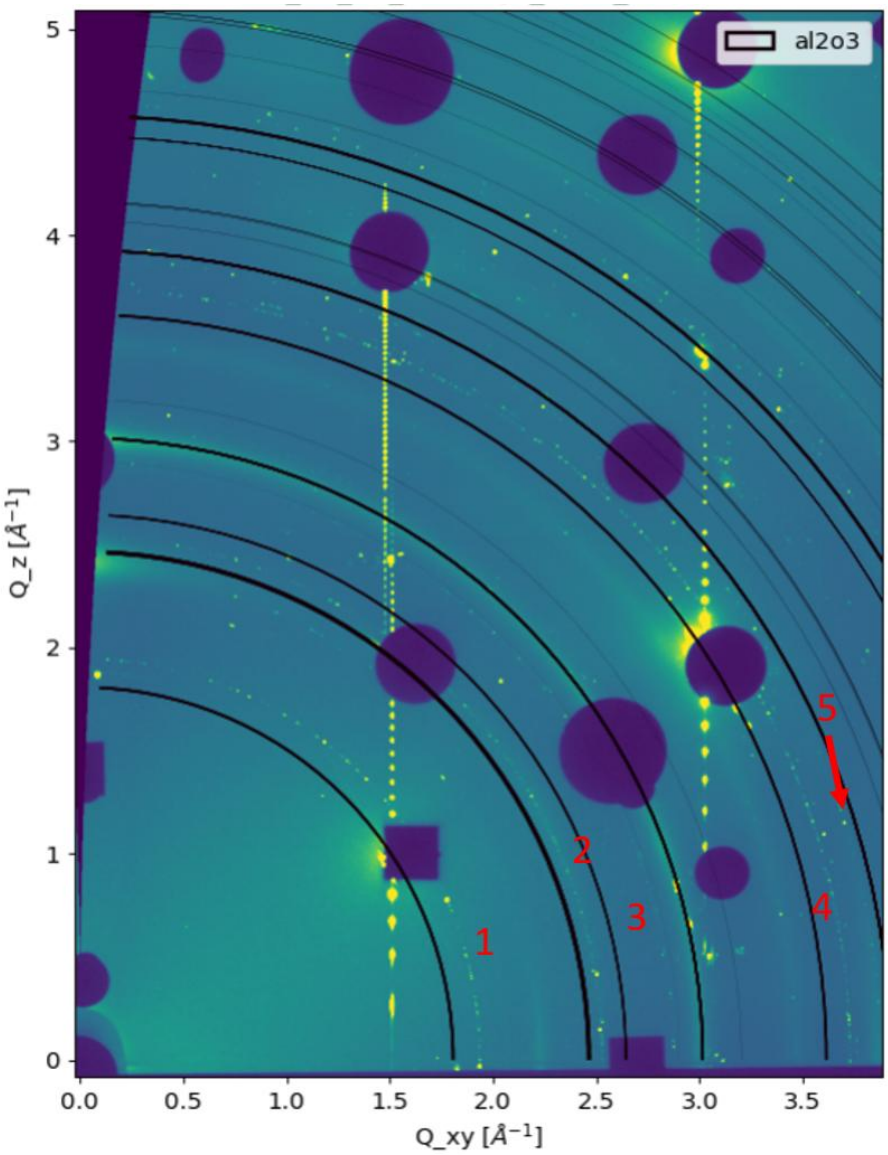

Figure 7.14. Maximum pixel image of the 2D detector data of "CZ-Al_2O_3-operando" measured at 550 K in H_2, at a total pressure of 30 bar over a 90° sample rotation. Black lines indicate the position of Al_2O_3 reflexes as Debye-Scherrer rings. Additional spotty rings are marked with red numbers and analysed in Table I.32.

ZnO-supported model catalyst at 611 K

Increasing the sample temperature to 611 K caused the disappearance of any spotty-Debye-Scherrer rings as shown in Figure 7.15. Smooth rings are still visible for Cu, and the azimuthal integration clearly shows, that all signals can be associated with either Cu or Al_2O_3. No noticeable changes were observed upon introduction of CO in a H_2:CO ratio of 4:1.

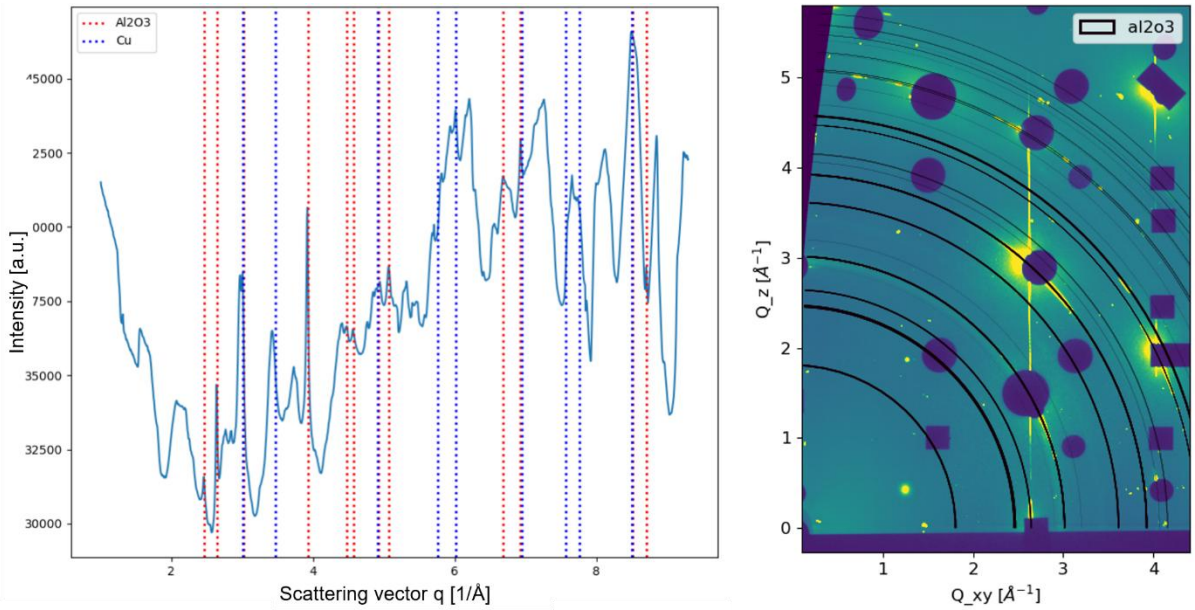

Figure 7.15. Maximum pixel image (right) and azimuthal integration results (left) of the 2D detector data set of "CZ-Al_2O_3-operando" measured at 611 K in H_2, at a total pressure of 30 bar over a 90° sample rotation. Black lines indicate the position of Al_2O_3 reflexes as Debye-Scherrer rings in the right image.

7.3. Summary and discussion

Structural evolution of Cu_2O particles during oxidation at high pressures

A simplified model systems of Cu nanoparticles on (001) Al_2O_3 as well as a ZnO-supported system of Cu nanoparticles on ZnO on (001) Al_2O_3, similar to the model systems investigated at ambient pressures, were analysed under true operando conditions using high energy X-rays. Room temperature measurements of both model systems performed at 23-30 bar of Ar pressure, showed signal associated with preferentially oriented Cu_2O domains with an increased lattice constant compared to the literature value of 2.28% for the simplified model system "Cu-Al_2O_3-operando" and 2.27% for the ZnO-supported sample "CZ-Al_2O_3-operando". The large increase of the lattice of the Cu_2O phase is associated with the high lattice mismatch between (111)-oriented Cu_2O particles and the sapphire support of 36.6%, inducing a significant amount of strain in the particles [88]. The observed gradual increase in strain within the Cu_2O particles under prolonged exposure to high-pressure oxidizing gas aligns with continued oxidation and growth of the Cu_2O layer. Literature indicates that strain in (111)-oriented Cu_2O particles on Al_2O_3 depends on layer thickness, with strain relaxation occurring only beyond a thickness of approximately 35 nm [89,104,105]. The elevated pressure of the oxidizing gas generates a higher oxidation potential, enabling further oxidation despite the accumulating strain, a phenomenon not observed at ambient pressure. This assumption is supported by the calculated exponential increase in the chemical potential of oxygen as a function of the oxygen partial pressure in the range associated with the trace amounts of oxygen and water in the Ar gas at ambient pressure and operando pressure of 1 ppm and about 30 ppm respectively, as shown in Figure I.1. Additionally, for both samples clear signal for (111)-oriented metallic Cu domains were observed as well, for which the lattice spacing matched with unstrained Cu. As observed and discussed for the ambient pressure experiments in the previous chapter, the (111)-oriented Cu domains show the expected epitaxial relationship for the deposition on (001) Al_2O_3 as described in the literature [69,86,106]. The increased lattice parameter for the Cu_2O phase was furthermore observed to expand the longer the samples are exposed to the high pressure Ar gas flow assumed to contain trace amounts of oxygen and water in the ~1 ppm range. While the Cu_2O lattice parameter for the simplified model system "Cu-Al_2O_3-operando" increased to the aforementioned 2.28% during a total of 20 hours under 23 bars of Ar pressure, a

further expansion of the lattice to 2.66% was observed upon an additional 90 minutes of exposure in the same conditions. The ZnO-supported model system was instead exposed to Ar gas flow at a pressure of 30 bar, causing an expansion of the lattice to 2.27% in just 3 hours. Additionally, while for the simplified model system only signal for (111)-oriented Cu nanoparticles was observed, with the Cu_2O phase only showing signal associated with a certain preferential orientation, the ZnO-supported system still showed signal from unstrained (111)-oriented Cu_2O after the shorter exposure time, similar to the observations made at the ambient pressure experiments. Analysis of the (111)-oriented particles on the ZnO-supported system revealed crystal domain sizes of 4-6 nm for Cu and 4 nm for Cu_2O in good agreement with the domain size of fully reduced Cu particles measured in ambient pressure of 8-10 nm. These results strongly suggest a progression in the oxidation of the Cu particles, beginning with the formation of a Cu-Cu_2O core-shell structure, for which the Cu_2O phase retains the same epitaxial orientation as the Cu particles. This core-shell structure was also observed to form due to native oxidation in air as observed for the samples exposed to ambient pressures described in the previous chapter. As oxidation continues, the increasing strain in the particles, caused by the lattice mismatch between Al_2O_3 and Cu_2O, leads to a gradual loss of the highly oriented nature of the Cu_2O phase. Eventually, the strain becomes significant enough that only a limited preferential orientation of the Cu_2O phase is observed. In agreement with the literature [105], a re-arrangement of the Cu_2O phase is apparently hindered by a limited mobility of the atoms at room temperature and below ~400 K, as the measurements at elevated temperatures showed the formation of (110)-oriented Cu_2O domains for the ambient pressure measurements and fully randomly oriented domains for the samples measured under operando pressures. Randomly oriented domains of fully reduced Cu were observed under Ar flow at a sample temperature of 685 K for the simplified model system and at 611 K for the ZnO-supported system. This indicates that sample temperature is the critical factor for Cu reduction, as reduction occurred even under 30 bar Ar containing both oxygen and H_2O—conditions previously shown to have a strong oxidizing effect at ambient pressure. In both cases, the Debye-Scherrer rings exhibited a spotty pattern, signifying significant coalescence of Cu particles into larger micro-particles, a degree of coalescence not observed under ambient pressure conditions. The increased particle size strongly influences the reduction behavior, as larger particles typically reduce more readily under these conditions.

Possible Cu-Zn alloy phase on the ZnO-supported model system

None of the measurements performed on the ZnO-supported model system revealed clear signal associated with phases containing Zn. Two possible explanations for this observation are discussed here, as the presence of Zn on the samples after the preparation was confirmed by post-deposition AES measurements. First, the Zn had already been depleted via the gas-phase from the sample surface at room temperature due to the exposure to the high pressure Ar gas flow. As mentioned in the previous chapter, Zn entering the gas-phase due to its high vapor pressure was observed at pressures of only several hundred millibar and at moderate temperature of 318 to 418 K [17,21]. A second explanation involves the formation of the $Cu_{0.2}Zn_{0.8}$ alloy phase, which is also believed to be present in the ZnO-supported samples investigated under ambient pressure. As discussed in detail in the previous chapter, the reflexes of the $Cu_{0.2}Zn_{0.8}$ phase would overlap with those of the Al_2O_3 support and could therefore be obscured by beamstops during operando measurements, assuming ordered alloy domains with (001) orientation along Al_2O_3 (001). This assumption could also account for the observation of spotty Debye-Scherrer rings in the ZnO-supported sample under high pressures, for which the reflex positions correspond to either Al_2O_3 or $Cu_{0.2}Zn_{0.8}$.

8. Summary and conclusion

This thesis aimed to provide a deeper understanding of the Cu-ZnO-Al_2O_3 (CZA) catalyst, used in the industrial synthesis of methanol from syngas. In-situ, surface-sensitive X-ray diffraction (XRD) measurements were employed to investigate the catalyst under various reaction gas mixtures, both at ambient pressures and under high pressures exceeding 30 bar, simulating real-world industrial conditions, so-called operando conditions. To explore the role of Zn within the catalyst, two model systems of the CZA catalyst were used: (1) a simplified model system of epitaxial Cu nanoparticles deposited on a single-crystal (001) Al_2O_3 support, and (2) a ZnO-supported model system for which the Cu deposition was performed after the deposition and subsequent oxidation of Zn onto the samples, again supported on (001) Al_2O_3. For the ZnO-supported model systems, a custom molecular beam epitaxy (MBE) chamber was designed and commissioned to facilitate the deposition of metallic Zn under ultra-high vacuum conditions.

To carry out the operando XRD investigations, a special high-pressure surface XRD setup was improved and utilized for in-situ monitoring of structural changes under conditions that closely mimic industrial environments, gaining yet unknown insight into the structural evolution of the Cu and Cu_2O phase of the CZA catalyst under gas pressures of 30 bar. This advanced setup was crucial in bridging the pressure gap between conventional surface-science experiments conducted usually between ultra-high vacuum conditions and up to ambient pressure, and the real-world industrial processes, in which the catalyst are operated under at least 50 bar pressure.

A key question in the study of the CZA catalyst regards the presence of an CuO_x-type structure or partially oxidized copper phase under reaction conditions. This thesis found no evidence of such a CuO_x phase at temperatures above 575 K, whether at ambient or operando pressure. Furthermore, the oxidation of copper in both model systems was only observed under pure Ar gas flow, which contained trace amounts of oxygen and water (around 1 ppm). During exposure to various reaction gas mixtures used in this work — ranging from, pure CO, pure CO_2, H_2:CO mixtures to H_2:CO:CO_2 mixtures - at sample temperatures of 575 K, copper remained in its metallic state. The MBE deposition under UHV yielded epitaxial (111)-oriented Cu with respect to the surface normal of the sapphire support corresponding to Cu (111) || Al2O3 (001), with a consistent in-plane particle diameter between 8-10 nm, observed for all investigated samples of this work.

Several days of native oxidation in air caused a partial oxidation of the Cu nanoparticles, yielding core-shell Cu-Cu_2O nanoparticles, for which the Cu_2O shell exhibited the same crystal orientation with respect to the support as the metallic Cu core. The Cu_2O shell persisted under reducing conditions in pure H_2 below 575 K at ambient pressure, with a full reduction of Cu only occurring at temperatures above 575 K, corresponding to a fully activated catalyst. Reduction of Cu_2O was observed to be driven solely by the sample temperature regardless of whether the samples were exposed to an oxidizing or reducing reaction gas, with reduction occurring at 611 K even under 30 bar pressure of Ar gas flow containing both oxygen and water. Additionally, exposure to different reaction gas mixtures under ambient pressures at 575 K, including a full oxidation of the previously activated Cu domains, revealed that the particles retain their epitaxial relationship with the Al_2O_3 substrate under varying reaction conditions. The structural integrity of the particles is associated with the formation of Cu-Al bonds, induced by a sapphire substrate preparation under UHV conditions that included Ar^+-sputtering and annealing cycles. On the contrary, for the samples intended for operando conditions, the support preparation omitted the Ar^+-sputtering, causing the fully oxidized Cu_2O nanoparticles to maintain a preferential orientation despite significant strain. For these samples however, activation of the catalysts resulted in the formation of randomly oriented Cu particles. Furthermore, a slow, stepwise increase of the sample temperature up to 575 K at ambient pressure caused the formation of (110)-oriented Cu particles on the simplified model catalyst of Cu particles supported directly on Al_2O_3. The (110)-oriented Cu particles remained stable throughout exposure to various reaction gas mixtures, revealing a significant difference in the oxidation and reduction behaviors of Cu (110)-oriented and Cu (111)-oriented particles. The Cu (110)-oriented particles were found to oxidize and reduce more quickly than the Cu (111)-oriented particles, despite having similar particle sizes. This finding aligns with the higher surface energy of Cu (110) facets and provides insight into the influence of crystal orientation on the phase stability of epitaxial model system of the catalyst.

Another highly debated issue surrounding the CZA catalyst is the formation of a Cu-Zn alloy during the catalytic reaction. The results of this work showed the presence of not only one, but two distinct Cu-Zn alloy phases at ambient pressure: $Cu_{0.2}Zn_{0.8}$ and $Cu_{0.64}Zn_{0.36}$. The data suggests a dynamic interplay between these two alloy phases, depending on the hydrogen content in the reaction gas mixture. Observations from this

thesis suggest that the $Cu_{0.2}Zn_{0.8}$ phase undergoes partial oxidation only in reaction gas mixtures with little or no hydrogen, leading to a transition to the more Cu-rich $Cu_{0.64}Zn_{0.36}$ phase. This transformation is accompanied by Zn diffusion from the Cu-Zn alloy phase into the metallic Cu particles, possibly also forming ZnO_x overlayers. The interplay between these two phases challenges the current understanding in the literature, which associates ZnO/ZnO_x formation with oxidizing conditions and Cu-Zn alloy phases with reducing conditions. However, the observations in this work suggest that it is not the overall oxidizing or reducing nature of the gas mixture that determines alloy formation. Instead, the amount of hydrogen in the reaction gas mixtures governs the oxidation of the $Cu_{0.2}Zn_{0.8}$ phase and its subsequent transformation to the $Cu_{0.64}Zn_{0.36}$ phase. Interestingly, no signals associated with the $Cu_{0.64}Zn_{0.36}$ phase were observed under operando pressures, even though the samples were exposed to the same reaction gas mixtures that led to its formation at ambient pressure. This observation further supports the conclusion that the formation of the $Cu_{0.64}Zn_{0.36}$ phase depends specifically on a lack of hydrogen in the gas mixture. While exposure to Ar with trace amounts of ~1 ppm water allowed phase formation at ambient pressure, the same gas mixture at 30 bar results in a higher partial oxygen pressure, which appears too high to allow formation of the $Cu_{0.64}Zn_{0.36}$ phase.

Additionally, the thesis investigated the stability of the Al_2O_3 support, which is known to play a crucial role in stabilizing the active phases of the catalyst, but is in recent years speculated to possibly be more actively involved in the catalysis. The results of this work demonstrated that Al_2O_3 remained stable under all tested conditions, including under high-pressure and high-temperature gas flow. Preparation of the sapphire supports using Ar^+-sputtering and annealing cycles was observed to cause the formation of a phase with a yet unknown chemical composition, but this unknown phase was observed not to affect the Cu-ZnO-Al_2O_3 system in any way during reaction conditions.

In summary, this thesis provided new insights into a more complex interplay between different Cu-Zn alloy phases present during the catalytic reaction and provided first insights into novel structural information about the Cu and Cu_2O phases of the catalyst under operando conditions. Furthermore, the improvements made to the high-pressure operando setup utilized in this work laid a robust foundation for future research of catalytic systems in high-pressure environments.

References

1. The Business Research Company. February 2024. Chemicals Global Market Report 2024 ID: 5781388, The Business Research Company.]. Available from: https://www.researchandmarkets.com/reports/5781388/chemicals-global-market-report.
2. Steinfeld JI, Francisco JS, Hase WL. 1999. *Chemical kinetics and dynamics*, 2nd edn. Prentice Hall, Englewood Cliffs, N.J.
3. Rothenberg G. 2008. *Catalysis. Concepts and green applications*. Wiley-VCH, Weinheim.
4. Friend CM, Xu B. 2017. Heterogeneous Catalysis: A Central Science for a Sustainable Future. *Acc Chem Res* 50:517–521.
5. Shaw WJ, Kidder MK, Bare SR, Delferro M, Morris JR, Toma FM, Senanayake SD, Autrey T, Biddinger EJ, Boettcher S, Bowden ME, Britt PF, Brown RC, Bullock RM, Chen JG, Daniel C, Dorhout PK, Efroymson RA, Gaffney KJ, Gagliardi L, Harper AS, Heldebrant DJ, Luca OR, Lyubovsky M, Male JL, Miller DJ, Prozorov T, Rallo R, Rana R, Rioux RM, Sadow AD, Schaidle JA, Schulte LA, Tarpeh WA, Vlachos DG, Vogt BD, Weber RS, Yang JY, Arenholz E, Helms BA, Huang W, Jordahl JL, Karakaya C, Kian KC, Kothandaraman J, Lercher J, Liu P, Malhotra D, Mueller KT, O'Brien CP, Palomino RM, Qi L, Rodriguez JA, Rousseau R, Russell JC, Sarazen ML, Sholl DS, Smith EA, Stevens MB, Surendranath Y, Tassone CJ, Tran B, Tumas W, Walton KS. 2024. A US perspective on closing the carbon cycle to defossilize difficult-to-electrify segments of our economy. *Nat Rev Chem* 8:376–400.
6. BMWK. Key principles of the Federal Government for a Carbon Management Strategy 2024.
7. Methanol Market Services Asia. 2020. Methanol price and supply/ demand.]. Available from: 2020. https://www.methanol.org/.
8. Carbon Recycling International. RENEWABLE METHANOL PLANT: FIRST PRODUCTION OF FUEL FROM CO_2 AT INDUSTRIAL SCALE. [cited 2024 August 8]. Available from: https://carbonrecycling.com/projects/george-olah.
9. Guido Steffen. 2019. Niederaussem becomes the setting for important technological progress. [cited 2024 August 8]. Available from: https://www.rwe.com/-/media/RWE/documents/07-presse/rwe-power-ag/2019/28-05-2019-niederaussem-becomes-the-setting-for-important-technological-progress.pdf.
10. Din IU, Shaharun MS, Alotaibi MA, Alharthi AI, Naeem A. 2019. Recent developments on heterogeneous catalytic CO2 reduction to methanol. *Journal of CO2 Utilization* 34:20–33.
11. Kuld S, Thorhauge M, Falsig H, Elkjær CF, Helveg S, Chorkendorff I, Sehested J. 2016. Quantifying the promotion of Cu catalysts by ZnO for methanol synthesis. *Science* 352:969–974.
12. Ye R-P, Ding J, Gong W, Argyle MD, Zhong Q, Wang Y, Russell CK, Xu Z, Russell AG, Li Q, Fan M, Yao Y-G. 2019. CO2 hydrogenation to high-value products via heterogeneous catalysis. *Nat Commun* 10:5698.
13. Kuld S, Conradsen C, Moses PG, Chorkendorff I, Sehested J. 2014. Quantification of zinc atoms in a surface alloy on copper in an industrial-type methanol synthesis catalyst. *Angewandte Chemie International Edition* 53:5941–5945.
14. Nakamura J, Choi Y, Fujitani T. 2003. On the issue of the active site and the role of ZnO in Cu/ZnO methanol synthesis catalysts. *Topics in Catalysis* 22:277–285.
15. Behrens M, Studt F, Kasatkin I, Kühl S, Hävecker M, Abild-Pedersen F, Zander S, Girgsdies F, Kurr P, Kniep B-L, Tovar M, Fischer RW, Nørskov JK, Schlögl R. 2012. The active site of methanol synthesis over Cu/ZnO/Al2O3 industrial catalysts. *Science* 336:893–897.
16. Kattel S, Ramírez PJ, Chen JG, Rodriguez JA, Liu P. 2017. Active sites for CO2 hydrogenation to methanol on Cu/ZnO catalysts. *Science* 355:1296–1299.

17. Song T, Li R, Wang J, Dong C, Feng X, Ning Y, Mu R, Fu Q. 2024. Enhanced Methanol Synthesis over Self-Limited ZnOx Overlayers on Cu Nanoparticles Formed via Gas-Phase Migration Route. *Angew Chem Int Ed Engl* 63:e202316888.
18. Lunkenbein T, Schumann J, Behrens M, Schlögl R, Willinger MG. 2015. Formation of a ZnO Overlayer in Industrial Cu/ZnO/Al 2 O 3 Catalysts Induced by Strong Metal–Support Interactions. *Angewandte Chemie* 127:4627–4631.
19. Lunkenbein T, Girgsdies F, Kandemir T, Thomas N, Behrens M, Schlögl R, Frei E. 2016. Bridging the Time Gap: A Copper/Zinc Oxide/Aluminum Oxide Catalyst for Methanol Synthesis Studied under Industrially Relevant Conditions and Time Scales. *Angewandte Chemie International Edition* 55:12708–12712.
20. Jensen S, Mammen MHR, Hedevang M, Li Z, Lammich L, Lauritsen JV. 2024. Visualizing the gas-sensitive structure of the CuZn surface in methanol synthesis catalysis. *Nat Commun* 15:3865.
21. Amann P, Klötzer B, Degerman D, Köpfle N, Götsch T, Lömker P, Rameshan C, Ploner K, Bikaljevic D, Wang H-Y, Soldemo M, Shipilin M, Goodwin CM, Gladh J, Halldin Stenlid J, Börner M, Schlueter C, Nilsson A. 2022. The state of zinc in methanol synthesis over a Zn/ZnO/Cu(211) model catalyst. *Science* 376:603–608.
22. Pacchioni G. 2024. From CO 2 to Methanol on Cu/ZnO/Al 2 O 3 Industrial Catalyst. What Do We Know about the Active Phase and the Reaction Mechanism? *ACS Catal.* 14:2730–2745.
23. Dang S, Yang H, Gao P, Wang H, Li X, Wei W, Sun Y. 2019. A review of research progress on heterogeneous catalysts for methanol synthesis from carbon dioxide hydrogenation. *Catalysis Today* 330:61–75.
24. Studt F, Behrens M, Kunkes EL, Thomas N, Zander S, Tarasov A, Schumann J, Frei E, Varley JB, Abild-Pedersen F, Nørskov JK, Schlögl R. 2015. The Mechanism of CO and CO 2 Hydrogenation to Methanol over Cu-Based Catalysts. *ChemCatChem* 7:1105–1111.
25. Schlögl R. 2022. Chemical Batteries with CO2. *Angewandte Chemie International Edition* 61:e202007397.
26. Liang B, Ma J, Su X, Yang C, Duan H, Zhou H, Deng S, Li L, Huang Y. 2019. Investigation on Deactivation of Cu/ZnO/Al 2 O 3 Catalyst for CO 2 Hydrogenation to Methanol. *Ind. Eng. Chem. Res.* 58:9030–9037.
27. Tarasov AV, Seitz F, Schlögl R, Frei E. 2019. In Situ Quantification of Reaction Adsorbates in Low-Temperature Methanol Synthesis on a High-Performance Cu/ZnO:Al Catalyst. *ACS Catal.* 9:5537–5544.
28. Chinchen GC, Denny PJ, Parker DG, Spencer MS, Whan DA. 1987. Mechanism of methanol synthesis from CO2/CO/H2 mixtures over copper/zinc oxide/alumina catalysts: use of14C-labelled reactants. *Applied Catalysis* 30:333–338.
29. Álvarez A, Bansode A, Urakawa A, Bavykina AV, Wezendonk TA, Makkee M, Gascon J, Kapteijn F. 2017. Challenges in the Greener Production of Formates/Formic Acid, Methanol, and DME by Heterogeneously Catalyzed CO2 Hydrogenation Processes. *Chem Rev* 117:9804–9838.
30. Jernigan GG, Somorjai GA. 1994. Carbon Monoxide Oxidation over Three Different Oxidation States of Copper: Metallic Copper, Copper (I) Oxide, and Copper (II) Oxide - A Surface Science and Kinetic Study. *Journal of Catalysis* 147:567–577.
31. Qiao J, Liu Y, Hong F, Zhang J. 2014. A review of catalysts for the electroreduction of carbon dioxide to produce low-carbon fuels. *Chem Soc Rev* 43:631–675.
32. Dasireddy VD, Likozar B. 2019. The role of copper oxidation state in Cu/ZnO/Al2O3 catalysts in CO2 hydrogenation and methanol productivity. *Renewable Energy* 140:452–460.
33. Gleißner R, Noei H, Chung S, Semione GDL, Beck EE, Dippel A-C, Gutowski O, Gizer G, Vonk V, Stierle A. 2021. Copper Nanoparticles with High Index Facets on Basal and Vicinal ZnO Surfaces. *J. Phys. Chem. C*.

34. Kim JY, Rodriguez JA, Hanson JC, Frenkel AI, Lee PL. 2003. Reduction of CuO and Cu2O with H2: H embedding and kinetic effects in the formation of suboxides. *J Am Chem Soc* 125:10684–10692.
35. HIMELFARB P. 1983. Oxidation states of copper during reduction of cupric oxide in methanol catalysts. *Journal of Catalysis* 83:469–471.
36. Spencer MS. 1999. *Catal Lett* 60:45–49.
37. WACHS I. 1978. The selective oxidation of CH3OH to H2CO on a copper(110) catalyst. *Journal of Catalysis* 53:208–227.
38. Behrens M. 2009. Meso- and nano-structuring of industrial Cu/ZnO/(Al2O3) catalysts. *Journal of Catalysis* 267:24–29.
39. Fisher IA, Bell AT. 1998. In Situ Infrared Study of Methanol Synthesis from H2/CO over Cu/SiO2and Cu/ZrO2/SiO2. *Journal of Catalysis* 178:153–173.
40. BIANCHI D, CHAFIK T, KHALFALLAH M, TEICHNER S. 1995. Intermediate species on zirconia supported methanol aerogel catalysts V. Adsorption of methanol. *Applied Catalysis A: General* 123:89–110.
41. RHODES M, BELL A. 2005. The effects of zirconia morphology on methanol synthesis from CO and H2H2 over Cu/ZrO2Cu/ZrO2 catalystsPart I. Steady-state studies. *Journal of Catalysis* 233:198–209.
42. Divins NJ, Kordus D, Timoshenko J, Sinev I, Zegkinoglou I, Bergmann A, Chee SW, Widrinna S, Karslıoğlu O, Mistry H, Lopez Luna M, Zhong JQ, Hoffman AS, Boubnov A, Boscoboinik JA, Heggen M, Dunin-Borkowski RE, Bare SR, Cuenya BR. 2021. Operando high-pressure investigation of size-controlled CuZn catalysts for the methanol synthesis reaction. *Nat Commun* 12:1435.
43. Beck A, Zabilskiy M, Newton MA, Safonova O, Willinger MG, van Bokhoven JA. 2021. Following the structure of copper-zinc-alumina across the pressure gap in carbon dioxide hydrogenation. *Nat Catal* 4:488–497.
44. TB Massalski, H Okamoto, PR Subramanian, L Kacprzak, WW Scott. 1986. *Binary alloy phase diagrams*.
45. Amann P, Degerman D, Lee M-T, Alexander JD, Shipilin M, Wang H-Y, Cavalca F, Weston M, Gladh J, Blom M, Björkhage M, Löfgren P, Schlueter C, Loemker P, Ederer K, Drube W, Noei H, Zehetner J, Wentzel H, Åhlund J, Nilsson A. 2019. A high-pressure x-ray photoelectron spectroscopy instrument for studies of industrially relevant catalytic reactions at pressures of several bars. *Review of Scientific Instruments* 90:103102.
46. Wu W, Xie K, Sun D, Li X, Fang F. 2017. CuO/ZnO/Al 2 O 3 Catalyst Prepared by Mechanical-Force-Driven Solid-State Ion Exchange and Its Excellent Catalytic Activity under Internal Cooling Condition. *Ind. Eng. Chem. Res.* 56:8216–8223.
47. Behrens M, Zander S, Kurr P, Jacobsen N, Senker J, Koch G, Ressler T, Fischer RW, Schlögl R. 2013. Performance improvement of nanocatalysts by promoter-induced defects in the support material: methanol synthesis over Cu/ZnO:Al. *J Am Chem Soc* 135:6061–6068.
48. Narkhede N, Zheng H, Zhang H, Zhang G, Li Z. 2020. Group 13 metal doped Cu/ZnO catalysts from phase pure precursors via an isomorphous substitution route: mechanistic insights into promotional effects for syngas hydrogenation to methanol. *Catal. Sci. Technol.* 10:7386–7398.
49. Prašnikar A, Pavlišič A, Ruiz-Zepeda F, Kovač J, Likozar B. 2019. Mechanisms of Copper-Based Catalyst Deactivation during CO 2 Reduction to Methanol. *Ind. Eng. Chem. Res.* 58:13021–13029.
50. Kunkes EL, Studt F, Abild-Pedersen F, Schlögl R, Behrens M. 2015. Hydrogenation of CO2 to methanol and CO on Cu/ZnO/Al2O3: Is there a common intermediate or not? *Journal of Catalysis* 328:43–48.

51. Li Y, Chan SH, Sun Q. 2015. Heterogeneous catalytic conversion of CO2: a comprehensive theoretical review. *Nanoscale* 7:8663–8683.
52. Wang R, Zhu B, Zhang G, Gao Y. 2020. Theoretical study of CO2 hydrogenation on Cu surfaces. *J Mol Model* 26:202.
53. Als-Nielsen J, McMorrow D. 2011. *Elements of Modern X-ray Physics*. Wiley.
54. Stierle A, Vlieg E. 2012. Surface-Sensitive X-Ray Diffraction Methods. In Mittemeijer EJ, Welzel U, eds, *Modern Diffraction Methods.* Wiley, pp 221–257.
55. Feidenhans'l R. 1989. Surface structure determination by X-ray diffraction. *Surface Science Reports* 10:105–188.
56. Baskaran S. 2010. Structure and regulation of yeast glycogen synthase.].
57. Chierchia R. 2007. Strain and crystalline defects in epitaxial GaN layers studied by high-resolution X-ray diffraction. *http://elib.suub.uni-bremen.de/diss/docs/00011449.pdf*.
58. Fairley N, Fernandez V, Richard-Plouet M, Guillot-Deudon C, Walton J, Smith E, Flahaut D, Greiner M, Biesinger M, Tougaard S, Morgan D, Baltrusaitis J. 2021. Systematic and collaborative approach to problem solving using X-ray photoelectron spectroscopy. *Applied Surface Science Advances* 5:100112.
59. Linford M. 2014. Introduction to Surface and Material Analysis and to Various Analytical Techniques. *Vacuum Technology & Coating* 27–33.
60. Seah MP. 1984. A review of the analysis of surfaces and thin films by AES and XPS. *Vacuum* 34:463–478.
61. Nibbering ETJ. 2014. Imaging techniques. Low-energy electron diffraction at ultrafast speeds. *Science* 345:137–138.
62. Azad A. 2018. *Scanning electron microscopy (SEM): A review*.
63. Velasco S, Román FL, White JA. 2009. On the Clausius–Clapeyron Vapor Pressure Equation. *J. Chem. Educ.* 86:106.
64. Mondal B, Mukherjee T, Finch NW, Saha A, Gao MZ, Palmer TA, DebRoy T. 2022. Vapor Pressure versus Temperature Relations of Common Elements. *Materials (Basel)* 16.
65. Schell N, King A, Beckmann F, Fischer T, Müller M, Schreyer A. 2013. The High Energy Materials Science Beamline (HEMS) at PETRA III. *MSF* 772:57–61.
66. Gleißner R, Beck EE, Chung S, Semione GDL, Mukharamova N, Gizer G, Pistidda C, Renner D, Noei H, Vonk V, Stierle A. 2022. Operando reaction cell for high energy surface sensitive x-ray diffraction and reflectometry. *Review of Scientific Instruments* 93:73902.
67. Gleißner R, Chung S, Semione GDL, Jacobse L, Wagstaffe M, Tober S, Neumann AJ, Gizer G, Goodwin CM, Soldemo M, Shipilin M, Lömker P, Schlueter C, Gutowski O, Muntwiler M, Amann P, Noei H, Vonk V, Stierle A. 2022. *Ambient Pressure Oxidation-Reduction Dynamics of Cu/ZnO Model Catalysts for Methanol Synthesis*.
68. Björck M, Andersson G. 2007. GenX : an extensible X-ray reflectivity refinement program utilizing differential evolution. *J Appl Crystallogr* 40:1174–1178.
69. OH S, SCHEU C, WAGNER T, TCHERNYCHOVA E, RUHLE M. 2006. Epitaxy and bonding of Cu films on oxygen-terminated α-Al2O3(0001) surfaces. *Acta Materialia* 54:2685–2696.
70. Kriegner D, Wintersberger E, Stangl J. 2013. xrayutilities: a versatile tool for reciprocal space conversion of scattering data recorded with linear and area detectors. *J Appl Crystallogr* 46:1162–1170.
71. Wang K, Reeber R. 1996. Thermal Expansion of Copper. *High Temperature and Materials Science* 35:181–186.
72. Khort A, Roslyakov S, Loginov P. 2021. Solution combustion synthesis of single-phase bimetallic nanomaterials. *Nano-Structures & Nano-Objects* 26:100727.

73. Beck LH, Smith CS. 1952. Copper-Zinc Constitution Diagram, Redetermined in The Vicinity of the Beta Phase by Means of Quantitative Metallography. *JOM* 4:1079–1083.
74. Fons P, Iwata K, Niki S, Yamada A, Matsubara K. 1999. Growth of high-quality epitaxial ZnO films on α-Al2O3. *Journal of Crystal Growth* 201-202:627–632.
75. Tran R, Xu Z, Radhakrishnan B, Winston D, Sun W, Persson KA, Ong SP. 2016. Surface energies of elemental crystals. *Sci Data* 3:160080.
76. 布村 紀. Density Functional Theory Study of Cu-Zn alloys. 富山大学総合情報基盤センター; University of Toyama.
77. Owen EA, Preston GD. 1923. X-ray analysis of zinc-copper alloys. *Proc. Phys. Soc. London* 36:49–66.
78. Krozer A, Kasemo B. 1980. Kinetics of initial oxidation of UHV prepared Zn films. *Surface Science Letters* 97:L339-L344.
79. Kieffer J, Wright JP. 2013. PyFAI: a Python library for high performance azimuthal integration on GPU. *Powder Diffr.* 28:S339-S350.
80. Knudsen EB, Sørensen HO, Wright JP, Goret G, Kieffer J. 2013. FabIO: easy access to two-dimensional X-ray detector images in Python. *J Appl Crystallogr* 46:537–539.
81. Foo ML, Huang Q, Lynn JW, Lee W-L, Klimczuk T, Hagemann IS, Ong NP, Cava RJ. 2006. Synthesis, structure and physical properties of Ru ferrites: BaMRu5O11 (M=Li and Cu) and BaM'2Ru4O11 (M'=Mn, Fe and Co). *Journal of Solid State Chemistry* 179:563–572.
82. Barth TFW. 1932. The cristobalite structures. *American Journal of Science* s5-23:350–356.
83. Achary SN, Jayakumar OD, Tyagi AK, Kulshresththa SK. 2003. Preparation, phase transition and thermal expansion studies on low-cristobalite type Al1−xGaxPO4 (x=0.0, 0.20, 0.50, 0.80 and 1.00). *Journal of Solid State Chemistry* 176:37–46.
84. Graetsch HA. 2003. Thermal expansion and thermally induced variations of the crystal structure of AlPO4 low cristobalite. *njmm* 2003:289–301.
85. Poulston S, Parlett PM, Stone P, Bowker M. 1996. Surface Oxidation and Reduction of CuO and Cu2O Studied Using XPS and XAES. *Surf Interface Anal* 24:811–820.
86. Scheu C. 2004. Manipulating Bonding at a Cu/(0001)Al 2 O 3 Interface by Different Substrate Cleaning Processes. *Interface Science* 12:127–134.
87. Leitner J, Sedmidubský D, Lojka M, Jankovský O. 2020. The Effect of Nanosizing on the Oxidation of Partially Oxidized Copper Nanoparticles. *Materials (Basel)* 13.
88. Li J, Mei Z, Ye D, Liang H, Liu Y, Du X. 2012. Growth of single-crystalline Cu2O (111) film on ultrathin MgO modified α-Al2O3 (0001) substrate by molecular beam epitaxy. *Journal of Crystal Growth* 353:63–67.
89. Wagner A, Scherg-Kurmes H, Waag A, Bakin A. 2013. Vapour phase epitaxy of Cu 2 O on a-plane Al 2 O 3. *Phys. Status Solidi C* 10:1284–1287.
90. Jensen MCR, Venkataramani K, Helveg S, Clausen BS, Reichling M, Besenbacher F, Lauritsen JV. 2008. Morphology, Dispersion, and Stability of Cu Nanoclusters on Clean and Hydroxylated α-Al 2 O 3 (0001) Substrates. *J. Phys. Chem. C* 112:16953–16960.
91. Hansen PL, Wagner JB, Helveg S, Rostrup-Nielsen JR, Clausen BS, Topsøe H. 2002. Atom-resolved imaging of dynamic shape changes in supported copper nanocrystals. *Science* 295:2053–2055.
92. Grunwaldt J-D, Molenbroek A, Topsøe N-Y, Topsøe H, Clausen B. 2000. In Situ Investigations of Structural Changes in Cu/ZnO Catalysts. *Journal of Catalysis* 194:452–460.
93. Narula ML, Tare VB, Worrell WL. 1983. Diffusivity and solubility of oxygen in solid copper using potentiostatic and potentiometric techniques. *Metall Trans B* 14:673–677.
94. López GA, Mittemeijer EJ. 2004. The solubility of C in solid Cu. *Scripta Materialia* 51:1–5.
95. Frei E, Gaur A, Lichtenberg H, Zwiener L, Scherzer M, Girgsdies F, Lunkenbein T, Schlögl R. 2020. Cu-Zn alloy formation as unfavored state for efficient methanol catalysts. *ChemCatChem*.

96. Harikumar KR, Santra AK, Rao C. 1996. An investigation of the Cu/ZnO/Zn system: evidence for the formation of Cu・Zn alloys by the inward diffusion of Cu. *Applied Surface Science* 93:135–141.
97. Xu CH, Liu YL, Shi SQ. 2011. Isothermal Oxidation Behavior of Cu-38at.%Zn Alloy at High Temperature. *High Temperature Materials and Processes* 30.
98. Spencer MS. 1999. The role of zinc oxide in Cu/ZnO catalysts for methanol synthesis and the water–gas shift reaction. *Top Catal* 8:259–266.
99. Fang Y, Xu B, Wang S, Liu H, Wang J, Si M. 2024. Highly stable localized surface plasmon resonance of Cu nanoparticles obtained via oxygen plasma irradiation. *Nanoscale* 16:9748–9753.
100. Fukamori Y, König M, Yoon B, Wang B, Esch F, Heiz U, Landman U. 2013. Fundamental Insight into the Substrate-Dependent Ripening of Monodisperse Clusters. *ChemCatChem* 5:3330–3341.
101. Krozer A, Kasemo B. 1980. Kinetics of initial oxidation of UHV prepared Zn films. *Surface Science* 97:L339-L344.
102. Tongnan V, Sornchamni T, Laosiripojana N, Hartley UW. 2018. Study of crystal growth and kinetic parameters of Zn/ZnO oxidation in the presence of H2O and CO2. *Reac Kinet Mech Cat* 125:99–110.
103. He BB. 2022. Crystallite size distribution by two-dimensional XRD. *Powder Diffraction* 37:76–83.
104. Brandt IS, Martins CA, Zoldan VC, Viegas AD, Da Dias Silva JH, Pasa AA. 2014. Structural and optical properties of Cu2O crystalline electrodeposited films. *Thin Solid Films* 562:144–151.
105. Ha T, Park I, Sim KI, Lee H, Bae J-S, Kim SJ, Kim JP, Kim T-T, Kim JH, Jang JI, Jeong S-Y. 2019. Single-crystalline Cu2O thin films of optical quality as obtained by the oxidation of single-crystal Cu thin films at low temperature. *APL Materials* 7.
106. SCHEU C, Gao M, Oh SH, Dehm G, Klein S, Tomsia AP, Rühle M. 2006. Bonding at copper–alumina interfaces established by different surface treatments: a critical review. *J Mater Sci* 41:5161–5168.
107. Holmes RD, Kersting AB, Arculus RJ. 1989. Standard molar Gibbs free energy of formation for Cu2O: high-resolution electrochemical measurements from 900 to 1300 K. *The Journal of Chemical Thermodynamics* 21:351–361.
108. CHASE M. W. Jr. 1985. JANAF Thermochemical Tables. *J. Phys. Chem. Ref. Data*.
109. Zhu Y, Mimura K, Isshiki M. 2002. Oxidation Mechanism of Copper at 623-1073 K. *Mater. Trans.* 43:2173–2176.
110. Orr RL, Argent BB. 1965. Heats of formation of the ?-brasses. *Trans. Faraday Soc.* 61:2126.
111. Parameswaran K, Healy G. 1978. A Calorimetric Investigation of the Copper-Zinc System. *Metallurgical Transactions B* 9:657–664.
112. Eastman CM, Zhang Q, Zhao J-C. 2020. Diffusion Coefficients and Phase Equilibria of the Cu-Zn Binary System Studied Using Diffusion Couples. *J. Phase Equilib. Diffus.* 41:642–653.
113. Fan G, Huang Z, Jiang J, Sun L. 2012. Standard molar enthalpy of formation of the ZnO nanosheets. *J Therm Anal Calorim* 110:1471–1474.
114. Reuter K, Scheffler M. 2007. Erratum: Composition, structure, and stability of RuO2(110) as a function of oxygen pressure [Phys. Rev. B 65, 035406 (2001)]. *Phys. Rev. B* 75.
115. GARCIAMARTINEZ O, ROJAS R, VILA E, DEVIDALES J. 1993. Microstructural characterization of nanocrystals of ZnO and CuO obtained from basic salts. *Solid State Ionics* 63-65:442–449.

I Supporting information

A. Thermodynamic parameters

Heat of formation and activation barriers for Cu oxidation

Formation of Cu_2O from Cu under the presence of an oxygen source proceeds via:

$$4\,Cu + O_2 \leftrightharpoons 2\,Cu_2O \tag{SI1}$$

The corresponding heat of formation of −(170.59 ± 0.08) kJ·mol^{-1} for Cu_2O at ambient pressure and 298 K is used as taken from [107]. Calculating the heat of formation at the experimental temperature of interest of 575 K was done using Kirchhoff's Law:

$$\Delta H_{f,Cu_2O}(575\ K) = \Delta H_{f,Cu_2O}(298\ K) + \int_{T_1=298\ K}^{T_2=575\ K} \Delta C_p dT \tag{SI2}$$

With the heat capacity ΔC_p of the reaction defined as:

$$\Delta C_p = C_{p,Cu_2O}(T) - 2C_{p,Cu}(T) - \frac{1}{2}C_{p,O_2}(T) \tag{SI3}$$

For the calculation, the integral in equation SI2 is approximated with a linear function using the values listed in Table I.1, taken from [108].

	C_p (Cu_2O) [J/mol·K]	C_p (Cu) [J/mol·K]	C_p (O_2) [J/mol·K]
At 298 K	62.538	24.469	29.338
At 575 K	72.896	26.409	31.862

Table I.1. Heat capacity of Cu, O_2 and Cu_2O at 298 K and 575 K.

Based on the linear approximation, the heat of formation for Cu_2O yields $\Delta H_{f,Cu2O}$(575 K) = -(168.31 ± 0.08) kJ/mol ≙ -(1.74 ± 0.0008) eV.

As an approximation, the activation energies for Cu oxidation towards Cu_2O for bulk samples are used as described by Zhu et. al. [109] in a temperature range between 573-773 K. The activation energy was determined to be 40 kJ/mol ≙ 0.42 eV under 1000 mbar of pure oxygen and 58 kJ/mol ≙ 0.601eV under Ar gas containing 1% oxygen. Similarly, the activation barrier for reduction of both CuO and Cu_2O directly to metallic copper under a reaction gas mixture of 5% H2 in He, at ambient pressure in a temperature range

of 423-573 K was determined by Kim et. al. to be 60.67kJ/mol ≙ 0.63eV and 114.65kJ/mol ≙ 1.19eV respectively [34].

Heat of formation and activation energies for Cu-Zn alloys and ZnO

The heat of formation for the α-brass alloys of Cu and Zn, for Zn contents between 5-34 at. % was determined by Orr and Argent at a temperature of 573 K as listed in Table I.2 [110].

Atomic % of Zn	5%	10%	15%	20%	25%	30%	34%
$\Delta H_{f,\alpha\text{-brass}}$ (573 K) [kJ/mol]	-1.088	-2.510	-4.102	-5.526	-6.570	-7.195	-9.082
$\Delta H_{f,\alpha\text{-brass}}$ (573 K) [eV]	-0.0113	-0.0260	-0.0425	-0.0573	-0.0681	-0.0746	-0.0942

Table I.2. Heat of formation for the incorporation of Zn into Cu for Zn contents between 5 to 34 at. %, at which the alloy is in the α-brass crystal structure.

The heat of formation for Cu-Zn alloys with high Zn content forming the ε-phase within the Cu-Zn phase diagram was investigated by Parameswaran and Healy [111]. The heat of formation of the ε-phase, which corresponds most closely to the $Cu_{0.2}Zn_{0.8}$ phase was determined at -6.02 kJ/mol ≙ -0.0624 eV for the formation at 573 K. The activation barriers for the formation of Cu-Zn alloys for bulk phases were determined by Eastman et. al. in the temperature range between 375-1025 K [112]. For the α-brass, the activation energy was observed to depend on the Zn content of the phase, with observed values between 120 kJ/mol ≙ 1.244 eV for very low Zn content and up to about 175 kJ/mol ≙ 1.814 eV for 35 at. % Zn content. Similarly, for the ε-phase of the alloy system, the activation energy was determined to be between 66-67 kJ/mol ≙ 0.68-0.69 eV depending on the Zn content of the phase in the range between 80-86 at. %.

The heat of formation for ZnO in the wurtzite structure was determined for nanosheets as an approximation for various nanoscale morphologies by Fan et. al. to be -(333.50 ± 0.29) kJ/mol ≙ -(3.456 ± 0.003) eV [113]. Data for the activation energies of the ZnO formation at elevated temperatures around 575 K have, to the best knowledge of the author, not been determined.

Chemical potential of oxygen and hydrogen

The calculation of the chemical potential of oxygen and hydrogen in the reaction gas was done according to the method described in the work of Reuter and Scheffler and the references described therein, based on principles of ab initio thermodynamics [114]. The calculation is based on the following equation:

$$\mu_O(T,p) = \mu_O(T,p^0) + \frac{1}{2}k_B T\ ln(\frac{p}{p^0}) \quad \text{(SI4)}$$

For which p^0 refers to ambient pressure of 1 bar. The reference chemical potential at 1 bar were obtained from thermodynamic tables. The chemical potential as a function of both the temperature at 1000 mbar pressure, as well as a function of oxygen partial pressure at 575 K are shown in Figure I.1.

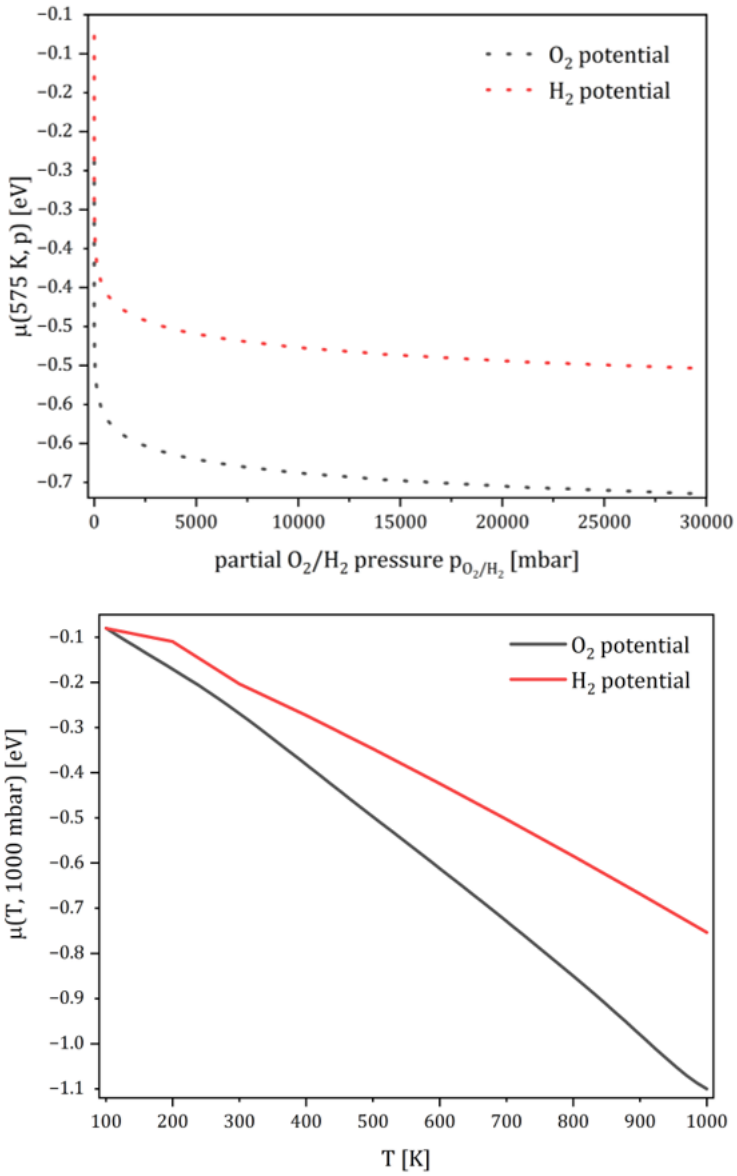

Figure I.1. Top: Chemical potential of O_2 (black) and H_2 (red) as a function of the partial pressure of the respective element calculated at 575 K. Bottom: Chemical potential of O_2 (black) and H_2 (red) as a function of the temperature at 1 bar pressure.

B. Design flaws of the operando setups

The first iteration of improvements to the operando SXRD setup were evaluated during a synchrotron experiment performed at DESY P07. While the modifications that were made dramatically improved the usability of the setup, a number of additional design flaws of the setup were observed and are discussed in this section.

I. Gas tight sealing of sapphire capillary using only a slightly adjusted Swagelok sealing mechanism

The main experimental cell containing the sample is a single crystal sapphire capillary which is held in place and connected to the gas handling system by the capillary holder which uses a normal Swagelok connection to create a tight seal of the capillary with the inlet- and outlet gas lines. Figure I.*2* shows a close-up of the capillary in the capillary holder during the temperature calibration.

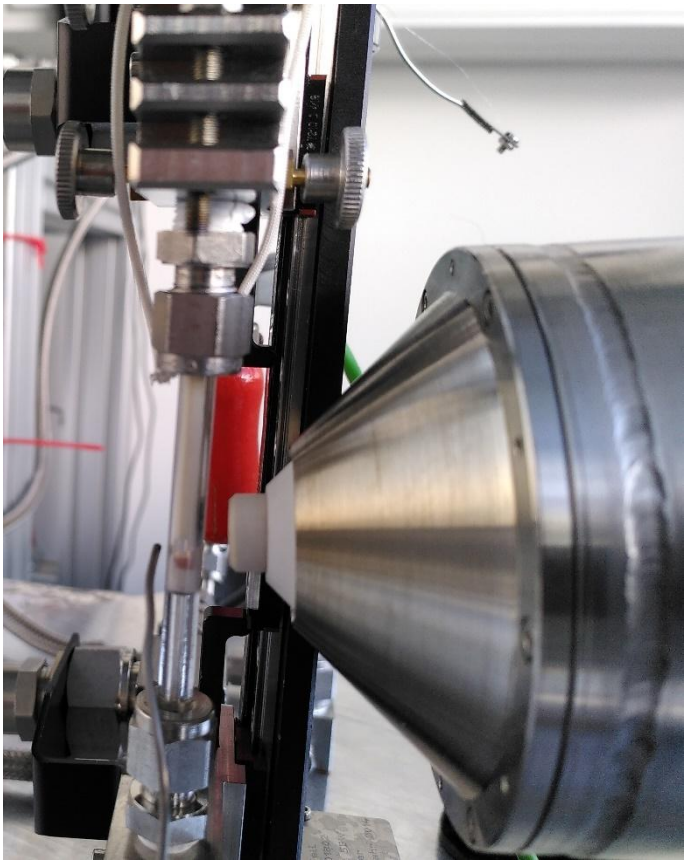

Figure I.2. Close-up of the capillary holder during temperature calibration. The sapphire capillary is sealed using a standard Swagelok connection.

The Swagelok sealing mechanism is however, designed to tightly connect gas lines of stainless steel. The mechanism is shown in Figure I.*3*. It relies on a metal ferrule, which is pushed onto the end of the gas pipe, sealing the connection by slightly deforming the metal pipe. The deformation of the pipe is caused by a shear force acting perpendicular onto the pipe surface. To ensure that the front ferrule which is pushed into the pipe material is not pushed along the gas pipe, a back ferrule is used as well, which holds the front ferrule in place. For the use of the same sealing mechanism with a sapphire capillary instead of a metal gas pipe, no additional changes were made, instead of exchanging the metal ferrule with a Vesper ferrule. Also, only the front ferrule was exchanged with a Vesper ferrule,

and no back ferrule was used. This caused a high movability of the Vesper ferrule on the sapphire capillary since no back ferrule was holding the front ferrule in place during tightening of the nuts. Additionally, the outer diameter of the gas pipe and the inner diameter of the ferrules are precisely engineered to limit the mobility of the ferrules in the original Swagelok setup as much as possible. The same precision of the outer diameter is simply not achievable for the single crystal sapphire capillary due to the already very difficult manufacturing process.

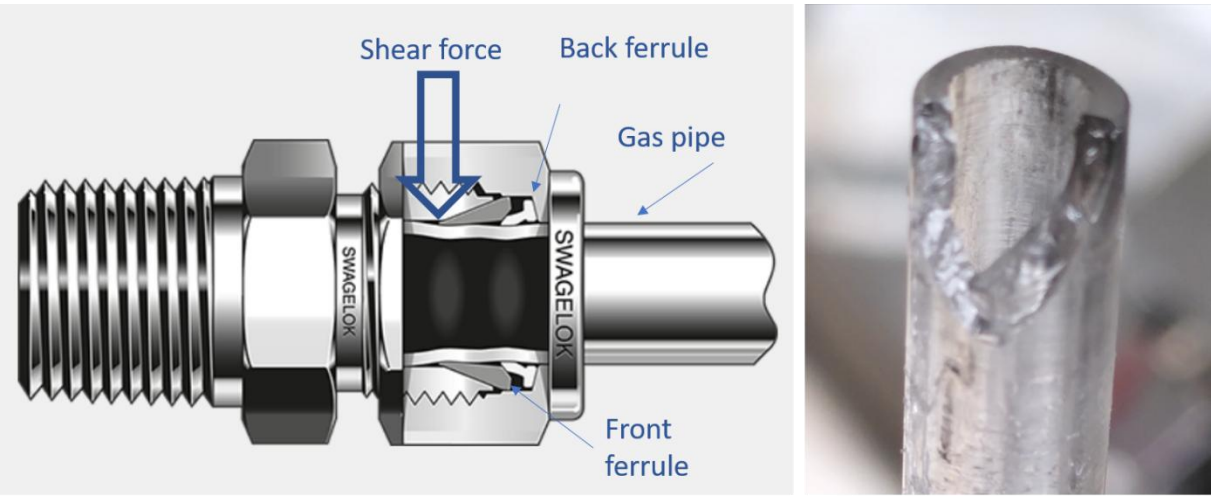

Figure I.3. Left: Schematic of the Swagelok sealing mechanism taken from the official company website. For the operando SXRD stage, the capillary was used instead of the metal gas pipe, and the metal ferrule was switched with a Vesper ferrule. Right: Used single crystal capillary broken at the top.

The higher movability of the Vesper ferrule on the sapphire capillary caused the ferrule to be pushed away from the capillary end during tightening of the nuts. The variance in the outer diameter of the capillary caused them to then come into direct contact with the metallic inner tubing of the connector during tightening, which then caused a shear force to act directly perpendicular onto the sapphire capillary. Since the sapphire capillary belongs to the material class of ceramics and glasses, is considerably weaker to any shear force than to tensile forces. Therefore, tightening of the nuts caused a lot of breaks in the capillaries as seen for example in the right image of Figure I.*3*.

II. Sample fixation and slow gas flow

One significant issue with the previous SXRD setup was the lack of fixation for the sample inside the capillary, as it was held in place solely by the gas flow. This configuration posed challenges, particularly when adjusting pressure or opening valves connected to the gas handling system. Any pressure difference between the gas lines and

the capillary could cause the sample to shift, or even be dislodged and sucked into the tubing. To prevent this, the valves could only be operated when the pressure inside the capillary precisely matched that of the gas lines. During one experiment, it became evident that the capillary was not entirely gas-tight. After closing the valves to the capillary for a few hours, pressure loss occurred, making it impossible to resume the experiment under controlled conditions. Without knowing the exact pressure inside the capillary, reopening the valves caused the sample to be displaced, landing upside down on the crown spacer. Additionally, any rapid pressure adjustment or gas composition change could only be carried out gradually, as even slight pressure differences between the inlet and outlet sides of the capillary could disrupt the sample's position. To mitigate this issue, pressure adjustments were made through the mass flow controllers, but their low maximum flow rate meant that achieving high pressures (e.g., 30 bar from ambient) could take several hours. This problem was exacerbated by the gas analyser system, which featured significantly smaller tubing compared to the 4 mm inner diameter tubing used throughout the rest of the gas handling system and experimental cell. The smaller tubing in the gas analyser caused further delays, with a lag of up to 30 minutes between changing the gas composition in the handling system and observing the corresponding changes in the analyser.

III. Gas bottle pressure reducer malfunction and gas backflow

A significant delay during the experimental proceedings was caused by a malfunction of the gas bottle pressure regulators, which, while not technically part of the core operando SXRD setup, are critical to its operation. For the gas handling system to function properly, the inlet gas pressure—i.e., the pressure of gas supplied directly from the gas bottles—must be maintained higher than the maximum experimental pressure. Since the experiments were consistently conducted at a maximum pressure of 30 bar, the inlet pressure from the gas bottles was set to 35 bar across all gases. While the pressure regulators for the Ar and CO_2 gas bottles performed as expected, maintaining a stable inlet pressure of 35 bar, the H_2 and CO gas line pressures gradually increased over time. By the time this issue was detected, the H_2 line pressure had risen to 80 bar and the CO line to 60 bar. Given that the system had been overpressure tested only up to 35 bar, the excessive H_2 pressure resulted in a leak within the gas handling system. This triggered the CO gas sensors—also highly sensitive to H_2—and led to an emergency lockdown of the experimental hutch. Since remote control of the gas handling system is limited,

DESY's technical emergency services were required to enter the hutch, wearing gas masks, to manually open the necessary valves and safely release the accumulated gases from the system. Toward the end of the experiment, another issue with the gas flow setup emerged as the H_2 gas bottle ran low. The gas handling system lacks one-way valves, and the inlet gas pressure from the bottles is manually controlled via gas cabinet operations. As a result, the drop in H_2 inlet pressure went unnoticed in time to prevent potential backflow of CO into the H_2 gas bottle. When gas bottles are depleted, the inlet pressure drops below the set point of 35 bar and can eventually fall below the experimental pressure of 30 bar. This creates a risk of reaction gas mixtures flowing backward through the gas lines into the gas bottles, posing a serious safety hazard.

IV. Other issues

Various other issue occurred during the beamtime causing further delays. Introduction of CO_2, caused a black spot on the capillary for a yet unknown reason as shown in Figure I.*4*.

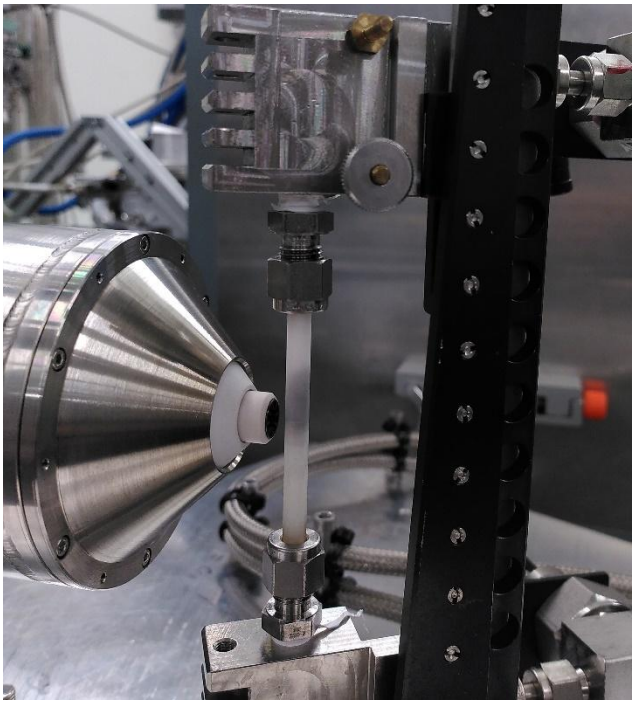

Figure I.4. A large black spot is seen inside the capillary after exposing the sample to a reaction gas mixture containing CO_2.

As discussed in Chapter 5, the carbonyl trap in the CO gas line, designed to filter Ni carbonyls from the CO gas, failed to function properly, leading to contamination of the sample with Ni. This contamination underscores the critical need for reliable filtration systems in the gas handling setup to ensure sample purity. In addition to the contamination issue, sample alignment proved to be a persistent challenge. During the

typical 90° sample rotations, the sample height varied significantly over a large range of angular rotations, complicating the alignment process. This problem was further exacerbated when the sample was heated, although the exact cause remains unclear. One potential explanation is related to the flatness of the samples. The operando stage requires the use of small, 3.5 mm diameter round substrates, as opposed to the larger square substrates typically used in other setups within the group. It is plausible that the smaller size and round shape of these substrates may introduce flatness issues during the manufacturing process, particularly around the edges. Another possible factor contributing to the alignment issues is the stationary positioning of the gas blower relative to the rotating capillary holder. It was hypothesized that slight changes in the distance between the heat blower orifice and the capillary walls during rotation could have affected alignment at elevated temperatures. However, this hypothesis remains inconclusive. A post-beamtime experiment with the heat blower demonstrated that varying the distance between the blower orifice and the capillary by several millimeters did not result in a measurable change in the sample temperature. Given that the capillary holder is securely mounted to the Huber table with several bolts, it is doubtful that minor variations in gas flow pressure from the heat blower would cause significant alignment issues.

Further investigation is required to conclusively determine the causes of these alignment challenges, particularly the potential influence of substrate flatness and temperature-induced effects during sample rotation.

V. Safety considerations and the necessity of improvements in the operando setup

While high safety standards are maintained at DESY, the complexity of the operando SXRD stage for high-pressure experiments introduces potential risks that must be addressed. Despite robust protocols, the safety of such experimental setups heavily depends on the user's actions and vigilance. It is, therefore, essential to eliminate any identified safety concerns, particularly those that might occur without visible or immediate warning.

One critical issue relates to the gas-tight sealing of the capillary. Cracks in the capillary material often form as the fastening nuts are tightened, making these defects invisible to the user during assembly. Notably, standard overpressure tests have been shown to be unreliable in detecting such cracks. On two separate occasions during prior experiments, capillary ruptures occurred at high gas pressures (30 bar of Ar and 30 bar of H_2,

respectively) while the author was present inside the experimental hutch. These incidents underscore the latent risk posed by undetected failures in the capillary under high-pressure conditions.

Additionally, thorough pre-experiment testing of the gas bottle pressure reducers is essential. If uncontrolled pressure increases occur within the system, it would compromise the validity of prior overpressure tests, thus significantly increasing the risk of failure during operation. Addressing these safety issues in the redesigned operando setup is imperative to ensure both the integrity of the experiments and the safety of personnel.

C. X-ray reflectivity results and fit parameters

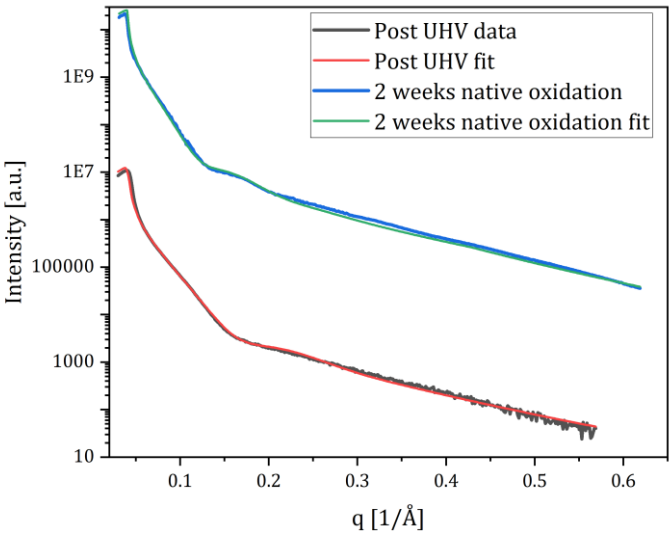

Figure I.5. X-ray reflectivity measurements and corresponding fits of sample "Cu-Al2O3" measured shortly after the UHV sample preparation (black) in air as well as after 2 weeks of native oxidation (blue) measured under Ar flow.

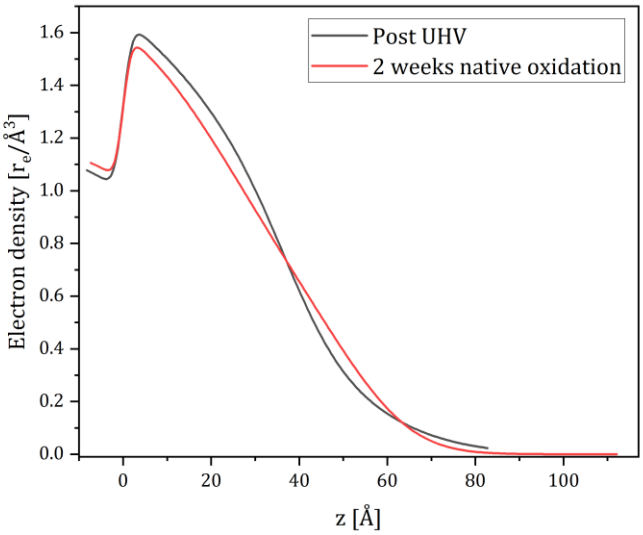

Figure I.6. Electron density profile corresponding to the two-layer fit of the data seen in Figure I.5.

Parameter	"Cu-Al_2O_3" Post UHV	"Cu-Al_2O_3" 2 weeks native oxidation
Substrate roughness σ_{Al2O3} [Å]	1.65	1.47
Layer thickness Cu d_{Cu} [Å]	28.1	24.9
Layer roughness Cu σ_{Cu} [Å]	25.6	20.1
Density Cu p_{Cu} [%]	0.0684/0.0862 = 79.4%	0.0595/0.0862 = 69.0%
Layer thickness Cu_2O d_{Cu2o} [Å]	9.37	28.9
Layer roughness Cu_2O σ_{Cu2o} [Å]	9.08	11.7
Density Cu_2O p_{Cu2o} [%]	0.00983/0.00983 = 100%	0.00878/0.00983 = 89.3%

Table I.3. Results of the two-layer model fit to the data seen in Figure I.5.

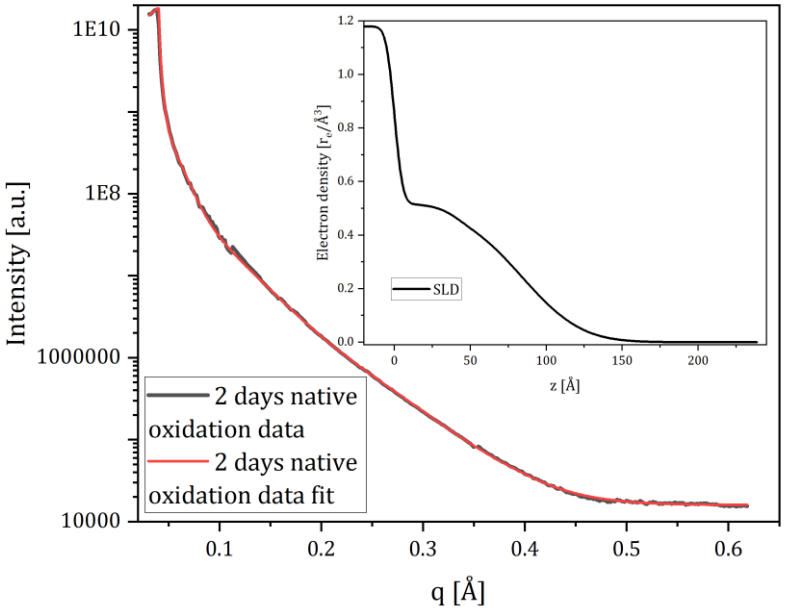

Figure I.7. X-ray reflectivity measurement (black) and fit (red) of sample "CZ-Al2O3" taken after 2 days of native oxidation and measured under Ar flow. Inlet: Electron density profile corresponding to the two-layer fit of the XRR curve.

Parameter	"CZ-Al_2O_3" 2 days native oxidation
Substrate roughness σ_{Al2O3} [Å]	4.36
Layer thickness Cu d_{Cu} [Å]	40.3
Layer roughness Cu σ_{Cu} [Å]	8.04
Density Cu p_{Cu} [%]	0.0178/0.0862 = 20.6 %
Layer thickness Cu_2O d_{Cu2o} [Å]	43.64
Layer roughness Cu_2O σ_{Cu2o} [Å]	30.98
Density Cu_2O p_{Cu2o} [%]	0.0108/0.00983 = 109.9%

Table I.4. Results of the two-layer model fit to the data seen in Figure I.7.

D. Additional data and fitting details for ambient pressure measurements

Peak	Cu ($1\bar{1}1$)	Cu (002)	Al_2O_3 (300)	Cu ($2\bar{2}0$)
In-plane rotation angle ω [°]	-64.04	-68.08	-64.34	-62.99
Scattering angle γ [°]	19.31	22.35	29.67	31.85
Corrected in-plane angle $\omega_{corrected}$ [°]	-73.70	-79.26	-79.18	-78.92

Table I.5. Calculation of the corrected in-plane angle for Cu and Al_2O_3 reflexes at ambient pressure under pure CO gas flow.

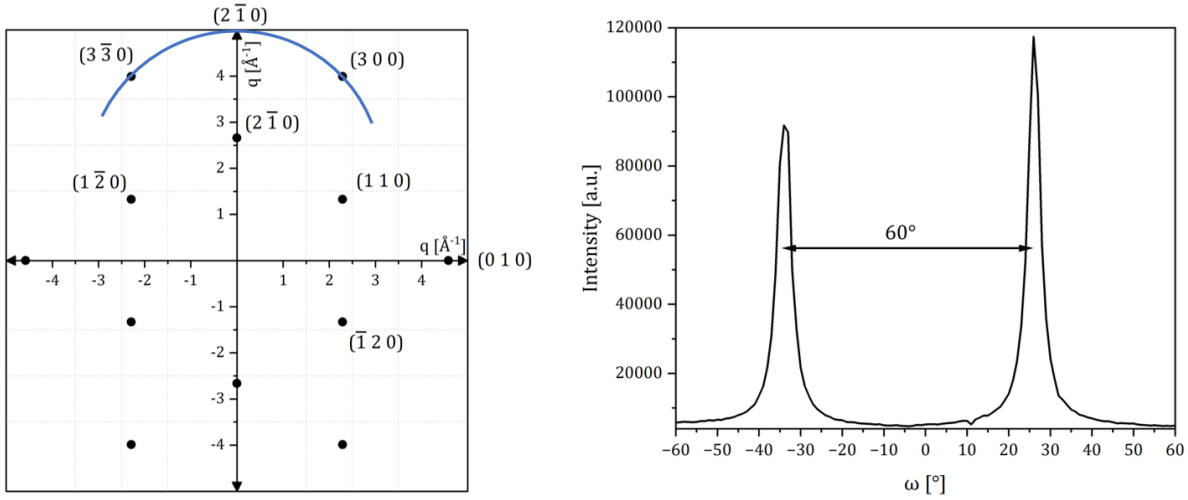

Figure I.8. Left: In-plane reciprocal space map of the ZnO-supported model catalyst "CZ-Al_2O_3" at 575 K under pure H_2 flow, with the Al_2O_3 reflexes marked with black circles and the scan seen on the right illustrated as a blue line. Right: Large azimuthal in-plane scan for Al_2O_3 (300) showing the direction of the high symmetry direction of the substrate and the 60-degree symmetry.

Reflex	Scan and peak number		Parameters		Scan and peak number		Parameters
Mo (110)	Cu (1$\bar{1}$1) scan	I	q [1/Å]	2.76			
			FWHM [1/Å]	0.014			
			Intensity [a.u.]	70			
			$\omega_{corrected}$ [°]	-73.83			
Cu (1$\bar{1}$1)	Cu (1$\bar{1}$1) scan	II	q [1/Å]	2.98	Radial scan along Cu (1$\bar{1}$1)	I	2.98
			FWHM [1/Å]	0.074			0.076
			Intensity [a.u.]	711			1058
			$\omega_{corrected}$ [°]	-74.53			-74.53
Be (1 1 0)	Cu (002) scan	I	q [1/Å]	3.18			
			FWHM [1/Å]	0.054			
			Intensity [a.u.]	12			
			$\omega_{corrected}$ [°]	-70.33			
Cu (002)	Cu (002) scan	II	q [1/Å]	3.45	Radial scan along Cu (1$\bar{1}$1)	II	3.44
			FWHM [1/Å]	0.094			0.091
			Intensity [a.u.]	263			351
			$\omega_{corrected}$ [°]	-71.2			-74.53

Al_2O_3 (300)	Cu ($2\bar{2}0$) scan	I	q [1/Å]	4.52	Cu_2O ($2\bar{2}0$) scan	I	4.50
			FWHM [1/Å]	0.928			0.183
			Intensity [a.u.]	5280			35281
			$\omega_{corrected}$ [°]	-57.77			10.12
Cu ($2\bar{2}0$)	Cu ($2\bar{2}0$) scan	II	q [1/Å]	4.87	Radial scan along Cu ($1\bar{1}1$)	III	4.87
			FWHM [1/Å]	0.085			0.091
			Intensity [a.u.]	376			620
			$\omega_{corrected}$ [°]	-59.02			-74.53
US1 (440) + Al_2O_3 (220)	Radial scan along Cu ($1\bar{1}1$)	IV	q [1/Å]	5.21			
			FWHM [1/Å]	0.627			
			Intensity [a.u.]	2384			
			$\omega_{corrected}$ [°]	-74.53			
Cu ($1\bar{1}3$)	Radial scan along Cu ($1\bar{1}1$)	V	q [1/Å]	5.71			
			FWHM [1/Å]	0.107			
			Intensity [a.u.]	176			
			$\omega_{corrected}$ [°]	-74.53			

Table I.6. Bragg peak fitting results for in-plane scans performed in H_2 at 575 K corresponding to Figure 6.14 for the ZnO-supported model system.

Peak	Cu (220)	Cu (113)	Background correction
35 minutes Ar			
L-Position [r.l.u.]	8.043	10.085	8.989
q [1/Å]	4.895	5.712	5.266
FWHM [1/Å]	0.234	0.092	0.792
Amplitude	12063	2534	6407
35 minutes Ar:CO_2 (1:1)			
L-Position [r.l.u.]	8.05	10.083	8.93
q [1/Å]	4.898	5.711	5.243
FWHM [1/Å]	0.237	0.087	0.777
Amplitude	10527	2358	7026

15 minutes H2			
L-Position [r.l.u.]	8.019	10.149	8.998
q [1/Å]	4.886	5.738	5.27
FWHM [1/Å]	0.08	0.066	1.673
Amplitude	1528	1027	9.784
25 minutes H2			
L-Position [r.l.u.]	8.019	10.139	9
q [1/Å]	4.886	5.734	5.271
FWHM [1/Å]	0.096	0.077	1.005
Amplitude	1669	1748	3165

Table I.7. Peak fitting results for the L-scan starting from the Cu ($1\bar{1}1$) in-plane reflex of the simplified model system "Cu-Al_2O_3" sample of Figure 6.15.

Reflex	Scan and peak number		Parameters		Scan and peak number		Para-meters	Scan and peak number		Para-meters
Mo (110)	Cu ($1\bar{1}1$) scan	I	q [1/Å]	2.77						
			FWHM [1/Å]	0.018						
			Intensity [a.u.]	68						
			$\omega_{corrected}$ [°]	-73.83						
Cu_2O (002)	Cu ($1\bar{1}1$) scan	II	q [1/Å]	2.93						
			FWHM [1/Å]	0.061						
			Intensity [a.u.]	243						
			$\omega_{corrected}$ [°]	-74.37						
$Cu_{0.64}Zn_{0.36}$ (002)	Cu ($1\bar{1}1$) scan	III	q [1/Å]	3.27	Cu (002) scan	I	3.24	Radial scan along Cu ($1\bar{1}1$)	I	3.25
			FWHM [1/Å]	0.2			0.119			0.78
			Intensity [a.u.]	1215			196			105
			$\omega_{corrected}$ [°]	-75.42			-70.33			-74.53

ZnO (110)	ZnO (110) scan	I	q [1/Å]	3.77						
			FWHM [1/Å]	0.074						
			Intensity [a.u.]	61						
			$\omega_{corrected}$ [°]	-29.5						
Cu_2O ($2\bar{2}0$)	Cu ($2\bar{2}0$) scan	I	q [1/Å]	4.15	Cu_2O ($2\bar{2}0$) scan	I	4.15	Radial scan along Cu ($1\bar{1}1$)	II	4.14
			FWHM [1/Å]	0.069			0.075			0.082
			Intensity [a.u.]	377			15782			390
			$\omega_{corrected}$ [°]	-56.59			11.46			-74.53
Al_2O_3 (300)	Cu ($2\bar{2}0$) scan	II	q [1/Å]	4.51	Cu_2O ($2\bar{2}0$) scan	II	4.54	Radial scan along Cu ($1\bar{1}1$)	III	4.59
			FWHM [1/Å]	0.943			0.178			0.1
			Intensity [a.u.]	9056			45101			251
			$\omega_{corrected}$ [°]	-57.77			10.12			-74.53
US1 (440) + Al_2O_3 (220)	Radial scan along Cu ($1\bar{1}1$)	IV	q [1/Å]	5.15						
			FWHM [1/Å]	0.626						
			Intensity [a.u.]	3430						
			$\omega_{corrected}$ [°]	-74.53						
$Cu_{0.64}Zn_{0.36}$ (113)	Radial scan along Cu ($1\bar{1}1$)	V	q [1/Å]	5.39						
			FWHM [1/Å]	0.126						
			Intensity [a.u.]	607						
			$\omega_{corrected}$ [°]	-74.53						

Table I.8. Bragg peak fitting results for in-plane scans performed under Ar flow at 575 K for the ZnO-supported model catalyst "CZ-Al_2O_3", corresponding to Figure 6.17.

#Peak	ω [°]	$\omega_{corrected}$ [°]
1	-77.29	-89.529
3	-17.21	-29.449
5	42.69	30.451
7	102.56	90.321
2	-55.51	-67.75
4	4.25	-7.989
6	64.14	51.901

Table I.9. Sample rotation angle and calculated corrected in-plane direction of the ZnO (110) reflexes as measured at 575 K under Ar flow for the ZnO-supported model system "CZ-Al_2O_3", as shown in Figure 6.18.

Reflex	Scan and peak number		Parameters		Scan and peak number		Parameters
Cu $(1\bar{1}1)$	Radial scan along Cu $(1\bar{1}1)$	I	q [1/Å]	2.99			
			FWHM [1/Å]	0.051			
			Intensity [a.u.]	696			
			$\omega_{corrected}$ [°]	-74.53			
Cu (002)	Radial scan along Cu $(1\bar{1}1)$	II	q [1/Å]	3.44			
			FWHM [1/Å]	0.077			
			Intensity [a.u.]	370			
			$\omega_{corrected}$ [°]	-74.53			
ZnO (110)	Radial scan along Cu $(1\bar{1}1)$	III	q [1/Å]	3.79	ZnO (110) scan	I	3.79
			FWHM [1/Å]	0.105			0.079
			Intensity [a.u.]	124			71
			$\omega_{corrected}$ [°]	-74.53			-29.5
US1 (224)	Cu_2O $(2\bar{2}0)$ scan	I	q [1/Å]	4.27	Radial scan along Cu $(1\bar{1}1)$	IV	4.36
			FWHM [1/Å]	0.088			0.2
			Intensity [a.u.]	1130			100
			$\omega_{corrected}$ [°]	9.19			-74.53
Al_2O_3 (300)	Cu $(2\bar{2}0)$ scan	II	q [1/Å]	4.55			
			FWHM [1/Å]	0.198			
			Intensity [a.u.]	41752			
			$\omega_{corrected}$ [°]	10.12			

Cu ($2\bar{2}0$)	Radial scan along Cu ($1\bar{1}1$)	V	q [1/Å]	4.87	
			FWHM [1/Å]	0.068	
			Intensity [a.u.]	417	
			$\omega_{corrected}$ [°]	-74.53	
US1 (440) + Al_2O_3 (220)	Radial scan along Cu ($1\bar{1}1$)	V	q [1/Å]	5.21	
			FWHM [1/Å]	0.691	
			Intensity [a.u.]	2429	
			$\omega_{corrected}$ [°]	-74.53	
Cu ($1\bar{1}3$)	Radial scan along Cu ($1\bar{1}1$)	VI	q [1/Å]	5.71	
			FWHM [1/Å]	0.082	
			Intensity [a.u.]	109	
			$\omega_{corrected}$ [°]	-74.53	

Table I.10. Bragg peak fitting results for in-plane scans performed in the H_2 condition post Ar exposure at 575 K for the ZnO-supported model system "CZ-Al_2O_3", corresponding to Figure 6.20.

	Peak	Cu (111)	ZnO (102)	Cu (200)	ZnO (103)	ZnO (104)	Cu (113)
	Number	I	II	III	IV	V	VI
Cu ($1\bar{1}1$) L-scan	q [1/Å]	3.00	3.25	3.44	4.08	5.32	5.70
	FWHM [1/Å]	0.76	2	0.289	1.413	2.373	Not fitted
	Intensity [a.u.]	5064	35016	1311	97220	68521	Not fitted
	$\omega_{corrected}$ [°]	-74.53	-74.53	-74.53	-74.53	-74.53	-74.53

Table I.11. Bragg peak fitting results for out-of-plane scan from Cu ($1\bar{1}1$) performed in the second H_2 condition at 575 K for the ZnO-supported model system "CZ-Al_2O_3", corresponding to Figure 6.21.

ZnO (110) L-scan		US1 (331)	US1 (224)	ZnO (112)	US1 (444)	ZnO (114)
	q [1/Å]	3.81	4.29	4.54	6.17	
	$\omega_{corrected}$ [°]	-29.5	-29.5	-29.5	-29.5	

Table I.12. Bragg peak fitting results for out-of-plane scan starting from the ZnO (110) in-plane reflexes performed in the second H_2 condition at 575 K for the ZnO-supported model system "CZ-Al_2O_3", corresponding to Figure 6.23.

Cu ($1\bar{1}1$)	H_2 first, ($1\bar{1}1$)	H_2 first, ($1\bar{1}1$)	H_2 second, ($1\bar{1}1$)	H_2 third, ($1\bar{1}1$)
q peak	2.99	2.99	2.98	2.98
q FWHM	0.0586	0.0585	0.0599	0.0618
Mu	-74.92	-64.26	-64.26	-64.26
Particle size (nm)	10.72	10.74	10.49	10.17
Time in gas	150 minutes	150 minutes	35 minutes	30 minutes
Cu (002)	H_2 first, (002)	H_2 first, (002)	H_2 first, (020)	H_2 second, (002)
q peak	3.45	3.46	3.45	3.44
q FWHM	0.0651	0.0675	0.0665	0.0622
Mu	-68.08	-69.07	20.93	-68.08
Particle size (nm)	9.65	9.31	9.45	10.1
Time in gas	160 minutes	260 minutes	240 minutes	30 minutes

Table I.13. Bragg peak fitting results for Cu ($1\bar{1}1$) and Cu (002) in-plane reflexes and corresponding average particle diameter determination for the simplified model system "Cu-Al_2O_3".

Cu ($2\bar{2}0$)	CO	H_2	Cu_2O (002)	Ar	Ar post CO_2
q peak	4.86	4.88	q peak	2.94	2.93
q FWHM	0.0689	0.0762	q FWHM	0.0641	0.0662
Mu	-65.8	-60.74	Mu	-64.26	-64.26
Particle size (nm)	9.12	8.25	Particle size (nm)	9.8	9.49
Time in gas	75 minutes	205 minutes	Time in gas	60 minutes	35 minutes

Table I.14. Bragg peak fitting results for Cu ($2\bar{2}0$) and Cu_2O (002) in-plane reflexes and corresponding average particle diameter determination for the simplified model system "Cu-Al_2O_3".

Peak	Scan	Parameters	CO	CO_2
$Cu_{0.64}$ $Zn_{0.36}$ $(1\bar{1}1)$	Cu $(1\bar{1}1)$ scan	q [1/Å]	2.82	2.82
		FWHM [1/Å]	0.04	0.10
		Intensity [a.u.]	137	224
		$\omega_{corrected}$ [°]	-73.99	-73.99
$Cu_{0.64}Zn_{0.36}$ (002)	Cu $(1\bar{1}1)$ scan	q [1/Å]	3.28	3.26
		FWHM [1/Å]	0.2	0.2
		Intensity [a.u.]	1546	1649
		$\omega_{corrected}$ [°]	-75.50	-75.50
	Cu (002) scan	q [1/Å]	3.24	3.24
		FWHM [1/Å]	0.136	0.150
		Intensity [a.u.]	211	305
		$\omega_{corrected}$ [°]	-70.53	-70.53
	Radial scan	q [1/Å]	3.25	3.25
		FWHM [1/Å]	0.088	0.103
		Intensity [a.u.]	157	178
		$\omega_{corrected}$ [°]	-74.53	-74.53
$Cu_{0.64}$ $Zn_{0.36}$ $(2\bar{2}0)$	Radial scan	q [1/Å]	4.58	4.59
		FWHM [1/Å]	0.176	0.078
		Intensity [a.u.]	340	204
		$\omega_{corrected}$ [°]	-74.53	-74.53

Table I.15. Bragg peak fitting results for the in-plane scans measured at 575 K at 1 bar total pressure for the ZnO-supported model system "CZ-Al_2O_3", corresponding to Figure 6.29.

Reflex	Scan and peak number		Parameters		Scan and peak number	Parameters
US1 ($2\bar{2}0$)	US1 ($2\bar{2}0$) scan	I	q [1/Å]	2.48		
			FWHM [1/Å]	0.084		
			Intensity [a.u.]	5986		
			$\omega_{corrected}$ [°]	-18.03		
Al_2O_3 (110)	US1 ($2\bar{2}0$) scan	II	q [1/Å]	2.62		
			FWHM [1/Å]	0.067		
			Intensity [a.u.]	22583		
			$\omega_{corrected}$ [°]	-18.23		
US1 (440) + Al_2O_3 (220)	Radial scan along Cu ($1\bar{1}1$)	IV	q [1/Å]	5.21		
			FWHM [1/Å]	0.627		
			Intensity [a.u.]	2384		
			$\omega_{corrected}$ [°]	-74.53		
			FWHM [1/Å]	0.107		
			Intensity [a.u.]	176		
			$\omega_{corrected}$ [°]	-74.53		

Table I.16 Bragg peak fitting results for initial in-plane scans performed in H_2 at 575 K for the ZnO-supported model system "CZ-Al_2O_3",corresponding to Figure 6.41.

Reflex	Scan and peak number		Parameters	
US1 ($2\bar{2}0$)	US1 ($2\bar{2}0$) scan	I	q [1/Å]	2.46
			FWHM [1/Å]	0.065
			Intensity [a.u.]	13534
			$\omega_{corrected}$ [°]	-18.03
Al_2O_3 (110)	US1 ($2\bar{2}0$) scan	II	q [1/Å]	2.62
			FWHM [1/Å]	0.112
			Intensity [a.u.]	12394
			$\omega_{corrected}$ [°]	-18.23

US1 (440) + Al_2O_3 (220)	Radial scan along Cu ($1\bar{1}1$)	IV	q [1/Å]	5.15
			FWHM [1/Å]	0.626
			Intensity [a.u.]	3430
			$\omega_{corrected}$ [°]	-74.53

Table I.17. Bragg peak fitting results for initial in-plane scans performed under Ar gas flow at 575 K for the ZnO-supported model system "CZ-Al_2O_3", corresponding to Figure 6.42.

Reflex	Scan and peak number		Parameters		Scan and peak number		Parameters
US1 ($2\bar{2}0$)	US1 ($2\bar{2}0$) scan	I	q [1/Å]	2.47			
			FWHM [1/Å]	0.065			
			Intensity [a.u.]	13429			
			$\omega_{corrected}$ [°]	-18.03			
Al_2O_3 (110)	US1 ($2\bar{2}0$) scan	II	q [1/Å]	2.63			
			FWHM [1/Å]	0.091			
			Intensity [a.u.]	6126			
			$\omega_{corrected}$ [°]	-18.23			
US1 (440) + Al_2O_3 (220)	Radial scan along Cu ($1\bar{1}1$)	V	q [1/Å]	5.21			
			FWHM [1/Å]	0.691			
			Intensity [a.u.]	2429			
			$\omega_{corrected}$ [°]	-74.53			
US1 (224)	Cu_2O ($2\bar{2}0$) scan	I	q [1/Å]	4.27	Radial scan along Cu ($1\bar{1}1$)	IV	4.36
			FWHM [1/Å]	0.088			0.2
			Intensity [a.u.]	1130			100
			$\omega_{corrected}$ [°]	9.19			-74.53
US1 (440) + Al_2O_3 (220)	Radial scan along Cu ($1\bar{1}1$)	V	q [1/Å]	5.21			
			FWHM [1/Å]	0.691			
			Intensity [a.u.]	2429			
			$\omega_{corrected}$ [°]	-74.53			

Table I.18. Bragg peak fitting results for in-plane scans performed in the second H_2 condition at 575 K for the ZnO-supported model system "CZ-Al_2O_3", corresponding to Figure 6.44.

E. Fit parameters for XRD analysis post reaction conditions

Peak	h	k	l	μ_corrected [°]	q_z [1/A]]	q_xy [1/Å]	q [1/Å]	q_calc [1/Å]	q_z_calc [1/Å]	q_xy_calc [1/Å]	Δq [%]	Δq_z [%]	Δq_xy [%]	|F| error	|F|	|F| max	|F| Cu0.64Zn0.36	|F| max without (111)	|F| Cu0.64Zn0.36 without (111)
1a	1	1	-1	29.85	2.2635	1.4161	2.8442	2.8472	0.9491	2.6844	0.1059	-3.2599	0.5347	41	1000	1000	1000		
	1	1	-1	-0.1	2.6682	0.0969	2.8442	2.8472	0.9491	2.6844	0.1059	-3.2599	0.5347	71	683				
	1	1	-1	59.89	1.2506	2.3590	2.8442	2.8472	0.9491	2.6844	0.1059	-3.2599	0.5347	81	678				
-1a	1	1	-1	29.6	-2.3789	1.2342	2.8501	2.8472	0.9491	2.6844	-0.1038	-2.2062	0.1621	53	921				
	1	1	-1	59.52	-1.4463	2.2563	2.8501	2.8472	0.9491	2.6844	-0.1038	-2.2062	0.1621	114	559				
	1	1	-1	89.59	-0.1211	2.6773	2.8501	2.8472	0.9491	2.6844	-0.1038	-2.2062	0.1621	54	838				
-2a	0	0	2	29.16	-2.3957	1.2012	3.2968	3.2876	1.8981	2.6844	-0.2780	-1.1525	0.1621	30	307	340	942	1000	1000
	0	0	2	59.19	-1.4729	2.2389	3.2968	3.2876	1.8981	2.6844	-0.2780	-1.1525	0.1621	93	236				
	0	0	2	89.18	-0.1566	2.6754	3.2968	3.2876	1.8981	2.6844	-0.2780	-1.1525	0.1621	32	277				
2a	0	0	2	0.29	2.6768	0.1319	3.2968	3.2876	1.8981	2.6844	-0.2780	-1.1525	0.1621	46	246				
	0	0	2	30.3	2.2520	1.4530	3.2968	3.2876	1.8981	2.6844	-0.2780	-1.1525	0.1621	27	340				
	0	0	2	60.27	1.2250	2.3836	3.2968	3.2876	1.8981	2.6844	-0.2780	-1.1525	0.1621	78	194				
-3a	2	2	0	27.13	-2.4568	1.0708	4.6663	4.6494	3.7962	2.6844	-0.3638	-0.6257	0.1621	23	264	264	771	776	818
	2	2	0	57.06	-1.5949	2.1538	4.6663	4.6494	3.7962	2.6844	-0.3638	-0.6257	0.1621	135	217				
	2	2	0	87.08	-0.3034	2.6628	4.6663	4.6494	3.7962	2.6844	-0.3638	-0.6257	0.1621	29	236				
3a	2	2	0	2.35	2.6657	0.2769	4.6663	4.6494	3.7962	2.6844	-0.3638	-0.6257	0.1621	35	234				
	2	2	0	32.35	2.1701	1.5726	4.6663	4.6494	3.7962	2.6844	-0.3638	-0.6257	0.1621	22	245				
	2	2	0	62.39	1.0913	2.4477	4.6663	4.6494	3.7962	2.6844	-0.3638	-0.6257	0.1621	77	178				
1b	-1	-1	3	-0.19	5.3371	0.3713	5.4372	5.4519	0.9491	5.3687	0.2700	-2.2062	0.3484	41	203	297	682	874	725
	-1	-1	3	29.8	4.4369	2.9894	5.4372	5.4519	0.9491	5.3687	0.2700	-2.2062	0.3484	32	296				
	-1	-1	3	59.77	2.3503	4.8061	5.4372	5.4519	0.9491	5.3687	0.2700	-2.2062	0.3484	122	168				
-1b	-1	-1	3	29.66	-4.8387	2.3059	5.4489	5.4519	0.9491	5.3687	0.0567	-3.2599	0.1621	36	169				
	-1	-1	3	59.74	-3.0313	4.4205	5.4489	5.4519	0.9491	5.3687	0.0567	-3.2599	0.1621	125	184				
	-1	-1	3	89.69	-0.4196	5.3436	5.4489	5.4519	0.9491	5.3687	0.0567	-3.2599	0.1621	25	259				
4a	1	1	3	4.09	2.6521	0.3859	5.4626	5.4519	4.7453	2.6844	-0.1954	-0.3096	0.1621	31	259	297	682	874	725
	1	1	3	34.07	2.1044	1.6595	5.4626	5.4519	4.7453	2.6844	-0.1954	-0.3096	0.1621	29	275				
	1	1	3	64.23	0.9857	2.4921	5.4626	5.4519	4.7453	2.6844	-0.1954	-0.3096	0.1621	99	297				
-4a	1	1	3	25.4	-2.4891	0.9660	5.4664	5.4519	4.7453	2.6844	-0.2656	-0.5203	0.5347	23	249				
	1	1	3	55.38	-1.6734	2.0805	5.4664	5.4519	4.7453	2.6844	-0.2656	-0.5203	0.5347	113	233				
	1	1	3	85.41	-0.4076	2.6387	5.4664	5.4519	4.7453	2.6844	-0.2656	-0.5203	0.5347	26	221				

Table I.19. Results of the peak analysis for the $Cu_{0.64}Zn_{0.36}$ structure of "CZ-Al_2O_3" as illustrated in Figure 6.32. The values of q_z, q_xy and q correspond to measured values, while the "calc" values were calculated from the given HKL using the fitted lattice parameter of 3.8223 Å. Values denoted with "Δ" refer to the difference in percent between measured and calculated values. "|F|" denotes the structure factor of a given measured reflex, while "|F| $Cu_{0.64}Zn_{0.36}$" serves as a reference to the

literature data of the Cu-Zn alloy phase [73]. “|F| max” are the maximum values taken from all the measurements of a particular reflex, while the rows denoted with “without (111)” are adjusted as if the (111) reflex was not measured due to a possible peak superposition.

2b	2	2	-2	-0.01	5.3346	0.4058	5.6841	5.6944	1.8981	5.3687	0.1805	-1.1525	0.3484	49	231	302	658	888	699
	2	2	-2	29.97	4.4180	3.0172	5.6841	5.6944	1.8981	5.3687	0.1805	-1.1525	0.3484	32	302				
	2	2	-2	59.97	2.3176	4.8220	5.6841	5.6944	1.8981	5.3687	0.1805	-1.1525	0.3484	143	272				
-2b	2	2	-2	29.47	-4.8629	2.2780	5.7029	5.6944	1.8981	5.3687	-0.1501	-1.1525	-0.0241	22	290				
	2	2	-2	59.59	-3.0632	4.4106	5.7029	5.6944	1.8981	5.3687	-0.1501	-1.1525	-0.0241	161	185				
	2	2	-2	89.47	-0.4587	5.3504	5.7029	5.6944	1.8981	5.3687	-0.1501	-1.1525	-0.0241	25	255				
3b	0	0	4	0.88	5.3314	0.5528	6.5761	6.5753	3.7962	5.3687	-0.0130	-0.3623	0.1621	43	166	216	578	635	614
	0	0	4	30.88	4.3407	3.1445	6.5761	6.5753	3.7962	5.3687	-0.0130	-0.3623	0.1621	30	216				
	0	0	4	60.88	2.1869	4.8936	6.5761	6.5753	3.7962	5.3687	-0.0130	-0.3623	0.1621	122	118				
4b	3	3	-1	1.6	5.3189	0.6625	7.1685	7.1653	4.7453	5.3687	-0.0450	-0.3096	0.1621	50	141	158	532	465	564
	3	3	-1	31.58	4.2762	3.2317	7.1685	7.1653	4.7453	5.3687	-0.0450	-0.3096	0.1621	27	158				
	3	3	-1	61.6	2.0857	4.9376	7.1685	7.1653	4.7453	5.3687	-0.0450	-0.3096	0.1621	118	136				
-5a	3	3	1	20.44	-2.5797	0.6883	7.1753	7.1653	6.6434	2.6844	-0.1397	-0.2494	0.5347	20	101	158	532	465	564
	3	1	-3	33.49	-2.3577	1.2531	7.1753	7.1653	6.6434	2.6844	-0.1397	-0.2494	0.5347	32	32				
	3	3	1	51.29	-1.8618	1.9138	7.1753	7.1653	6.6434	2.6844	-0.1397	-0.2494	0.5347	119	84				
	3	3	1	67.53	-1.2523	2.3581	7.1753	7.1653	6.6434	2.6844	-0.1397	-0.2494	0.5347	79	20				
	3	3	1	80.37	-0.6969	2.5774	7.1753	7.1653	6.6434	2.6844	-0.1397	-0.2494	0.5347	40	96				
5a	3	3	1	9.09	2.5839	0.6726	7.1753	7.1653	6.6434	2.6844	-0.1397	-0.2494	0.5347	38	96				
	3	3	1	26.1	2.2741	1.3990	7.1753	7.1653	6.6434	2.6844	-0.1397	-0.2494	0.5347	46	25				
	3	3	1	39.08	1.9018	1.8741	7.1753	7.1653	6.6434	2.6844	-0.1397	-0.2494	0.5347	64	91				
	3	3	1	52.95	1.3971	2.2753	7.1753	7.1653	6.6434	2.6844	-0.1397	-0.2494	0.5347	126	26				
	3	3	1	69.05	0.7113	2.5735	7.1753	7.1653	6.6434	2.6844	-0.1397	-0.2494	0.5347	58	96				
6a	2	2	4	12.37	2.5408	0.8526	8.0587	8.0531	7.5925	2.6844	-0.0699	-0.0989	0.1621	30	123	123	472	362	502
	2	2	4	42.33	1.7755	2.0075	8.0587	8.0531	7.5925	2.6844	-0.0699	-0.0989	0.1621	75	112				
	2	2	4	72.48	0.5270	2.6277	8.0587	8.0531	7.5925	2.6844	-0.0699	-0.0989	0.1621	56	120				
-6a	2	2	4	17.19	-2.6307	0.5118	8.0587	8.0531	7.5925	2.6844	-0.0699	-0.0989	0.1621	22	82				
	2	2	4	47.08	-2.0257	1.7547	8.0587	8.0531	7.5925	2.6844	-0.0699	-0.0989	0.1621	64	83				
	2	2	4	77.21	-0.8712	2.5344	8.0587	8.0531	7.5925	2.6844	-0.0699	-0.0989	0.1621	31	50				

Table I.20. Extension of Table I.19.

Peak	h	k	l	μ_corrected [°]	q_z [1/A]]	q_xy [1/Å]	q [1/Å]	q_calc [1/Å]	q_z_calc [1/Å]	q_xy_calc [1/Å]	Δq [%]	Δq_z [%]	Δq_xy [%]
10a	-1	0	1	19.4959	1.3677	-2.1177	2.5210	2.5346	1.3431	2.1495	0.5389	1.8282	1.4786
10b	-1	0	1	32.1359	1.3677	-2.1177	2.5210	2.5346	1.3431	2.1495	0.5389	1.8282	1.4786
10c	-1	0	1	79.5159	1.3677	-2.1177	2.5210	2.5346	1.3431	2.1495	0.5389	1.8282	1.4786
65a	1	0	1	24.1112	1.3735	2.0962	2.5061	2.5346	1.3431	2.1495	1.1252	2.2600	2.4788
65b	1	0	1	36.6412	1.3735	2.0962	2.5061	2.5346	1.3431	2.1495	1.1252	2.2600	2.4788
65c	1	0	1	84.1312	1.3735	2.0962	2.5061	2.5346	1.3431	2.1495	1.1252	2.2600	2.4788

Table I.21. Results of the peak analysis for ZnO of "CZ-Al_2O_3" as illustrated in Figure 6.37. The values of q_z, q_xy and q correspond to measured values, while the "calc" values were calculated from the given HKL using the literature lattice parameter of a=5.2151 Å and c= 3.2535 Å [115]. Values denoted with "Δ" refer to the difference in percent between measured and calculated values.

Peak	h	k	l	q_z [1/A]]	q_xy [1/Å]	q [1/Å]	q_calc [1/Å]	q_z_calc [1/Å]	q_xy_calc [1/Å]	Δq [%]	Δq_z [%]	Δq_xy [%]
1a	1	1	-1	0.5467	1.4349	1.5355	1.5296	0.5099	1.4421	-0.3890	-7.2262	0.4987
-1a	1	1	-1	0.5342	-1.4428	1.5385	1.5296	0.5099	1.4421	-0.5851	-4.7746	-0.0491
1b	0	-1	2	0.5306	1.902	1.9746	1.9747	0.5099	1.9077	0.0021	-4.0685	0.2992
-1b	0	-1	2	0.5304	-1.9081	1.9804	1.9747	0.5099	1.9077	-0.2928	-4.0293	-0.0205
1c	1	1	-2	0.0438	2.1611	2.1615	2.1631	0.0000	2.1631	0.0737		0.0942
-1c	1	1	-2	0.0453	-2.1702	2.1707	2.1631	0.0000	2.1631	-0.3483		-0.3265
1d	-2	2	0	0.0453	2.4852	2.4856	2.4978	0.0000	2.4978	0.4870		0.5035
-1d	-2	2	0	0.1148	-2.4923	2.4949	2.4978	0.0000	2.4978	0.1135		0.2193
1e	-1	-1	3	0.5371	2.8652	2.9151	2.9289	0.5099	2.8842	0.4710	-5.3434	0.6582
1g	1	2	-3	0.0466	3.2754	3.2757	3.3042	0.0000	3.3042	0.8630		0.8731
-1g	1	2	-3	0.0487	-3.2867	3.2871	3.3042	0.0000	3.3042	0.5202		0.5311
1h	2	2	-3	0.513	3.5997	3.6361	3.6411	0.5099	3.6052	0.1382	-0.6165	0.1534
1j	2	2	-4	0.0437	4.3058	4.3060	4.3263	0.0000	4.3263	0.4682		0.4733
-1j	2	2	-4	0.0484	-4.317	4.3173	4.3263	0.0000	4.3263	0.2081		0.2144
1k	-4	4	0	0.0448	4.985	4.9852	4.9956	0.0000	4.9956	0.2072		0.2113
-1k	-4	4	0	0.0468	-4.9861	4.9863	4.9956	0.0000	4.9956	0.1848		0.1892
1l	-1	-3	5	0.5546	5.1884	5.2180	5.2245	0.5099	5.1995	0.1248	-8.7757	0.2142
-1l	-1	-3	5	0.5402	-5.1972	5.2252	5.2245	0.5099	5.1995	-0.0139	-5.9514	0.0449
1x	1	1	2	2.0691	0.7202	2.1909	2.1631	2.0394	0.7210	-1.2815	-1.4550	0.1173
-1x	1	1	2	2.0672	-0.7253	2.1907	2.1631	2.0394	0.7210	-1.2764	-1.3618	-0.5900
1y	0	2	1	1.5608	1.2402	1.9935	1.9747	1.5296	1.2489	-0.9557	-2.0418	0.6957
-1y	0	2	1	1.566	-1.248	2.0025	1.9747	1.5296	1.2489	-1.4077	-2.3817	0.0711
2a	0	0	2	1.0415	1.4362	1.7741	1.7662	1.0197	1.4421	-0.4470	-2.1366	0.4086
-2a	0	0	2	1.0428	-1.4323	1.7717	1.7662	1.0197	1.4421	-0.3116	-2.2641	0.6790
2b	1	2	-1	1.0544	1.904	2.1765	2.1631	1.0197	1.9077	-0.6158	-3.4016	0.1944
-2b	1	2	-1	1.05	-1.9105	2.1800	2.1631	1.0197	1.9077	-0.7807	-2.9701	-0.1463
2e	2	2	-2	1.0197	2.8756	3.0510	3.0591	1.0197	2.8842	0.2647	0.0013	0.2976
-2e	2	2	-2	1.0401	-2.8818	3.0638	3.0591	1.0197	2.8842	-0.1508	-1.9993	0.0827
2g	2	3	-2	1.5689	3.2939	3.6485	3.6411	1.5296	3.3042	-0.2019	-2.5713	0.3132
-2g	2	3	-2	1.5802	-3.3027	3.6613	3.6411	1.5296	3.3042	-0.5537	-3.3101	0.0469
2i	1	3	-3	0.5419	3.7987	3.8372	3.8493	0.5099	3.8154	0.3163	-6.2848	0.4381
2j	3	3	-3	1.5596	4.3057	4.5795	4.5887	1.5296	4.3263	0.2017	-1.9633	0.4756
-2j	3	3	-3	1.5563	-4.3233	4.5949	4.5887	1.5296	4.3263	-0.1347	-1.7476	0.0688
2k	-3	5	1	1.5533	4.9833	5.2198	5.2245	1.5296	4.9956	0.0900	-1.5514	0.2453
-2k	-3	5	1	1.553	-4.9932	5.2291	5.2245	1.5296	4.9956	-0.0892	-1.5318	0.0471
2l	0	-2	6	2.0721	5.1946	5.5926	5.5852	2.0394	5.1995	-0.1330	-1.6021	0.0949

Table I.22. Results of the detailed peak analysis for the US1 structure of "CZ-Al_2O_3" as illustrated in Figure 6.46. The values of q_z, q_xy and q correspond to the measured values, while the q_z calc, q_xy calc and q calc values were calculated from the HKL of the reflex using the fitted lattice

parameter of 7.1149 Å. The values denoted with Δ refer to the difference in percent between the measured value and the calculated value. A negative Δ value corresponds to a ratio in which the measured value is larger than the calculated value and vice versa.

2y	1	3	2	3.0854	1.2428	3.3263	3.3042	3.0591	1.2489	-0.6673	-0.8584	0.4875
-2y	1	3	2	3.0814	-1.248	3.3245	3.3042	3.0591	1.2489	-0.6140	-0.7277	0.0711
3a	2	2	0	2.0649	1.4343	2.5142	2.4978	2.0394	1.4421	-0.6561	-1.2491	0.5403
3b	2	3	0	2.5864	1.9038	3.2115	3.1841	2.5493	1.9077	-0.8629	-1.4560	0.2049
-3b	2	3	0	2.5921	-1.9124	3.2212	3.1841	2.5493	1.9077	-1.1673	-1.6796	-0.2459
3d	1	5	3	4.6056	2.4841	5.2328	5.2245	4.5887	2.4978	-0.1595	-0.3681	0.5476
-3d	1	5	3	4.6073	-2.4918	5.2380	5.2245	4.5887	2.4978	-0.2582	-0.4051	0.2393
3e	0	0	4	2.0788	2.8769	3.5494	3.5324	2.0394	2.8842	-0.4804	-1.9306	0.2526
3i	2	4	-2	2.0767	3.7987	4.3293	4.3263	2.0394	3.8154	-0.0698	-1.8277	0.4381
-3i	2	4	-2	2.0706	-3.8083	4.3348	4.3263	2.0394	3.8154	-0.1971	-1.5286	0.1865
3j	4	4	-2	3.0902	4.3069	5.3008	5.2986	3.0591	4.3263	-0.0422	-1.0153	0.4479
-3j	4	4	-2	3.0874	-4.314	5.3050	5.2986	3.0591	4.3263	-0.1204	-0.9238	0.2838
4e	3	3	-1	2.5719	2.8712	3.8547	3.8493	2.5493	2.8842	-0.1386	-0.8872	0.4502
-4e	3	3	-1	2.5728	-2.8862	3.8665	3.8493	2.5493	2.8842	-0.4447	-0.9225	-0.0699
4i	1	-1	5	2.5802	3.8096	4.6011	4.5887	2.5493	3.8154	-0.2709	-1.2128	0.1525
-4i	1	-1	5	2.5867	-3.8164	4.6104	4.5887	2.5493	3.8154	-0.4730	-1.4678	-0.0258
5a	3	3	1	3.5938	1.4325	3.8688	3.8493	3.5690	1.4421	-0.5052	-0.6950	0.6652
-5a	3	3	1	3.5918	-1.4404	3.8699	3.8493	3.5690	1.4421	-0.5331	-0.6390	0.1173
5e	1	1	5	3.641	2.8736	4.6384	4.5887	3.5690	2.8842	-1.0822	-2.0175	0.3670
5i	3	5	-1	3.6161	3.803	5.2478	5.2245	3.5690	3.8154	-0.4457	-1.3198	0.3254
6a	2	2	4	4.1126	1.4334	4.3552	4.3263	4.0789	1.4421	-0.6695	-0.8274	0.6027
-6a	2	2	4	4.1091	-1.4412	4.3545	4.3263	4.0789	1.4421	-0.6526	-0.7416	0.0619
6e	4	4	0	4.1097	2.8688	5.0120	4.9956	4.0789	2.8842	-0.3282	-0.7563	0.5334
-6e	4	4	0	4.1226	-2.8796	5.0287	4.9956	4.0789	2.8842	-0.6637	-1.0725	0.1589
6i	2	0	6	4.1147	3.8064	5.6053	5.5852	4.0789	3.8154	-0.3600	-0.8789	0.2363
-6i	2	0	6	4.1174	-3.8147	5.6129	5.5852	4.0789	3.8154	-0.4964	-0.9451	0.0188

Table I.23. Extension of Table I.22. Results of the detailed peak analysis for the US1 structure of "CZ-Al_2O_3" as illustrated in Figure 6.46. The values of q_z, q_xy and q correspond to the measured values, while the q_z calc, q_xy calc and q calc values were calculated from the HKL of the reflex using the fitted lattice parameter of 7.1149 Å. The values denoted with Δ refer to the difference in percent between the measured value and the calculated value. A negative Δ value corresponds to a ratio in which the measured value is larger than the calculated value and vice versa.

Peak	h	k	l	Normed intensity [a.u.]	Averaged intensity [a.u.]	Averaged adjusted intensity [a.u.]	|F| AlPO4	Averaged adjusted intensity [a.u.] without (111)	|F| AlPO4 without (111)
-1a	1	1	-1	173	474	1000	1000		
1a	1	1	-1	109					
	1	1	-1	318					
-2a	0	0	2	17	50	104	131	175	148
2a	0	0	2	30					
	0	0	2	16					
1b	0	-1	2	13	40	85	191	143	216
	-1	0	2	9					
	0	-1	2	14					
-1b	0	-1	2	4					
1y	0	2	1	29					
-1y	0	2	1	25					
	0	2	1	25					
1c	1	1	-2	12	33	69	128	116	144
	1	1	-2	12					
-1c	1	1	-2	18					
2b	1	2	-1	25					
	2	1	-1	8					
	1	2	-1	12					
-2b	1	2	-1	3					
	2	1	-1	2					
	1	2	-1	2					
1x	1	1	2	44					
	1	1	2	15					
-1x	1	1	2	13					
1d	-2	2	0	331	1000	597	885	1000	1000
-1d	-2	2	0	119					
3a	2	2	0	1000					
	2	2	0	239					
1e	-1	-1	3	32	65	138	474	230	535
	-1	-1	3	23					
2e	2	2	-2	157	209	441	149	740	168
	2	2	-2	50					
-2e	2	2	-2	58					
3b	2	3	0	37	53	112	94	188	106
	2	0	3	13					
	2	3	0	14					
-3b	2	3	0	26					
	3	2	0	24					
	2	3	0	21					

Table I.24. Peak intensity comparison of the reflex associated with the US1 structure of "CZ-Al_2O_3" as illustrated in Figure 6.46. "|F| $AlPO_4$" serves as a reference to the literature data of the aluminium phosphate phase [83]. The "Averaged intensity" refers to the average of all the measured intensity of all peaks belonging to one type of reflex. The "adjusted" values are normalized so that the highest value equals 1000. Rows denoted with "without (111)" are adjusted as if the (111) reflex was not measured due to possible peak superposition with the $(1\bar{1}1)$ substrate reflex.

1g	1	2	-3	39	149	314	59	526	67
	2	1	-3	22					
	1	2	-3	28					
	1	2	-3	94					
	2	1	-3	72					
	1	2	-3	96					
	2	1	-3	98					
	1	2	-3	94					
	2	1	-3	64					
-2y	1	3	2	85					
	1	3	2	88					
2y	1	3	2	12					
	3	2	1	56					
	1	3	2	31					
3e	0	0	4	47	86	183	551	306	622
	0	0	4	26					
1h	2	2	-3	22	31	65	32	109	36
	2	2	-3	5					
2g	2	3	-2	30					
	3	2	-2	6					
	2	3	-2	8					
-2g	2	3	-2	15					
	3	2	-2	8					
	2	3	-2	10					
2i	1	3	-3	67	157	331	458	555	518
	3	1	-3	25					
	1	3	-3	34					
4e	3	3	-1	127					
	3	3	-1	28					
5a	3	3	1	201					
	3	3	1	47					
-4e	3	3	-1	26					
-5a	3	3	1	41					
1j	2	2	-4	217	202	427	515	715	582
	2	2	-4	98					
-1j	2	2	-4	114					
3i	2	4	-2	78					
	4	2	-2	49					
	2	4	-2	44					
-3i	2	4	-2	54					
	4	2	-2	52					
	2	4	-2	51					
6a	2	2	4	124					
	2	2	4	69					
-6a	2	2	4	75					
2j	3	3	-3	90	141	297	331	497	374
	3	3	-3	42					
-2j	3	3	-3	46					

Table I.25. Extension of Table I.24.

4i	1	-1	5	27	87	183	311	307	351
	-1	1	5	19					
	1	-1	5	31					
-4i	1	-1	5	54					
	-1	1	5	31					
	1	-1	5	29					
5e	1	1	5	55					
	1	1	5	47					
1k	-4	4	0	120	214	452	422	757	477
-1k	-4	4	0	124					
	-4	4	0	109					
6e	4	4	0	118					
	4	4	0	35					
-6e	4	4	0	36					
2k	-3	5	1	43	88	186	272	312	308
1l	-1	-3	5	20					
	-3	-1	5	17					
	-1	-3	5	21					
-2k	-3	5	1	41					
	-3	5	1	35					
-1l	-1	-3	5	40					
	-3	-1	5	10					
	-1	-3	5	10					
3d	1	5	3	71					
-3d	1	5	3	96					
	1	5	3	74					
5i	3	5	-1	44					
	5	3	-1	15					
	3	5	-1	22					
3j	4	4	-2	40	51	108	39	181	44
	4	4	-2	15					
-3j	4	4	-2	10					
2l	0	-2	6	28	71	149	320	250	362
	-2	0	6	17					
	0	-2	6	25					
6i	2	0	6	27					
	0	2	6	24					
	2	0	6	38					
-6i	2	0	6	66					
	0	2	6	24					
	2	0	6	20					

Table I.26. Extension of Table I.24.

Peak	μ [°]	h	k	l	h_s	k_s	L_s	Δ [°]
1a	1	1	-1	-1	2	-2	1	0.02
1a	61.02	1	1	-1	2	0	1	0
-1a	58.46	1	1	-1	2	0	1	0.2
1b	20.49	2	0	-1	1	2	1	0.42
1b	41.91	1	0	-2	2	1	1	-0.21
1b	80.45	-1	0	2	3	-1	1	-0.22
-1b	17.39	2	0	-1	1	2	1	-0.03
1c	1.4	1	-2	1	3	-3	0	0.33
1c	61.44	1	1	-2	3	0	0	0.01
-1c	58.06	1	1	-2	3	0	0	0.04
1d	31.63	2	0	-2	2	2	0	-0.68
-1d	27.83	2	0	-2	2	2	0	0.98
1e	2.02	1	-3	1	4	-4	1	1
1e	61.98	-1	-1	3	4	0	1	0.1
-1g	8.40	1	-3	2	1	4	0	0.06
1h	2.57	2	-3	2	5	-5	1	0.12
1h	62.55	2	2	-3	5	0	1	-0.29
1j	3.05	2	-4	2	6	-6	0	0.25
1j	63.04	2	2	-4	6	0	0	-0.24
-1j	56.44	2	2	-4	6	0	0	0.14
1k	33.56	4	0	-4	4	4	0	0.6
-1k	25.9	4	0	-4	4	4	0	0.09
-1k	85.91	-4	0	4	8	-2	0	3.16
1l	17.68	1	-5	3	2	6	1	-3.22
1l	49.72	3	1	-5	6	2	1	-3.58
1l	77.75	-3	-1	5	8	-2	1	0.11
-1l	9.63	1	-5	3	2	6	1	0.1
-1l	41.79	3	1	-5	6	2	1	-1.36
-1l	69.69	-3	-1	5	8	-2	1	-1.36
1x	4.74	2	1	1	1	-1	4	0.05
1x	65.1	1	1	2	1	0	4	0.09
-1x	55	1	1	2	1	0	4	-0.04
1y	32.05	1	0	2	1	1	3	0
-1y	27.33	2	1	0	1	1	3	0.24
-1y	87.31	0	1	2	2	-1	3	-1.73
2a	1.41	2	0	0	2	-2	2	-1.38
2a	61.42	0	0	2	2	0	2	-1.75
-2a	58.06	0	0	2	2	0	2	1.52
2b	20.91	1	-1	2	1	2	2	2.02
2b	42.15	2	1	-1	2	1	2	1.59
2b	80.86	1	2	-1	3	-1	2	-0.19
-2b	17.14	1	-1	2	1	2	2	-0.5
-2b	38.46	2	1	-1	2	1	2	-0.5
-2b	77.19	1	2	-1	3	-1	2	0.06
2e	2.22	2	-2	2	4	-4	2	0.08
2e	62.18	2	2	-2	4	0	2	-0.39
-2e	57.25	2	2	-2	4	0	2	-0.01
2g	13.92	2	-2	3	1	4	3	-0.36
2g	51.76	3	2	-2	4	1	3	0.18
2g	73.89	2	3	-2	5	-1	3	0.65
-2g	7.74	2	-2	3	1	4	3	0.11
-2g	45.49	3	2	-2	4	1	3	0.13
-2g	67.81	2	3	-2	5	-1	3	0.05
2i	21.76	1	-3	3	2	4	1	0.12
2i	43.62	3	1	-3	4	2	1	-0.89
2i	81.77	1	3	-3	6	-2	1	-0.88
2j	3.47	3	-3	3	6	-6	3	1.17
2j	63.47	3	3	-3	6	0	3	-4.94
-2j	55.96	3	3	-3	6	0	3	-4.9
2k	33.91	1	-3	5	4	4	3	5.2
-2k	25.51	1	-3	5	4	4	3	0.09
-2k	85.53	-3	1	5	8	-4	3	0.1
2l	18.24	6	0	-2	2	6	4	0.09
2l	50.48	0	-2	6	6	2	4	-0.33
2l	78.26	-2	0	6	8	-2	4	-0.36
3a	3.13	2	0	2	2	-2	4	-0.33
3a	63.13	2	2	0	2	0	4	0.55
3b	23.14	2	0	3	1	2	5	0.6
3b	44.57	3	2	0	2	1	5	0.56
3b	83.16	2	3	0	3	-1	5	6.93
-3b	14.96	2	0	3	1	2	5	-6.72
-3b	36.24	3	2	0	2	1	5	-6.95
-3b	74.89	2	3	0	3	-1	5	-0.12
3d	38.11	3	1	5	2	2	9	-0.12
-3d	21.26	5	3	1	2	2	9	0.36
-3d	81.34	1	3	5	4	-2	9	-0.5
3e	3.06	4	0	0	4	-4	4	-0.61
3e	63.06	0	0	4	4	0	4	-0.49
3i	22.6	2	-2	4	2	4	4	0.87
3i	44.41	4	2	-2	4	2	4	0.74
3i	82.6	2	4	-2	6	-2	4	0.88
-3i	15.08	2	-2	4	2	4	4	-2
-3i	36.81	4	2	-2	4	2	4	-2.05
-3i	75.07	2	4	-2	6	-2	4	0.1
3j	4.7	4	-2	4	6	-6	6	0.12
3j	64.75	4	4	-2	6	0	6	0.11
-3j	54.76	4	4	-2	6	0	6	-2.75
4e	3.68	3	-1	3	4	-4	5	-2.73
4e	63.67	3	3	-1	4	0	5	2.95
-4e	55.71	3	3	-1	4	0	5	0.06
4i	22.98	5	1	-1	2	4	5	0.22
4i	44.87	1	-1	5	4	2	5	-0.01
4i	82.97	-1	1	5	6	-2	5	-0.07
-4i	14.55	5	1	-1	2	4	5	0.1
-4i	36.46	1	-1	5	4	2	5	0.14
-4i	74.54	-1	1	5	6	-2	5	0.04
5a	7.74	3	1	3	2	-2	7	0.32
5a	67.7	3	3	1	2	0	7	0.3
-5a	51.67	3	3	1	2	0	7	-4.26
5e	5.4	5	1	1	4	-4	7	4.56
5e	65.45	1	1	5	4	0	7	4.48
5i	24.33	3	-1	5	2	4	7	-1.36
5i	46.18	5	3	-1	4	2	7	-1.43
5i	84.4	3	5	-1	6	-2	7	-1.43
6a	9.9	4	2	2	2	-2	8	-0.8
6a	70.13	2	2	4	2	0	8	-0.85
-6a	49.57	2	2	4	2	0	8	1.01
6e	6.43	4	0	4	4	-4	8	-0.21
6e	66.41	4	4	0	4	0	8	-0.25
-6e	53.04	4	4	0	4	0	8	-0.23
6i	25.13	6	2	0	2	4	8	-1.88
6i	47.01	2	0	6	4	2	8	-1.98
6i	85.14	0	2	6	6	-2	8	-1.89
-6i	12.46	6	2	0	2	4	8	2.19
-6i	34.33	2	0	6	4	2	8	2.1
-6i	72.5	0	2	6	6	-2	8	2.15

Table I.27. Overview of the analysed reflexes associated with the US1 structure and the corresponding surface coordinates. Δ denotes the difference between the measured in-plane angle of the reflex with the calculated peak position from a hexagonal lattice.

F. Fit parameters for XRD analysis at operando pressures

Powder ring [#]	q measured [1/ Å]	q Al_2O_3 [1/ Å]	Δ measured vs Al_2O_3 [%]	q Cu_2O [1/ Å]	Δ measured vs Cu_2O [%]
1	2.503	2.464	1.58	2.55	1.88
2	2.881	2.86	0.73	2.945	2.21
3	3.027	3.015	0.4	-	
4	4.074	4.067	0.17	4.164	2.22
5	4.773	4.707	1.4	4.883	2.31
6	4.765	4.707	1.23	4.883	2.49
7	4.986	4.928	1.18	5.1	2.28
8	5.745	5.719	0.45	5.889	2.5
9	6.272	6.181	1.47	6.417	2.31
10	6.434	6.404	0.47	6.584	2.34
		Mean	0.91		2.28
		Mean deviation	0.46		0.12

Table I.28. Momentum transfer of the measured powder rings at 23 bar pressure under Ar flow at room temperature measured for the simplified model system "Cu-Al_2O_3-operando", as shown in Figure 7.1. The data set is compared with both Al_2O_3 and Cu_2O reflexes and the difference in percent is calculated as Δ.

Powder ring [#]	q measured [1/ Å]	Δ measured first vs second scan [%]	q Al_2O_3 [1/ Å]	Δ measured vs Al_2O_3 [%]	q Cu_2O [1/ Å]	Δ measured vs Cu_2O [%]
1	2.499	0.16	2.464	1.42	2.55	2.05
2	2.868	0.453	2.86	0.28	2.945	2.67
3	3.03		3.015	0.5	-	
4	4.06	0.345	4.067	-0.17	4.164	2.55
5	4.747	0.463	4.707	0.85	4.883	2.87
6	4.967	0.383	4.707	0.79	4.883	2.67
7	5.712	0.578	4.928	-0.12	5.1	3.1
8	6.253	0.304	5.719	1.16	5.889	2.63
9	6.41	0.374	6.181	0.09	6.417	2.72

	Mean	0.38		0.53		2.66
	Mean deviation	0.09		0.46		0.19

Table I.29. Momentum transfer of the measured powder rings at 23 bar pressure under Ar flow at room temperature measured for the simplified model system "Cu-Al_2O_3-operando", as shown in Figure 7.2. The data set is compared with the first measurement as seen in Figure 7.1, as well as both Al_2O_3 and Cu_2O reflexes and the difference in percent is calculated as Δ.

Powder ring [#]	q measured [1/ Å]	q Al_2O_3 [1/ Å]	Δ measured vs Al_2O_3 [%]	q Cu_2O [1/ Å]	Δ measured vs Cu_2O [%]
1	2.499	1.42	1.58	2.55	2.00
2	2.871	0.37	0.73	2.945	2.53
3	3.036	0.71	0.4	-	-
4	4.069	0.04	0.17	4.164	2.29
		Mean	0.64		2.27
		Mean deviation	0.43		0.18

Table I.30. Momentum transfer of the measured powder rings at 30 bar pressure under Ar flow at room temperature measured for the ZnO-supported model system "CZ-Al_2O_3-operando", as shown in Figure 7.7. The data set is compared with both Al_2O_3 and Cu_2O reflexes and the difference in percent is calculated as Δ.

Peak [#]	q_xy [1/ Å]	q_z [1/ Å]	q [1/ Å]	Reference [1/ Å]	Average FWHM [1/ Å]	Nanoparticle size [nm]
1	2.8302	1.0641	3.0236	Cu (111) 3.01	0.10925	5.75
2	2.7887	2.0714	3.4738	Cu (220) 3.47	0.15475	4.06
3	2.2096	1.2884	2.5578	Cu_2O (111) 2.55	0.1476	4.26

Table I.31. Fit results and nanoparticle size calculations for the ROIS of Figure 7.8 to Figure 7.10 measured at 30 bar pressure under Ar flow at room temperature measured for the ZnO-supported model system "CZ-Al_2O_3-operando".

Powder ring [#]	q_xy [1/ Å]	q_z [1/ Å]	q [1/ Å]	Al_2O_3 Reference [1/ Å]	Δ [%]
1	1.775	0.774	1.936	1.8067	7.14
2	2.501	0.414	2.535	2.464	2.87
3	2.855	0.321	2.873	2.902	-1
4	3.669	0.623	3.722	3.614	3
5	1.1482	3.698	3.872	3.926	-1.36
				Mean	2.13
				Mean deviation	2.65

Table I.32. Analysis of the powder rings of Figure 7.14 measured at 30 bar pressure under H_2 flow at 550 K measured for the ZnO-supported model system "CZ-Al_2O_3-operando". The data set is compared with both Al_2O_3 and the difference in percent is calculated as Δ.

Acknowledgements

First, I would like to express my deepest gratitude to my supervisor, Prof. Dr. Andreas Stierle, for the opportunity to pursue this research in his group. His invaluable guidance, feedback, and support have been essential throughout my work on this thesis. I am especially thankful for our productive discussions and his insightful advice, which greatly contributed to the progress of this project. His attention to detail and constructive feedback on the final draft were instrumental in bringing this work to completion.

I would also like to extend my sincere appreciation to Dr. Vedran Vonk, my second supervisor, for his invaluable expertise in SXRD analysis and his generous support throughout my research. His technical expertise, insightful discussions, and meticulous proof-reading have enriched this thesis significantly. I am deeply grateful for his guidance and the many fruitful conversations that have enhanced the quality of my work.

My heartfelt thanks go to Dennis Renner for his hands-on support and dedication in navigating the challenges of my PhD journey. His expertise was invaluable, particularly in designing the UHV Zn chamber and helping with its construction, installation, and maintenance at the DESY Nanolab UHV facility. Dennis's technical knowledge, assistance in improving the high-pressure SXRD setup, and his constant moral support were indispensable, making this project and experience immensely rewarding.

I am also deeply grateful to my fellow PhD students and postdocs, Jan-Christian Schober, Dr. Marcus Creutzburg, and Dr. Simon Chung, for their constant support and collaboration. Their willingness to engage in helpful discussions, provide hands-on assistance in the lab, and always keep their doors open for advice was invaluable. Their camaraderie and expertise made this work both enriching and enjoyable.

My sincere thanks go to the many scientists who supported me during various beamtimes of my research: Dr. Vedran Vonk, Dr. Heshmat Noei, Dr. Marcus Creutzburg, Dr. Michael Wagstaffe, Dr. Robert Gleißner, Dr. Mona Kohantorabi, Jan-Christian Schober, Ming Chao Kao, Silvan Dolling, Lydia Bachmann, Mohammad Ebrahim Haji Naghi Tehrani, Artem Zaidman, Alexander Meinhardt, Nastasia Mukharamova, and Radik Batraev. I am equally grateful to the beamline staff members who provided invaluable assistance during these beamtimes: Olof Gutowski and Dr. Ann-Christin Dippel (DESY P07), Dr. Dmitri Novikov (DESY P23), and Dr. Patrick Zeller (BESSY ISISS beamline). Additionally, I want to thank

Dr. Thomas Keller, Dr. Jagrati Dwivedi, Arno Jeromin, and Satishkumar Kulkarni for their contributions to the SEM, EDX, and Scanning Auger measurements, as well as for their insightful scientific discussions. Special thanks also go to Katharina Röper for her support with administrative work and moral encouragement.

I am grateful to Prof. Dr. Bernhard Klötzer for serving as the second examiner of this thesis and to the additional members of the thesis examination committee—Prof. Dr. Daniela Pfannkuche, Prof. Dr. Andreas Stierle, Dr. Vedran Vonk, and Dr. Dieter Lott—for their time and commitment.

Finally, my deepest thanks go to my wife for her unwavering support, encouragement, advice, patience, and love. Her dedication in managing so many aspects of family and home life allowed me the freedom to focus on my thesis work, for which I am profoundly grateful.